Stony Brook University

Modulation of Mesoscale Convective Systems by Environmental Kinematics and Thermodynamics

A Dissertation Presented

by

Diego Adolfo Alfaro Berea

to

The Graduate School

in Partial Fulfillment of the

Requirements

for the Degree of

Doctor of Philosophy

in

Marine and Atmospheric Science

Stony Brook University

May 2015

Stony Brook University

The Graduate School

Diego Adolfo Alfaro Berea

We, the dissertation committee for the above candidate for the

Doctor of Philosophy degree, hereby recommend

acceptance of this dissertation.

Dr. Marat Khairoutdinov - Dissertation Advisor
Associate Professor
School of Marine and Atmospheric Sciences, Stony Brook University

Dr. Brian A. Colle - Chairperson of Defense
Professor, Director of the Institute of Terrestrial and Planetary Atmospheres
School of Marine and Atmospheric Sciences, Stony Brook University

Dr. Marvin Geller
Professor
School of Marine and Atmospheric Sciences, Stony Brook University

Dr. Edmund Chang
Professor
School of Marine and Atmospheric Sciences, Stony Brook University

Dr. George H. Bryan
Scientist III
Mesoscale and Microscale Meteorology Laboratory, National Center for Atmospheric Research

This dissertation is accepted by the Graduate School

Charles Taber
Dean of the Graduate School

Abstract of the Dissertation

Modulation of Mesoscale Convective Systems by Environmental Kinematics and Thermodynamics

by

Diego Adolfo Alfaro Berea

Doctor of Philosophy

in

Marine and Atmospheric Science

Stony Brook University

2015

The structural dependence of quasi-linear mesoscale convective systems, herein referred to as squall lines (SLs), on the characteristics of the embedding environment is investigated, contemplating the latent instability properties of air throughout the atmospheric column. The focus of this thesis is on idealized SLs, simulated in tropical and mid-latitude environments with the System for Atmospheric Modeling. The soundings used for simulating storms are specified using an original method, in which temperatures and moisture are prescribed primarily via vertical profiles of the convective available potential energy (CAPE) and the level of free convection (LFC). Analyses are based on latent instability concepts and the layer-lifting conceptual model, emphasizing inter-comparisons among simulated storms.

Results show that the precipitable water accounts for much of the precipitation rate variation for a given strength of the low level shear, irrespective of the CAPE profile. The precipitation efficiency is lower in the environments with weaker shear and dryer mid-tropospheric

conditions. A key finding is that, while frequently used CAPE indices are generally unsuitable for diagnosing SL characteristics, the integrated CAPE (ICAPE) is an environmental diagnostic which, for a given value of environmental shear, discriminates the amplitude of the storm induced heating. The skill of ICAPE follows from its relation to the buoyancy attained by the low and mid-tropospheric parcels as they ascend over the cold pool through layer-lifting convection. The dependence of the storm induced heating on environmental kinematics is also explained via the layer-lifting model, as the low level shear modulates the fraction of inflowing latent unstable air among the total storm relative inflow. Mid-latitude storms are weakly affected by LFC variations for a given CAPE profile, while the sensitivity of tropical SLs to the LFC is more noticeable, possibly due to their relatively shallow cold pools.

It is shown that cold pool shear-balance does not robustly predict the verticality of updrafts or the intensity of storm attributes within varying thermodynamic environments. Two-dimensional simulations using a simplified microphysics scheme confirm that latent instability variations can substantially affect the verticality and intensity of simulated updrafts, for a given degree of cold pool-shear balance. These simulations also indicate that the propagation speed of SLs is weakly affected by the amplitude of the storm induced heating, in contrast to steady analytical models of organized convection.

Table of Contents

List of Tables

Chapter 3 **Page**

Chapter 4

Chapter 5

List of Figures

Chapter 1 **Page**

Chapter 2

Chapter 3

Chapter 4

List of Abbreviations

AFTRF	Ascending front-to-rear flow.
CPBS	Cold pool-shear balance as measured by c / ΔU.
CRM	Cloud resolving model.
DCN	Density current nose.
DFTRF	Descending front-to-rear flow.
FTRF	Front-to-rear flow.
JWP	Jet wind profile, characterized by a reversal of the horizontal wind shear at low levels.
LTLR	Low-tropospheric lapse rate.
LTSP	Low-tropospheric shear profile, characterized by horizontal shear at low levels and unsheared winds aloft.
MAULS	Moist absolutely unstable layers.
MCS	Mesoscale convective system.
PE	Precipitation efficiency as measured by (water vapor inflow rate) / (surface precipitation rate) [%].
PR	Domain wide surface precipitation rate [mm day^{-1}].
PS	Propagation speed of the cold pool edge [m s^{-1}].
RH	Relative humidity [%].
RIJ	Rear inflow jet.
SAM	System for Atmospheric Modeling as described by Khairoutdinov and Randall (2003).
SGS	Sub-grid scale.
SL	Squall line.
SLIF	Shear layer inflow fraction, defined as the system-relative mass flux of air from the shear layer with respect to the total system-relative mass flux [%].
UTS	Upper-tropospheric sounding
WVIF	Water vapor inflow rate, defined as the rate of system-relative mass inflow of water vapor computed using environmental winds and moisture.

Acknowledgments

I am extremely grateful to my advisor, Dr. Marat Khairoutdinov, for continuously providing insightful guidance, while also encouraging me to conduct independent research. His constant support has enabled me to initiate a career as an atmospheric scientist. I am also very thankful to my dissertation committee, integrated by Dr. Brian Colle, Dr. Marvin Geller, Dr. Edmund Chang, and Dr. George Bryan. They have all contributed in different ways to my professional development, and I really appreciate the time they have dedicated to review my dissertation. I want to express gratitude to Dr. Sultan Hameed, for welcoming me to the School of Marine and Atmospheric Sciences, and to Dr. Daniel Knopf and Dr. Christopher Wolfe, who I was fortunate enough to have as professors. In addition, I want to thank Carol Dovi, Christina Fink, Gina Gartin, Mark Lang, and Steve Ortega, for being so attentive and cordial whenever I needed administrative and technical assistance.

This dissertation would not have been possible without the support I received from my parents, Malou Berea and Samuel Alfaro. They encouraged me to pursue graduate studies, and assisted me throughout this project in so many ways. I am also very grateful to my family in law, who were also exceedingly supportive. Finally, I want to thank my wife, Amalia King. She helped proofreading and editing the text, and she assisted me in the creation of some figures. She patiently listened when I talked to her about my research, and gave me valuable feedback. Amalia helped me manage my time, and she constantly motivated me to see this project through to completion.

Chapter 1:

Introduction

1.1 The subject of study: squall lines

Mesoscale convective systems (MCS) are the manifestation of organized deep convection, characterized by a life-span of several hours and horizontal scales that are in the order of 100 km (Houze 2004). With dynamics that fundamentally distinguish them from isolated thunderstorms, MCSs generally produce stratiform precipitation throughout a mesoscale region where circulations are driven by the latent heating and cooling. It is important that we understand the dynamics of MCSs, as they contribute significantly to seasonal cumulative precipitation across different regions in the tropics (Rickenbach and Rutledge 1998) and in mid-latitudes (Fritsch et al. 1986; Jirak et al. 2003), sometimes producing severe weather conditions (e.g. Ashley and Mote 2005).

The focus of this study will be on linear MCSs, where deep convection occurs along a nearly contiguous line, and which will hereafter be referred to as squall lines (SLs). SLs are a frequent form of MCS in both the tropics (Rickenbach and Rutledge 1998; LeMone et al. 1998) and in mid-latitudes (Jirak et al. 2003). A remarkable feature of such storms is that, once convection has been triggered, they can sustain continuous and long-lasting deep convective motions in the absence of forcing produced by synoptic or planetary scale disturbances (e.g. Rotunno et al. 1988), a property termed by LeMone et al. (1998) as self-organization. What is needed for the self-organization of SLs is an environmental flow (i.e. the surrounding airflow not strongly affected by moist convection) with significant horizontal wind shear and latent instability (e.g. Schultz et al. 2000). In fact, the structure of SLs is strongly dependent on the kinematic (Thorpe et al. 1982; Dudhia et al. 1987; Rotunno et al. 1988; Weisman et al. 1988; Fovell and Ogura 1989) and thermodynamic (Nicholls et al. 1988; Weisman 1992; Lucas et al. 2000; James et al. 2006; Takemi 2010) characteristics of the environmental flow. The spectrum of SL manifestations can be appreciated by comparing severe mid-latitude storms (e.g. see Houze et al. 1989; Bryan and Parker 2010), which can develop 4 km deep cold pools and updraft speeds exceeding 30 m s^{-1}, with tropical SLs (e.g. see Zipser 1977; Jorgensen et al. 1997; LeMone et al. 1998), with cold pools that are shallower than 1 km and characteristic updraft speeds of 10 ms^{-1} (Cotton et al. 2011).

This work addresses the mechanisms through which the environmental flow constrains the morphology of SLs. The objective is to understand the means by which different environmental features determine relevant storm characteristics, such as the propagation speed, surface precipitation rates, maximum surface wind speed, and the effects of SL convection on the large scale flow. These matters are of central importance in severe weather forecasting, as well as for parameterizing the effects of SL convection in numerical models. As a first step toward

understanding the modulation of SLs by the environmental flow, a general description of the characteristics of these storms is presented below.

1.2 Background

a. The structure of squall lines

Figure 1.1 presents a schematic representation of a mature SL, including a radar reflectivity plot on the horizontal plane in Fig. 1.1a, and the archetypical circulations in a plane perpendicular to the deep convective line in Fig. 1.1b. The deep convective line corresponds to the red area in Fig. 1.1a, with the stratiform region to the left. Some mid-latitude SLs display a local reflectivity maximum behind and separated from the deep convective line, which results from melting of ice hydrometeors (Houze et al. 1989). Radar reflectivity images have been used extensively for classifying MCSs. The direction of propagation, which is indicated by the thick arrows to be from left to right, implies that the SL has a trailing stratiform precipitation region. Parker and Johnson (2000) document observed mid-latitude SLs with leading and parallel stratiform precipitation regions, the distinction resulting mainly from the advection of hydrometeors by mid and upper-tropospheric winds. That study also notes that systems with trailing stratiform precipitation are the most commonly observed. Bluestein and Jain (1985) classify several SLs over Oklahoma by the evolution of the radar signature during their formative stages. SLs that develop a bow shaped deep convective line are called bow echoes (Weisman 2001), and long-lived linear systems that produce long swaths of damaging surface winds are referred to as derechos (Evans and Doswell 2001).

The rightmost arrows in Fig. 1.1b, which represent system-relative environmental winds, show the presence of low-tropospheric horizontal wind shear perpendicular to the deep convective line.[1] Tropical SLs develop frequently in environments with a reversal of the horizontal wind shear at mid-tropospheric levels (Barnes and Sieckman 1984; Alexander and Young 1992; LeMone et al. 1998). The effect of the line-perpendicular wind shear on the structure of SLs has received much attention in the past, as will be described shortly. The deep convective line is depicted in red, and it is collocated with the edge of the cold outflow at low levels. This is meant to represent the role of the cold outflow for continuously triggering deep convection, even though convection may be elevated (Parker 2008), or triggered ahead of the cold outflow edge by gravity waves (Fovell et al. 2006). Many studies use the term cold pool to refer to the cold outflow, although these concepts will be treated separately in chapter 3. A slowly ascending and positively buoyant front-to-rear flow (FTRF) is located behind the deep convective line. The rear-inflow jet (RIJ) flows beneath the FTRF, cooling by precipitating hydrometeors as it descends due to the horizontal buoyancy gradient at the FTRF-RIJ boundary (Lafore and Moncrieff 1989). The deep convective line and the cold outflow are highly advective in nature, while the RIJ and the FTRF are the gravity wave response of the troposphere to the patterns of latent heating and cooling produced by microphysical processes (Pandya and Durran 1996). Gravity waves can also perturb the flow on the downshear side of the cold pool edge.

One important geometrical characteristic of SLs is that deep layers of environmental air must ascend and cross the deep convective line in the presence of a propagating cold outflow, as implied by the inflowing environmental winds in Fig. 1.1b. Thus, all environmental air of storm-

[1] Some linear MCSs are organized parallel to mean the horizontal wind shear (e.g. slow-moving cloud lines in Barnes and Sieckman 1984), but this work will exclusively consider linear systems that are perpendicular to the low-tropospheric wind shear.

relative inflow takes part in the deep convective process, with the storm-relative mass influx at each layer being constrained by the kinematic characteristics of the environment. This form of convection, referred to as layer-lifting convection (Mechem et al. 2002; Houze 2004) or slantwise layer overturning (Moncrieff 2010), differs fundamentally from the archetypical and non-propagating plume-like updraft, which entrains air at its boundaries through gravity wave circulations and turbulent processes (Bretherton and Smolarkiewicz 1989; de Rooy et al. 2013). The implications of such differences will be central to the methodology and analyses considered in this work.

Two additional considerations are worth highlighting. First, the storm depicted in Fig. 1.1 represents a SL at maturity. The stratiform region is absent during the formative stages (Houze et al. 1989), during which the deep convective region may not be linearly organized (Bluestein and Jain 1985). During the decaying stages, the intensity of deep convection is significantly reduced until the stratiform precipitation is all that remains. Second, there may exist variability along the SL, with bookend vortices forming at the edges of the deep convective line (Weisman 1993), or asymmetries developing as a result of the Coriolis force (Houze et al. 1989; Skamarock et al. 1994). In the latter case, the cyclonic vortex can seed a midlevel mesoscale convective vortex (MCV).

b. The role of environmental shear for squall line organization

The association between environmental shear and the existence of SLs has been recognized at least since the seminal work by Newton (1950), who suggested that SLs derive kinetic energy from the environment to propagate ahead of their parent cold front. A clearer picture about the role of shear emerged from analyses of numerically simulated storms. Numerical investigations by Thorpe et al. (1982), who simulated mid-latitude SLs in a variety of kinematic environments, showed that storms are steadier and more intense when simulated in environments with shear confined to low-tropospheric levels. They argued that a given magnitude of low-tropospheric shear can maintain the storm aligned with the cold outflow edge, while the mid to upper-tropospheric shear would deplete updrafts of their energy (e.g. see Lilly 1979).

A different interpretation was presented by Rotunno et al. (1988) (hereafter RKW88), who noted that, in cases with low-level shear, deep convection by parcels lifted above their level of free convection (LFC) is inhibited when SLs are simulated in weakly sheared environments. RKW88 argued that updrafts triggered by the cold outflow would tilt depending on the strength of the low-tropospheric environmental shear relative to the cold pool intensity (c), the latter being defined as

$$c = \left(-2\int_0^{z'} b(z)dz \right)^{.5}$$

where b is the vertical profile of buoyancy within the SL, and z' is the height at which neutral buoyancy is first attained (i.e. the integration is throughout levels of contiguous surface-based negative buoyancy). According to RKW88, a vertically oriented updraft can exist when the vorticity in the shear layer balances the vorticity generated at the edge of the cold outflow, i.e. $\Delta U = c$, where ΔU measures the difference between surface winds and winds at the top of the shear layer. According to RKW88, the updraft will tilt in the absence of such balance, upshear when $\Delta U < c$, and downshear when $\Delta U > c$, as illustrated in Fig. 1.2. This dependence of the updraft orientation on the balance between ΔU and c is commonly referred to as RKW theory, and it has been a matter of much scientific debate (e.g. see Nicholls et al. 1988; Lafore and Moncrieff 1989; Rotunno et al. 1990; Xu 1992; Xue et al. 1997; Xue 2000; Coniglio and Stensrud 2001, 2006;

Weisman and Rotunno 2004; Stensrud et al. 2005; Bryan et al. 2006; Coniglio et al. 2012; Bryan and Rotunno 2014). A more thorough and detailed analysis of RKW concepts will be presented in chapter 5.

c. Squall line environments: tropical marine systems

Tropospheric temperatures over the tropical oceans are dynamically constrained to have nearly moist-adiabatic profiles, which results from a weak Coriolis force in a convective quasi-equilibrium regime (Arakawa and Schubert 1974; Yano and Plant 2012). The convective available potential energy (CAPE), a popular measure of latent instability, is also highly constrained by convective quasi-equilibrium. Hence the limited variations in the thermodynamic environments of SLs observed during the Equatorial Mesoscale Experiment (EMEX) (Alexander and Young 1992) and the Tropical Ocean Global Atmosphere (TOGA) Coupled Ocean–Atmosphere Response Experiment (COARE) (LeMone et al. 1998). This state of affairs complicates an observational verification of any direct relationship between CAPE and SL morphology (Alexander and Young 1992), as implied by steady analytical models of Moncrieff and collaborators (e.g. Moncrieff and Miller 1976; Liu and Moncrieff 1996; see also chapter 5). Nonetheless, numerical investigations by Nicolls et al. (1988) and Lucas et al. (2000) show that precipitation rates and updraft intensities are enhanced in cases with greater relative humidity (RH) above the boundary layer, while Mechem et al. (2002) found that layer-lifting convection is suppressed in relatively dry environments. Those studies show that tropical SLs are sensitive to environmental thermodynamic variations, but the workings behind such dependence remain poorly understood.

With regards to environmental kinematics, observational studies from the GARP Atlantic Tropical Experiment (GATE) (Barnes and Sieckman 1984), EMEX (Alexander and Young 1992), and TOGA COARE (LeMone et al. 1998) have consistently found that SLs organize perpendicular to the low-tropospheric wind shear and move parallel to it when ΔU is greater than .02 m s^{-1} hPa^{-1}. Those studies show that typical shear values are $\Delta U \approx 10$ m s^{-1} over the lowermost 2 km. More details about the organized storms in convective quasi-equilibrium emerged from a numerical study by Robe and Emanuel (2001), where a cloud resolving model (CRM) is used in order to simulate radiative-convective equilibrium states with different shear values. They found an increasing degree of linear convective organization for stronger low-tropospheric shear. That study also notes that when the shear is lower than the optimal value given by RKW theory, SLs organize perpendicular to the shear vector; on the other hand, when the shear is greater than the RKW optimal, SLs organize at an angle to the shear vector, such that ΔU is near RKW optimality. This result suggests that $\Delta U > c$ does not occur in radiative-convective equilibrium states, and it corroborates the importance of cold pool-shear balance.

d. Squall line environments: continental mid-latitude systems

Observational studies reveal that severe mid-latitude SLs over the continental United States occur in environments with CAPE values around 2250 J kg^{-1} (e.g. Bluestein and Jain 1985; Wyss and Emanuel 1988; Evans and Doswell 2001; Cohen et al. 2007), which is higher than the 1300 J kg^{-1} characteristic of tropical environments (Barnes and Sieckman 1984; LeMone et al. 1988). In addition, a large inter-case CAPE variability is observed in mid-latitudes, ranging between 1000 and 6000 J kg^{-1} (Evans and Doswell 2001; Cohen et al. 2007). Such a build-up of latent instability can result from capping layers, which form as air from mountainous regions, heated by a high surface sensible heat fluxes, flows over moist air at lower altitudes (e.g. Carlson et al. 1983). These triggered instances of deep convection arise in a manner that differs fundamentally from the

convective quasi-equilibrium regime (e.g. see Emanuel et al. 1994). Such configurations occur in just a few continental regions, such as southern Brazil and northern Argentina (Houze 2012), the plains and Middle West of the United States (Carlson et al. 1983), and possibly near Darwin in northern Australia, where mid-latitude-like SLs were observed by Keenan and Carbone (1992).

Despite the large CAPE variability that can occur in mid-latitude SL environments, there is no observational evidence linking CAPE to the storm propagation speed, precipitation rates, or the severity of surface winds (Wyss and Emanuel 1988; Evans and Doswell 2001; Cohen et al. 2007). Such state of affairs contrasts with the numerical investigations of Weisman (1993), who showed that SLs simulated in environments with greater CAPE lead to greater surface wind speeds. Yet, a number of later studies have shown that, for a given amount of CAPE, simulated SLs are also sensitive to the low to mid-tropospheric temperature lapse-rate (Takemi 2007, 2010) and moisture (James et al. 2006; James and Markowski 2010). Such findings may explain why observational studies have failed to identify significant correlations between CAPE and different characteristics of SLs. But a robust conceptual framework for understanding SL sensitivity to the thermodynamic environment, as RKW theory does for environmental kinematics, remains elusive.

Severe mid-latitude SLs organize perpendicular to the environmental shear between 1 km and 3 km height (Bluestein and Jain 1985; Wyss and Emanuel 1988), with ΔU as low as 5 m s^{-1}, and reaching ΔU = 30 m s^{-1} (Evans and Doswell 2001). Analyzing proximity soundings, Cohen et al. (2007) found that SLs which produce severe surface winds tend to occur in environments with greater ΔU than non-severe MCSs. This result may be related to RKW concepts, but such a hypothesis cannot be rigorously tested exclusively through proximity soundings, as these do not provide reliable information about c, a parameter that can range between 20 and 35 m s^{-1} in mid-latitude SLs (Bryan et al. 2005). It is worth mentioning that observational studies have not yet evinced the workings of RKW theory, despite various numerical experiments showing a robust intensification of storm attributes as SLs become more RKW optimal (RKW88; Weisman et al. 1988; Fovell and Ogura 1989; Weisman 1992, 1993; Weisman and Rotunno 2004; Bryan et al. 2006). This state of affairs is probably related to the fact that SLs are strongly affected by the thermodynamic characteristics of the environment, in ways that are not well understood. In this regard, it is important to consider that the spectrum of environments in which SLs are observed is much more diverse than those contemplated by idealized SL simulations, as noted by Evans and Doswell (2001). This observation is central to this thesis.

e. Idealized squall line simulations

It is difficult to stress enough the important role that cloud resolving models (CRMs) have played in shaping our comprehension about the dynamics of deep convection. CRMs can provide detailed output data, and allow simulations to be performed under controlled and simplified settings. These features can be useful for identifying physical processes and testing relevant hypotheses. For instance, our understanding about the organization of deep convection into long-lived multicell and supercell storms was very limited before numerical studies by Klemp and Wilhelmson (1978), Wilhelmson and Klemp (1978), Weisman and Klemp (1982, 1984), among others. Regarding SLs, their morphological dependence on the environmental shear at low levels has been revealed through numerical investigations by Thorpe et al. (1982), Dudhia et al. (1987), RKW88, Weisman et al. (1988), Fovell and Ogura (1989), among others. It is important to note that there are uncertainties inherent to CRMs, which may result from the numerical framework employed (e.g. Weisman et al. 1997; Bryan et al. 2003; Bryan 2005; Bryan and Morrison 2012), or the parameterization of physical processes (Takemi and Rotunno 2003; Morrison et al. 2009).

Nonetheless, there can be no doubt that CRMs constitute a key tool for analyzing the dynamics of atmospheric convection.

While CRMs led to the formulation of RKW theory, which has become the dominant paradigm for understanding the modulation of SL morphology by environmental kinematics, a general framework for incorporating environmental thermodynamics does not yet exist. This is so despite the possibility of using CRMs to simulate idealized SLs in carefully designed thermodynamic environments. But the task of specifying thermodynamic soundings is in itself challenging. For instance, it may be difficult to determine a priori which cases constitute relevant sensitivity tests. In addition, such sensitivity tests must be designed under consideration of physical constraints, such as water vapor sub-saturation and dry static stability. And even after the sensitivity tests have been determined, the generalization of results may not be straight forward, which requires either contemplating soundings representative of the spectrum of naturally occurring SL environments, or developing a robust conceptual framework (e.g. RKW theory). Such complications will be exemplified through a review of some numerical studies which have investigated the dependence of simulated SLs on the thermodynamic environment.

Weisman (1993) specified different thermodynamic soundings using analytic profiles of relative humidity (RH) and potential temperature, the latter interpolating between prescribed values at the surface and the tropopause, as described in Weisman and Klemp (1982). Thermodynamic variations consisted of modifying the boundary layer moisture and varying the potential temperature at the tropopause, implying different temperature lapse rates. The study focused on CAPE as a means for characterizing the environmental thermodynamics. Weisman (1993) concluded that CAPE of at least 2000 J kg^{-1} is required to sustain severe long-lived bow echoes, which is an overestimate according to data by Evans and Doswell (2001); in addition, the study noted that SLs tend to produce greater surface winds in higher CAPE environments, a feature that is not apparent in results by Cohen et al. (2007). Furthermore, more recent studies by Takemi (2007, 2010), who use the same method for generating soundings as Weisman (1993), show that SLs of varying intensity can be simulated for a given value of CAPE and environmental shear. The authors propose that the average low-to-mid-tropospheric temperature lapse rate is a fundamental factor modulating a SL's intensity. But Takemi did not propose a dynamical explanation for their conclusions, obscuring the generality of their results.

McCaul and Weisman (2001) proposed a more flexible technique for generating soundings, determining temperatures above the mixed layer via specification of the buoyancy profile of a pseudoadiabatically lifted surface parcel. This method was designed to allow temperature modifications, which are directly related to buoyancy, for a given CAPE. James et al. (2006) used this method to simulate bow echoes, specifying RH profiles in a manner analogous to Takemi (2007, 2010). The study concluded that low levels of specific humidity favors the cold pool development, thus leading to more organized and intense SLs. These conclusions contrast with findings by James and Markowski (2010), who showed that dry mid-tropospheric conditions are detrimental to SL intensity. Moreover, inspection of the soundings considered by James et al. (2006) and Takemi (2010) suggests that both studies analyzed analogous inter-case thermodynamic variations, produced similar systematic changes in SL characteristics, but elaborated different interpretations of their results. In both studies, the soundings with lower levels of mid-tropospheric specific humidity were also the ones with greater low-to-mid-tropospheric temperature lapse rates, and led to more intense storms.

Idealized numerical studies have contemplated very narrow types of mid-latitude soundings, as noted by Evans and Doswell (2001). Inter-case environmental variations have focused on modifying the boundary layer moisture and the temperature lapse rate aloft. But observations by Bluestein and Jain (1985) indicate that the temperature variability is greatest near the surface, while dew-point temperatures vary the most in the mid-troposphere. Thermodynamic environments of tropical SL also seem to be underrepresented in the literature of idealized simulations, with only a few studies contemplating systematic sounding variations (e.g. Nicholls et al. 1988; Lucas et al. 2000). Deepening our knowledge of the dependence of organized convection on the environment may be crucial for understanding tropical intra-seasonal oscillations (Zhang 2005; Moncrieff 2010), as well as for improving the representation of convection in numerical models.

1.3 Motivation

CAPE is probably the most commonly used environmental diagnostic for describing the thermodynamic state of the atmosphere, in the context of deep convection. It is related to the cloud-work function (Arakawa and Schubert 1974), such that both diagnostics are identical in the limit of convection without entrainment and with unit normalized convective vertical momentum (Yano and Plant 2012). This justifies the use of CAPE as a parameter for the cumulus parameterization of Zhang and McFarlane (1995), which is the deep convective scheme in the community atmospheric model (CAM). One question that motivates this study is whether CAPE is an appropriate parameter in the context of MCSs, and whether more useful thermodynamic diagnostics can be formulated.

The aforementioned studies of idealized SL simulations have emphasized CAPE, even though there is no observational evidence linking CAPE to SL characteristics. Conventionally, CAPE is an index computed by integrating the buoyancy of an ascending parcel, the origins of which are near the surface. CAPE can be thought of as the kinetic energy attained by an infinitesimally small and non-mixing thermal of near-surface air as it ascends while accelerating upward due exclusively to the buoyancy force. Although highly idealized, this simple model is widely used in practical applications, partly justified by the small observed variability of CAPE in convective quasi-equilibrium regimes, relative to the tendency for it to change due to surface and radiative heat fluxes (e.g. Emanuel 1994). However, the applicability of this model for characterizing SL environments is conceptually questionable because it does not conform to layer-lifting convection, wherein deep layers of atmospheric air are lifted by a propagating cold outflow. Layer-lifting processes affect the mesoscale circulations in SLs, which in turn impact significantly on the interaction between deep convection and the large scale flow (Houze 2004). These processes are unlikely to be captured by the latent instability properties of a single parcel.

This thesis presents an investigation into the environmental modulation of SLs through a framework which contemplates the vertical profiles of CAPE and LFC throughout the whole atmospheric column, i.e. computing these indices for parcels originating at different levels on the sounding. This characterization of the thermodynamic environment is conceptually appropriate for studying layer-lifting convection, while taking advantage of the simplicity afforded by parcel theory. For instance, the latent heating of ascending mid-tropospheric parcels, which is likely to affect the mesoscale circulations in SLs, can be investigated by considering variations in CAPE values above the boundary layer. In practical terms, this perspective serves as the basis of a new method for specifying thermodynamic soundings, in which low and mid-tropospheric

temperatures and water vapor mixing ratios are determined via the vertical profiles of CAPE and LFC, as described in chapter 2. This method will aid the design of environments in which to numerically simulate idealized SLs, such that the sensitivity of storms to variations of different environmental features can be readily interpreted in terms of layer-lifting convection, while appealing to relevant indices in the context of latent instability. These investigations are the subject of chapters 3 and 4, which focus on severe mid-latitude storms and tropical SLs, respectively. An investigation into the effects of latent heating on the structure of upshear tilted updrafts is explored in chapter 5, providing an assessment of RKW theory in cases with varying latent instability profiles. To end this work, chapter 6 presents concluding remarks.

Figure 1.1. Two different schematic views of a mature squall line are represented. In a) the horizontal radar reflectivity pattern typical of squall lines with trailing stratiform precipitation is displayed, with arrows pointing in the direction of propagation of the system. Red represents high reflectivity values, with moderate values in yellow, and lower reflectivity is in green. In b) the airflow typical of squall lines is displayed in a plane perpendicular to the deep convective line. The rightmost arrows represent environmental winds. The deep convective line is shown in red. See text for further details.

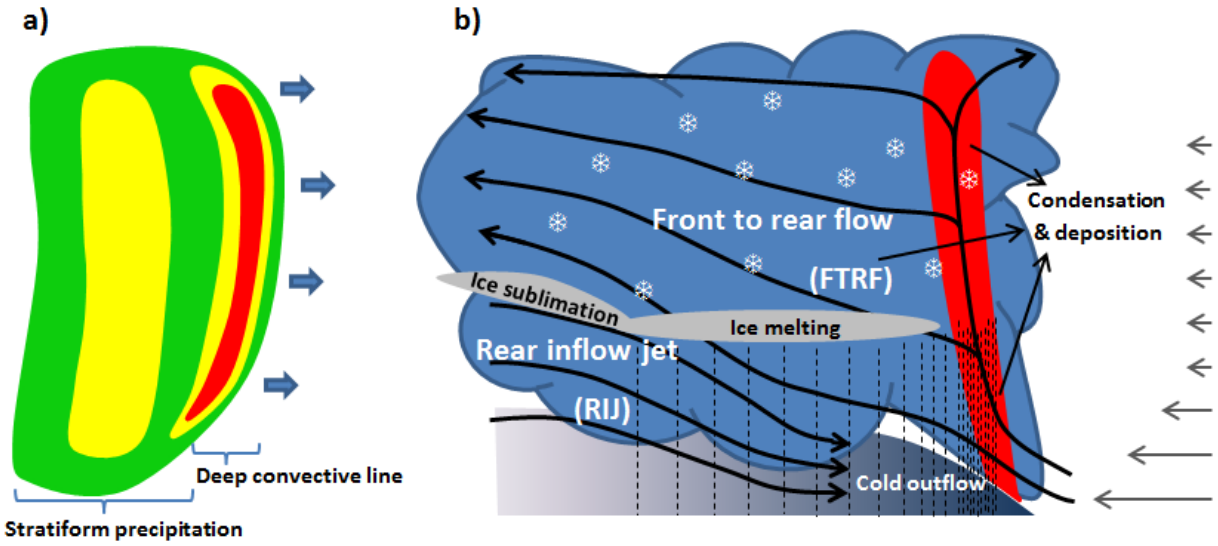

Figure 1.2. The trajectories followed by low-tropospheric air in different cold pool-shear configurations, as implied by RKW theory. The gray area in the lower left corner represents a cold outflow produced by a storm, with $\rho_1 < \rho_2$.

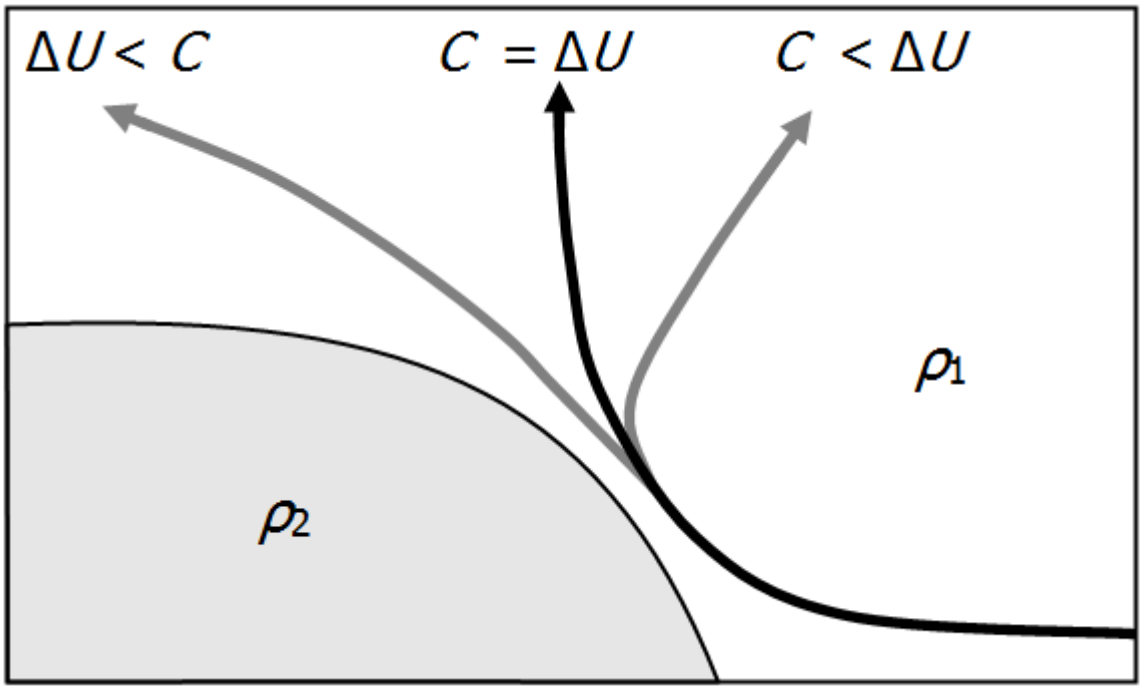

Chapter 2:

Thermodynamic framework: latent instability, parcel theory, and a method for generating soundings via vertical profiles of CAPE and LFC

It is known that the morphology of SLs is modulated by the thermodynamic environment, but how this operates remains poorly understood. This is so despite the availability of CRMs, which allow controlled experiments to be performed in idealized settings. This state of affairs may reflect the lack of a robust conceptual framework for characterizing the thermodynamic environment in layer-lifting convection, with past studies focusing mainly on CAPE derived from a near-surface parcel. This chapter will present an alternative framework which contemplates the vertical distribution of parcel indices throughout the atmospheric column. It will be argued that this perspective is more appropriate for studying SLs, in which mid-tropospheric air takes part in the convective process, alongside near-surface air.

The outline of this chapter is as follows: Section 2.1 is devoted to providing background on concepts that underlie the framework proposed herein, including a discussion on latent instability and parcel theory. The mathematical relations through which thermodynamic soundings are constrained by vertical profiles of parcel indices will follow in section 2.2, including a graphical description of the underlying mathematical relations, and an outline for generating soundings in practice. A brief discussion is presented in section 2.3, followed by a summary in section 2.4.

2.1 Background: latent instability and parcel theory

a. Latent instability

Deep moist convection in the atmosphere results from an instability in which air that is displaced above its initial position accelerates upward due to positive buoyancy, which arises from latent heating. This discussion will pertain to cases in which the instability results from fluid perturbations within a fixed basic state, as opposed to instabilities arising from the evolution of the basic state itself (e.g. potential instability; see Sherwood 2000).[2] The type of instability under consideration is sometimes called conditional instability, a term that has led to some confusion because it is also used to refer to a temperature lapse rate that is greater than pseudoadiabatic and lower than dry-adiabatic. To avoid such confusion, and following the terminology proposed by Schultz et al. (2000), conditional instability will be reserved for the definition pertaining to the lapse rate, while the actual instability described above will be referred to as latent instability. The

[2] The distinction can also be stated in terms of whether perturbations are horizontally global (e.g. potential instability) or localized (latent instability).

existence of conditional instability in the atmosphere is necessary, although not sufficient, for the manifestation of latent instability (Sherwood 2000).

In terms of basic physical principles, *latent instability results from the coupling between moist thermodynamics and vertical motions by means of the hydrostatic equation*, regardless of the fact that deep convection in the atmosphere may depend fundamentally on non-hydrostatic effects. To see this, consider the hydrostatic equation

$$\frac{dp}{dz} = -g\rho \tag{2.1}$$

where p is pressure, g is the acceleration due to gravity, and ρ is density. Equation (2.1) establishes the rate of pressure decrease with height in a hydrostatic atmosphere, thus linking a thermodynamically relevant variable, p, with the vertical coordinate, z. And even though the dynamics of deep convective storms can be highly non-hydrostatic (e.g. Rotunno and Klemp 1982), there do not exist atmospheric phenomena in which the vertical distribution of p between the surface and the tropopause is not predominantly determined by (2.1). This can be argued more formally by using (2.1) to estimate the magnitude of hydrostatic pressure differences throughout the troposphere, and compare such value to the typical magnitude of non-hydrostatic pressure perturbations. Using the ideal gas equation, $p = \rho TR$, where T is temperature and R is the ideal gas constant, and integrating Eq. (1) between the surface ($z_0 = 0$) and the height of the tropopause (z_{tr}) gives

$$\frac{p_{tr}}{p_0} = \exp\left(-\frac{g}{R}\int_{z_0}^{z_{tr}} T^{-1} dz \right) \tag{2.2}$$

where subscripts 0 and *tr* respectively denote evaluation at the surface and the tropopause. Given that the argument of the exponential on the right hand side of eq. (2) is negative, and that the exponential function is strictly increasing in its argument, an upper bound for the left hand side of (2.2) can be established through a lower bound of $\int_{z_0}^{z_{tr}} T^{-1} dz$. Using the fact that $f(x) = 1/x$ is convex, Jensen's inequality implies that

$$\left(\int_{z_0}^{z_{tr}} T dz \right)^{-1} < \int_{z_0}^{z_{tr}} T^{-1} dz$$

Using $\int_{z_0}^{z_{tr}} T dz < \int_{z_0}^{z_{tr}} 300 dz$ as a very conservative bound of average tropospheric temperatures, and letting $z_{tr} = 12000$ km and $p_0 =$ 1000 hPa, it follows that pressure decreases at least 750 hPa between the surface and the tropopause. Comparing this estimate to the 2.5 hPa corresponding to the maximum pressure perturbation arising from a Rankine vortex in cyclostrophic balance, near the surface, and with maximum wind speeds of 50 m s^{-1} (an F2 tornado; e.g. see Markowski and Richardson 2010), and considering that non-hydrostatic pressure perturbations tend to be spatially localized, it becomes clear that (2.1) largely determines the overall vertical distribution of tropospheric pressure.

In order to incorporate atmospheric thermodynamics, consider the adiabatic relationship between pressure and temperature as derived from the first law of thermodynamics for moist air

$$T = T_0 \left(\frac{p}{p_0} \right)^{R/c_p} \tag{2.3}$$

where R and c_p are the effective gas constant and the heat capacity of the air sample (i.e. of the mixture of water vapor and air; see Emanuel 1994), respectively. Having established that pressure in the atmosphere tends to decrease with height, then (2.3) implies that temperature will also tend to decrease under adiabatic ascent, in the absence of phase transitions. This has important consequences for water vapor phase transitions, as can be elucidated by the Clausius-Clapeyron equation, which to a good enough approximation for the present discussion states that (e.g. see Emanuel 1994)

$$e^* = 6.112 \exp\left[\frac{17.67(T - 273.15)}{T - 29.65} \right] \tag{2.4}$$

where e^* [hPa] is the saturation water vapor pressure. Using (2.4) and (2.3), e^* can be formulated as a function of pressure under adiabatic motions. On the other hand, the water vapor pressure (e) of the air sample following adiabatic motions satisfies $e = p \times q_v/(0.622+q_v)$, where q_v is the water vapor mixing ratio, which is conserved in the absence of phase transitions. Fig. 2.1 shows how different e and e^* curves corresponding to adiabatic motions of surface air cross when pressure becomes sufficiently small, implying water condensation. Considering the aforementioned link between pressure and height, it follows that ascending motions in the atmosphere can lead to water condensation.

The condensation of water under the ascent of moist air has profound consequences because it occurs in association with latent heating. Equation (2.3) is no longer valid under such circumstances, as air will cool less rapidly by a rate of $L_v dq_v/dt$, where L_v is the latent heat of vaporization. It is due to this phenomenon that there exist certain states of a moist atmosphere that are stable to infinitesimally small perturbations (i.e. satisfying dry static stability), but in which air may become positively buoyant under large enough upward displacements, thus accelerating further away from its level of origin. This is the essence of latent instability, and it drives deep convection in the atmosphere.

Throughout this work latent instability will be understood as a state of a dry statically stable atmospheric column, i.e. with a temperature lapse rate that is everywhere lower than the dry adiabatic lapse rate, in which air may become positively buoyant when lifted. Given that the troposphere is mostly stable or neutrally stable to infinitesimal vertical fluid displacements, latent instability is a subcritical instability (Sherwood 2000), in which fluid displacements need to exceed a certain threshold in order to grow. Thus, latent instability differs from the more common instability concept, which characterizes the state of a physical system in which infinitesimal perturbations grow. Therefore, small enough perturbations will not necessarily grow in a latent-unstable atmosphere, which has consequences for the storage of energy available for deep convective motions.

b. Parcel theory

Parcel theory is one of the most popular frameworks for diagnosing latent instability. It builds on the concept of the air parcel, a dimensionless sample of atmospheric air, the pressure of which adjusts instantaneously to that of the surrounding environment without inducing perturbations (Wallace and Hobbs 2006). Further assumptions on parcel thermodynamics under

water phase transitions (e.g. reversible or pseudoadiabatic; see Emanuel 1994), as well as suppositions regarding mixing with surrounding environmental air, determine the thermodynamic properties of the parcel under vertical displacements.[3] The buoyancy can then be measured, and latent instability can be diagnosed depending on whether there exists an air parcel on an atmospheric sounding which may become positively buoyant if lifted above its level of origin.

Parcel theory is frequently used to characterize latent instability in a quantitative manner. For a given thermodynamic sounding, the following indices are commonly associated with a latent-unstable parcel, i.e. one that becomes positively buoyant when lifted a certain distance, which are generally computed by lifting the parcel either reversible-adiabatically or pseudoadiabatically:

- Lifting condensation level (LCL): the highest pressure level (lowermost height) at which the parcel is saturated, i.e. p such that $e^*(p) = e(p)$.
- Level of free convection (LFC): pressure levels at which the parcel is in unstable equilibrium with the environment.[4] In other words, the parcel is neutrally buoyant and any perturbation will accelerate it away from its equilibrium level. There may be more than one LFC associated to a parcel.
- Equilibrium level (EL): pressure levels (other than the level of origin) where the parcel is in stable equilibrium with the environment. There may be more than one EL associated to a parcel.
- Convective available potential energy (CAPE): the kinetic energy per unit mass attained through buoyant accelerations of a parcel which, being at rest at an LFC, reaches the nearest EL aloft.
- Convective inhibition (CIN): the work per unit mass needed to displace a motionless parcel at its level of origin to the nearest LFC aloft.

The LCL, LFC, and EL are often presented as in units of spatial distance above the surface, which is derived from the hypsometric equation. This is reasonable because the vertical distribution of pressure is to a large extent determined by (2.1), but in some instances it may not be accurate (e.g. within an intense tornado).

A more quantitative treatment of pseudoadiabatic parcel indices will be presented in section 2.2. For now it is highlighted that there are many well-known drawbacks associated with parcel theory. For instance, the neglect of pressure perturbations arising from deep convective motions may render $w_{\max} = \sqrt{2\mathrm{CAPE}}$, the maximum vertical velocity that can be attained by a parcel at rest at its LFC, as an unrealistic overestimate (e.g. Weisman et al. 1997). In addition, microphysics and entrainment affect parcel properties in a manner that is flow dependent, which is why it is difficult to accurately account for these processes. To give an example, the sounding in Fig. 2.2 has latent-unstable parcels, but the manifestation of latent instability requires that air

[3] It is common to neglect mixing of the air parcel with environmental air, but this is central to the stochastic mixing model of Raymond and Blyth (1986), which is based on parcel theory.

[4] In the case of pseudoadiabatic ascent, where the parcel loses its liquid water, the instability is one sided in the sense that the parcel is formally stable to downward displacements but unstable to infinitesimal upward displacements. Analogous considerations apply to the equilibrium level.

from near the surface must rise a considerable distance through very dry surroundings. In this case, latent instability may not be achievable by realistic atmospheric motions, as entrainment of sub-saturated air is likely to preclude buoyant ascent of lifted air. Nonetheless parcel theory remains very popular, as it constitutes simple conceptual framework which provides some guidance into the complexities of latent instability.

Most practical applications of parcel theory consider indices derived from only one parcel. Some commonly used indices contemplate the surface parcel, the most unstable parcel (the one with greatest CAPE), or the mixed layer parcel (which has q_v and potential temperature equal to the average throughout the lowermost portion of the sounding, usually the lowest 100 hPa), also called mean layer parcel. In general it is not evident which reference parcel is the most appropriate, which probably depends on the specific phenomena under consideration. This has implications for forecasting and parameterizing deep convective phenomena, as parcel indices can be very sensitive to the parcel which is taken as reference (e.g. Bunkers et al. 2002). Furthermore, a single parcel may not be sufficient for adequately characterizing how latent instability will manifest itself, especially in layer-lifting convection.

2.2 Vertical profiles of parcel indices, and a new technique for generating soundings

Much of this work is concerned with the dependence of SLs on the thermodynamic characteristics of the environment in which they are embedded. It will thus be useful to establish a framework for characterizing the thermodynamic environment in a physically meaningful way. Taking advantage of the simplicity afforded by parcel theory, while leaving aside the limitation of having to select a single parcel, the framework proposed herein contemplates the vertical distribution of parcel indices throughout the atmospheric column. In this context, parcel indices are functions of pressure, providing a correspondence between the level of origin of parcels on a given sounding and their respective index (e.g. Fig. 2.3 illustrates the pseudoadiabatic displacement of parcels originating at different levels).[5] This perspective could prove suitable for studying layer-lifting convection, as it contemplates latent instability properties of low and mid-tropospheric parcels, all of which may ascend within a SL.

In what follows, it will be shown that, given a low-tropospheric lapse rate (LTLR) and an upper-tropospheric sounding (UTS), the low and mid-tropospheric portion of the sounding can be uniquely determined by prescribing vertical profiles of CAPE and LFC. Resting on this result, a technique for specifying soundings primarily through vertical distributions of CAPE and LFC will be described. This method will then be used to design different environments by means of parameters that are physically meaningful in the context moist convection: CAPE, which measures the potential updraft intensity, and LFC, which determines the distance a parcel must be lifted to trigger latent-instability.

a. Notation

Let $T(p)$, $q_v(p)$ and $s_{ps}(p)$, respectively, denote the temperature, water vapor mixing ratio and pseudoentropy (e.g. see Emanuel 1994) describing a sounding, each assumed to be a smooth

[5] The vertical distribution of CAPE as considered herein differs from that contemplated by Blanchard (1998), who focused on varying the level up to which buoyancy is integrated from the LFC of a single parcel.

function of pressure, p.[6] It is assumed that parcels move pseudoadiabatically. The temperature of a parcel with pseudoentropy s_{ps} when at pressure level p' and with 100% RH is denoted by $T_{ps}(s_{ps}, p')$. Then, neglecting virtual effects for notational simplicity, the set

$$P = \{\, p \mid T(p') < T_{ps}(\, s_{ps}(p), p') \text{ for some } p' < p \,\}$$

contains the pressure levels on the sounding of latent-unstable parcels, i.e. parcels that can become positively buoyant when lifted, as shown in Fig. 2.3. The vertical distribution of LFC [Pa] is given by

$$\mathrm{LFC}(p) = \max \{p' \mid T(p') < T_{ps}(s_{ps}(p), p') \text{ for some } p' < p\}$$

and similarly for the EL [Pa],

$$\mathrm{EL}(p) = \min \{p' \mid T(p') < T_{ps}(s_{ps}(p), p') \text{ for some } p' < p\}$$

while CAPE [J kg^{-1}] is defined as,

$$\mathrm{CAPE}(p) = R \int_{\mathrm{EL}(p)}^{\mathrm{LFC}(p)} \left[T_{ps}\left(s_{ps}(p), p'\right) - T(p')\right] d\ln p'$$

These are expressed as functions of the levels of origin of latent-unstable parcels, and thus have P as their domain. As will be mentioned shortly, the soundings under consideration have the property that each latent-unstable parcel has only one LFC and one EL. Finally, let $\Gamma(p)$, $\Gamma_d(p)$ and $\Gamma_{ps}(p)$ respectively represent the environmental, dry-adiabatic and pseudoadiabatic lapse rates in pressure coordinates (i.e. $\Gamma = dT/dp$) evaluated at the point $T(p)$.

b. Class of soundings under consideration

For reasons discussed below, soundings are assumed to satisfy the following restrictions on Γ, as illustrated in Fig.2.3:

1. $\Gamma_{ps}(p) < \Gamma(p) < \Gamma_d(p)$, i.e. Γ is conditionally unstable, for $\mathrm{LFC}(p^*) = \mathrm{LFC}^* < p < p_0$, where p_0 is the surface pressure and $p^* = \inf(P)$.

2. $\Gamma(p) < \Gamma_{ps}(p)$, i.e. Γ is absolutely stable, for $p < \mathrm{LFC}^*$.

3. EL is finite.

Restrictions 1 and 2, together with the smoothness of T, imply that there exists a unique point of tangency between T and pseudoadiabats, found at height LFC^* (e.g. see Fig. 2.3). The key observation for linking the CAPE and LFC profiles to T and q_v is that each point $T(p)$ for $\mathrm{LFC}^* < p \leq \mathrm{MULFC} = \max_p [\mathrm{LFC}(p)]$ corresponds to the point where some latent-unstable parcel attains its LFC (MU is a prefix used to denote that the index applies to the most unstable parcel). This follows from condition 1, which guarantees that each pseudoadiabat given by $T_{ps}(s_{ps}(p), p')$ for $p \in P$ will cross T only once below LFC^* (i.e. T is nowhere parallel to pseudoadiabats below LFC^*), and analogous observations apply by conditions 2 and 3 to $\mathrm{EL}(p)$ above LFC^* (see Fig. 2.3). Therefore, the functions LFCs and ELs defined as $\mathrm{LFCs}[s_{ps}(p)] = \mathrm{LFC}(p)$ and $\mathrm{ELs}[s_{ps}(p)] = \mathrm{EL}(p)$ are well defined, respectively relating the values in the ranges of LFC and EL to the values in the set $S = \{s_{ps}(p) \mid p \in P\}$. Consequently,

[6] Subscripts *ps* refer to variables related to pseudoadiabats.

$$\mathrm{CAPEs}\,(s_{ps}) = R\int_{\mathrm{ELs}\,(s_{ps})}^{\mathrm{LFCs}\,(s_{ps})} \left[T_{ps}\left(s_{ps}, p'\right) - T\left(p'\right)\right] d\ln p' \tag{2.5}$$

defines the values in the range of CAPE as a function of the values in *S*. These functional relations allow the recovery of T and q_v from CAPE and LFC profiles via s_{ps}, as is described below. It is important to highlight that restriction 1 excludes soundings with strong capping inversions, which are commonly observed in the environments of severe mid-latitude storms over the Great Plains in the United States (Carlson et al. 1983). Nonetheless, examples given below show that a wide variety of soundings can be generated with the proposed technique, including realistic features such as elevated nearly dry-adiabatic layers overlying air with relatively large dry-static stability (e.g. see Bryan et al. 2005).

c. Constraining soundings by vertical profiles of CAPE and LFC

The computation of the vertical profiles of CAPE and LFC for a given atmospheric sounding is straight forward. Here it will be shown how the T and q_v of a thermodynamic sounding can be uniquely determined from knowledge of CAPE and LFC profiles. To do so, it is first assumed that Γ is known below MULFC (the LTLR), as are T and q_v above LFC* (the UTS). The former is needed so that T and q_v can be uniquely determined throughout the lower troposphere, while the latter determines EL(p) implicitly via pseudoadiabatic curves. To find T and q_v below LFC*, the chain rule is used to relate the derivatives of CAPE and CAPEs,

$$\frac{d\mathrm{CAPE}}{dp} = \left(\frac{d\mathrm{CAPEs}}{ds_{ps}}\right)\left(\frac{ds_{ps}}{dp}\right)$$

which by applying Leibniz integral rule to (2.5) gives

$$\frac{d\mathrm{CAPE}}{dp} = \left(R\int_{\mathrm{ELs}}^{\mathrm{LFCs}} \frac{\partial T_{ps}\left(s_{ps}, p\right)}{\partial s_{ps}} d\ln p\right)\left(\frac{ds_{ps}}{dp}\right) \tag{2.6}$$

additional terms being zero because $T[\mathrm{LFCs}(s_{ps})] = T_{ps}[s_{ps}, \mathrm{LFCs}(s_{ps})]$ and $T[\mathrm{ELs}(s_{ps})] = T_{ps}[s_{ps}, \mathrm{ELs}(s_{ps})]$. The fact that $0 < \partial T_{ps}(s_{ps}, p')/\partial s_{ps}$ holds everywhere allows the transposition of Eq. (2.6), such that ds_{ps}/dp can be integrated to give

$$s_{ps}\left(p\right) - s_{ps}\left(p^*\right) = \int_{p^*}^{p}\left(\frac{d\mathrm{CAPE}}{dp}\right)_{p'}\left(R\int_{\mathrm{EL}(p')}^{\mathrm{LFC}(p')} \frac{\partial T_{ps}\left(s_{ps}\left(p'\right), p\right)}{\partial s_{ps}} d\ln p\right)^{-1} dp' \tag{2.7}$$

where $(d\mathrm{CAPE}/dp)_{p'}$ is the derivative of CAPE evaluated at p'. Note that, if CAPE is known, then (2.7) can be used to uniquely determine s_{ps}.

Therefore, starting with the value $s_{ps}(p^*)$ implicit in the UTS's $T(\mathrm{LFC}^*)$, $s_{ps}(p)$ can be recovered from CAPE, LFC, and EL, the latter given by levels where pseudoadiabats cross the UTS. Then, T can be determined between LFC* and MULFC by the temperature that a saturated parcel originating at p and with pseudoetropy $s_{ps}(p)$ attains at LFC(p), which is given by $T_{ps}[s_{ps}(p), \mathrm{LFC}(p)]$ for $p \in P$. This reflects the fact that, ignoring virtual effects, the LFC of a parcel is always reached at a point on the environmental temperature curve (see Fig. 2.3). Below MULFC, T values follow from the prescribed LTLR. Once $T(p)$ is known, $q_v(p)$ can

be deduced for $p \in P$ by requiring that the sounding does indeed have pseudoentropy $s_{ps}(p)$ at level p. Therefore, $q_v(p)$ must be prescribed explicitly $\forall p \notin P$.

d. Graphical description of link between CAPE and LFC profiles and the sounding

To grasp the relationship between the CAPE-LFC profiles and T-q_v, it will be useful to consider a new function, CAPE′, defined by the relation CAPE′[LFC(p)] = CAPE(p) for $p \in P$ (i.e. CAPE′ is CAPE represented as a function of LFC). The usefulness of CAPE′ resides in that it uniquely determines T throughout the layer between LFC* and MULFC. The basic underlying principle is that parcels with a given CAPE′ will cross the T curve on a thermodynamic chart at the pressure level LFC, following a pseudoadiabat aloft because the parcel is saturated. Therefore, given a UTS, T can be integrated downward from LFC* by requiring that pseudoadiabats crossing the sounding at each level in the range of LFC imply CAPE′(LFC), which is equivalent to the description given in the previous subsection.

The downward integration procedure is illustrated by the schematic skewT-lnp chart in Fig. 2.4a. A temperature point on the sounding, T(LFC) with LFC* < LFC < MULFC is chosen, and it is assumed that T is known aloft (throughout this paragraph, LFC refers one value in the range of LFC(p)). The value of CAPE′(LFC) is thus determined via the unique pseudoadiabat passing through it. Two cases are depicted for a fixed pressure increment of ΔLFC, which imply different CAPE′ increments, ΔCAPE′ = CAPE′(LFC+ΔLFC) – CAPE′(LFC): assuming $\Delta\text{CAPE}'_2 < \Delta\text{CAPE}'_1$, as in Fig. 2.4a, then the pseudoadiabat passing through T(LFC+ΔLFC) = T(LFC) + ΔT must be greater in the latter case than in the former, which can be stated as $\Delta T_2 < \Delta T_1$. In general, a greater dCAPE′/dLFC will lead to greater Γ.

Regarding q_v, first assume that T has been determined through the above described procedure, so that the temperature of each parcel at its level of origin is known. Then, $q_v(p)$ must be such that the parcel originating at p has temperature T(LFC(p)) when pseudoadiabatically lifted to LFC(p), as illustrated by the two examples in Fig. 2.4b. It follows that, for a given T profile, if $\text{LFC}_2(p) < \text{LFC}_1(p)$ then $q_{v2}(p) < q_{v1}(p)$.

e. Generating thermodynamic soundings

Using the aforementioned results, one can specify thermodynamic soundings via CAPE and LFC profiles, once the UTS and LTLR have been prescribed. This method is envisioned primarily as a tool for designing sensitivity tests for studying the dependence of numerically simulated storms on thermodynamic variations in the environment. This can be done by choosing a *baseline* sounding satisfying conditions 1 and 2, then compute its CAPE(p) and LFC(p) profiles, and then generate soundings through variations of *baseline*'s CAPE(p), LFC(p), UTS, and LTLR (subject to the restrictions stated at the end of this section). The function CAPE′ can provide some guidance in terms of the resulting temperature variations, as shown in Fig 2.4a.

For example, assume the interest is on studying how simulated storms respond to variations of the vertically integrated CAPE,

$$\text{ICAPE} = \int_P g^{-1}\text{CAPE}(p)dp$$

and that the *baseline* sounding is similar to the one considered in RKW88, and many other idealized numerical studies of SLs (e.g. Weisman et al. 1988; Weisman 1992, 1993; Bryan et al.

2003; Weisman and Rotunno 2004; Bryan 2005; Bryan et al. 2006; Morrison et al. 2009; Seigel et al. 2013), which is shown in Fig. 2.5.

First, one may consider ICAPE variations in cases with *baseline*'s UTS, LTLR, and LFC, while multiplying the CAPE profile by a constant. These variations lead to changes in Γ, as shown in Fig. 2.6. This is consistent with the fact that $d\text{CAPE}'/d\text{LFC}$ is also scaled by a constant: if the constant is greater than 1, then $d\text{CAPE}'/d\text{LFC}$ increases, and so does Γ, the contrary being the case for a constant less than 1. Note that while the value of MUCAPE differs among the two soundings in Fig. 2.6, both have MUCAPE layers of equal depth.

Another sensitivity test can be designed in such a way that *T* equals that of *baseline*, while ICAPE is modified via mid-tropospheric moisture variations. This is a case where CAPE′ is useful, as it solely determines temperatures, while mid-tropospheric moisture can be modified by varying the LFC.[7] Fig. 2.7 shows two soundings which differ only in their mid-tropospheric moisture, both having identical CAPE, but differing in their CAPE and LFC profiles. Clearly, the drier sounding, i.e. the one with dew point temperatures represented by the dotted line in Fig. 2.7a, has lower CAPE throughout the latent-unstable layer, and will thus have lower ICAPE.

Finally, in order to test the skill of ICAPE, one may want to consider the cases displayed in Fig. 2.8. The sounding in blue has *baseline*'s CAPE and LFC profiles, but has a UTS which is 3 K warmer than *baseline* and with identical RH. This type of sensitivity tests may be relevant for studying SL characteristics under future climate scenarios. Another sensitivity test is given by the thin temperature and dew point temperature curves at low-tropospheric levels, which has baseline's CAPE, LFC, and UTS, but with a smaller LTLR. This sounding, which may be considered as representative of nocturnal SLs (Parker 2008), has higher low-tropospheric moisture than *baseline*, which is required so that CAPE does not vary as a consequence of lower temperatures therein. The red sounding in Fig. 2.8a has the same CAPE, UTS, and LTLR as *baseline*, but with different CAPE′ and LFC profiles, as shown in Figs. 2.8b and 2.8d. Note that this sounding has a relatively dry mid-troposphere, as well as an elevated nearly dry-adiabatic layer, features that are not unusual in severe weather environments (Carlson et al. 1983; Bryan et al. 2005).

The examples considered above are not exhaustive of sensitivity tests in which focus is placed on ICAPE. For instance, MUCAPE may not be necessarily found at the surface, especially in nocturnal SLs (e.g. Trier et al. 2006; Parker 2008). But the purpose of the examples presented above is to show how the present technique for generating soundings may be used in practice. In this regard, it is important to bear in mind the following considerations:

- Uniqueness of $q_v(p)$ for $p \in P$ is guaranteed only if CAPE is strictly positive therein.
- For consistency with the type of soundings under consideration, the relation $\text{CAPE}(p) \leftrightarrow \text{LFC}(p)$ for $p \in P$ must be bijective.
- $\text{CAPE}(p^*) = 0$
- $0 \leq \text{CAPE}$
- $\text{LFC}(p) < p$

[7] One can prescribe any two among the CAPE, CAPE′ and LFC profiles, from which the remaining profile can be uniquely recovered.

- LFC* must be identical to the value derived from the UTS.
- $d\mathrm{CAPE}'/dp$ is bounded by dry static stability (see Fig. 2.4a and the description given in the text).
- The LTLR may be lower than Γ_{ps}, but care is needed to avoid saturation.

2.3 Discussion

Previous investigations into the dependence of organized convection on the thermodynamic environment have used two different techniques for generating soundings, as described in the introduction. Weisman and Klemp (1982) used analytic profiles of RH and potential temperature, the latter interpolating between prescribed potential temperatures at the surface and the tropopause. Another method was suggested by McCaul and Weisman (2001), whereby the temperature profile is specified for a given surface based CAPE (SBCAPE) by prescribing the buoyancy profile of a pseudoadiabatically lifted surface parcel. This method is often used in association with the RH function of Weisman and Klemp (1982) (e.g. McCaul and Cohen 2002; James et al. 2006; James and Markowski 2010).

The method detailed in this chapter has several advantages over the aforementioned alternatives. For instance, the present technique accounts for the buoyancy attained by ascending mid-tropospheric parcels through the CAPE profile, while the method of McCaul and Weisman (2001) focuses exclusively on near-surface parcels (the method of Weisman and Klemp (1982) is not formulated in terms of CAPE). This matter may be particularly important in layer-lifting convection. In addition, the technique proposed herein specifies both moisture and temperatures throughout the low and mid-troposphere via relevant indices in the context of latent instability, namely CAPE and LFC. In contrast, the other techniques determine thermodynamic soundings primarily through temperatures, moisture being a byproduct which follows from an arbitrary RH profile. In this regard, it is worth mentioning that moisture above the mixed layer is known to be important for the development of non-organized deep convection (e.g. Raymond 1995; Khairoutdinov and Randall 2006), as well as for the morphology of supercell storms (i.e. McCaul and Cohen 2004), and SLs (Nocholls et al. 1988; Lucas et al. 2000; Mechem et al. 2002; James and Markowski 2010).

In addition to the method for generating soundings, the results presented herein can be used for determining the degree to which the vertical distribution of CAPE constrains Γ, as suggested by Takemi (2010). That study proposes that the depth of the layer where CAPE ≈ MUCAPE is determined by the low-to-mid-tropospheric lapse rate (Γ_T), which is defined as

$$\Gamma_T = \frac{T\left(z\left(\theta_e \min\right)\right) - T\left(z\left(\theta_e \max\right)\right)}{z\left(\theta_e \min\right) - z\left(\theta_e \max\right)}$$

where $z\left(\theta_e \min\right)$ and $z\left(\theta_e \max\right)$ are, respectively, the height of minimum and maximum equivalent potential temperature. Specifically, Takemi (2010) hypothesizes that a larger Γ_T leads to deeper layers with high CAPE. The soundings in Fig. 2.7 clearly show that this is not necessarily true, both having identical Γ_T but with varying depth of the MUCAPE layer. Furthermore, different Γ_T can be achieved by varying the LTLR, without modifying the vertical distribution of CAPE, as shown by the sounding with small LTLR in Fig. 2.8. Nonetheless, it is true that there exists a link between Γ_T and CAPE, which follows from the connection between $\partial\mathrm{CAPE}'/\partial p$ and Γ (see Fig.

2.4a); but this relation does not imply a strong constraint, as moisture information is needed in order to completely specify the CAPE profile. The conclusions of Takemi (2010) followed from a qualitative inspection of soundings generated by the method of Weisman and Klemp (1982), which encompasses a limited class of thermodynamic environments.

2.4 Summary

This chapter has established the conceptual framework under which the thermodynamic environment will be considered throughout this work. The physical principles underlying latent instability are discussed, and parcel theory is appraised as a simple model for characterizing it. Motivated by the layer-lifting convection associated with SLs, the thermodynamic framework proposed herein contemplates vertical distributions of parcel indices, in contrast with the traditional focus on one parcel originating near the surface. The mathematical relations linking a varied class of soundings to vertical profiles of CAPE and LFC are formally established, providing the basis for a method for generating soundings via parcel indices. This technique determines both temperature and moisture through relevant parameters in the context of latent instability, incorporating information regarding the ascent of mid-tropospheric parcels. It remains to test the usefulness of such framework through actual numerical simulations of SLs, which will be done in subsequent chapters.

Figure 2.1. Curves of e corresponding to different q_v (green) and curves of e^* corresponding to different surface temperatures (red) as a function of p for adiabatic motions.

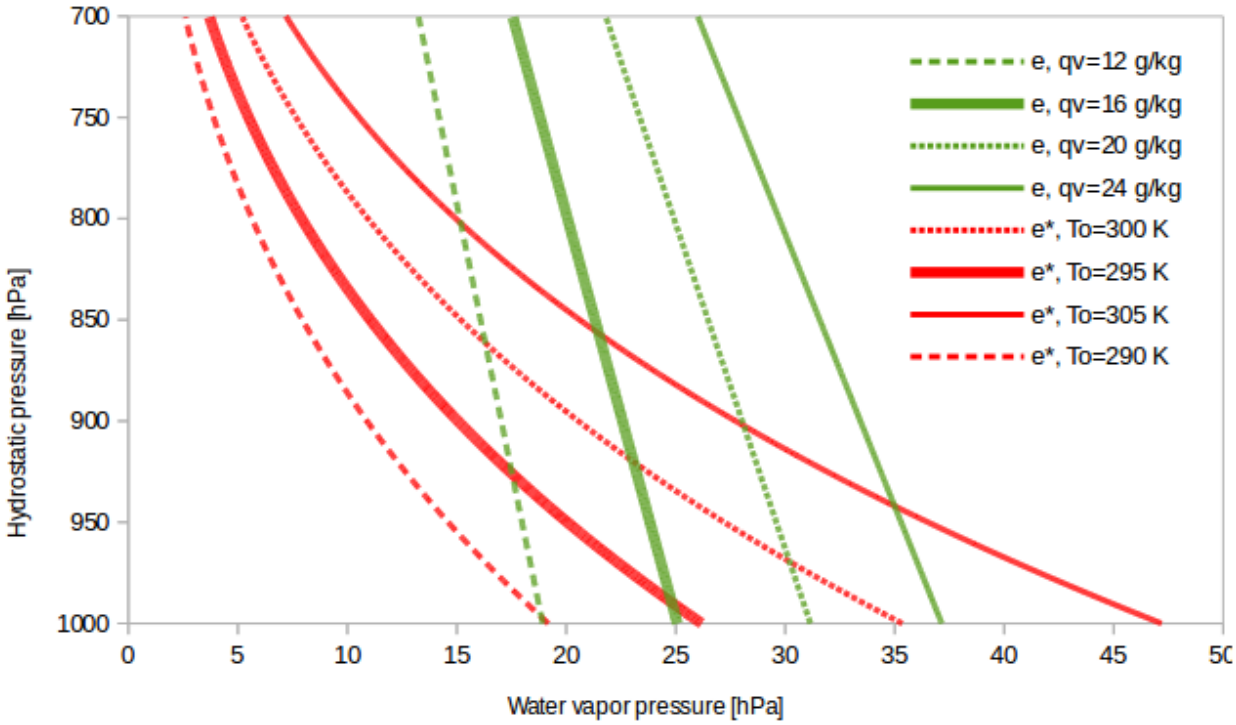

Figure 2.2. Atmospheric sounding on a skewT-lnp chart. Temperatures and dew point temperatures are represented by the black solid line and the dashed line, respectively. The thick gray line traces the thermodynamic properties of a surface parcel under pseudoadiabatic processes.

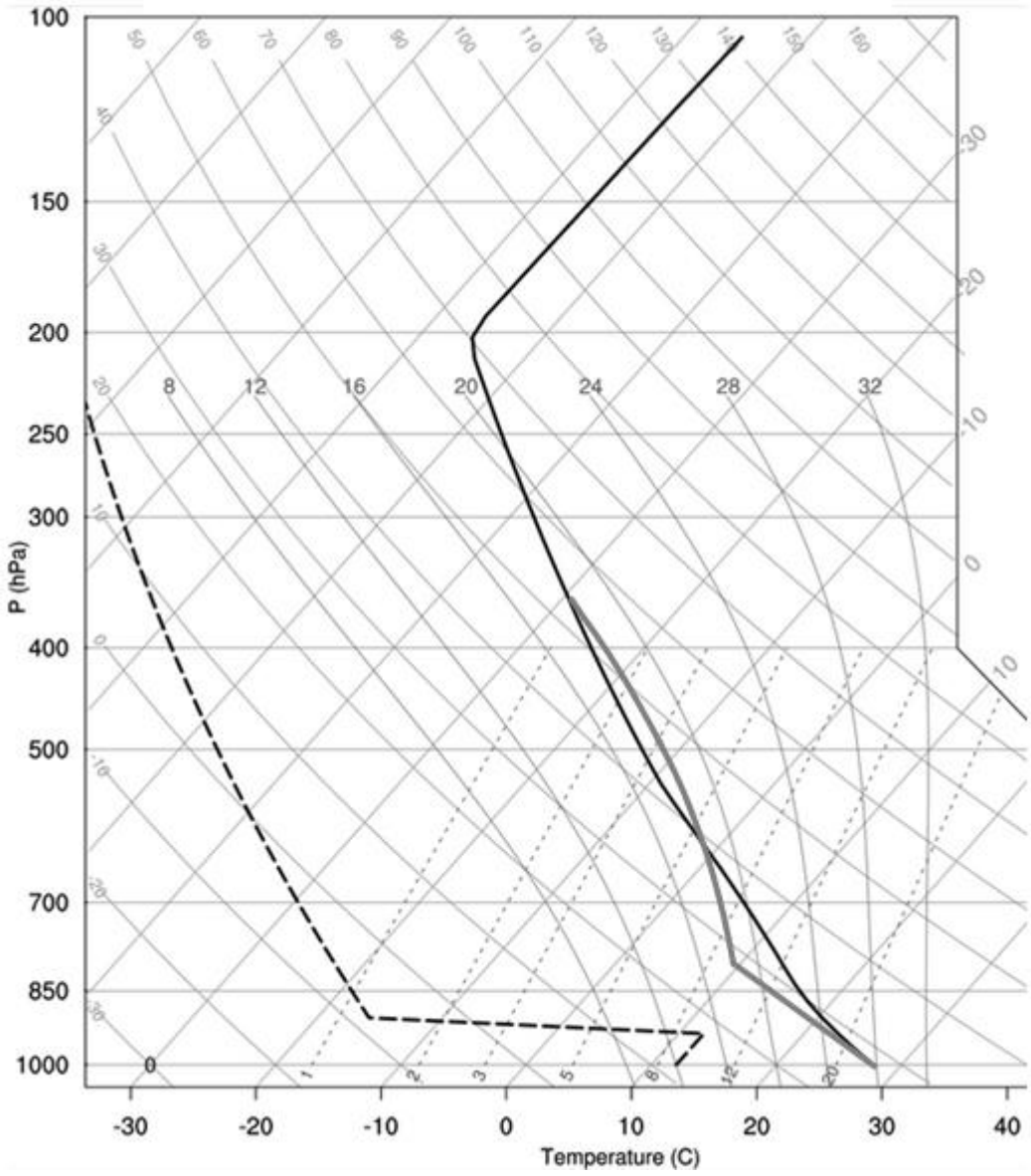

Figure 2.3. Schematic representation of the type of soundings under consideration as displayed on a SkewT-lnp chart. The black and blue thick solid lines represent temperatures and dew-point temperatures, respectively. The dashed lines correspond to pseudoadiabats of latent-unstable parcels, which are those originating at pressure levels in the set *P*. Portions of dry-adiabats and water vapor mixing ratio lines, corresponding to the green and purple lines, respectively, were added to visualize the displacement of parcels from different heights in *P*.

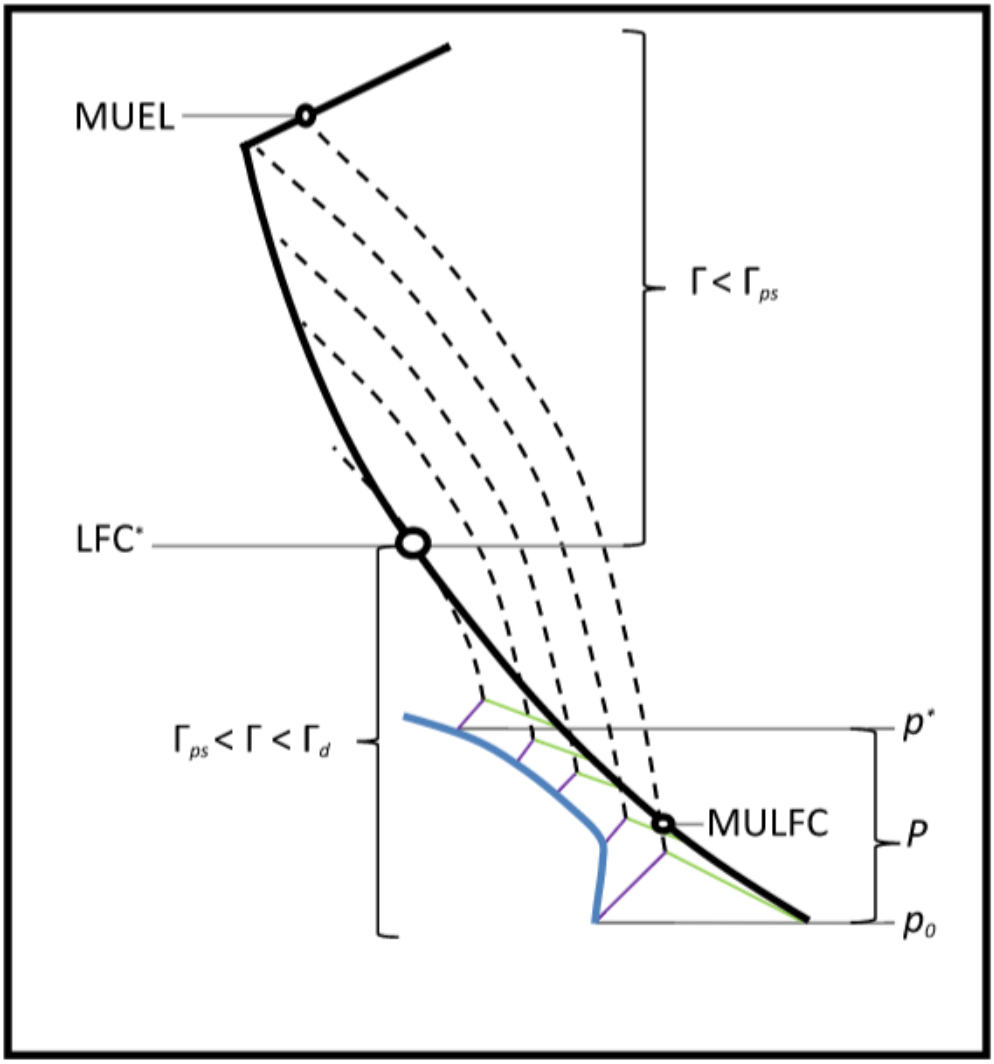

Figure 2.4. Schematic SkewT-lnp charts showing the procedure for generating soundings. T is determined via CAPE′ as illustrated in a), where the temperature difference between levels LFC and LFC+ΔLFC (ΔT) is considered for two cases, both having identical T above LFC, but which differ in their respective CAPE′ increments (ΔCAPE′). Here, $\Delta\text{CAPE}'_2 < \Delta\text{CAPE}'_1$, their values respectively given by the shaded and horizontally stippled areas, leading to $\Delta T_2 < \Delta T_1$. In b) it is shown how q_v can be determined at a given pressure level p for a given T curve (thick solid line). Two cases are depicted, with $\text{LFC}_2(p) < \text{LFC}_1(p)$, leading to $q_{v2}(p) < q_{v1}(p)$. The thin black solid line is the dry-adiabat followed in both cases by the parcel originating at p. Constant water vapor mixing ratio lines associated with $q_{v1}(p)$ and $q_{v2}(p)$ are respectively given by the dotted and dashed lines, and the gray lines represent $s_{ps}(p)$, again dotted for case 1 and dashed for case 2.

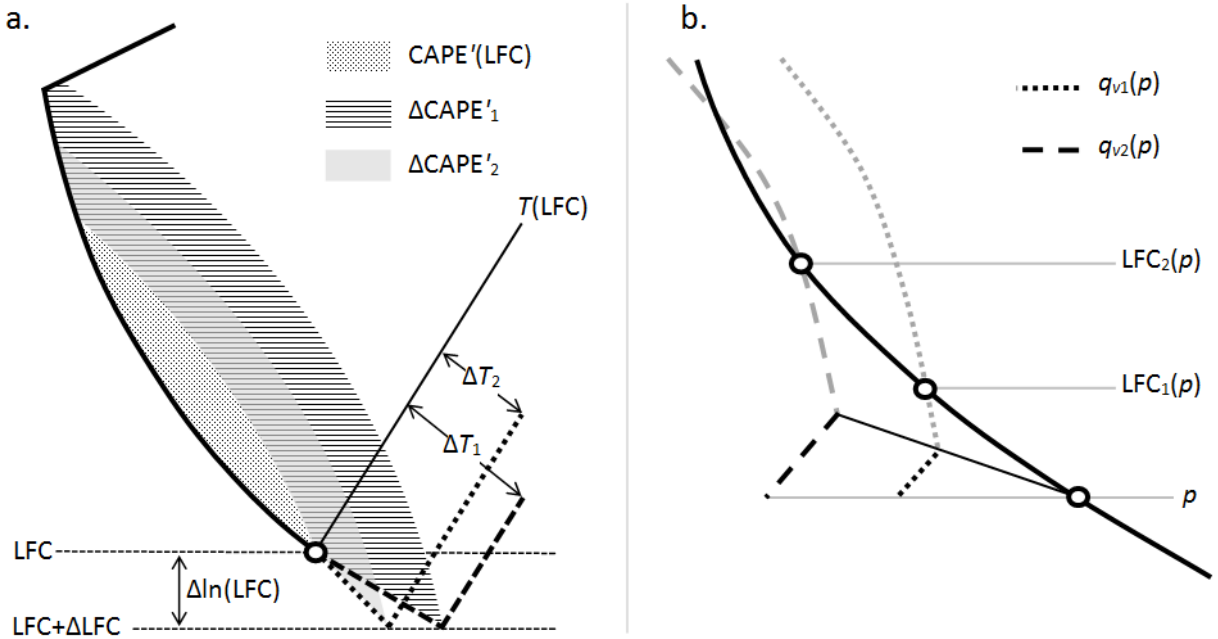

Figure 2.5 In a) the *baseline* sounding is displayed, with temperatures and dew-point temperatures represented by the solid and dashed lines, respectively. The CAPE′, CAPE and LFC profiles corresponding to the sounding are shown in b), c) and d), respectively.

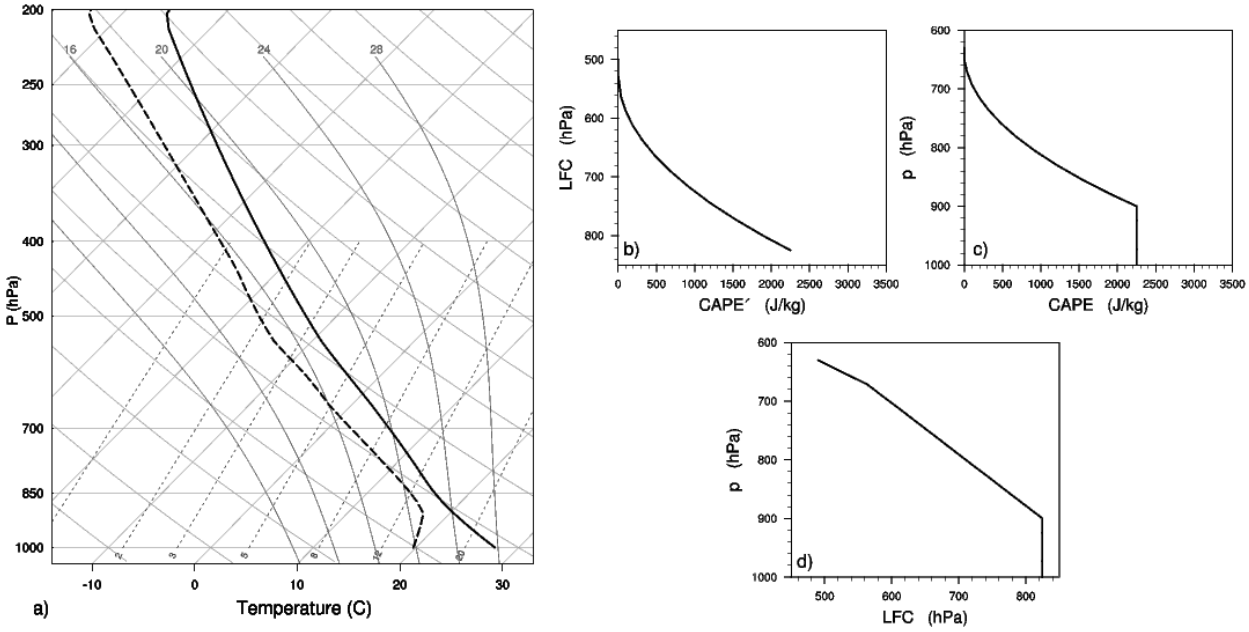

Figure 2.6. As in Fig. 2.5, depicting two soundings generated with *baseline*'s UTS, LTLR and LFC, but where the *baseline*'s CAPE profile was multiplied by a constant, i.e. CAPE→αCAPE. The dashed curves describe the sounding with $1 < \alpha$, while solid curves depict a case with $\alpha < 1$.

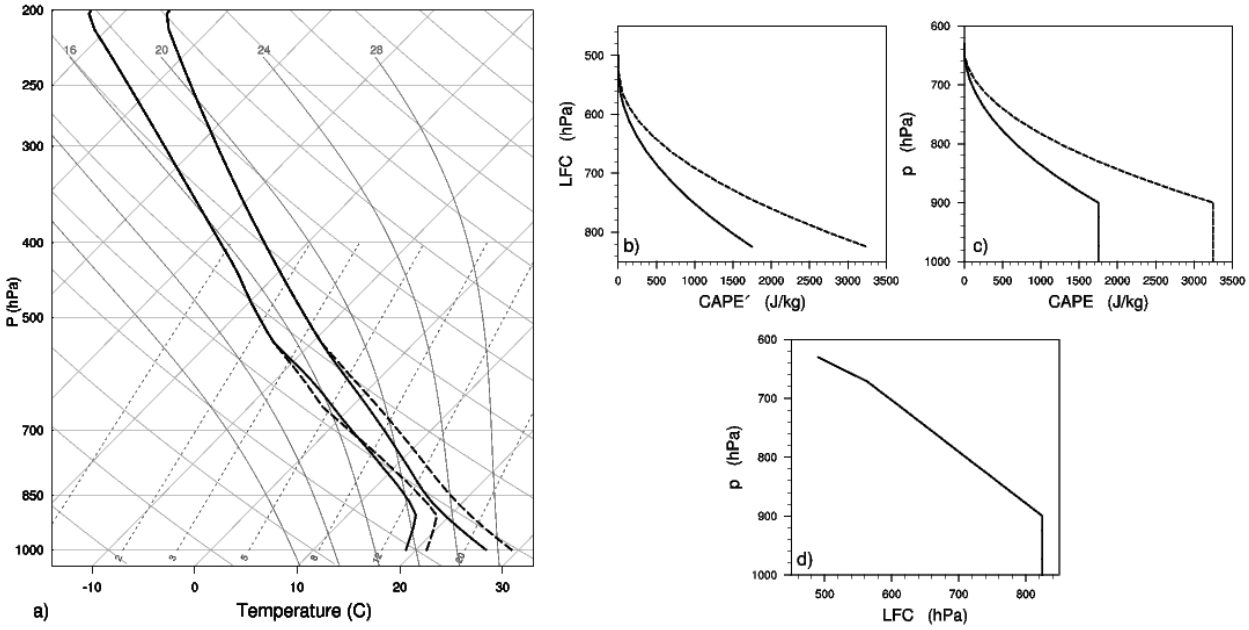

Figure 2.7. As in Fig. 2.5, depicting two soundings generated with *baseline*'s UTS, LTLR and CAPE′, but where the *baseline*'s LFC profile was modified throughout the midtroposphere. In the case depicted by the dotted lines, LFC was is lower in magnitude than *baseline*'s between 925 and 650 hPa, while the dashed lines represent a case with a greater LFC profile than *baseline*'s between 900 and 650 hPa. Even though both cases have identical CAPE′, and thus identical temperatures, they have very different CAPE profiles, with lower LFC leading to lower q_v and thus lower CAPE values.

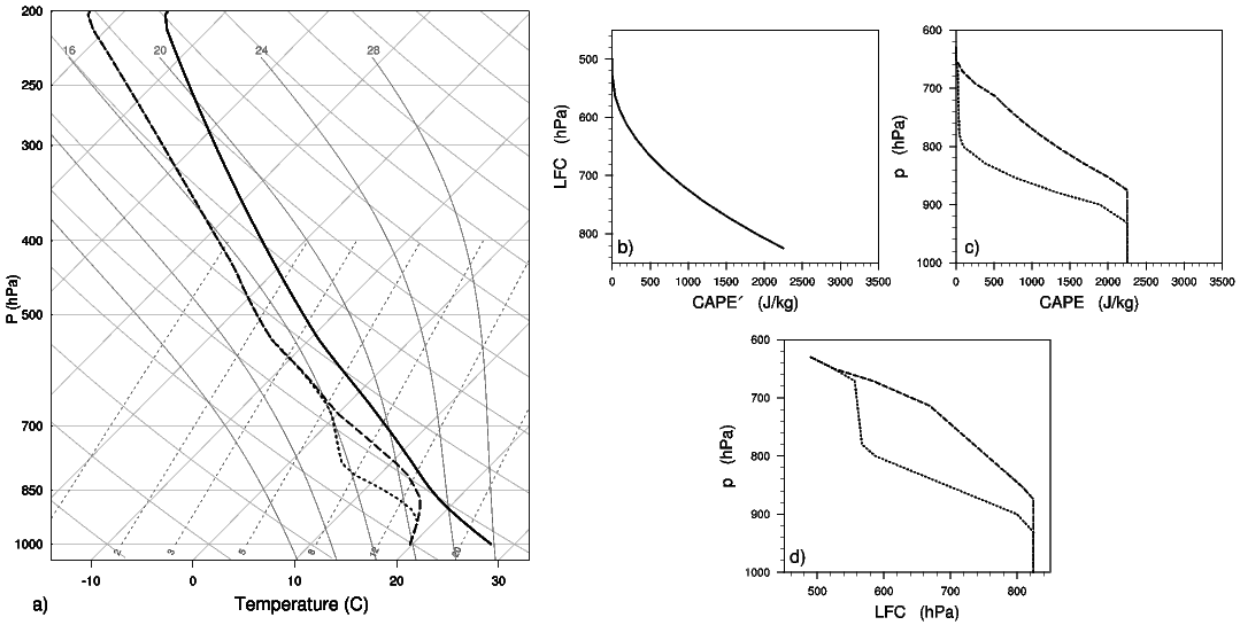

Figure 2.8. As in Fig. 2.5, depicting four soundings having *baseline*'s CAPE profile. In a), the *baseline* sounding is represented by the thick black lines, and was overlaid on top of the other soundings. The thin black lines show a case with a relatively low LTLR, being identical to *baseline* elsewhere. The blue sounding was generated by adding 3°C to *baseline*'s UTS, and the red sounding corresponds to a case where both CAPE′ and LFC profiles were modified, but leaving CAPE unchanged, as shown in b), c) and d).

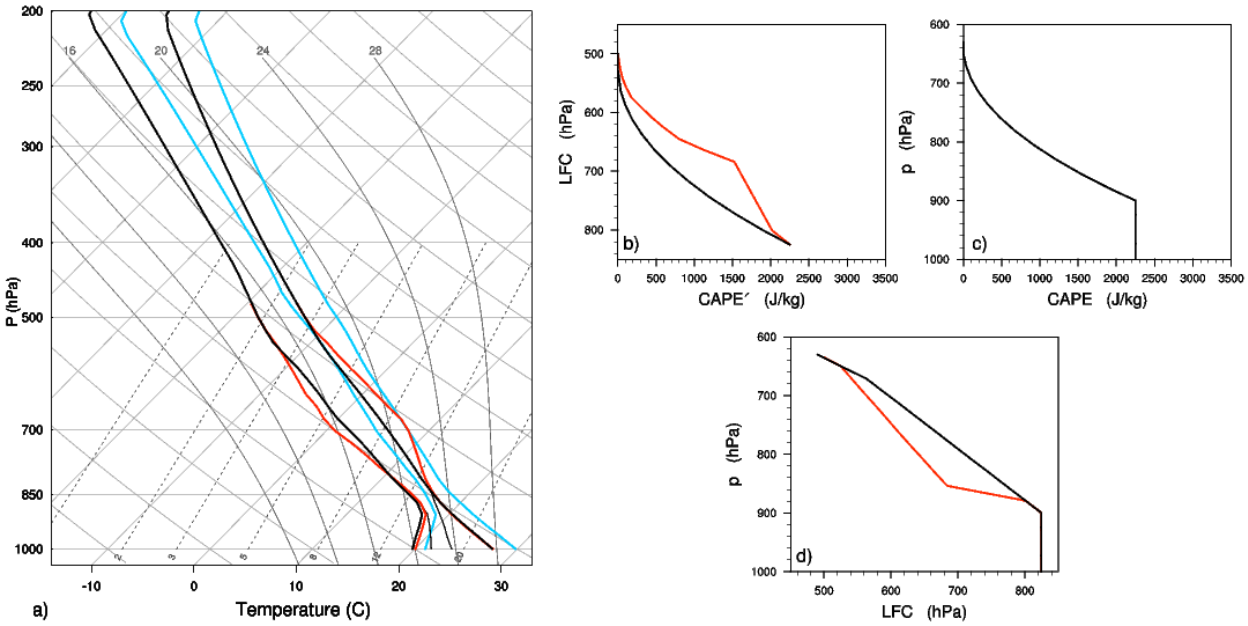

Chapter 3:

Numerically simulated idealized mid-latitude squall lines

This chapter is devoted to the analysis of numerically simulated SLs in mid-latitude environments. The thermodynamic framework presented in the previous chapter will form the basis for specifying soundings, as well as for interpreting the dependence of SLs on the environment. The focus will be on inter-case comparisons, and the primary features of interest are manifested as thermodynamic perturbations induced by the storms, one being the cold pool and the other being the upper-tropospheric heating.

The organization of this chapter is as follows. The numerical framework used for simulating SLs is described in section 3.1, followed by a description of the environments to be considered in section 3.2. Results from numerical simulations are presented in section 3.3, including a brief description of the baseline simulation, inter-case comparisons of the along-line averaged fields produced by moderately sheared simulations, a description of Lagrangian particle trajectories, and extensions of results to weakly and strongly sheared environments. A discussion will follow in section 3.4, including a review of the previous literature in light of results presented herein, and followed by the description of a schematic diagram to summarize the main results. A brief summary is given in section 3.5.

3.1 Numerical framework

The numerical simulations were performed with the System for Atmospheric Modeling, SAM, which is a non-hydrostatic CRM based on the anelastic fluid equations, as described in Khairoutdinov and Randall (2003). Horizontal boundaries are doubly periodic; thus, a relatively long domain is required in the across-line direction to prevent perturbations from traversing the domain and affecting the storm. The conserved thermodynamic variable in SAM is the liquid/ice water static energy; consequently, moist static energy in temperature units, given by $h = T + c_p^{-1}(gz + L_v q_v)$, is employed instead of the more frequently used equivalent potential temperature. Subgrid-scale (SGS) processes were accounted for by a first order Smagorinsky closure model. No significant variations in the fields analyzed herein were observed when using a 1.5-order closure similar to the model of Deardoff (1980). A version of the double-moment microphysics parameterization of Morrison et al. (2005) was employed for cloud (water and ice) and precipitating (rain, snow and graupel) phenomena. As in most idealized SL simulations, the lower boundary condition is free slip, with all surface fluxes, Coriolis effects, and radiative heat fluxes being neglected. It is important to mention that Skamarock et al. (1994) found that the Coriolis force can affect the direction of system propagation, leading also to asymmetries at the along-line edges of mid-latitude SLs, while Trier et al. (1996) showed that surface friction and heat fluxes can impact the realism of simulated storm characteristics. Nonetheless, those same studies also concluded that such effects are not necessary for simulating the most salient features of SLs.

The numerical simulations were carried out for 7.5 hours with a 2.5 s time step. The horizontal domain extends 128 × 1536 km^2 (along-line × across-line directions respectively), with 500 m grid spacing in both directions. The domain extends to 28.5 km in the vertical through 64

levels with variable spacing, this being 100 m near the surface and gradually increasing up to 500 m at 5000 m height, above which it stays constant at 500 m. Bryan et al. (2003) argued that SLs require greater resolution than that used here to resolve turbulent processes up to the inertial subrange; yet, the same study showed that even simulations with 1 km grid spacing display the general characteristics of the storms as revealed by results using higher resolution, justifying the expectation that the resolution achieved herein is sufficient for identifying systematic variations in the simulations under different environmental configurations.

Newtonian damping is applied to prognostic variables in the upper third portion of the domain. In addition, pointwise nudging to the initial kinematic and thermodynamic state was performed between 768 km and 1536 km in the across-line direction. This represents a boundary condition which maintains environmental conditions nearly constant throughout the simulation. All storms remained distanced from the nudged portion of the domain throughout the simulation. The time frequency used for nudging the region between 968 km and 1336 km was 3600^{-1} s^{-1}, and linearly decreasing to 0 s^{-1} between 968 km and 768 km, and also between 1336 km and 1536 km.

The initialization procedure is analogous to that used by Morrison et al. (2015), consisting of horizontal wind convergence centered on x_c=384 km (across-line direction), with horizontal radius x_r=10 km, maximum height z_r=10 km, and defined as follows:

$$\frac{\partial u}{\partial t} = \gamma \cos\left[\frac{\pi(x - x_c)}{2x_r}\right] \times \left(\cosh\left[\frac{2.5z}{z_r}\right]\right)^{-2}$$

where x is the across-line coordinate, z is height, and γ is a time dependent variable equal to 0.1 m s^{-2} between initiation and 3300 s, linearly decreasing to 0 m s^{-2} at 3600 s. One advantage of using this method for initializing SLs is that it avoids incorporating large thermodynamic disturbances for triggering convection, such as a cold pool (e.g. Trier et al. 1996; Weisman 1997; Parker and Johnson 2004) or a warm bubble (e.g. RKW; Fovell and Ogura 1988). Random temperature perturbations of .8 K amplitude were added at initialization in the region of convergence forcing in order for the system to develop 3-dimensionality.

The Lagrangian particle tracking algorithm described in Yamaguchi and Randall (2012) was also used. The trajectories were computed every model time step using 3rd order Lagrange interpolation in space and 3 half time-step iterations using a second order Runge-Kutta method. SGS effects were neglected in the Lagrangian particle trajectories, and further specifications will be described alongside the corresponding results.

3.2 Design of mid-latitude environments

The thermodynamic environments considered herein are very similar to the examples given in chapter 2. Different environments are specified through perturbations to the CAPE and LFC profiles of a sounding that will be referred to as *baseline* (black solid lines in Fig. 3.1a and 3.1b, respectively; see also thick solid lines in Fig. 3.2). Two perturbations having *baseline*'s CAPE profile will be considered. The *base_sens* sounding has a lower LFC than *baseline* above the boundary layer (gray line in Fig. 3.1b; see also dashed lines in Fig. 3.2), which implies that parcels

in the former environment must be lifted further in pressure coordinates to attain neutral buoyancy. This environment has an elevated nearly dry-adiabatic layer (e.g. Carlson et al. 1983; Bryan et al. 2005) and a relatively dry mid-troposphere, which are commonly observed in mid-latitude SL environments. Both *baseline* and *base_sens* have identical boundary layers, being nearly dry adiabatic. The other sounding with *baseline*'s CAPE will be referred to as *stable* (thin solid lines in Fig. 3.2a), with an LFC profile identical to *baseline*, but with a relatively moist and stable boundary layer. This case is meant to represent nocturnal systems (e.g. Parker 2008).

Two sensitivity tests where designed where the CAPE profile is modified. The *low* and *high* soundings (respectively the thin and thick lines in Fig. 3.2b) are meant to test the impact of decreasing and, respectively, increasing *baseline*'s CAPE (dashed and dotted lines in Fig. 3.1a, respectively) while holding LFC fixed. Thus, parcels originating at the same pressure level in *low* and *high* reach their LFC at identical pressure levels aloft, but have very different CAPE values. On the other hand, the cases *shallow* (dotted dew point line in Fig. 3.2c) and *deep* (dashed dew point line in Fig. 3.2c) were designed to study the impact of varying LFC (the dashed and dotted lines in Fig. 3.1b, respectively) while maintaining *baseline*'s temperature profile. Consequently, the CAPE profiles of *deep* (dark gray line in Fig. 3.1a) and *shallow* (light gray line in Fig. 3.1a) differ, the latter having a shallower layer with most unstable CAPE (MUCAPE; i.e. maximum CAPE) than *deep*. The *low*, *high*, *deep*, and *shallow* environments have the same boundary layer lapse rate as *baseline*. The prescribed upper-tropospheric sounding was specified through the analytical profile of Weisman and Klemp (1982), being the same for all environments, except for *base_sens*, where a slightly different profile was used in order for its boundary layer to be identical to that of *baseline*.

The general characteristics of the soundings are listed in Table 3.1. Except for *shallow*, MUCAPE equals the mean layer CAPE (MLCAPE; i.e. CAPE of a parcel with the average characteristics of the lowermost 100 hPa) in each sounding; in *shallow*, MLCAPE is ≈ 3% lower than MUCAPE. The precipitable water (PW; with units kg m^{-2}) varies between *baseline*, *shallow*, and *deep*, but MUCAPE is identical among these cases. Similarly, the *stable*, *baseline*, and *base_sens* environments differ in their PW, while having identical CAPE profiles.

A variable of interest is ICAPE, as defined in chapter 2, which measures the bulk latent-instability present throughout the atmospheric column. It is considered herein as a potentially useful diagnostic in layer-lifting convection. Note that *low* and *shallow* have similar values of ICAPE, even though the former has much lower MUCAPE and MLCAPE than the latter. On the other hand, ICAPE differs between *shallow* and *deep*, both of which have identical MUCAPE and very similar MLCAPE.

The initial wind profile is zero above 3.5 km, while below it has constant wind-shear directed perpendicular to the line of convective initiation discussed in the previous section. This frame of reference differs from the more common specification with zero environmental surface winds speed, which was done in order to guarantee that the storms remain near the region of convective initiation, and distanced from the portion of the domain that is nudged toward the initial conditions (see the numerical specifications in section 3.1). This does not affect the nature of the results, as the lack of surface interactions renders the systems horizontally Galilean-invariant.

It is important to highlight that the environments considered herein do not contemplate line-parallel shear. James et al. (2005) showed that the line parallel shear can diminish the cellular structure at the deep convective line, favoring slabular convective motions instead. Given that

shear oriented along the deep convective line does not affect convection in linear Boussinesq flows without any along-line variability (e.g. refer to the discussion of roll circulations in Emanuel 1994, chapter 3), such effects are not likely to affect the generality of the conclusions reached herein, as long as the simulated SLs remain nearly two-dimensional (see results in 3.3a). Due to the importance of kinematics in determining SL morphology, simulations were performed with three different values of shear for each thermodynamic sounding: $\Delta U = 8$ m s^{-1}, $\Delta U = 16$ m s^{-1}, and $\Delta U = 24$ m s^{-1}, where ΔU is the difference between horizontal wind speed at 3.5 km and at the surface. These kinematic configurations are illustrated in Fig. 3.3. As reported by Evans and Doswell (2001) and Cohen et al. (2007), these wind-shear values are within the ranges of observed SL environments. Simulations with different environmental shear will be distinguished by an underscore followed by the corresponding ΔU value, e.g. *baseline_24*, *shallow_16*, etc.

3.3 Results

a. A brief description of the baseline simulations

The purpose of this subsection is to provide a reference of the characteristics of the simulated storms, describing features of the *baseline* SLs that are common to the other environments. Results presented herein regarding the evolution of the storms and the morphological differences resulting from varying kinematic environments will not be discussed in depth, as these matters have been addressed by previous numerical studies (e.g. RKW88; Weisman et al. 1988; Fovell and Ogura 1989; Weisman 1992; Weisman 1993). Starting with the radar reflectivity produced by *baseline_16*, Fig. 3.4 shows snapshots at 2, 4 and 6 h of simulation time of the radar reflectivity [dBZ] (e.g. see Houze 1993) in a plane perpendicular to the deep convective line, averaged in the along-line direction. The progressive broadening of the storm is evident in Fig. 3.4, especially the area with reflectivity values near 35 dBZ, which corresponds to the region of stratiform precipitation. Also apparent in Fig. 3.4 is a nearly linear area of maximum reflectivity at 4 km height, which results from the melting of ice beneath the 273.15 K line. Fig 3.5 shows that storms with different ΔU produce similar reflectivity patterns, although the storm broadening is less pronounced in the strongly sheared environment (Fig. 3.5c), while the reflectivity pattern is shallower in the weakly sheared environment (Fig. 3.5a). Radar reflectivity fields in the horizontal plane at 1 km height are shown in Fig. 3.6, revealing that the storms remain nearly linear throughout the simulation, which justifies the relevance of along-line averaged fields as a tool for analyzing storm morphology. It is also worth noting that Fig. 3.6 suggests that the degree of along-line variability depends on ΔU, with Fig. 3.6a displaying greater reflectivity variations in the along-line direction than Fig. 3.6c.

Along-line averaged contours of horizontal winds, pressure perturbations, and the buoyancy field of the *baseline_16* simulation are displayed in Fig. 3.7 at 2, 4 and 6 h of simulation time. Note that horizontal winds are in a surface-relative frame of reference, rather than relative to the system's leading edge, which is done to aid the interpretation of these fields in terms of environmental perturbations when comparing among different simulations. The mesoscale circulations commonly associated with SLs are distinguishable through the horizontal wind field, where the negative momentum flow above the cold pool is the FTRF, while the mid to upper-tropospheric flow with positive momentum at the rear of the storm corresponds to the RIJ (see Fig. 1.1b). Here, the cold pool is defined as the surfaced based flow with negative buoyancy on the downshear side of the RIJ, while the shallower positive momentum flow within it will be referred to as cold outflow. This distinction is relevant because, as revealed by particle trajectories shown

below, the upper portion of the cold pool constitutes a descending FTRF branch, which to my knowledge is not discussed in the previous literature.[8]

At 2 h the SL has developed a relatively deep cold outflow (Fig. 3.7a), which propagates downshear as it progressively becomes shallower. It is interesting that the across-line location where the RIJ subsides to feed the cold outflow remains near x = 475 km throughout the simulation. This is a property of the field of reference with static environmental winds aloft. The FTRF-RIJ boundary evolves to become more horizontal with time. The upper-tropospheric heating accomplished by the storm can be seen in the buoyancy field above 4 km, it being responsible for the hydrostatic component of the meso-low, i.e. the negative pressure perturbation feature at mid-tropospheric levels. The upper-tropospheric heating amplifies and broadens as the FTRF-RIJ boundary flattens. Buoyancy and kinematic perturbations can be appreciated ahead of the storm, which are produced by gravity waves (e.g. Pandya and Durran 1996). Notice the wind field that develops ahead of the SL at upper-tropospheric levels, which reflects the convective adjustment process in the presence of a heat source, as described by Bretherton and Smolarkiewicz (1989).

Fig. 3.8 depicts along-line averaged fields of latent cooling produced by the SL at 2 h, 4 h, and 6 h, including contours of precipitating hydrometeors. Vigorous latent cooling occurs at the FTRF-RIJ boundary, where low h RIJ air subsides, aided by snow sublimation and rain evaporation, which partially counter the adiabatic warming caused by downward motions. It is worth noting that the RIJ air near the FTRF-RIJ boundary remains near neutral buoyancy in Fig. 3.7, suggesting that the descent of this airflow is constrained by microphysical processes, and cannot be modelled by assuming a saturated downdraft. Contours without averaging (not shown) also reveal sub-saturated conditions throughout the RIJ. Melting of ice is evident in the relatively intense latent cooling observed near 4 km height in Fig. 3.8b, coinciding with a transition between ice hydrometeors and rain. Rapidly falling graupel is found near the deep convective line, while slowly falling snow accumulates near the FTRF-RIJ boundary, both contributing to produce the stratiform precipitation as they fall on the upshear side of the storm. Latent cooling and downdrafts weaken as the cold outflow propagates away from the FTRF-RIJ boundary, a consequence of the increasing distance between the deep convective line and the FTRF-RIJ boundary. It thus seems unlikely that the *baseline_16* storm can persist indefinitely, contrasting with results by Fovell and Ogura (1988), who simulated storms that evolve periodically. This difference might be due to

b. Simulations with ΔU = 16

Fig. 3.9 shows the time evolution of the domain wide surface precipitation rate (PR; with units mm day^{-1}) for all ΔU = 16 simulations. In all cases PR remains near maximum values after 4 hours of simulation time, an indication that the storms have reached a mature state. Given that this study is concerned with SLs at maturity, all results will correspond to fields at and after 4 h.

Table 3.2 presents some diagnostics of the ΔU = 16 simulations, which will be discussed alongside related results. Regardless of the CAPE distributions, PR can be ordered by PW (Fig. 3.9), with a couple of minor exceptions: PR in *baseline_16* is barely distinguishable from *stable_16*'s, even though the latter environment has more PW; also, the PR in *high_16* is larger than in *deep_16*, despite almost identical PW in both environments. These exceptions are

[8] The distinction between the cold pool and the cold outflow is similar to the distinction made between the density current and the region with negative buoyancy in Liu and Moncrieff (2000), who found that density currents in stratified environments could produce negative buoyancies aloft as a result of adiabatic cooling by air lifted on top of the density current.

indicative of the relevance of the water vapor inflow rate (WVIR), i.e. the rate at which water flows into the storm. For example, note that the aforementioned storms have very similar precipitation efficiencies (PE; %), defined as (precipitation rate [kg s^{-1}]) / (WVIR [kg s^{-1}]), where the WVIR was computed with respect to the initial environment, as in Fovell and Ogura (1989). Thus, *high_16* precipitates more than *deep_16* due to its larger WVIR, which results mainly from a greater surface-relative storm propagation speed (PS; m s^{-1}) in the former storm (note that wind shear also contributes to differences in WVIR, because the vertical distribution of water vapor differs among these cases). By analogy, the similarity in PR between *stable_16* and *baseline_16* can be explained by the greater PS attained by the latter. It is important to highlight that the WVIR is not an environmental diagnostic, and it is insufficient for fully characterizing the PR, as implied by the relatively low PE in simulations with low mid-tropospheric RH, *base_sens_16* and *shallow_16* (see Table 3.2). Despite its limitations, the PW seems to be a useful environmental diagnostic for the PR potential in the ΔU=16 cases considered herein.

Contours of horizontal winds, pressure perturbations, and the buoyancy field are displayed in Fig. 3.10, each averaged in the along-line direction, and corresponding to the ΔU=16 simulations with identical CAPE profiles: *baseline_16* (3.10a), *base_sens_16* (3.10b), and *stable_16* (3.10c). The three simulations in Fig. 3.10 produce similar upper-tropospheric buoyancy fields, which hydrostatically lead to similar meso-lows. Cold pools, on the other hand, differ in their height and buoyancy structure, with *base_sens_16* producing a relatively deep cold pool, with a notable mid-tropospheric minimum located towards its upshear end, while *stable_16* produces near surface buoyancy values of relatively small amplitude. The similarity in within-storm soundings taken roughly through the center of the meso-low, depicted by Fig. 3.11a, suggests that these contrasting features result mainly from environmental temperatures, i.e. *base_sens_16*'s relatively warm mid-troposphere and *stable_16*'s relatively cold low-troposphere. Notwithstanding their contrasting low and mid-tropospheric environments, these simulations produced similar cold pool intensities (c [m s^{-1}] in Table 2), which were computed as

$$c = \left(-2 \int_0^{z'} \bar{b}(z) dz \right)^{.5}$$

where $\bar{b}$ is the buoyancy averaged in the along-line direction and at the across-line location of the within-storm sounding in Fig. 3.11, while z' is the height where neutral buoyancy is first attained. A matter worth noting is that there are no apparent differences between *baseline_16* and *base_sens_16* that may be directly attributable to the vertical distribution of LFC. Therefore the LFC, which may be more relevant to convective triggering, will not be discussed further in this chapter. It is also important to highlight the similarity between the cold pool intensities of *baseline_16* and *stable_16*, which are storms that produce very different near surface buoyancy values. The vertical distribution of the temperature component of buoyancy within the cold pools of these storms, displayed in Fig. 3.11c, shows that this is possible due to lower buoyancy in *stable_16* than in *baseline_16* between 1300 m and 3500 m. To visualize how such differences lead to similar values of c, Fig. 3.11d shows the computation of c by integrating the temperature induced buoyancy from the surface to different heights, leading to a $\approx$ 1 m s^{-1} difference in c.

Regarding kinematics, *stable_16* produced the deepest outflow, with maximum horizontal wind speeds remaining elevated near this storm's cold pool edge (Fig. 3.10c), as opposed to maximum wind speeds descending to the surface in *baseline_16* (Fig. 3.10a) and in *base_sens_16* (Fig. 3.10b). Weisman (1992) argued that, for a given ΔU and c, these features, which are relevant

in terms of the potential for wind induced damage, depend on the magnitude of the horizontal buoyancy gradient at the FTRF-RIJ boundary, with a stronger gradient producing more elevated winds at the cold outflow edge (see their figures 15 and 23). However, the three simulations under consideration produced very similar *c* (Table 3.2), while Figs. 3.10 and 3.11a show that there are no significant differences between the buoyancy fields above their cold pools. In fact, *stable_16* is the only ΔU=16 simulation where maximum outflow winds do not spread to the surface, as manifested by its relatively low maximum surface wind speeds in Table 3.2.[9] This behavior could result from a slower decrease of the cold pool buoyancy with height in *stable_16*, a feature that Droegemeier and Wilhelmson (1987) found to affect the circulations near the edge of simulated outflows. Such matters require further investigation.

In respect of cases with varying CAPE, Fig. 3.12 displays the along-line averaged fields of *low_16*, *high_16*, *deep_16*, and *shallow_16*. Despite marked differences in their upper-tropospheric buoyancy fields, all simulations depicted in Fig. 3.12 developed maximum outflow winds that spread to the surface, showing that this feature is not strongly modulated by the mid and upper-tropospheric buoyancies, as suggested by Weisman (1992). Clearly, *high_16* (Fig. 3.12b) and *deep_16* (Fig. 3.12d) produced perturbation fields of greater amplitude than *low_16* (Fig. 3.12a) and *shallow_16* (Fig. 3.12c), as is also revealed by PS, *c*, and maximum surface wind speeds in Table 3.2. The contrasting appearances of *shallow_16* and *deep_16* are noteworthy, since both environments have identical temperature soundings, the same MUCAPE, and very similar MLCAPE. In this regard, it is also worth highlighting that *low_16* produces a more intense storm than *shallow_16* by several measures (i.e. PS, PR, and maximum surface wind speeds) despite the former environment's lower MUCAPE, MLCAPE, and low to mid-tropospheric temperature lapse rate. These results manifest the limitations of some commonly used parcel indices and temperature lapse rates (e.g. Takemi 2010) for capturing relevant dynamical features of SLs.

Within-storm soundings in Fig. 3.13 reveal interesting characteristics of simulated cold pools. For instance, *shallow_16* stands out for producing a relatively warm (Fig. 3.13a) and dry (Fig. 3.13b) cold outflow, as is the case for *base_sens_16* in Figs. 3.11a and 3.11b, thus linking the low PE in these storms to their relatively dry mid-tropospheric environments. These inter-case differences contrast with the similarity in surface cold pool temperatures among all simulations shown in Figs. 3.11a and 3.13a. This result indicates that surface cold pool temperatures are highly constrained by the mid and upper-tropospheric portion of the sounding, as all the environments have nearly identical soundings above $\approx$ 600 hPa. This observation is not surprising under the model of saturated pseudoadiabatic descent of air from the level of minimum *h* (e.g. Fawbush and Miller 1954), but it is not trivial because turbulent mixing and subsaturated conditions prevail in downdrafts (e.g. see Gilmore and Wicker 1998). It remains to test whether this statement holds for different values of shear, a matter that will be addressed shortly. But as a consequence of the aforementioned results on cold pool properties, and in agreement with observations by Bryan et al. (2005), it follows that *c* cannot be estimated exclusively through surface temperature measurements, as proposed by Evans and Doswell (2001) and Stensrud et al. (2005).

Contrasting with results for simulations with identical CAPE profiles, temperatures above the melting line in Fig. 3.13a differ among the simulations, with *low_16* and *shallow_16* being notably colder therein than *high_16* and *deep_16*. Interestingly, the upper-tropospheric

[9] For comparison with naturally occurring events or other simulations, the surface wind speed values in Table 3.2 must be adjusted to the appropriate horizontal frame of reference.

temperatures in the ΔU=16 simulations can be ordered by ICAPE, which is shown by the soundings in Fig. 3.14. This is of great dynamical importance, given that positive buoyancy values above the cold pool drive horizontal motions at the RIJ via the associated meso-low, while also leading to descent of mid-tropospheric air into the cold outflow through vorticity generation and cooling by microphysical processes (e.g. Lafore and Moncrieff 1989; Weisman 1992). Pandya and Durran (1996) showed the importance of the heating and cooling profiles for driving the mesoscale circulations in SLs through gravity waves, while Fig. 3.14 suggests that ICAPE constrains the amplitude of the upper-tropospheric heating. To aid the interpretation of this result, the next subsection will analyze the simulated convective process through particle trajectories.

c. Particle Trajectories

To shed more light into the convective processes in the present simulations, Lagrangian particles were placed at 4 h of simulation time with initial position at different heights near 6 km and 15 km ahead of the cold pool edge, and with 1 km spacing in the along-line direction. As an example, Fig. 3.15 displays trajectories relative to the cold pool edge traced by 40 particles projected onto the across-line/height plane in the *baseline_16* simulation. The data used for this plot is from output at 5 min intervals of trajectories computed every time step, with the paths colored according to the particle's temperature with respect to the initial environment. The along-line averaged *h* field at 6 h is contoured in the background for reference.

One of the most salient characteristics of the convective process portrayed in Fig. 3.15 is that all low and mid-tropospheric particles cross the deep convective line, reflecting the propagation of the simulated SL with respect to environmental winds at those heights. This is the essence of layer-lifting convection, where deep layers of environmental air constitute the core of the convective process. Such convective modes differ fundamentally from models where air from a single layer constitutes the updraft core, as is implicitly assumed in traditional interpretations of parcel theory, and in the stochastic mixing model of Raymond and Blyth (1986), which James and Markowski (2010) applied to SLs. To characterize convection in the present simulations, it is necessary to contemplate the thermodynamic properties of air from all layers of storm-relative inflow, which mix turbulently at the deep convective line, in fractions that are strongly dependent on the storm-relative inflow rate.

The highly turbulent conditions within the deep convective line are reflected in Fig. 3.15 by the variety of trajectories followed by particles with identical initial thermodynamic conditions, i.e. originating at the same height. The intense turbulent mixing in the deep convective line can also be discerned in the *h* contours displayed in Fig. 3.16, which show that rapidly ascending air (black contours) undergoes considerable dilution, as it lacks air with high *h*. The diffusive nature of turbulent mixing is also evident when comparing the distribution of *h* on the upshear side of the cold pool edge, i.e. the environmental *h*, to the more homogeneous distribution of *h* throughout the FTRF region, i.e. within-storm *h*. While the resolution used here is too coarse to accurately resolve turbulent processes, a simulation by Bryan et al. (2003) performed at 125 m grid spacing and under similar environmental characteristics displays analogous signs of mixing (their figure 1). It is possible that the high degree of turbulent mixing that occurs in these simulations results from moist absolutely unstable layers (MAULs; Bryan and Fritsch 2000), which is present in the region enclosed by the thick black contour in Fig. 3.16.

The relevance of ICAPE as a diagnostic in layer-lifting convection is evident in the trajectories in Fig. 3.15, where all low and mid-tropospheric parcels ascend, mix at the deep

convective line, and traverse the storm nearly horizontally at a level determined by a buoyancy sorting process (Raymond and Blyth 1986). The histograms of particle heights at 5 h simulation time displayed in Fig. 3.17 further suggest that ICAPE modulates the convective processes, showing that more low and mid-tropospheric particles reach above 8 km in simulations having greater ICAPE.[10][11] On the other hand, there is no clear indication that convection from any single layer is dependent on its respective CAPE. For example, the number of low-tropospheric particles reaching above 8 km is greater in *low_16* than in *shallow_16*, notwithstanding similar *c* values and larger low-tropospheric CAPE characterizing the latter environment. Furthermore, in each simulation the number of particles that reach above 8 km is greatest when the level of origin is 1800 m, despite having lower CAPE than the particles originating at 300 m.

Before proceeding to the next subsection, it is worth highlighting that particles ending up beneath 4 km after crossing the deep convective line in Fig. 3.10 cool and slowly descend as they traverse the SL. These particles, which formally constitute the upper portion of the cold pool, take part in a relatively intense downdraft at a crossover zone between this descending FTRF branch and the RIJ, where mixing is likely to occur. The descending FTRF is separated from its ascending counterpart by the melting line, and the cooling experienced by slowly descending particles results mainly from melting of ice. Note that the mid-tropospheric buoyancy minimum at the rear of *base_sens_16*'s cold pool in Fig. 3.10b is related to this descending FTRF, and that the contour representing enhanced melting in Fig. 3.16 is collocated with a band of relatively low *h*. It is therefore plausible that the neglect of ice microphysics in early SL simulations may be the reason why this mesoscale flow was not discussed before, which may also explain why cold pools observed by Bryan et al. (2005) were deeper than those reproduced by many numerical simulations.

d. Simulations with ΔU=8 and ΔU=24

In general, the aforementioned systematic morphological variations of SLs in different thermodynamic environments are also present in the Δ*U*=8 and Δ*U*=24 simulations, as shown by the different variables in Tables 3.3 and 3.4. It is important to note that *shallow_24* did not reach a mature state, which can be seen in the PR oscillation between 1 and 4 hours in Fig 3.18a, after which the PR remains low relative to its peak value, attained at 1.7 h. The discrimination of PR by PW is evident in Figs. 3.18a and 3.18b, while Tables 3.3 and 3.4 show that the environments with driest mid-tropospheric conditions, i.e. *shallow* and *base_sens*, have the lowest PE, regardless of Δ*U*. Also apparent in Figs. 3.9 and 3.18 is the systematic increase in PR as Δ*U* becomes stronger, which has been reported in many past studies (e.g. RKW88; Weisman et al. 1988; Weisman and Rotunno 2004; Bryan et al. 2006). Fovell and Ogura (1989) attributed this behavior mainly to the WVIR, but Tables 3.2, 3.3, and 3.4 show that the PE varies with Δ*U*, a matter related to the fraction of latent-unstable air among the total storm-relative inflow, as explained below.

Regarding upper-tropospheric thermodynamics within the storms, the ordering of temperatures by ICAPE still holds for the strongly and weakly sheared simulations. To illustrate

[10] This fact does not result from cold pool-shear optimality (e.g. RKW88), as the most optimal storms among those under consideration are *shallow_16* and *low_16*.

[11] All simulations considered herein produced layer-lifting convection, in contrast with tropical SLs simulated by Mechem et al. (2002), where dry mid-tropospheric conditions inhibited layer-lifting.

this, a scatter plot depicting all simulations on an ICAPE-*W* plane is shown in Fig. 3.19a, where *W* measures the upper-tropospheric warming caused by the storm, defined as

$$W = \left(2 \int_{4km}^{12km} \bar{b} dz \right)^{.5}$$

$\bar{b}$ being the along-line averaged buoyancy at an across-line location near the center of the meso-low. The lower limit of integration for *W* is at 4 km because it is near the line of neutral buoyancy in all simulations, and the upper limit at 12 km was chosen because it is near the tropopause. For each environmental shear, a nearly linear relation between ICAPE and *W* is evident in Fig. 3.19a, resulting from the layer-lifting process revealed by Fig. 3.10. This result should be contrasted with a similar scatter plot in Fig. 3.19b depicting the simulations in a MUCAPE-*W* plane, which explicitly shows that relatively large differences in *W* can be accomplished by storms in environments with identical MUCAPE. In addition, Fig. 3.19 shows that simulations with more strongly sheared environments produce greater *W*, consistent with findings by Fovell and Ogura (1989), Lafore and Moncrieff (1989), and Weisman (1992). The latter study attributed such behavior to the decrease in turbulent mixing due to faster lifting of low-tropospheric parcels in more optimal configurations, i.e. cases with $c / \Delta U$ closer to 1 (e.g. Weisman and Rotunno 2004). The validity of this interpretation by itself is not clear, given that greater vertical velocities could produce enhanced mixing due to greater stress at the updraft boundaries. In fact, the histograms in Fig 3.17 and the soundings in Fig. 3.14 show that *deep_16* displaces more parcels to the upper-troposphere and develops greater upper-tropospheric temperatures than *shallow_16*, despite identical low-tropospheric CAPE and a less optimal cold pool-shear configuration in the former simulation.

I propose that the dependence of *W* on ΔU for a given sounding results from the modulation of storm-relative environmental winds by the kinematic environment, i.e. ΔU in the environments considered herein. To illustrate this, Fig. 3.20 presents a scatter plot where the simulations are represented according to their PS and their shear-layer inflow fraction (SLIF), which is the storm-relative mass flux of air from the environmental shear layer as a fraction of the total storm-relative mass flux. The results in Fig. 3.20 are consistent those of Fovell and Ogura (1989), who found higher SLIF in more strongly sheared cases. The relevance of the SLIF in the environments considered herein follows from the fact that most of the latent-unstable layer, i.e. the layer through which CAPE is defined, is found within the sheared layer. The latent-unstable parcels are precisely those which may cause upper-tropospheric warming when lifted, CAPE providing a measure for buoyancy under parcel ascent; thus the relevance of ICAPE as a measure of buoyancy under layer-lifting. On the other hand, the inflowing air above the sheared layer will mix with latent-unstable parcels at the deep convective line, potentially cooling by rain evaporation, ice sublimation, or by subsaturated ascent. Hence, in environments where shear and latent-instability are concentrated at low-tropospheric levels, a greater SLIF will tend to produce higher upper-tropospheric temperatures, and by the same reasoning, a greater PE.

With respect to surface cold pool temperatures, Fig. 3.21 shows that, with the exception of *shallow_8* and *base_sens_8*, the inter-case variations among the previously described environments are small. The outlying behavior of *shallow_8* and *base_sens_8* is likely due to their relatively dry mid-tropospheric environments, to which surface cold pool temperatures in weakly sheared environments become highly sensitive (notice the small PE of these storms in Table 3.3, as well as their low SLIF in Fig. 3.20). Leaving these two cases aside, the inter-case similarity in

temperatures displayed by Fig. 3.21 warrants further consideration of the origins of surface cold pool air. To this end, Fig. 3.22 shows a histogram of the height reached by backward trajectories of surface cold pool air in *baseline_16* at 4 h of simulation time, computed back to the initial simulation time. It shows that the major source of cold pool air is the 3-4 km layer, where 37% of trajectories are found at initiation; but 55% of trajectories correspond to air with origins above 4 km, which contains the layer with minimum h, and wherein there are barely any inter-case environmental variations. These results are consistent with the contention that the small variation in surface cold pool temperatures among different simulations results from the similarity in mid and upper-tropospheric environmental thermodynamics.

Figure 3.21 suggests that surface cold pool temperatures can be accurately determined by the mid and upper-tropospheric portion of the sounding, as long as the environment is characterized by high mid-tropospheric RH or moderate to strong shear. To test this hypothesis, two additional simulations with $\Delta U = 16$ were performed, both having the same CAPE, LFC, and boundary layer lapse rate as *baseline*, but with different prescribed upper-tropospheric soundings: *dry*, with identical upper-tropospheric temperatures, but with 80% of *baseline*'s RH above the latent-unstable layer, and *warm*, being 3 K warmer than *baseline* but maintaining the same RH throughout the upper-troposphere. As portrayed in Fig. 3.21, *dry* produces surface cold pool temperatures similar to those from previously described simulations, while *warm* produces much higher temperatures therein. The lower than 3 K difference in surface cold pool temperatures between *warm* and *baseline_16* results in part from decreasing pseudoadiabatic lapse rates with increasing temperature. These results show that mid and upper-tropospheric temperatures can be used to provide accurate estimates of surface cold pool temperatures, while moisture plays a limited role due to low q_v found at such heights, a consequence of the constraint implicit in the Clausius-Clapeyron relation.

3.4 Discussion

a. Previous studies in light of the present results

Most of the previous literature on the dependence of mid-latitude SLs on the thermodynamic environment has focused on CAPE, e.g. Weisman (1992, 1993), James et al. (2006), Takemi (2007, 2010), and James and Markowski (2010). It is interesting that the main conclusions reached in such studies can be interpreted within the framework proposed herein. For instance, the soundings considered by Weisman (1992, 1993) are such that cases with greater CAPE also have greater ICAPE, as is shown in Fig. 3.23, thus explaining the systematic behavior of storms simulated in different CAPE environments. In fact, the environmental variations considered by those studies are rather similar to the ones between *high* and *low*, i.e. consisting on changes in the temperature lapse rate, the main difference being that Weisman (1992, 1993) specified identical surface temperatures in all environments.

Similar observations apply to results by James et al. (2006) and Takemi (2007, 2010), where soundings with greater temperature lapse rates and lower mid and upper-tropospheric q_v are the ones with greater ICAPE (see figure 15 in Takemi 2010). In fact, Takemi (2010) mentions the importance of the vertical distribution of CAPE for modulating the intensity of simulated SLs, but does not provide any argument relating this feature to the upper-tropospheric heating. Instead, the vertical distribution of CAPE was proposed as a physical explanation for why the temperature lapse rate modulates storm intensity, as deeper layers of MUCAPE were found in soundings with

steeper lapse rates (this is discussed in section 2.3). However, results presented herein show the importance of the latent-instability properties of air above the layer with MUCAPE, as exemplified by the simulations in *low* and *shallow* environments, the latter producing more intense storms despite having a smaller temperature lapse rate and lower CAPE values throughout the low-troposphere. Furthermore, the latent-heating of ascending air with origins above the latent-unstable layer is also important for determining the upper-tropospheric warming, as evinced by the deep reaching trajectories of particles originating at 4800 m in Fig. 3.15d. This is probably the main reason why James and Markowski (2010) found dry mid-tropospheric conditions to be detrimental for the intensity of SLs in environments having similar ICAPE.

In respect of the cold pool, it is worth mentioning that there is no clear link between SL morphology and DCAPE, an index that has been associated with the downdraft strength and cold pool properties (e.g. Evans and Doswell 2001 and Cohen et al. 2007). Consistent with results by Gilmore and Wicker (1998), subsaturated conditions were present throughout the RIJ of simulated storms (not shown), suggesting that the downdraft is constrained by the rate of latent cooling. Nonetheless, the finding pertaining to the lack of sensitivity in surface cold pool temperatures among the simulations with similar mid and upper-tropospheric temperatures may be relevant for forecasting and parameterizing cold pool properties. To my knowledge, this fact has not been reported in previous numerical studies, probably because sounding variations have been mainly accomplished through changes to mid and upper-tropospheric temperatures.

b. Conceptual model of convection in SLs

To summarize the results presented throughout this study, Fig. 3.24 shows a shematic diagram depicting the kinematic and thermodynamic structure of a mature mid-latitude SL with trailing stratiform precipitation. Environmental winds are represented on a frame of reference with a static cold pool edge, green reflecting the presence of latent-instability (the brighter the tone, the higher CAPE is in that layer). The highly turbulent deep convective line, represented by the area in red, mixes the air from all levels of storm relative inflow, followed by a buoyancy sorting of air parcels, as described by Raymond and Blyth (1986). The positively buoyant and slowly ascending FTRF (AFTRF) is found above the melting line, being near saturation and with temperatures determined by the storm-relative flux of environmental latent-instability at all heights. Beneath it is the descending FTRF branch (DFTRF), which remains negatively buoyant as it slowly descends, mainly due to melting of ice particles throughout the stratiform region. To the rear of the FTRF is the RIJ, which encounters the DFTRF at a crossover zone where mixing is likely to occur. Most of the DFTRF air enters the rear exit flow, where it joins RIJ air that does not feed the cold outflow. Temperatures within the cold outflow are modulated by the thermodynamic properties of RIJ air, while its buoyancy structure is determined by low and mid-tropospheric environmental temperatures.

Notable features in Fig. 3.24 which are not highlighted in other archetypical schematic depictions of mid-latitude SLs (e.g. Houze et al. 1989) are the inclusion of the DRTRF and its associated crossover zone with RIJ, the distinction between the cold pool and the cold outflow, as well as the emphasis on system-relative winds and the latent instability of air from all heights. System-relative winds at all heights are also emphasized in the conceptual model of tropical SLs proposed by Zipser (1977) (their figure 13), with their model having the particularity that low *h* mid-tropospheric air crosses over with low-tropospheric air with high *h*. Thus, the conceptualization by Zipser (1977) seems to assume a lower degree of turbulent mixing at the leading line than that reflected by the trajectories in Fig. 3.15. As mentioned above, one

explanation for the highly turbulent conditions at the deep convective line is the presence of moist absolutely unstable layers (Bryan and Fritsch 2000) in the simulations considered herein (see Fig. 3.16).

Even though turbulent mixing is recognized as a defining characteristic of the deep convective line, I caution against the stochastic mixing framework of Raymond and Blyth (1986) to conceptualize SL convection, as proposed by James and Markowski (2010). The present analyses suggest two reasons why stochastic mixing in its traditional form may not be appropriate for the type of storms simulated herein. First, all inflowing air takes part in SL convection in proportions determined by the structure of storm-relative air mass flux, contrary to the assumption that near surface air constitutes the core of the updraft, implicit in the stochastic mixing framework. Second, although parcels do seem to be vertically distributed by a buoyancy sorting process, their final height is not determined by the environmental sounding itself, as within-storm temperatures differ greatly from environmental values. Nonetheless, I think that the stochastic mixing model could provide a useful conceptual framework if mixing between air samples from all heights is incorporated, with the storm-relative inflow structure modulating the mixing fractions, and if the buoyancy sorting process acknowledges within-storm thermodynamics.

3.5 Summary

This chapter has been devoted to analyses of numerically simulated mid-latitude squall lines in thermodynamic environments carefully designed via vertical distributions of CAPE and LFC, using the technique for generating soundings presented in chapter 2. For a given value of environmental wind shear, ICAPE discriminates simulated storms in terms of upper-tropospheric heating, which feedbacks on the RIJ and cold pool development. This result is interpreted in terms of layer-lifting convection, where all layers of storm-relative inflow take part in the convective process, with ICAPE providing a bulk metric of buoyancy under the vertical displacement of mid and low-tropospheric air. However, by itself ICAPE cannot account for the characteristics of SLs, as it does not fully capture the thermodynamic properties of air above the layer of latent-instability, while its formulation does not contemplate the structure of storm-relative air inflow. In this regard, I found that environmental shear plays a fundamental role, modulating the fraction of inflowing latent-unstable air, and thus explaining the increase in within-storm heating associated with storms in more strongly sheared environments.

With the exception of simulations in low shear and dry mid-tropospheric environments, surface cold pool temperatures are insensitive to the low-tropospheric shear value, as well as to changes in mid and low-tropospheric environmental thermodynamics. Cold pool temperatures above the surface varied among simulated storms, with drier mid-tropospheric environments producing relatively warm outflows. In addition, the subsiding FTRF branch, a mesoscale airflow which to my knowledge has not been described in the previous literature, could have an important impact on cold outflow air, due to mixing at a crossover zone with the RIJ air. Hence, although highly constrained at the surface, cold pool properties aloft are regulated by complex processes involving mid-to-upper-tropospheric thermodynamics, environmental shear, as well as air interactions at the FTRF-RIJ boundary.

Results reported in this chapter show the potential usefulness of precipitable water as an environmental diagnostic of the surface precipitation rate, regardless of the vertical distribution of CAPE. For a given value of low-tropospheric wind shear, I found that the rate of water vapor

processed by SLs is the main factor affecting surface precipitation rates. However, the precipitation efficiency decreased as the environments had lower values of shear and mid-tropospheric relative humidity. In addition, a relevant feature in terms of flood potential is the relatively low propagation speed produced under the environment with smaller low-tropospheric temperature lapse rate, although this environment appears to be the least conductive to wind-induced damage.

Table 3.1. MUCAPE, MLCAPE, DCAPE, and CIN are in units of J kg^{-1}, ICAPE is in J m^{-2} x 10^{-6}, and PW is in kg m^{-2}. The parcel used for MLCAPE has the average potential temperature and water vapor mixing ratio of the lowermost 100 hPa. The definition of DCAPE is as in Gilmore and Wicker (1998), and CIN is the convective inhibition of the surface parcel.

Case	MUCAPE	MLCAPE	ICAPE	DCAPE	CIN	PW
baseline	2250	2250	4.3	1060	32	44.6
base_sens	2250	2250	4.3	1200	32	43.5
Stable	2250	2250	4.3	970	32	45.8
Low	1750	1750	3.3	950	31	43.5
high	3250	3250	6.2	1250	35	46.6
shallow	2250	2180	3.1	1040	28	41.1
deep	2250	2250	5.2	1070	35	46.6

Table 3.2. The surface Precipitation Rate (PR) is in mm day^{-1}. The Propagation Speed (PS), cold pool intensity (c), maximum across-line surface speed ($\max(u_0)$), and the maximum along-line averaged u_0 ($\max(\overline{u_0})$) are in m s^{-1}. The precipitation efficiency (PE) is presented as a percentage, and it was computed using environmental fields. Values at 4 h (see text for further details).

Case	PR	C	PS	$\max(u_0)$	$\max(\overline{u_0})$	PE
baseline	17	32	6.5	35.3	15.5	46
base_sens	15	32	7.3	35.6	16.2	39
stable	17	31	4.8	31.4	8.7	50
low	15	29	5.4	36.5	15.5	46
high	22	37	8.5	35.8	19.8	50
shallow	11	29	4.7	28	9.6	37
deep	20	34	7	34.8	16.7	51

Table 3.3. Fields as in Table 3.2 corresponding to ΔU=8 simulations.

Case	PR	*c*	PS	$\max(u_0)$	$\max(\overline{u_0})$	PE
baseline	11	30	11	38.6	26.8	29
base_sens	9	29	10.5	37.9	17.4	25
stable	13	29	9.7	32.2	16.4	36
low	8	27	9.7	33.4	17.4	24
high	16	35	13.5	39.6	22.8	35
shallow	5	26	9.2	32.7	15.9	16
deep	15	32	11.7	40	22.2	36

Table 3.4. Fields as in Table 3.2 corresponding to ΔU=24 simulations. The *shallow_24* data is omitted because the storm did not reach a mature state (see text).

Case	PR	*c*	PS	$\max(u_0)$	$\max(\overline{u_0})$	PE
baseline	22	35	1.8	24.1	4.8	62
base_sens	20	33	2.4	33	4.6	55
stable	22	34	.9	28.2	-.5	64
low	20	31	1.3	25.3	3.3	61
high	27	39	3.6	28.4	9.9	64
shallow	-	-	-	-	-	-
deep	25	37	2.6	26.9	6.2	65

Figure 3.1. In a) the different CAPE profiles used for generating soundings are displayed, with the *y*-axis representing the pressure level of parcel origin. The line labeled as baseline corresponds to the environments *baseline*, *base_sens*, and *stable*. In b) the LFC profiles used for generating soundings are displayed, the *y*-axis being as in a). The line labeled as baseline corresponds to the environments *baseline*, *stable*, *low*, and *high*.

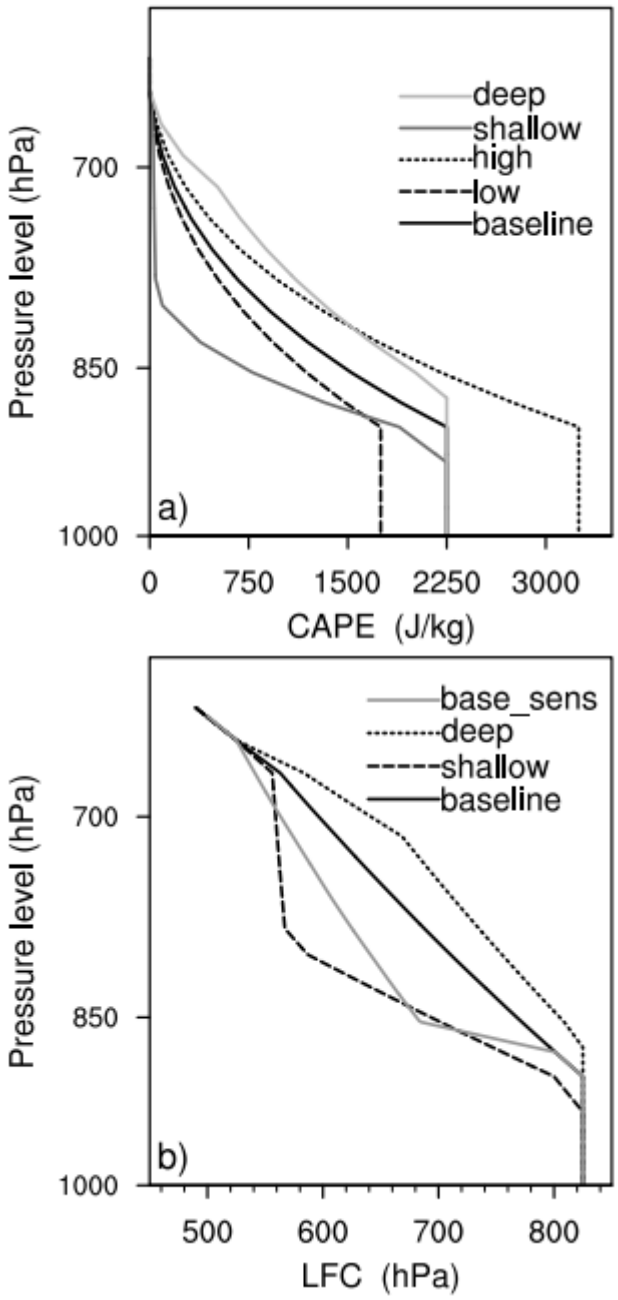

Figure 3.2. Soundings representative of a) environments with identical CAPE, where the thick solid lines correspond to *baseline*, the dashed lines represent *base_sens*, and the thin solid lines depict *stable*. Soundings of environments with identical LFC and where CAPE is varied are shown in b), where *high* is given by the thick lines, while the thin lines correspond to *low*. In c) environments that differ in both CAPE and LFC profiles from *baseline* are displayed, with the dew point temperatures of *deep* and *shallow* in dashed and dotted lines respectively (the solid line is temperature). All soundings in b) and c) are identical to *baseline* above 500 hPa.

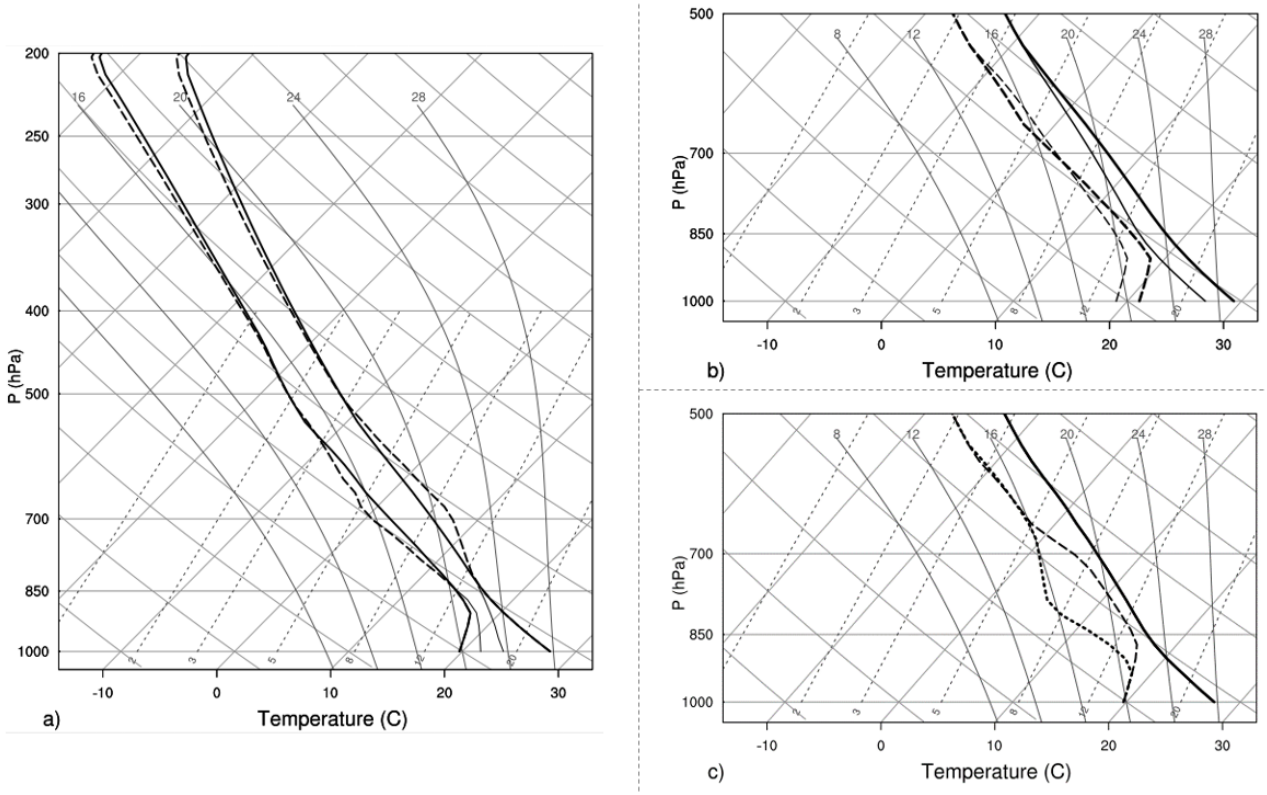

Figure 3.3. Profiles of horizontal winds (across-line direction) used in association to each sounding in Fig. 3.2.

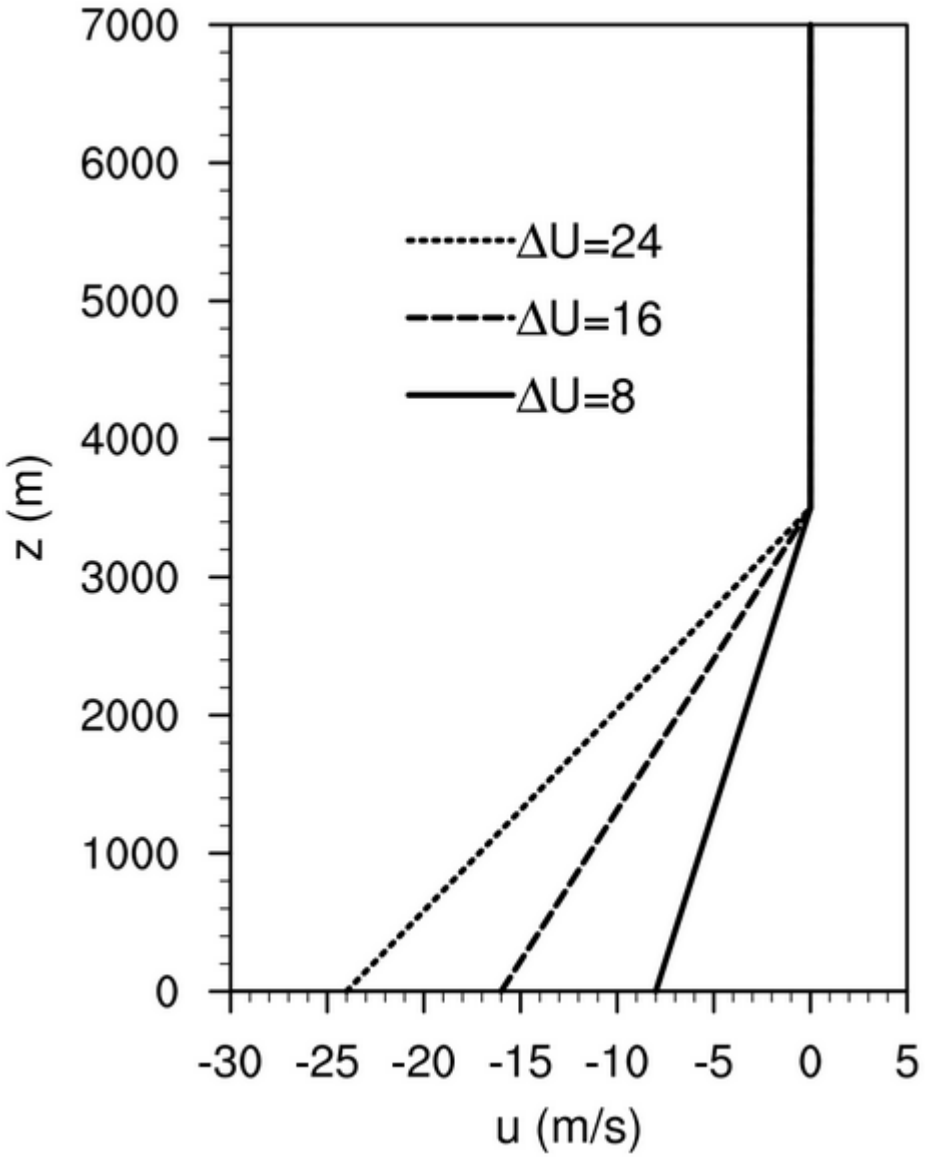

Figure 3.4. Along-line averaged radar reflectivity in a plane perpendicular to the deep convective line corresponding to *baseline_16* at a) t = 2 h, b) t = 4 h, and c) t = 6 h.

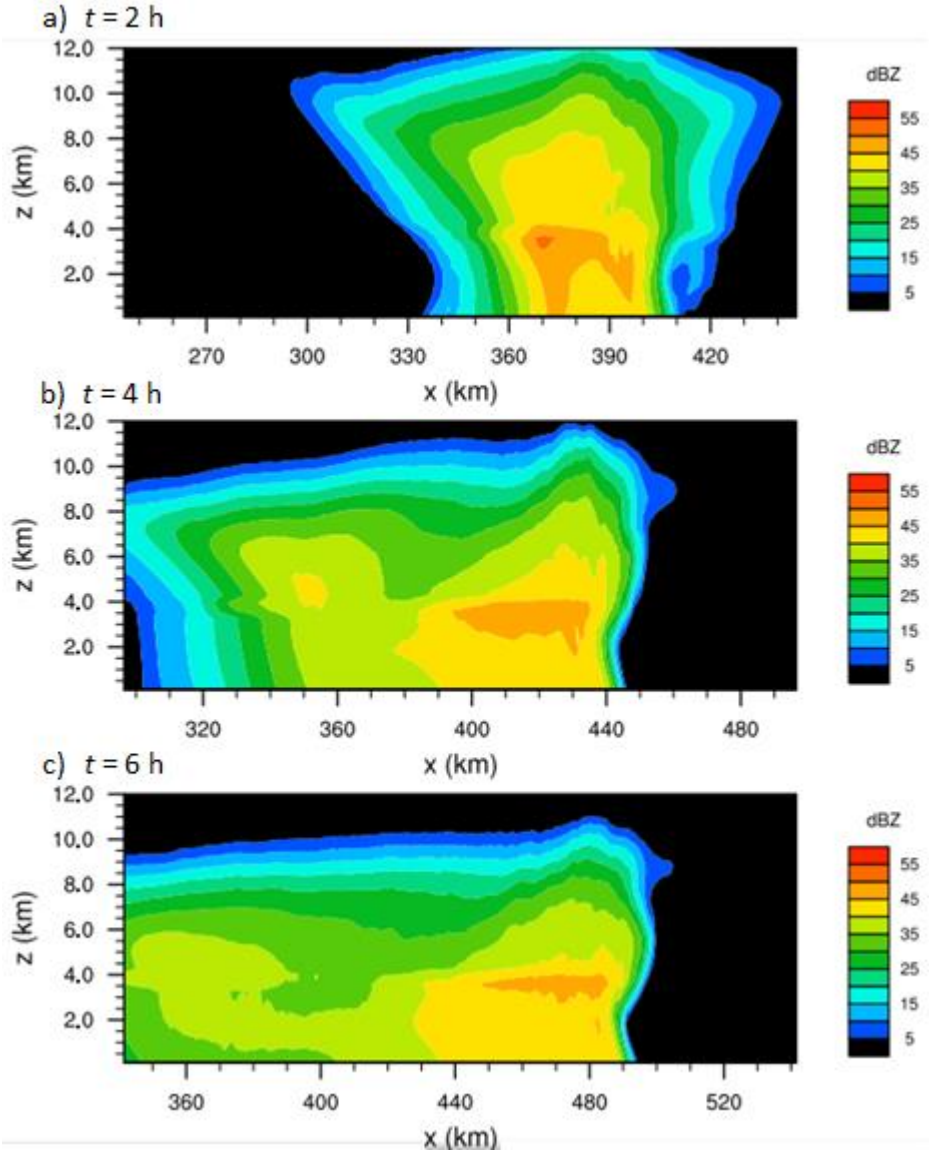

Figure 3.5. Along-line averaged radar reflectivity in a plane perpendicular to the deep convective line at 4 h corresponding to a) *baseline_8*, b) *baseline_16*, and c) *baseline_16*.

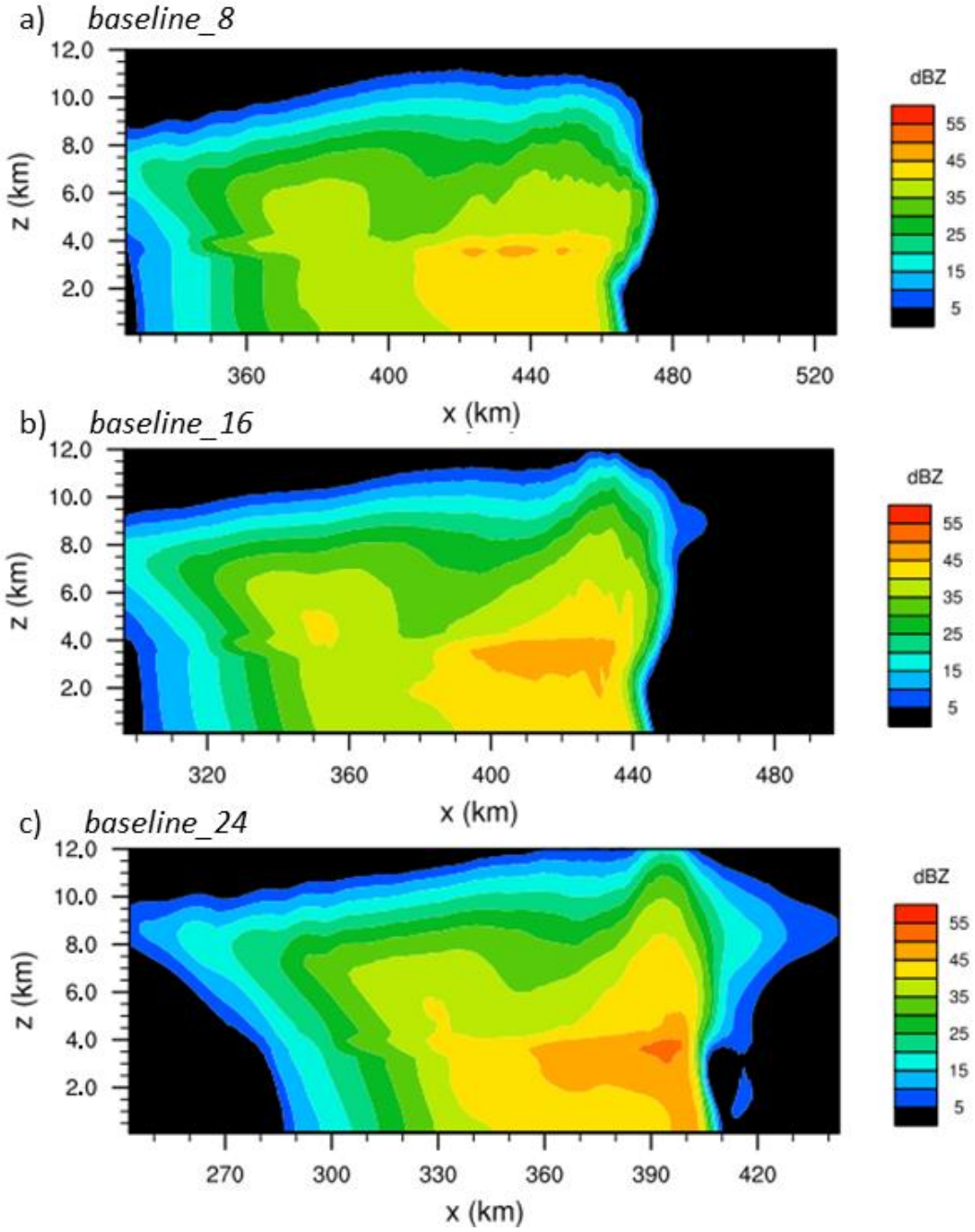

Figure 3.6. Radar reflectivity in the horizontal plane at 1 km height corresponding to a) *baseline_8*, b) *baseline_16*, and c) *baseline_16*.

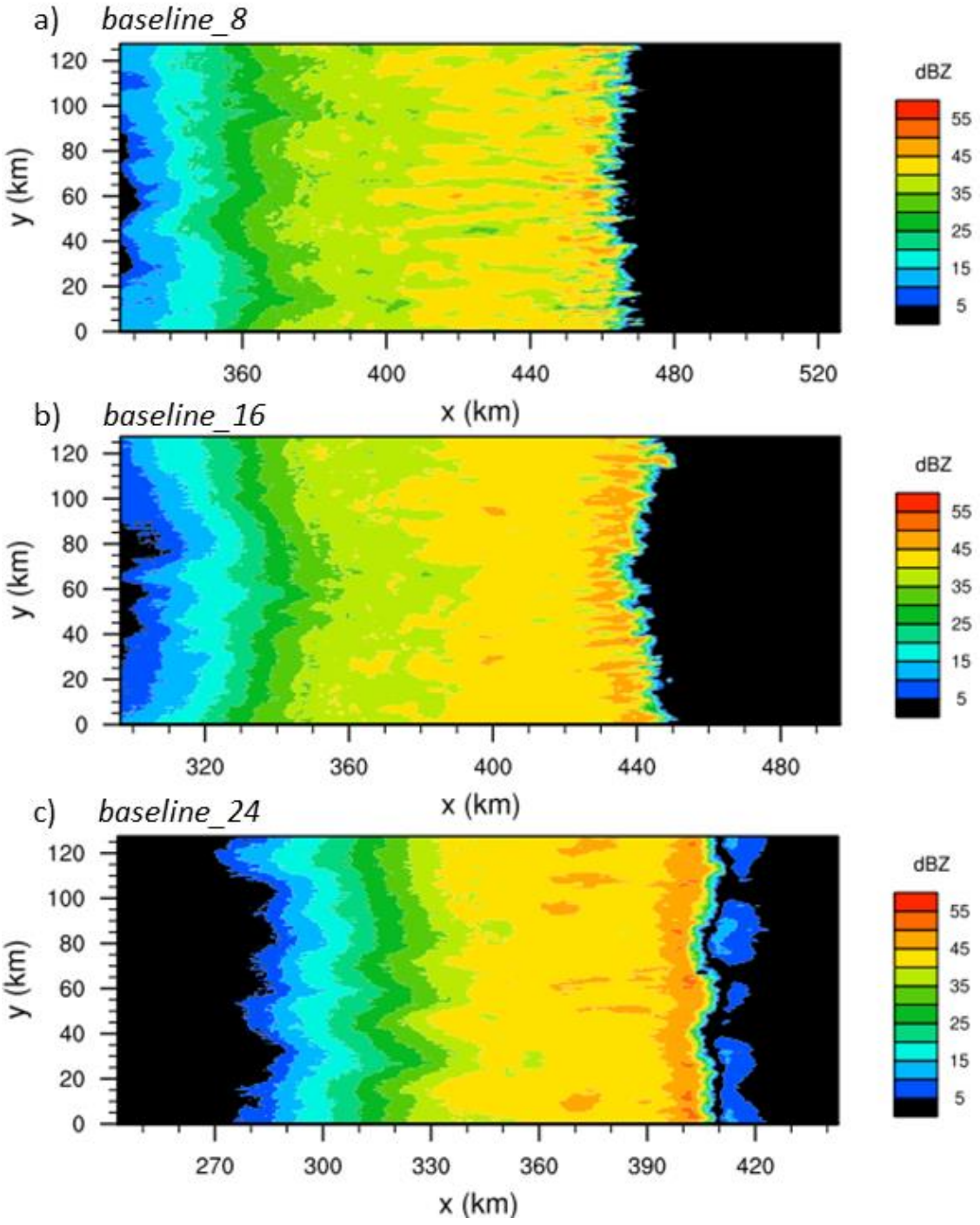

Figure 3.7. Along-line averaged surface-relative horizontal velocity contours (red and every 5 m s^{-1}) and pressure perturbation contours (black and every 50 Pa) overlaid on the buoyancy field (color filled, as in the color table) for *baseline_16* at a) t = 2 h, b) t = 4 h, and c) t = 6 h. The white line corresponds to neutral buoyancy, and the thick red and black lines respectively denote zero horizontal winds and pressure perturbations. Negative contours are dashed in the case of the horizontal velocity and pressure perturbations.

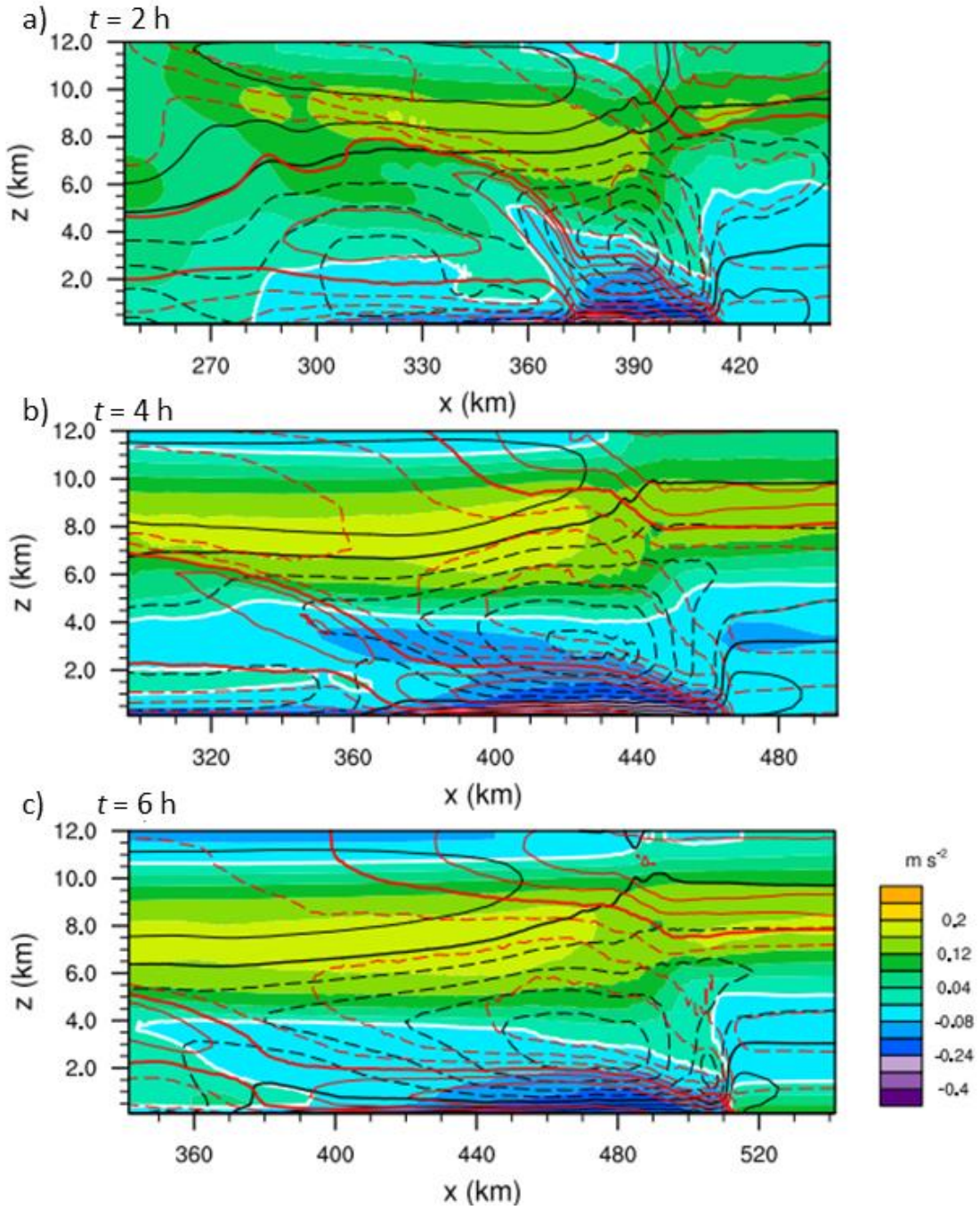

Figure 3.8. Contours of along-line averaged cooling produced by microphysical processes in *baseline_16* are color-filled according to the values given by the color table. Contours of mixing ratios of graupel (black and every .4 g kg^{-1}), show (orange and every .15 g kg^{-1}), and rain (red and every .15 g kg^{-1}) are included every. The white contour encloses the region where the along-line averaged *w* is less than -1 m s^{-1}.

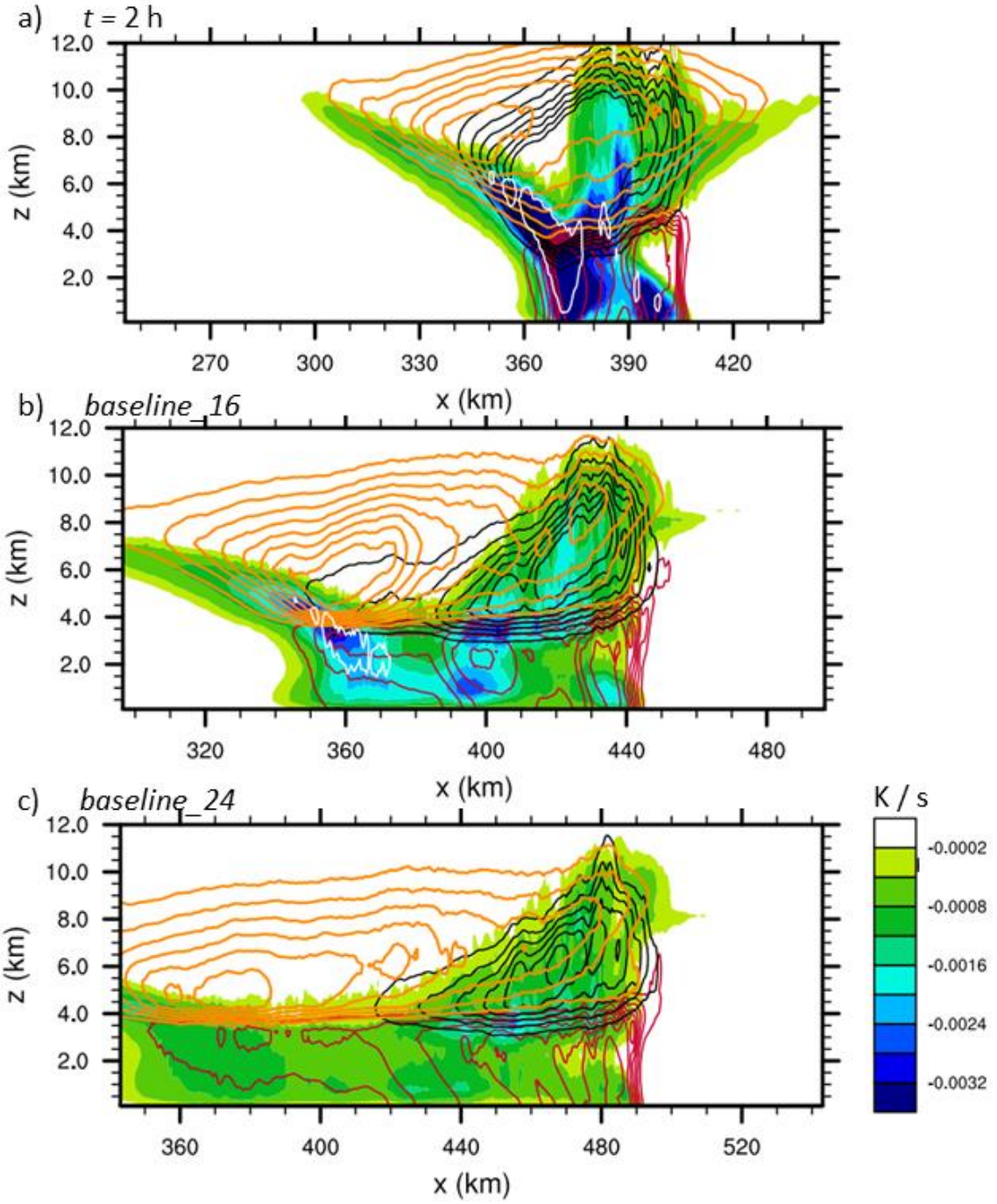

Figure 3.9. Domain averaged surface precipitation rate (PR) in mm/day for ΔU = 16 simulations. The lines are colored according to the PW, as shown by the label bar.

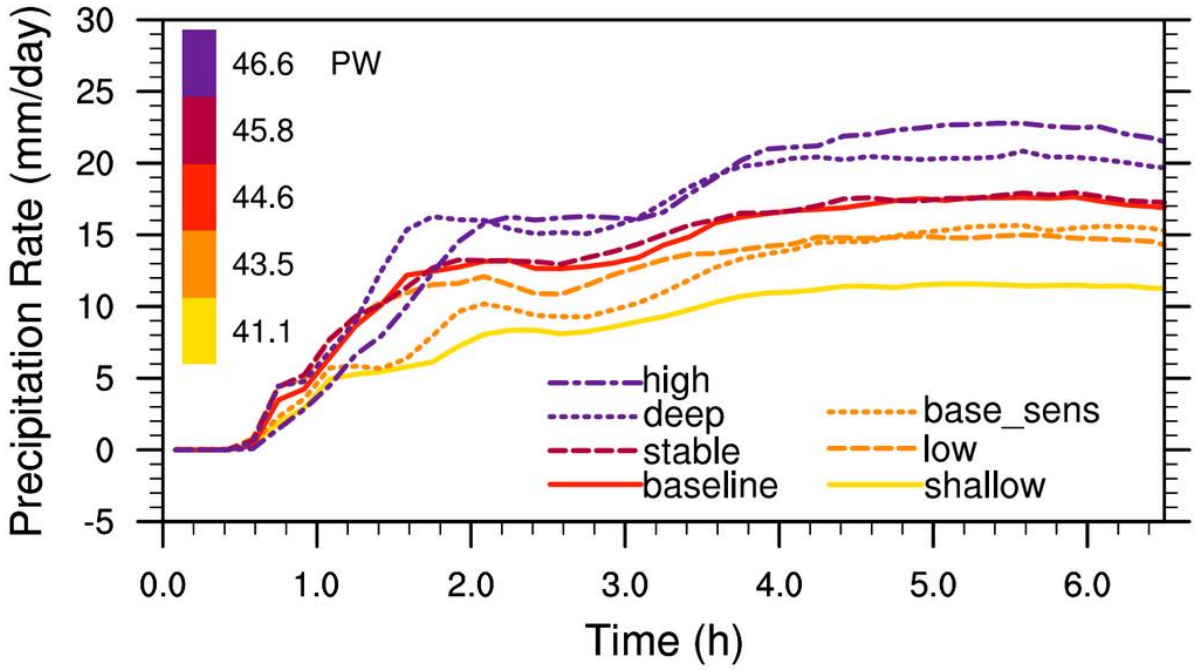

Figure 3.10. Fields as in Fig. 3.7 at 4 h in a) *baseline_16*, b) *base_sens_16*, and c) *stable_16*.

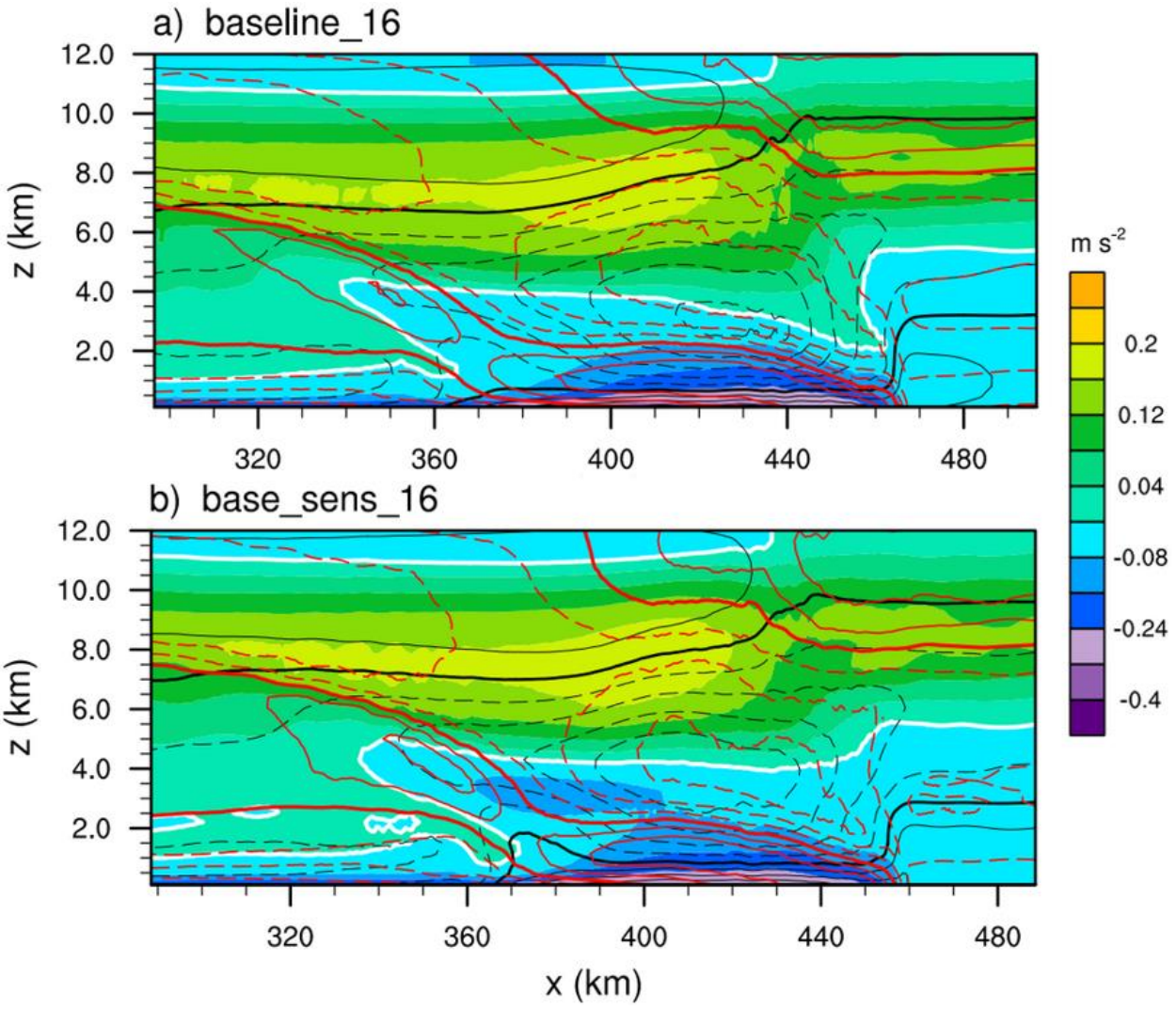

Figure 3.10. Continued.

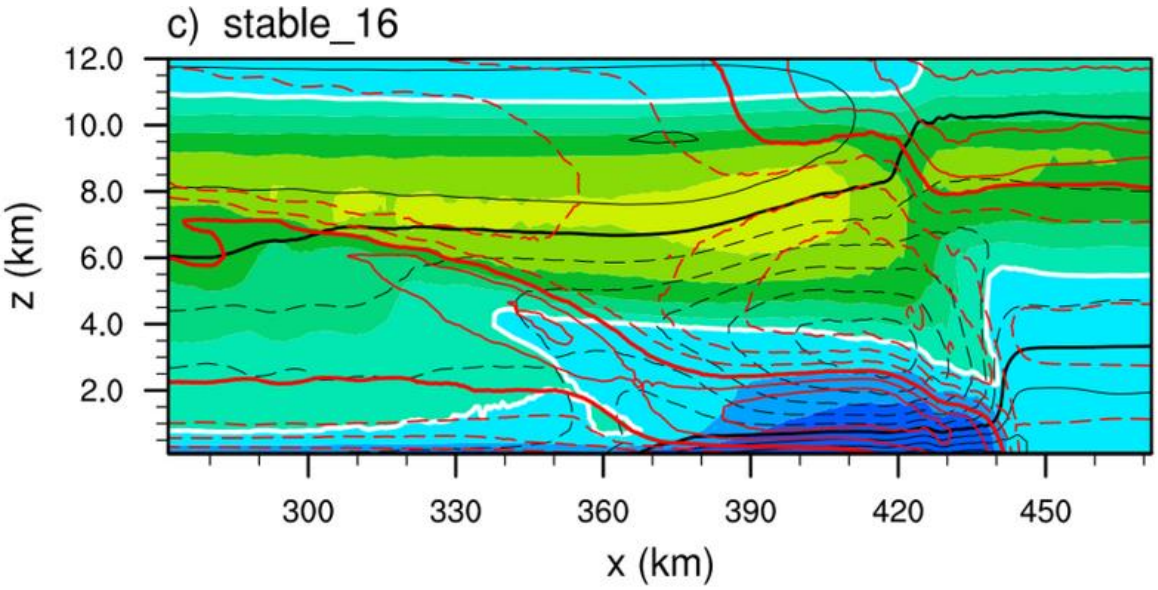

Figure 3.11. Soundings passing roughly through the center of the meso-low at 4 h of simulation time. In a) the temperature soundings of *baseline_16* (solid; black), *base_sens_16* (dashed), and *stable_16* (dotted) are shown alongside *stable_16*'s dew-point temperatures (gray), the other two moisture profiles omitted for readability. In b) the RHs corresponding to the soundings in a). The temperature component of the buoyancy profile of the cold pools of *baseline_16* and *base_sens_16* are shown in c), and the corresponding vertical profiles of cold pool intensity are shown in d).

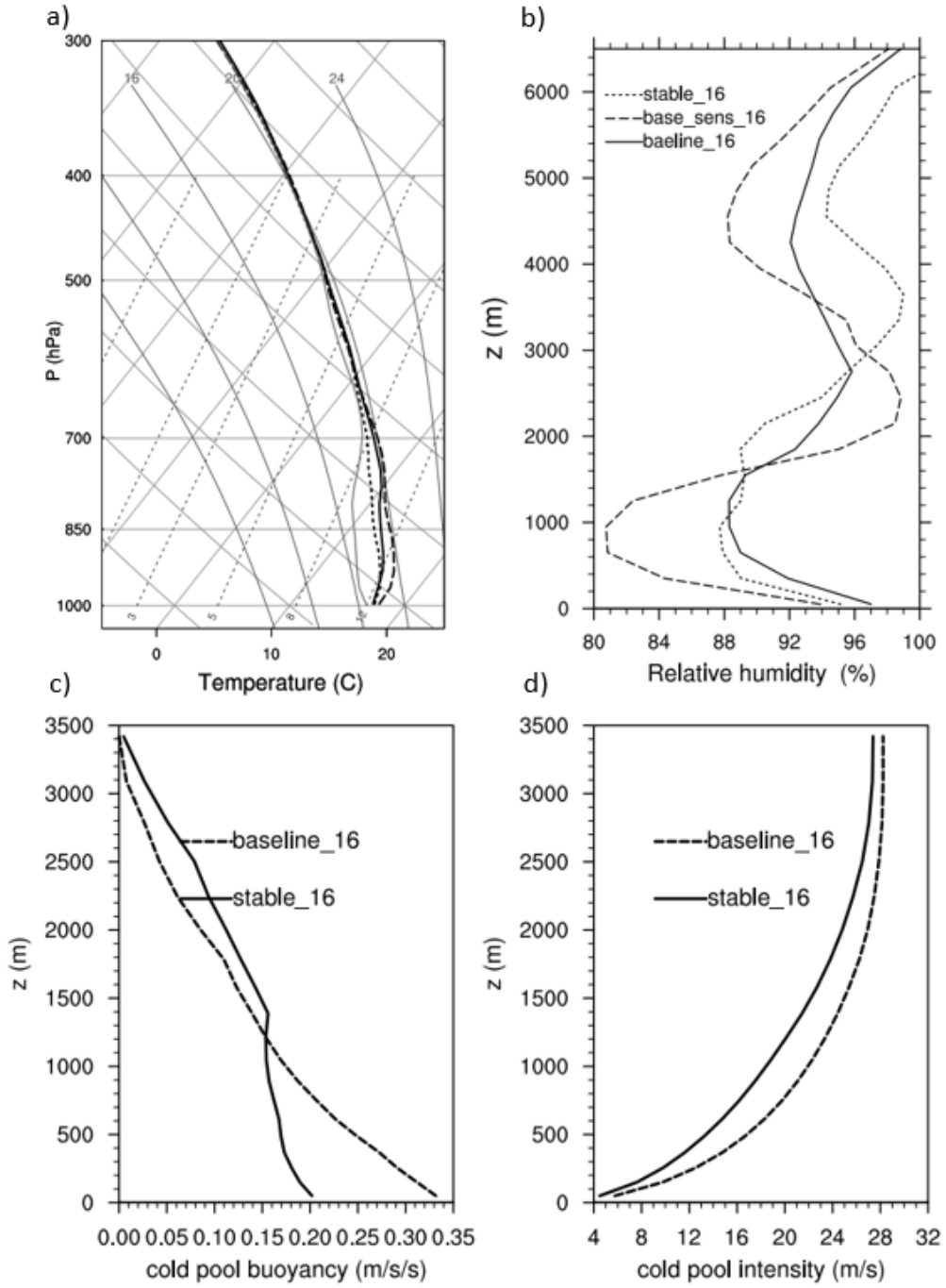

Figure 3.12. Fields as in Fig. 3.7 at 4 h in a) *low_16*, b) *high_16*, c) *shallow_16*, and d) *deep_16*.

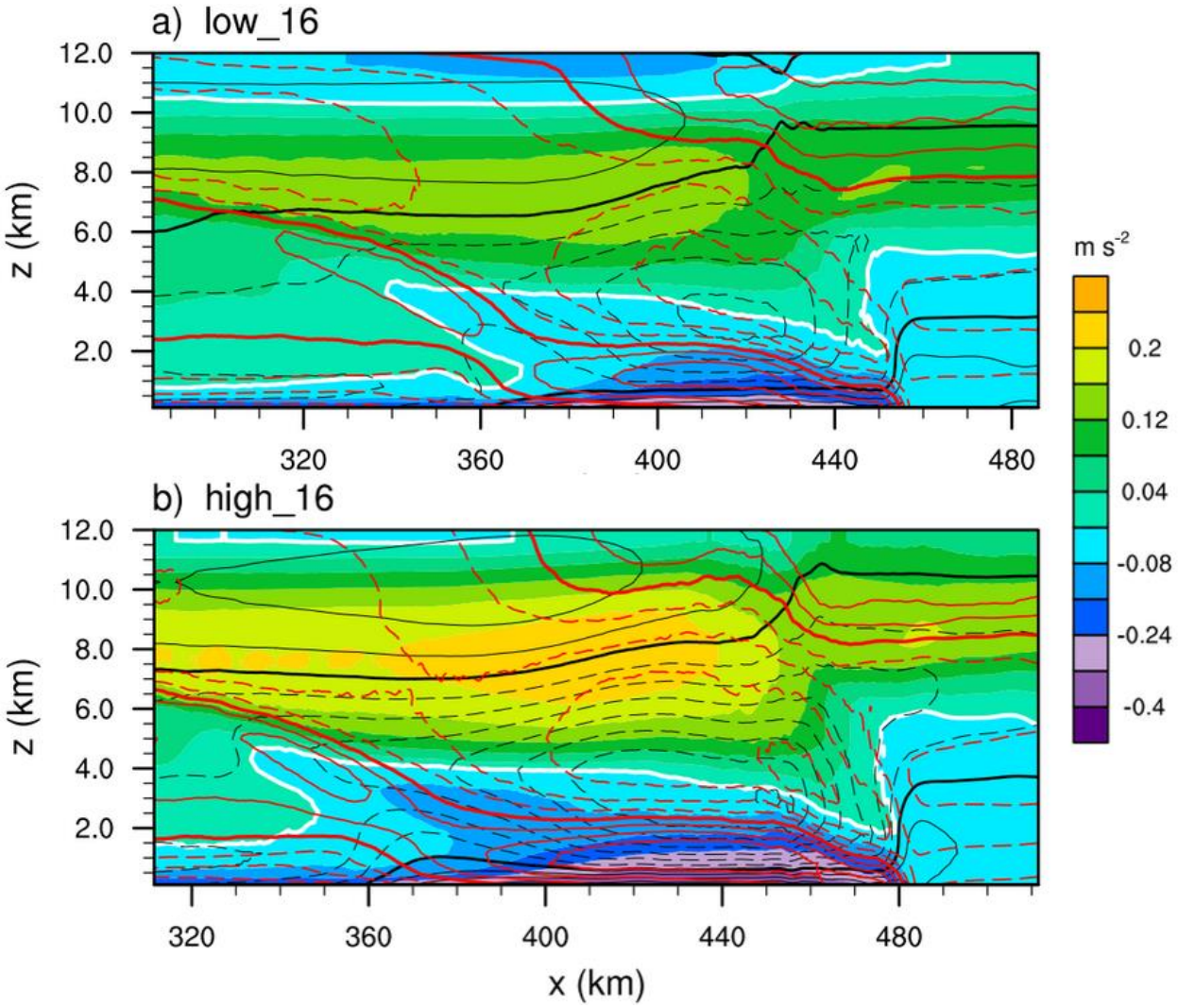

Figure 3.12. Continued.

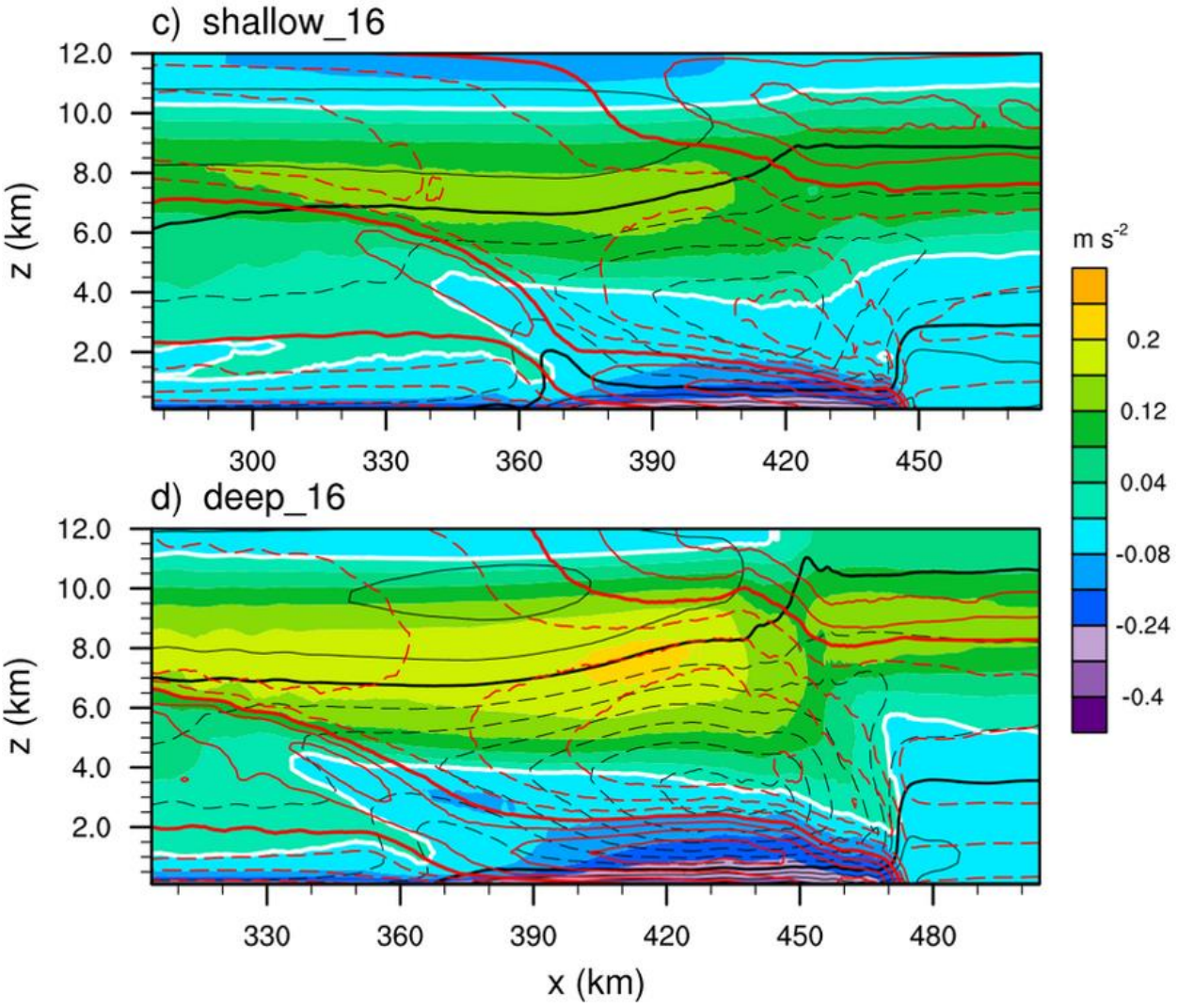

Figure 3.13. Soundings in a) are as in Fig. 3.11a, and RH in b) are as in Fig. 3.11b, corresponding to cases where the CAPE profile is varied: *low_16* (solid), *high_16* (dashed), *shallow_16* (dotted), and *deep_16* (dash-dotted).

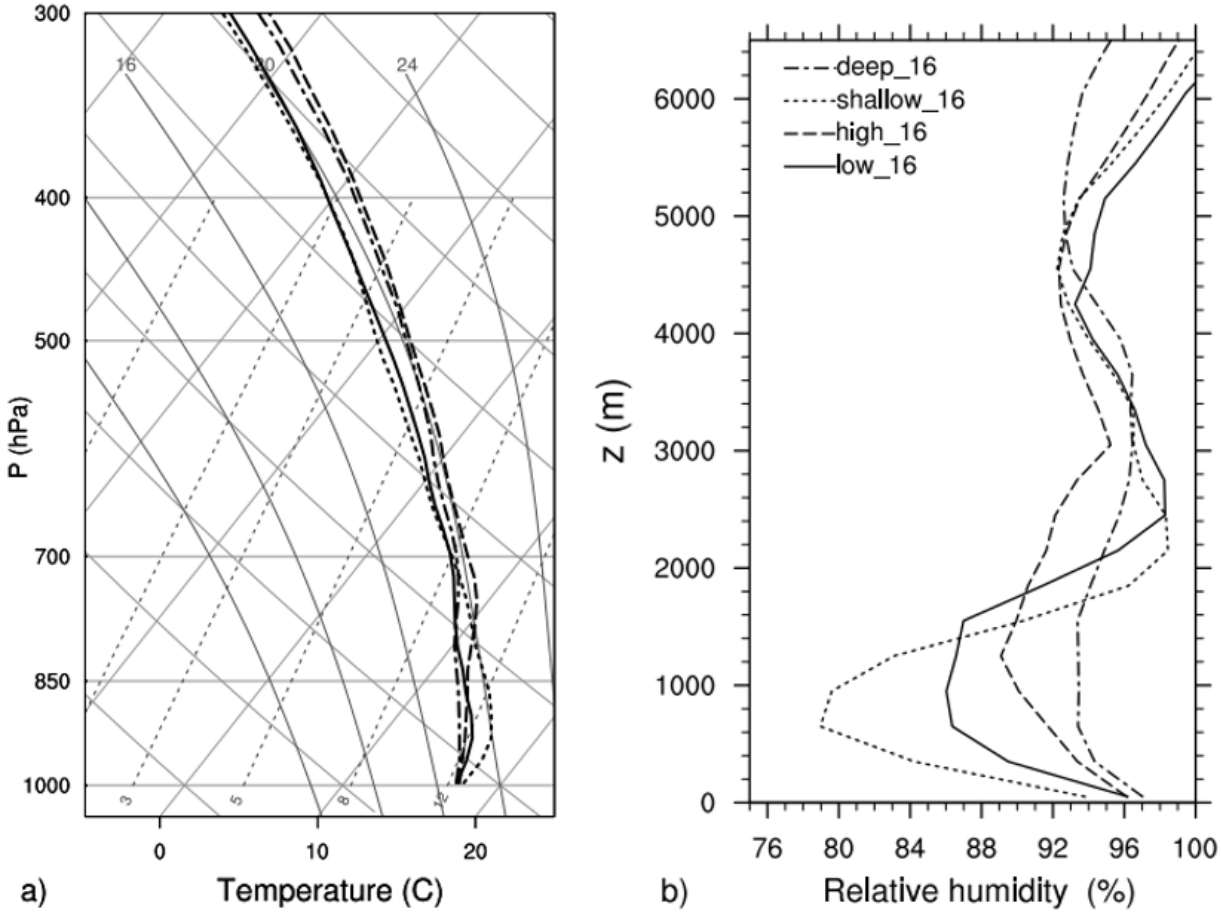

Figure 3.14. Upper portion of within-storm temperatures on a SkewT-lnp chart for all ΔU = 16 simulations, colored according to environmental ICAPE, as shown by the label bar.

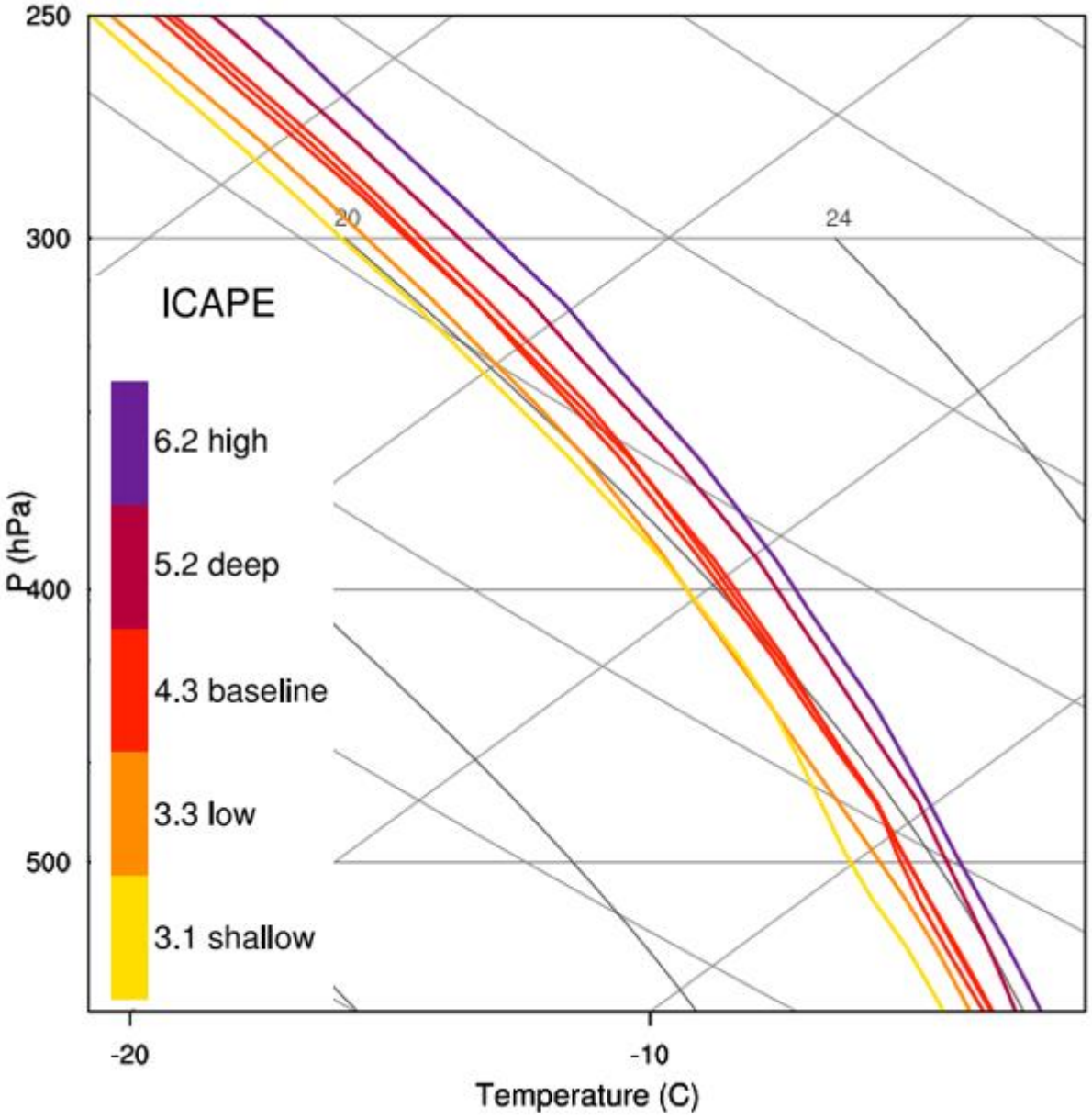

Figure 3.15. Particle trajectories projected onto the across-line/height plane. The particles were placed ≈ 6 km ahead of the cold pool edge at 4 h of simulation time, spaced by 1 km in the along line direction, and at height a) 300 m, b) 1800 m, c) 3300 m, and d) 4800 m. The paths are colored based on the temperature difference of the parcel and the initial sounding, with the black dots indicating 5 h simulation time. Contours of along-line averaged *h* at 6 h and every 3 K are included in the background for reference.

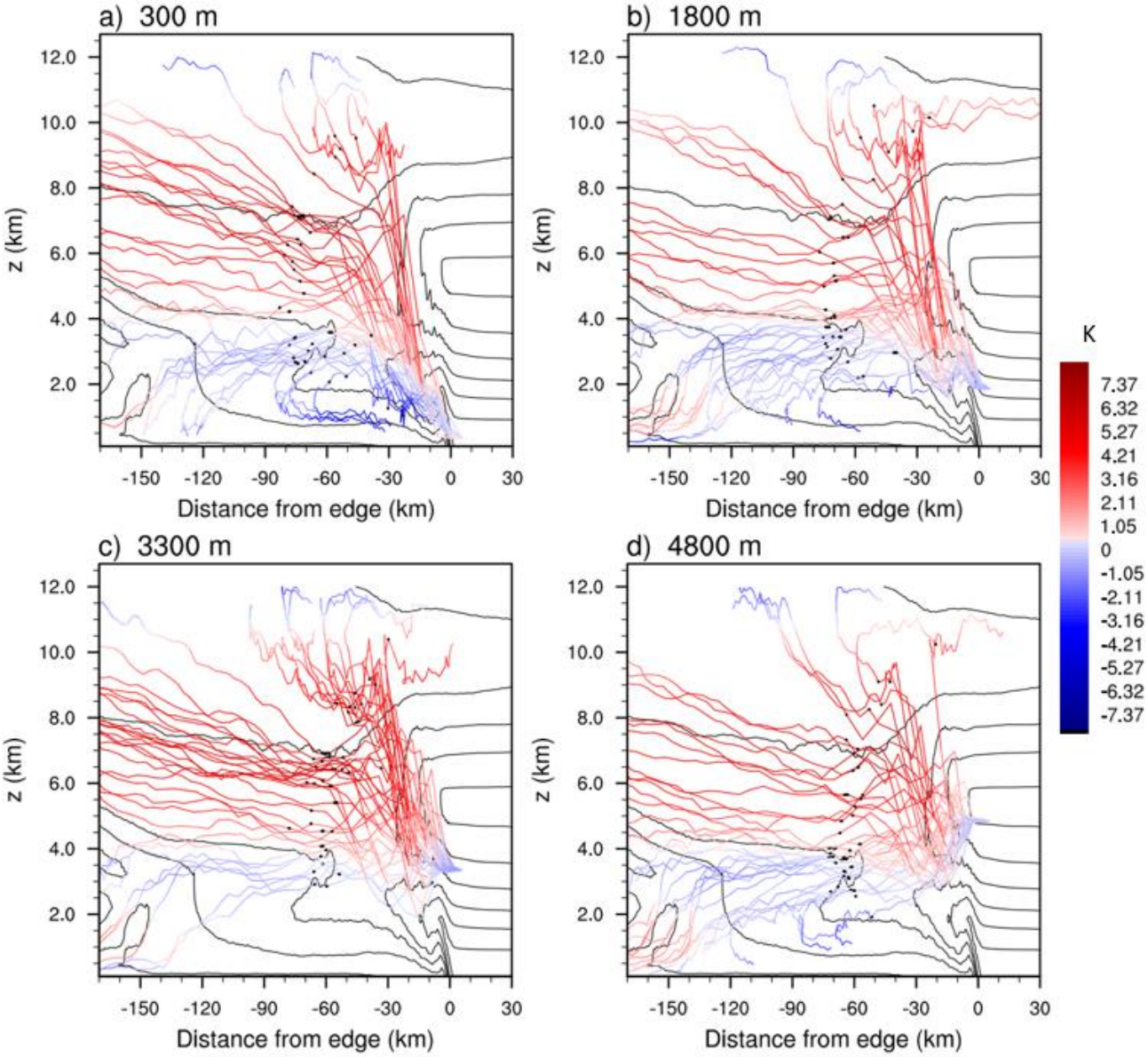

Figure 3.16. Contours of *h* at 4 h in *baseline_16*, without any averaging. The thin black line encloses updrafts with exceeding 10 m s^{-1}. The thin white line encloses the region where cooling due to melting of ice exceeds .0003 K s^{-1}. The thick black contour encloses the region of MAULS.

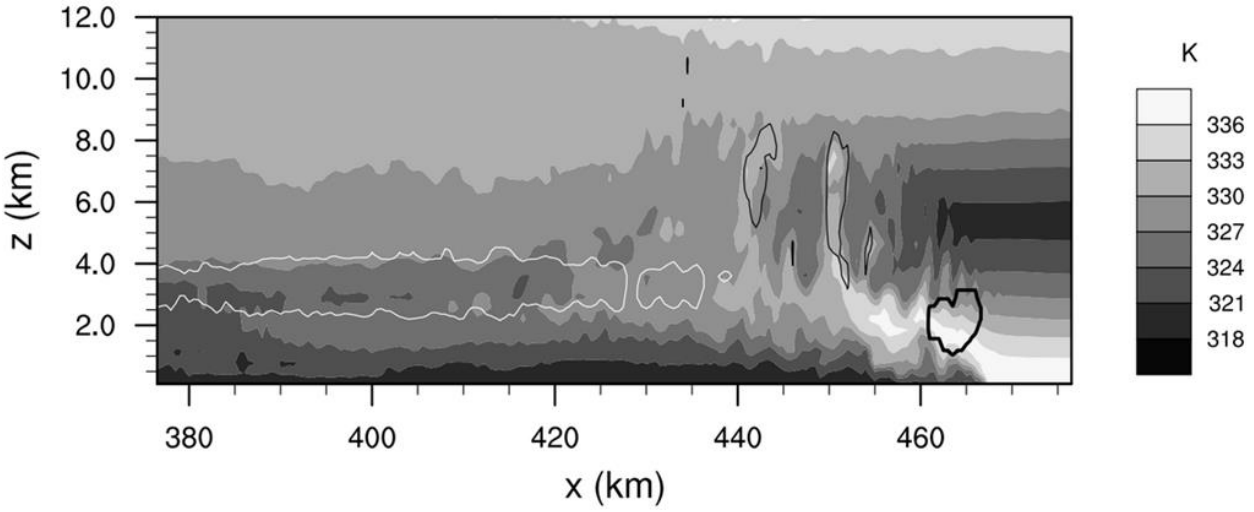

Figure 3.17. Histograms showing the number count of particle heights at 5 h for different ΔU = 16 simulations, identified by color through the label bar in d). Particles originate at a) 300 m, b)1800 m, c)3300 m, and d) 4800 m, and were specified as in Fig. 3.15.

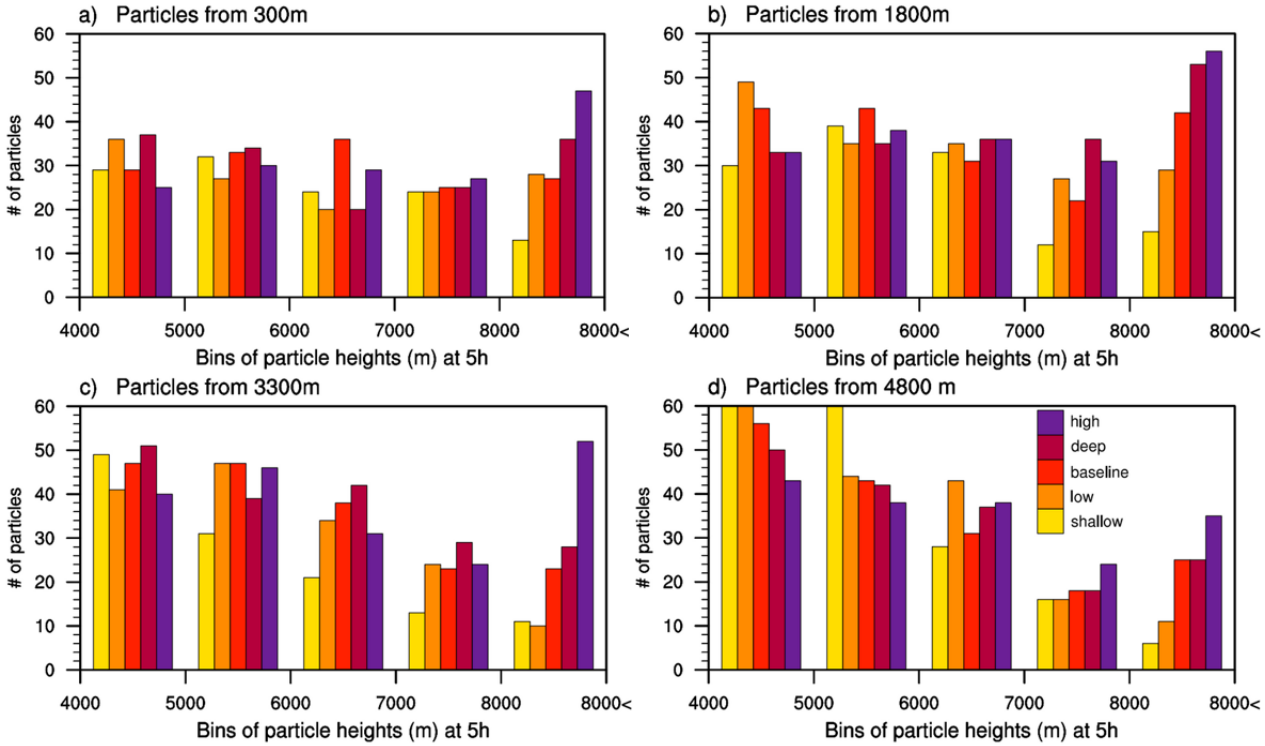

Figure 3.18. As in Fig. 3.9, representing cases with $\Delta U = 8$ in a), and cases with $\Delta U = 24$ in b).

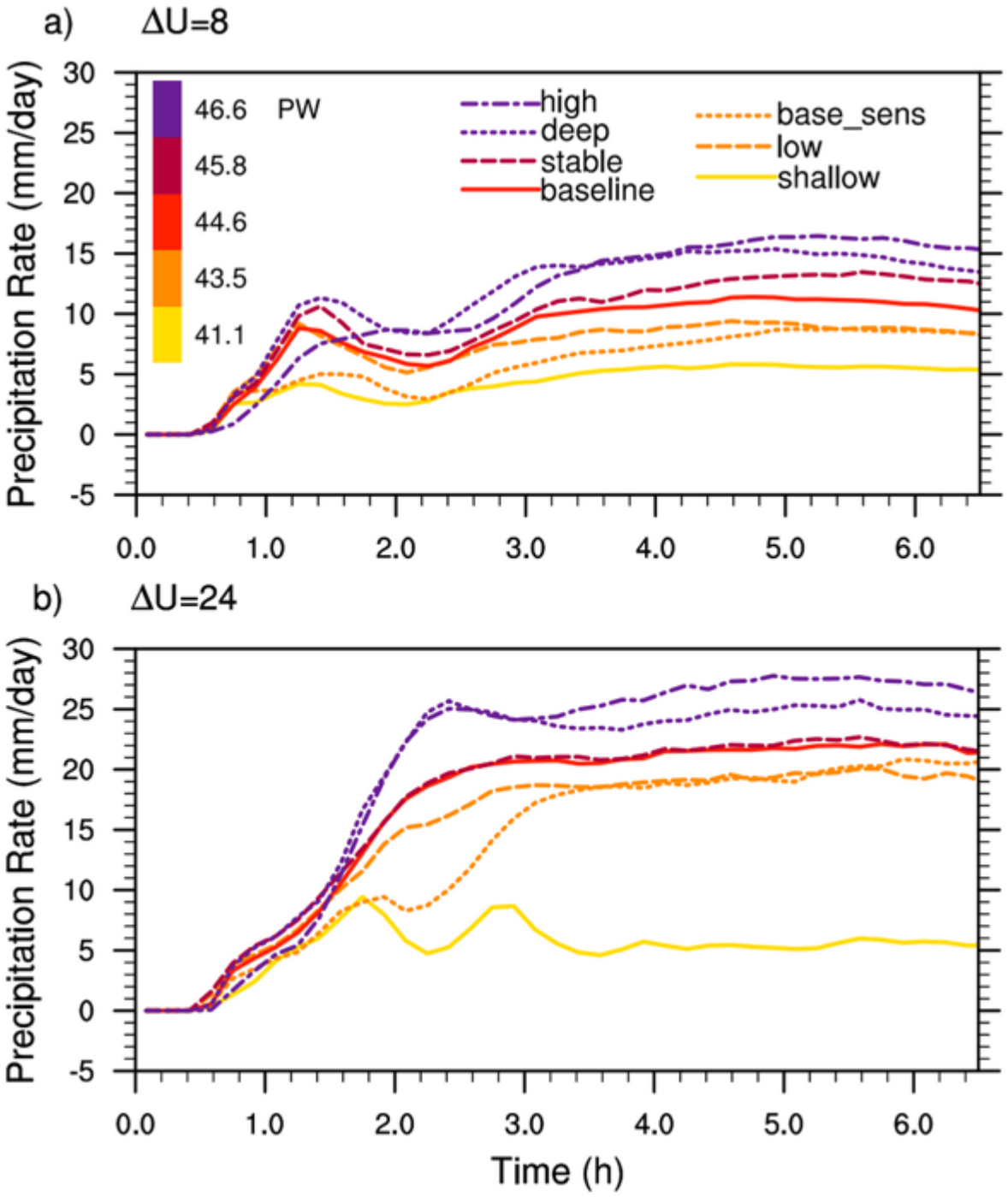

Figure 3.19. Scatter plot representing all simulations on an ICAPE-*W* plane in a) and on a MUCAPE-*W* plane in b) (see text for further details).

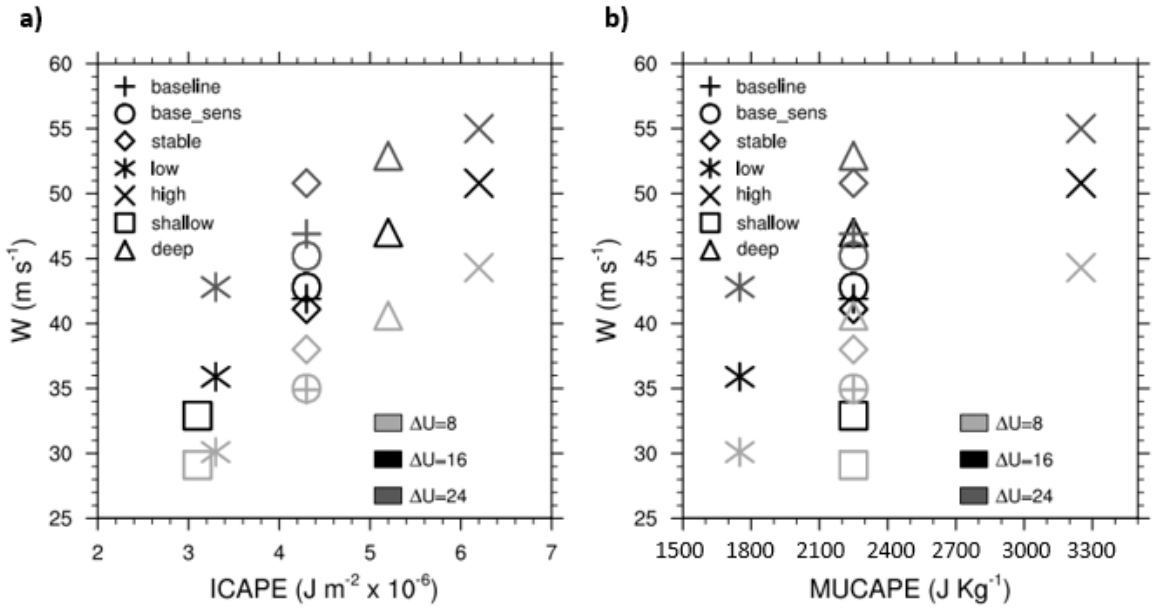

Figure 3.20. Scatter plot representing all simulations on a PS-(shear layer inflow fraction) plane (see text for further details).

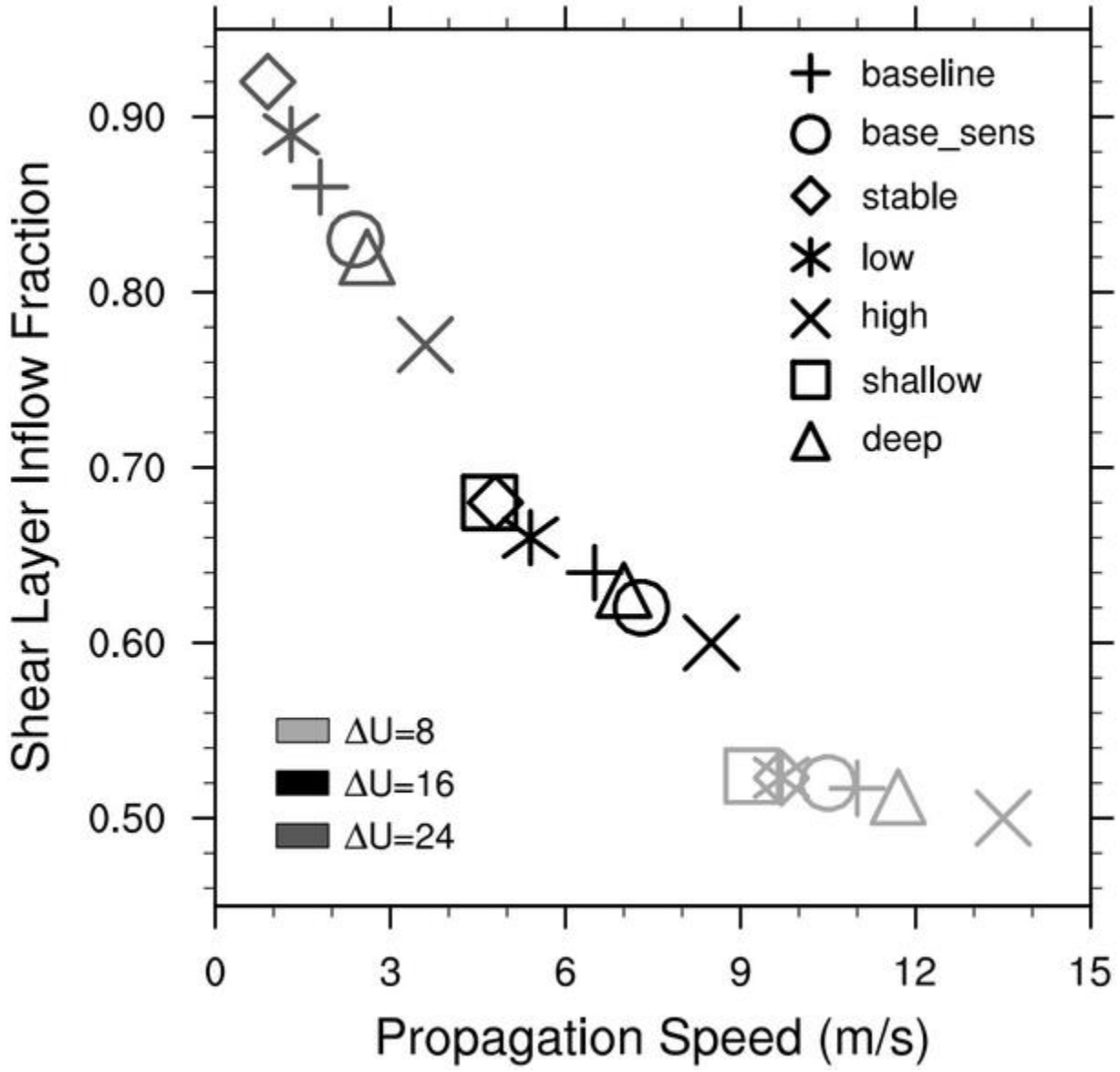

Figure 3.21. Along-line averaged cold pool temperatures at the lowest height of model output (50 m), with the across-line location selected as in Figures 3.11 and 3.13.

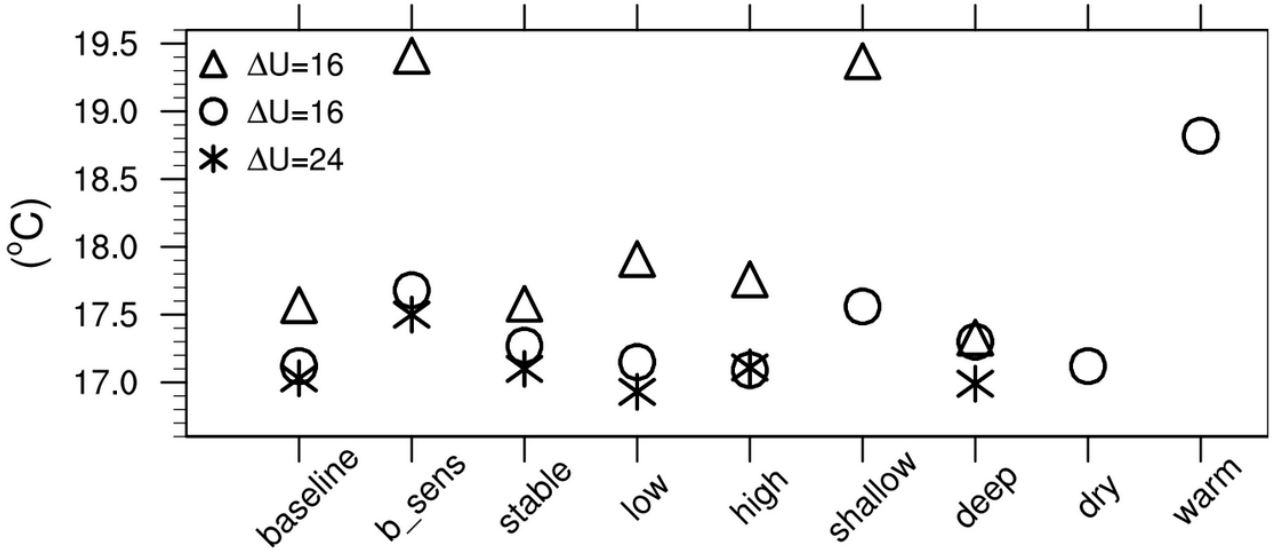

Figure 3.22. Histogram of heights attained at the time of model initiation by backward trajectories computed from the *baseline_16* simulation with data outputted every minute. The trajectories initiated at 75 m height and within 20 km of the across-line location of the sounding in Fig. 3.11.

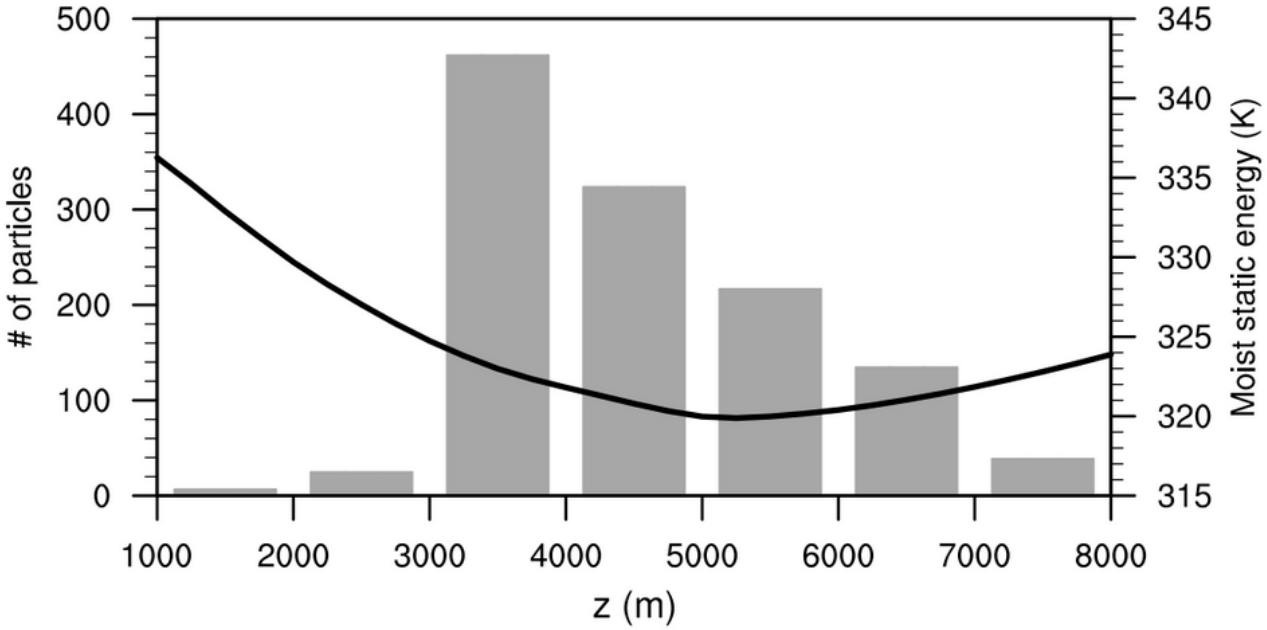

Figure 3.23. As in Fig. 3.1a, but for three different soundings meant to represent the thermodynamic environments considered by Weisman (1992, 1993). These soundings were specified using the analytical profiles of equivalent potential temperature and RH presented in Weisman and Klemp (1982).

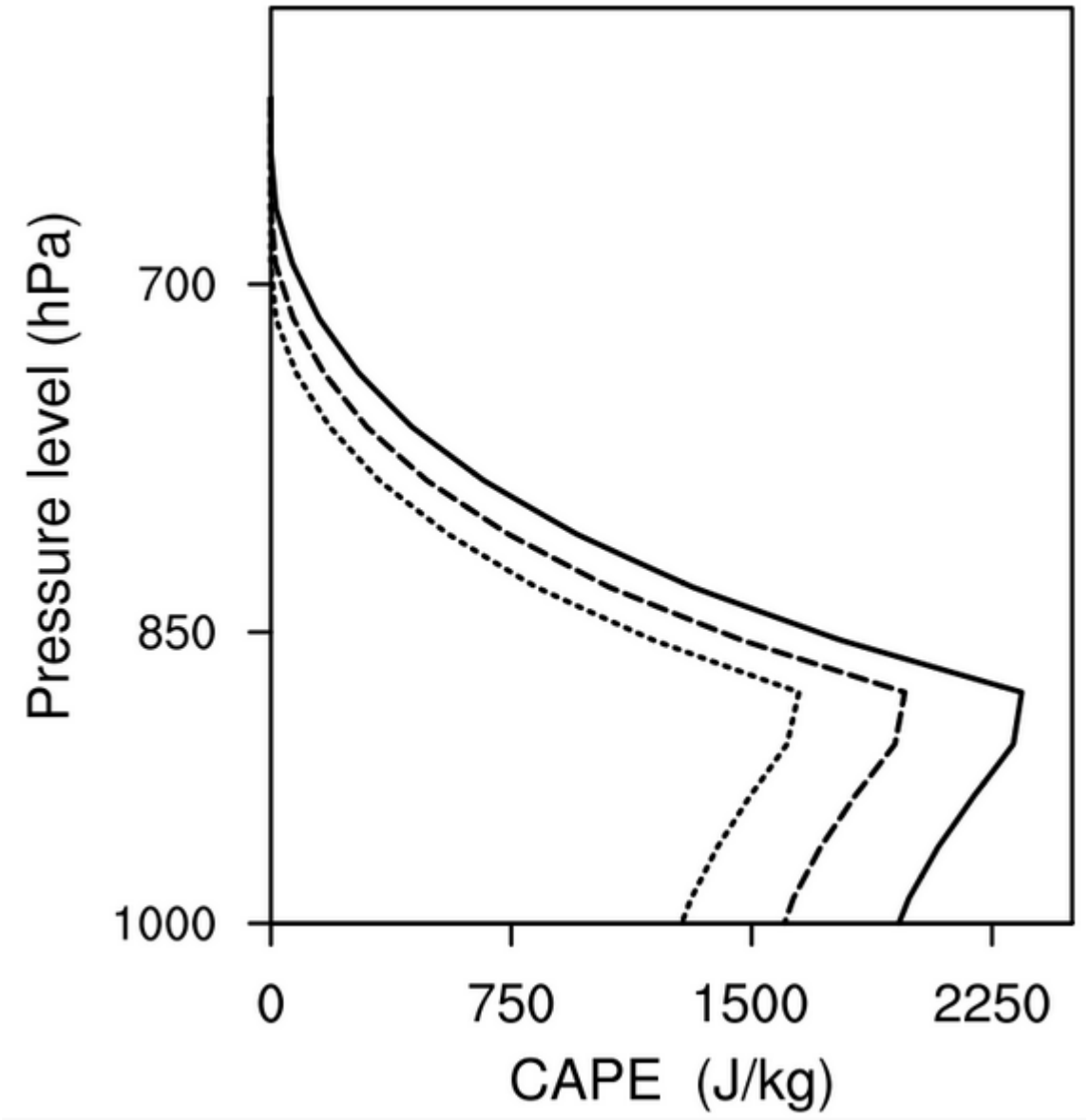

Figure 3.24. Schematic representation of the airflow characterizing a mid-latitude SL when viewed on a plane perpendicular to the line of deep convection. Environmental winds relative to the system are represented by the rightmost arrows, with green colors reflecting the presence of latent-instability. The brighter the green color, the greater CAPE corresponding to the parcel originating at that level. Behind the deep convective line, which is represented by the area in red, the different airflows are represented through arrows, which are separated by thick black lines (see text for further details). The colors of the arrows within the storm are meant to denote buoyancy, red corresponding to positive values, while blue and purple denote negative buoyancy. The meso-low and the high surface pressure perturbations near the cold outflow's edge are respectively denoted by L and H. The length of within-storm arrows do not represent wind speed.

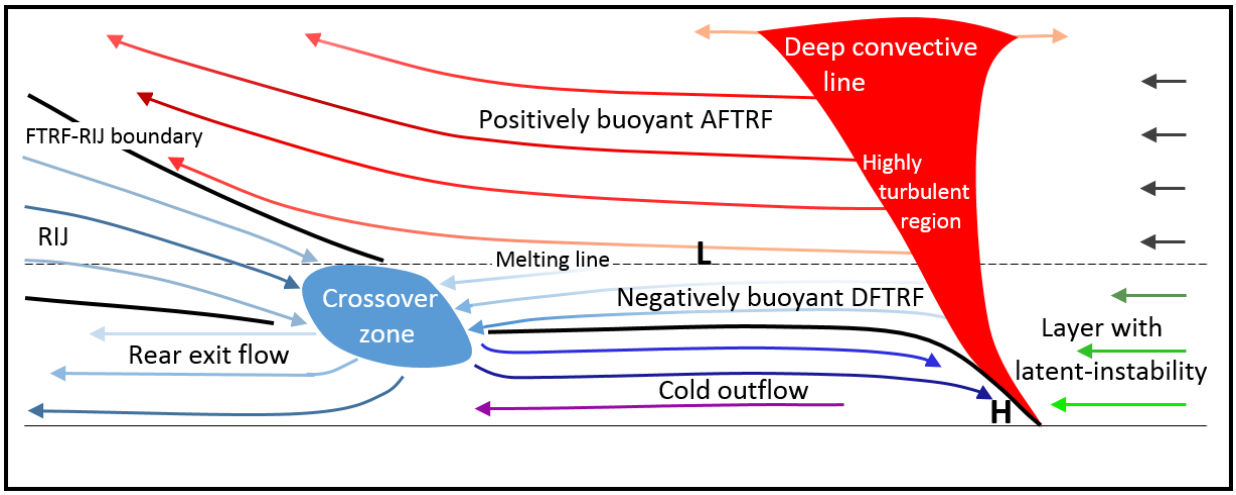

Chapter 4:

Numerically simulated idealized tropical squall lines

The previous chapter established the importance of the vertical distribution of CAPE for determining the structure of mid-latitude SLs. This chapter generalizes those results to tropical environments. Although tropical and mid-latitude SLs have a similar structure (e.g. see Cotton et al. 2011), their behavior can differ significantly due to their contrasting environments. For instance, tropical SLs induce temperature perturbations that are small compared to those of their mid-latitude counterparts. This is consistent with the high RHs and nearly pseudoadiabatic tropospheric temperature profiles found throughout the tropics, which constrain cold pools to be relatively shallow and weak, and also limit the amplitude of the upper-tropospheric heating. As a result, the convective and mesoscale circulations in tropical SLs are not as intense as in severe mid-latitude storms. In addition, environments of tropical SLs characteristically display a reversal of the line-perpendicular wind shear (e.g. Barnes and Sieckman 1984; LeMone et al. 1998), which is known to greatly affect the structure of simulated storms (Dudhia et al. 1987; Nicholls et al. 1988; Lafore and Moncrieff 1989).

The organization of this chapter is analogous to that of chapter 3. The numerical framework will be described in section 4.1, highlighting the differences with the framework used in the previous chapter. The design of environments will be outlined in section 4.2. Results from numerical simulations are presented in section 4.3, including a brief description of the *baseline* simulation, inter-case comparisons of storms in environments with weak low-tropospheric shear, and a brief discussion of simulations in moderate and strong low-tropospheric shear. A discussion will follow in section 4.4, and this chapter will end with a brief summary in section 4.5.

4.1 Numerical framework

This section will only specify details in which the numerical framework used herein differs from the one used in chapter 3. The simulations were carried out for 7 hours with a 10 s time step. The horizontal domain extends 128 × 1024 km^2 (along-line × across-line directions respectively), with 500 m grid spacing in both directions. The domain is shorter in the along-line direction than the one used to simulate mid-latitude SLs, which was 1536 km. A sensitivity test showed that this has little effect on the fields of interest. The vertical extent is 28.5 km, with 64 levels with variable spacing, this being 75 m near the surface, and gradually increasing up to 500 m at 5000 m height, above which it stays constant at 500 m.

Pointwise nudging to the initial kinematic and thermodynamic state was performed between 512 km and 1024 km in the across-line direction. All storms remained distanced from the nudged portion of the domain throughout the simulation. The time period used for nudging the

region between 762 km and 874 km was $\tau = 3600$ s^{-1}, and linearly decreasing to 0 s^{-1} between 752 km and 512 km, and also between 874 km and 1024 km.

Storms are initialized by a prescribed region of cooling, which causes the formation of a cold pool. The cooling is maintained for the first 3000 s of the simulation in the region 244 km < x < 268 km and z < 3 km, being determined as

$$\left(\frac{\partial T}{\partial t}\right)(x,y,z) = -\left[T(x,y,z) - Tps_{\min}(z)\right] \times \tau^{-1}$$

where T is temperature, $Tps_{\min}$ is the temperature profile of the pseudoadiabat corresponding to the minimum pseudoentropy on the initial sounding, and τ is a relaxation time period of 3000 s. This cooling specification was adopted because it is effective for initiating storms in the diverse environments considered herein, with temperatures bounded by the minimum values that can be attained through rain evaporation. Initiation of simulated SLs by a region of prescribed cooling is frequently done in numerical studies of tropical storms (e.g. Dudhia et al. 1987; Nicholls et al. 1988; Lafore and Moncrieff 1989; Lucas et al. 2000).

The initialization of SLs via imposed cooling is favored over the horizontal wind convergence technique used for mid-latitude storms due to its simplicity and reliability for initiating long lasting storms. After having tested several horizontal wind convergence formulations, with various vertical distributions and intensities, I found it difficult to define a reliable scheme for initiating SLs without inducing large temperature perturbations relative to the ones produced by the mature storms. The relatively large temperature perturbations produced by horizontal wind convergence, which affect the development of the mesoscale circulations of the SLs (Pandya and Durran 1996), results from two factors in which tropical SLs environments differ from their mid-latitude counterparts: larger dry static stability at low and mid-tropospheric levels, which implies more warming under adiabatic subsidence; and the smallness of the buoyancies produced by tropical SLs, which are the reference for determining the amplitude of the temperature perturbations. One drawback of initializing storms through a prescribed cooling region is that it directly affects simulated cold pool temperatures, and therefore results pertaining to cold pool properties must be interpreted with caution.

4.2 Design of tropical SL environments

The thermodynamic environments considered herein are similar to the sounding presented in Trier et al. (1996), which was derived from TOGA COARE observations of a SL which occurred on 22 February 1993. The *baseline* sounding, depicted by the black solid lines in Fig. 4.1a, is absolutely stable above 750 hPa and conditionally unstable below, having a 70 hPa deep boundary layer. The layer of latent instability spans the lowermost 150 hPa, being less than half as deep as in the mid-latitude environments considered in chapter 3. Fig. 4.2 shows that the surface based CAPE of *baseline* is around 1700 J kg^{-1}, and the MLCAPE given by a parcel with properties averaged over the lowest 50 hPa is 1520 J kg^{-1}, similar to the value reported in Trier et al. (1996) (note that this definition of MLCAPE differs from that used in the previous chapter, reflecting the shallow mixed layers found in the marine tropics, relative to continental mid-latitudes).

Thermodynamic variations from the baseline sounding were designed using the technique described in chapter 2. A sounding with *baseline*'s temperature, CAPE, and LFC profiles, but having a lower mid-tropospheric RH is referred to as *dry*. The dew-point temperature profile of

dry is represented by the dashed line in Fig. 4.1a, which is determined by an RH equal to 80% between 850 hPa and 500 hPa. Such values of mid-tropospheric RH are within the range of SL environments observed during TOGA COARE (LeMone et al. 1998). This case is relevant because it implies water vapor mixing ratio variations in the order of 2 g kg^{-1} near levels from which cold pool air might originate. Two sensitivity tests based on modifications of the vertical distribution of CAPE are considered. First, the soundings in Fig. 4.1b represent variations in which the CAPE profile of *baseline* is multiplied by a constant, as shown by the black dashed and dotted lines in Fig. 4.2a, both having *baseline*'s LFC. In analogy to the nomenclature of the previous chapter, the sounding with higher CAPE es referred to as *high*, the other case being *low*. The other sensitivity test, depicted by the soundings in Fig. 4.1c, accomplishes variations in the CAPE profile by changing the distribution of moisture while maintaining the same temperatures as *baseline*. The *shallow* sounding is dryer than *baseline* above the boundary layer, thus having lower CAPE (Fig. 4.2a) and LFC (Fig. 4.2b) values therein, the contrary being the case for *deep*.

Table 4.1 summarizes some characteristics of the soundings under consideration. The *shallow*, *baseline*, and *deep* environments have the same SBCAPE, the latter having a slightly greater MLCAPE than *shallow* and *baseline*. The *low* environment has the lowest SBCAPE and MLCAPE of all cases considered herein, the contrary holding for *high*. The environments with lower PW than *baseline*, listed in ascending order of that variable, are *dry*, *shallow*, and *low*. The sounding with greatest PW is *deep*, followed by *high*. A variable of interest is ICAPE, which was shown in chapter 3 to be related to the potential upper-tropospheric heating induced by mid-tropospheric SLs. Note that *shallow* has a greater ICAPE than *low*, despite its lower PW; analogously, *high* has a larger ICAPE than *deep*, the latter having more PW.

Two types of line-perpendicular horizontal wind profiles were specified, both having low-tropospheric shear, but with different winds aloft, as displayed in Fig. 4.3: one case has calm winds above 2 km (relative to the surface), which will be referred to as the low-tropospheric shear profile (LTSP); the other case has a reversal of the shear at 2 km height, and it will be referred to as the jet wind profile (JWP). The JWP is characteristic of the environment of many tropical SLs (Barnes and Sieckman 1984; Alexander and Young 1992; LeMone et al. 1998). It is worth mentioning that the environment of the SL studied by Trier et al. (1996) has a JWP. Different LTSP and JWP kinematic environments are specified by varying the shear between the surface and 2 km, as shown in Fig. 4.3, with values $\Delta U = 8$ m s^{-1}, $\Delta U = 10$ m s^{-1}, and $\Delta U = 12$ m s^{-1}, where ΔU is equal to the difference between winds at the surface and at 2 km. The frame of reference with calm environmental winds at 2 km height guarantees that the storms remain near the region of convective initiation, and distanced from the portion of the domain that is nudged toward the initial conditions (see the numerical specifications in section 4.1). Simulations with different kinematic environments will be distinguished by an underscore followed by the corresponding ΔU value, and cases with a JWP will be identified by a *J* at the end, e.g. *baseline_8J*, *shallow_10*, etc.

4.3 Results

a. A brief description of the baseline simulations

This section provides a reference of the characteristics of the simulated storms, describing features of the *baseline* SLs that are common to the other environments. In particular, the reversal of the shear at mid-tropospheric levels has profound impacts in simulated SLs, as found by previous studies (e.g. Dudhia et al. 1987; Nicholls et al. 1988; Lafore and Moncrieff 1989). Radar

reflectivity plots at 4 h of simulation time corresponding to *baseline_10* and *baseline_10J* are shown in Fig. 4.4, indicating that these two environments lead to very different storms. The *baseline_10J* storm (Figs. 4.4a and 4.4c) is broader and has a wide area of stratiform precipitation, while *baseline_10* (Figs. 4.4b and 4.4d) displays a deep convective line that reaches further into the upper-troposphere, without a discernible region of stratiform precipitation. This morphological dependence of SLs on the shear reversal was noted by Dudhia et al. (1987), who distinguished between unicell and multicell SLs, with *baseline_10* resembling the former, and *baseline_10J* akin to the latter. Hence the larger variability in radar reflectivity along the deep convective line in *baseline_10J* (Fig. 4.4c) relative to that in *baseline_10* (Fig. 4.4d). This distinction between multicell and unicell convective structures, which will manifest in particle trajectories shown below, is similar to the distinction made in James et al. (2005) between slabular and cellular convection in mid-latitude SLs.

More details about these storms are displayed in the along-line averaged contours of horizontal winds (in the same frame of reference as Fig. 4.3), pressure perturbations, and the buoyancies displayed in Fig. 4.5. The horizontal wind field in Fig. 4.5a shows that after 3 h *baseline_10J* produces a robust FTRF overlaying a weak but clearly discernible RIJ centered near 2 km height. This FTRF leads to a rearward advection of the convective cells initiated at the edge of the cold outflow, which is important for the development of the stratiform precipitation region. The positive buoyancies induced by the SL are found mainly between 1.5 km and 5 km height, which is around the level where pseudoadiabatically lifted latent unstable parcels attain maximum buoyancy (see Fig. 4.1). This is considerably lower than the maximum buoyancy near 7 km height developed by the simulations described in chapter 3. Note that the magnitude of the perturbations produced ahead of the storm is comparable to those found within the storm itself, which suggests the importance of convective adjustment through gravity waves (e.g. Bretherton and Smolarkiewicz 1989; Nicholls et al. 1991; Mapes 1993). Fig. 4.5c shows that at 5 h the mid-tropospheric positive buoyancies produced by *baseline_10J* increase slightly, and that the cold outflow broadens as the FTRF-RIJ boundary moves towards the rear of the SL. The fact that the cold pool edge barely moves with time is consistent with observations by LeMone et al. (1998), who noticed that TOGA COARE SLs propagate at a speed close to the horizontal wind maxima implied by the jet (in the present frame of reference, this wind maxima is static relative to the surface; see Fig. 4.3).

Contrasting with the description given above, Fig. 4.5b shows that 3 h after initiation *baseline_10* has not yet developed a robust FTRF, and that its RIJ is weaker than that of *baseline_10J*. At 5 h of simulation time *baseline_10* has a weak FTRF at mid-tropospheric levels. Note that the negative buoyancies in the lower troposphere are of greater amplitude in *baseline_10J* (Figs. 4.5a and 4.5c) than in *baseline_10* (Figs. 4.5b and 4.5d), with the former SL producing a cold outflow which is wider and with more intense winds near the surface. On the other hand, upper-tropospheric buoyancies in *baseline_10* are slightly larger than those developed by *baseline_10J*.

To further analyze the effects that a reversal of the shear has on the structure of the simulated SLs, it will be useful to consider Lagrangian particle trajectories computed with the particle tracking algorithm of Yamaguchi and Randall (2012) (see section 3.1). The trajectories shown in Figs. 4.6 and 4.7 reveal that the paths followed by air particles flowing into the SLs differ between the JWP and the LTSP environments. The trajectories in *baseline_10J* (Fig. 4.6) are less buoyant, more tilted, and shallower than in *baseline_10* (Fig. 4.7). This distinction is due to the

interaction between updrafts and environmental winds aloft. Following Nicholls et al. (1988), the impact of the reversal of the environmental wind shear can be explained through the dynamic pressure perturbation terms of the flow linearized about its mean state (e.g. see Rotunno and Klemp 1982), which in the anelastic approximation satisfies

$$\nabla \cdot \left(\overline{\alpha} \nabla p'_{dyn} \right) = -2 \frac{d\overline{u}}{dz} \frac{\partial w}{\partial x} \tag{4.1}$$

where $\overline{u}$ and $\overline{\alpha} = \left(\overline{\rho} \right)^{-1}$ are the environmental wind and specific volume, respectively, and the subscript *dyn* refers to the dynamic component of the pressure perturbation (a more detailed description of the diagnostic pressure perturbation equation is given in chapter 5). The JWP environments considered herein are such that $d\overline{u} / dz < 0$ within the layer with the reversal of the low-tropospheric shear (see Fig. 4.3), while $\partial w / \partial x$ is positive on the left flank of the updraft, and negative on its right flank. By noting the similarity between the left hand side of (4.1) and the Laplacian of p'_{dyn}, it can be inferred that a local pressure maximum is likely to occur on the right flank (downshear with respect to low-tropospheric winds) of the updraft, where the right hand side of (4.1) is negative, while a local pressure minimum is likely to develop on the left flank of the updraft. As a result, a pressure gradient tending to accelerate winds from right to left will develop in the JWP, leading to tilted updrafts as shown in Fig. 4.6, which are associated with a relatively intense FTRF. This pressure gradient can be seen on the rightmost edge of the FTRF in Fig. 4.5a. It is interesting that the pressure gradient within the updraft of *baseline_10* (Fig. 4.5b) points in the opposite direction, i.e. tending to accelerate the flow downshear with respect to low-tropospheric winds.

Having shown how the updrafts are affected by the reversal of the low-tropospheric shear, the aforementioned differences between the along-line averaged fields of the two storms can be explained. For instance, the robust FTRF in *baseline_10J* leads to the development of the stratiform region, where sub-saturated air within the RIJ experiences latent cooling due mainly to rain evaporation. Fig. 4.8 displays along-line averaged contours of mixing ratios of rain, snow, and graupel, overlaid on top of the latent cooling field which incorporates rain evaporation, ice melting, and ice sublimation. The erect updraft in *baseline_10* produces latent cooling within a relatively narrow vertical column (Fig. 4.8b), while the tilted updraft in *baseline_10J* advects hydrometeors towards the rear of the storm, thus developing a wide region of latent cooling (Fig. 4.8a) which causes the progressive displacement of the FTRF-RIJ boundary (Figs. 4.5a and 4.5c). The cold outflow of *baseline_10J* broadens and becomes more intense as the cooled RIJ air subsides at the FTRF-RIJ boundary, producing relatively large surface wind speeds due to the conversion of vertical momentum into the horizontal (e.g. see Mahoney et al. 2009). This distinction between the behavior of *baseline_10J* and *baseline_10* is important for the thermodynamic and momentum feedbacks between MCSs and the large scale flow, as *baseline_10J* will produce greater cooling within the boundary layer and stronger wind perturbations near the surface.

Another perspective of particle trajectories is shown in Fig. 4.9, in which low-tropospheric particles are projected onto the along-line–height plane. The trajectories that reach above 8 km in *baseline_10J* (Figs. 4.9c and 4.9d) are clustered mainly around y = 40 km and y = 75 km. On the other hand, deep reaching particles in *baseline_10* (Figs. 4.8a and 4.8b) are found throughout the deep convective line. This distinction serves to contrast the multicell behavior of *baseline_10J*,

where deep convective elements are localized and triggered intermittently, to the unicell (slabular) type of convection in *baseline_10*.[12]

Before proceeding to the next subsection, it is worth mentioning that the strength of the low-tropospheric shear (ΔU) has noticeable impacts on the simulated SLs. For instance, simulations with *low* and *shallow* soundings failed to produce long-lived SLs in LTSP environments with $\Delta U = 10$. In fact, only *deep* and *high* simulations led to mature SLs when $\Delta U = 12$. Considering that the main purpose of this study is to analyze systematic variations of SLs when simulated in various thermodynamic environments, and that all environmental configurations with $\Delta U = 8$ led to long-lasting storms, detailed inter-case comparisons for $\Delta U = 8$ are given in the next subsection, followed by a brief presentation of results with $\Delta U = 10$ and.

b. Inter-case comparisons: simulations with $\Delta U = 8$

This section focuses on inter-case comparisons between SLs simulated in different thermodynamic environments having $\Delta U = 8$, with some diagnostics of the storms presented in Tables 4.2 and 4.3. One difficulty of analyzing SLs simulated in tropical environments is that many of their relevant characteristics, such as the cold pool intensity (c), the propagation speed (PS), the maximum surface wind speeds, are not as steady as in mid-latitude storms. Lafore and Moncrieff (1989) also found the PS and c to vary with time. Therefore the diagnostics in Tables 4.2 and 4.3 correspond to fields averaged throughout 1 hour around the time when peak PRs are attained. This constitutes an objective way for computing diagnostics that are representative of mean values around the time of greatest storm intensity, as measured by PR.

The evolution of PRs for the $\Delta U = 8$ simulations is shown in Fig. 4.10. PRs in LTSP environments (Fig. 4.10b) tend to be greater than those in JWP (Fig. 4.10a), which results from less water evaporation (e.g. see Fig. 4.8) and diminished updraft dilution by inflowing air aloft in the former environments. This is consistent with the precipitation efficiencies (PEs) being greater in Table 4.2 than in Table 4.3. The PE was computed with respect to environmental winds, as in chapter 3, neglecting layers of water vapor outflow in cases with negative PS. Note that Table 4.2 has an additional definition of PE, PE_{LTSP}, which is computed assuming LTSP environmental winds in JWP simulations. Moisture inflow contributions by the reversal of the low-tropospheric shear, i.e. surface-relative winds above 2 km, are disregarded in the computation of PE_{LTSP}, which is done in order to have parameter which may allow comparing data between LTSP and JWP storms. Note that the environmental water vapor which is most likely to precipitate is found within the layer of latent instability, which is shallower than 2 km in the present environments. Thus, PE_{LTSP} accounts for the fraction of water that precipitates among the inflowing "effectively precipitable" water vapor, without assigning too low PEs to JWP simulations relative to those in LTSP environments due to enhanced water vapor inflow aloft.

Another interesting feature displayed in Fig. 4.10 is the near ordering of the PR by the PW in each kinematic environment. One exception in both environments is *dry*, which precipitates more than *low* and *shallow* while having the lowest PW. This result is related to the fact that the PR production is more strongly affected by moisture within the latent unstable layer than by moisture content aloft, especially in the LTSP environment. Moisture above the latent-unstable layer plays a bigger role in JWP because of enhanced evaporation (see Fig. 4.8) due to a greater inflow of sub-saturated air aloft. The other exception to the ordering of PRs by PW results from

[12] All simulated mid-latitude SLs discussed in chapter 3 developed slabular convection.

high_8J precipitating slightly more than *deep_8J*. The lower PE accomplished by the former storm suggests that this behavior follows from differences in PS, such that *high_8J* has a greater water vapor inflow rate than *deep_8J* due to its higher PS (see section 3.3.2).

Along-line averaged fields allow for a more detailed analysis of differences between simulated storms. Starting by considering the effects of moisture variations above the layer of latent instability, Fig. 4.11 shows that *baseline* simulations (Figs. 4.11a and 4.11c) lead slightly more intense storms than *dry* (Figs. 4.11b and 4.11d), as manifested in the intensity of the RIJ, *c*, and the mid and upper-tropospheric heating. A measure of the intensity of the RIJ is given by u_{RIJ} in Tables 4.2 and 4.3, corresponding to the maximum surface-relative wind speed within the RIJ. Note that u_{RIJ} is larger in *baseline* than in *dry*, which is consistent with greater upper-tropospheric heating in the former environment. Regarding the cold pool intensity, two definitions are given in Tables 4.2 and 4.3: *c* measures the cold pool intensity near the leading edge, which is commonly associated to the morphology of the updraft (e.g. RKW88); $\bar{c}$ corresponds to the cold pool intensity averaged throughout the 60 km behind the leading edge, providing a more robust measure of the low-tropospheric cooling induced by the storms. The fact that *baseline* produces larger *c* and $\bar{c}$ than *dry* (see Tables 4.2 and 4.3) is a noteworthy result, as many studies associate lower mid-tropospheric RH to stronger cold pools due to enhanced cooling by water evaporation (e.g. Lafore and Moncrieff 1989; Mechem et al. 2002). Such reasoning would be valid if both environments produced similar precipitation patterns, but contours of latent cooling and mixing ratios of precipitating variables shown in Fig. 4.12 indicate that more vigorous latent cooling and greater amounts of hydrometeors are produced by *baseline_8J* (Fig. 4.12a) than by *dry_8J* (Fig. 4.12b). In the case of the *dry* simulations, latent cooling is limited by the production of hydrometeors, so that the maximum potential cooling of mid-tropospheric air by rain evaporation does not provide a good diagnostic for *c*. Such differences in hydrometeor production and latent cooling, which are less evident but also discernible in LTSP environments (not shown), arise from the enhanced dilution experienced by latent unstable air when it mixes with drier surroundings, as explained by James and Markowski (2010).

The morphological differences among storms simulated in environments with varying ICAPE, shown in Figs. 4.13 (*low* and *high*) and 4.14 (*shallow* and *deep*), are more pronounced than those arising from moisture variations above the latent-unstable layer (Fig. 4.11). The systematic variation in the intensity of storm attributes (e.g. u_{RIJ}, *c*, $\bar{c}$, PS) as a result of changes in ICAPE is similar to the trend seen in mid-latitude SLs. The simulations with environments having a greater ICAPE, i.e. *high* (Figs. 4.13b and 4.13d) and *deep* (Figs. 4.14b and 4.14d), produce mesoscale circulations of greater intensity (e.g. u_{RIJ} in Tables 4.2 and 4.3), and in general they induce greater pressure and temperature perturbations than storms in low ICAPE environments, i.e. *low* (Figs. 4.13a and 4.13c) and *shallow* (Figs. 4.14a and 4.14c). The contrasts between the weak SLs in *shallow* (Figs. 4.14a and 4.14c) relative to those in *deep* (Figs. 4.14b and 4.14d) environments are noteworthy, as both have identical temperature profiles, the same MUCAPE and similar MLCAPE; but these environments differ in their latent instability properties above the boundary layer. This observation corroborates the importance of the latent instability properties throughout the whole atmospheric column for modulating the morphology of tropical SLs, in agreement with results from chapter 3.

It is worth mentioning that the near-surface wind fields in Figs. 4.13c, 4.14a, and 4.14c show that *low_8*, *shallow_8J*, and *shallow_8*, respectively, fail to maintain a density current. Density currents, which are highly advective, require a stagnation point near their leading edge (in

a frame of reference with a static leading edge). These simulations, characterized by having low ICAPE, sustain long lasting deep convective motions through a nearly stationary wave (relative to the surface), manifested as a slowly decaying buoyancy gradient that is forced by continuous rain evaporation. Similar modes of long lasting deep convection induced by a wave, rather than a density current, were simulated by Lafore and Moncrieff (1989). That *low_8J* produces a density current shows once again how the reversal of the shear can impact significantly on the developing the cold outflow.

The temperature perturbations produced by the different storms at the end of the simulations (t = 7 h) are shown in Fig. 4.15, which displays the horizontally averaged temperature perturbation throughout the portion of the domain which is not nudged (i.e. 0 km < x < 512 km). Considering the low-tropospheric temperatures produced by the storms (Figs. 4.15a and 5.15b), the JWP environments induce greater cooling of the boundary layer. This is related to the aforementioned tilting of updrafts in the presence of the shear reversal: a tilted updraft will precipitate more into subsaturated air, causing enhanced cooling due to ice sublimation and rain evaporation. The enhanced low-tropospheric cooling in the JWP environment is consistent with a greater $\bar{c}$ developed by JWP simulations (Table 4.2) than in LTSP (Table 4.3).

Regarding mid and upper-tropospheric temperatures in Figs. 4.15c and 4.15d, maximum temperature perturbations are found between 2.5 km and 3.5 km height. This is the layer where pseudoadiabatically lifted latent unstable parcels attain maximum buoyancy. Also apparent is that LTSP simulations produce greater mid and upper-tropospheric warming than JWP storms. The small mid and upper-tropospheric temperature perturbations in JWP storms results from enhanced mixing, which is corroborated by slightly lower h in trajectories of ascending particles in JWP than in LTSP environments (not shown).

In each sensitivity test where ICAPE is varied, i.e. *low-high* and *shallow-deep*, the simulations with greater ICAPE produce larger temperature perturbations, as shown in Fig. 4.15. But ICAPE does not provide a perfect ordering of cases by induced mid and upper-tropospheric warming. For example, *dry* produces smaller temperature perturbations than *baseline* (both environments have identical ICAPE), especially in the JWP environment (Fig. 4.15a). In addition, mid and upper-tropospheric warming is greater in *low* than in *shallow* simulations, the former having lower ICAPE than the latter. Similarly, *deep* leads to larger temperature perturbations than *high*, the latter being the environment with greatest ICAPE. The next subsection will show that similar observations apply to ΔU = 10 storms, so that these trends constitute robust features of the present environments. Possible explanations for this behavior are given below.

The relatively weak warming in *dry* can be readily explained as a result from the dilution of latent unstable air by inflowing dry mid-tropospheric air, with greater effects in the JWP environment, due to enhanced mixing. As to why temperature perturbations are greater in *deep_8* than in *high_8*, one possible explanation can be formulated in terms of the PS. The PS of *high_8* is greater than that of *deep_8* (Table 4.3), so it has a greater inflow fraction of air from above the latent-unstable layer, which will reduce the storm induced heating. It can be argued that this effect is not as large in JWP environment (Fig. 4.15a) due to enhanced storm-relative inflow above 2 km, implying that the fractional change of inflowing air resulting from differences in PS is lower in that environment. But, by this same reasoning, the near surface storm-relative inflow of air (where CAPE has largest values) is greater in *high* than in *deep*, so it is not clear to what extent differences in PS account for the larger mid-tropospheric heating in *deep* than in *high*. In addition, this explanation in terms of PS does not apply to *low* and *shallow*, which actually develop slightly

negative PS. Another possible explanation can be formulated by noting that the environments with highest RHs above the boundary, i.e. *low* and *deep* (see Fig. 4.16), are those that lead to greater heating aloft. It is thus reasonable ponder the importance of RHs in SL convection.

Referring to the vertical distribution of parcel indices, RHs are intimately linked to the lifting condensation level (LCL), such that the higher the RH of a given parcel, the smaller the distance it will usually need to be lifted in order to become saturated. Higher RHs will also tend to reduce the distance a parcel needs to be lifted in order to attain its LFC. Indeed, among the soundings considered herein, parcels in environments with lower RHs require greater lifting in order to reach their LCL and LFC, as Fig. 4.17 exemplifies for the *deep* and *high* environments. Therefore, appealing to layer-lifting as a conceptual model for convection, I suggest that the higher the RH of a given environment, the greater the probability that latent-unstable parcels originating above the boundary layer will reach saturation and will attain positive buoyancy. This argument is relevant for tropical SLs because their cold pools are only ≈ 500 m deep, which is considerably shallower than the depth of the layer of latent instability in the present environments (≈ 1500 m), and it is similar in magnitude to the distance that parcels need to be lifted in order to reach their LFC. This hypothesis, the formal corroboration of which requires further investigation, implies the sensitivity of tropical SLs to the LFC and the LCL, contrasting with severe mid-latitude storms (e.g. compare *baseline* and *base_sens* simulations).

Corroborating that convection in the simulations considered herein is accomplished through layer-lifting, Fig. 4.18 shows histograms of the height reached at the end of the simulation by particles placed around 10 km ahead of the SLs at 3 h of simulation time. Comparison between Figs. 4.18a and 4.18b shows that more particles reach the upper-troposphere in the LTSP environments, consistent with their more vertical updrafts. Note that there are many deep reaching particles originating at 1.3 km and 2.3 km height, corroborating the importance of mid-tropospheric moisture and the vertical distribution of latent instability properties. It is worth highlighting that there is no clear indication in Fig. 4.18 that the mid-tropospheric RH by itself modulates whether layer-lifting convection occurs, as found by Mechem et al. (2002). For example, *low* has higher mid-tropospheric RHs than *dry*, despite of which the latter simulation seems more efficient at lifting mid-tropospheric particles. The results of Mechem et al. (2002) were produced with horizontally inhomogeneous initial conditions, and incorporated prescribed large-scale forcing, which might be related to these contrasting results.

c. Simulations with ΔU = 10

It was mentioned above that simulations with *low* and *shallow* soundings and LTSP did not produce long-lasting SLs for ΔU = 10, and that *deep* and *high* were the only environments conductive to organized convection for ΔU = 12. Nonetheless, many inter-case comparisons described above are also applicable among simulations that developed long-lived SLs in ΔU = 10 environments, indicating the generality of the results presented herein. Cases with ΔU = 12 will not be discussed further due to the limited number of simulations leading to mature storms. Diagnostics of the simulated storms are given in Table 4.4 and 4.5, and surface precipitation rates are displayed in Fig. 4.19.

The PRs of the simulated storms in Fig. 4.19 present an ordering which is similar to that of the ΔU = 8 simulations. But a couple of differences are worth mentioning. Fig. 4.20b shows that *dry_10* produces a slightly greater PR than *baseline_10*, despite having lower PW, and in contrast with ΔU = 8 storms. Also of interest is the similarity in PR evolution by the JWP simulations with

relatively dry mid-tropospheric environments, *shallow_10J* and *dry_10J* (Fig. 4.19a). This behavior could reflect the intensification of cold pools which occurs for larger ΔU as a result of the increase in water vapor inflow. Recall that the cold pools in these simulations are strongly constrained by the production of hydrometeors, so an enhancement of the water vapor inflow can affect the production of hydrometeors, and thus the development of cold pools. Evidence of a pronounced enhancement of the cold pool intensity in dry environments due to stronger ΔU is found in data from Tables 4.3 and 4.5, which show that *dry_10* produced greater *c* than *baseline_10* (Table 4.5), in contrast to storms with $\Delta U = 8$ (Table 4.3). A stronger ΔU for the JWP simulations leads to an enhancement in *c* of *shallow* and *dry*, as shown in Tables 4.2 and 4.4, although this enhancement is not particularly large compared to that of other environments.

Of primary importance to this study is the relationship between ICAPE and the upper-tropospheric heating caused by the storms, in respect of which Fig. 4.20 shows that the ordering of horizontally averaged temperatures accomplished by the different soundings is similar to that in Fig. 4.15. Again, the similarity in temperature profiles between *deep* and *high* and between *shallow* and *low* despite having different ICAPE might be indicate of the storms being sensitive to the LFC: convection is diminished as the height at which parcels attain their LFC increases. One notable difference between the $\Delta U = 8$ and the $\Delta U = 10$ simulations with LTSP is the large temperature perturbations produced by *dry_10* relative to those in *baseline_10* in Fig. 4.20b. This distinction, which is consistent with the greater PR produced by *dry* than by *baseline* in Fig. 4.19b, is also found in additional simulations performed with soundings slightly perturbed from those of *baseline* and *dry*. It therefore seems that dry environmental conditions above the layer of latent instability may be favorable for the development of intense storms in cases with enough water vapor inflow.

4.4 Discussion

Previous studies have recognized the sensitivity of simulated tropical SLs to the RH at mid-tropospheric levels (Nicholls et al. 1988; Lucas et al. 2000; Mechem et al. 2002). Nicholls et al. (1988) found that reducing the mid-tropospheric moisture can diminish the intensity of storms, although they found that stronger cold pools were developed in dryer environments. Lucas et al. (2000) also found dry conditions above the boundary layer to be detrimental for the intensity of convection in SLs, attributing this behavior to the dilution of updrafts caused by entrainment. The latter study varied moisture levels throughout different layers above the boundary layer, finding that variations near cloud base ($\approx$ 950 hPa) had the strongest impact, with noticeable sensitivity for moisture variations up to 700 hPa height.

Results presented herein generally agree with the findings of such studies, but the interpretation is different. This chapter contemplates two means by which environmental moisture variations can affect the structure of SLs, one being through turbulent mixing into saturated updrafts, while the other contemplates the impacts of moisture through vertical profiles of CAPE and LFC. Lucas et al. (2000) consider mainly turbulent mixing effects, implicitly assuming that updrafts are primarily composed of boundary layer air. This view does not incorporate the layer-lifting of air above the boundary layer produced by organized convective storms, as exemplified by the particle trajectories presented herein and in Mechem et al. (2002). The propagating nature of SLs, and especially those that develop intense cold pools with density current behavior, implies that the core of updrafts are poorly constrained by the characteristics of the boundary layer. Analyses presented herein indicate the usefulness of considering the latent instability

characteristics throughout the atmospheric column, in the context of SL convection.

One important feature in which tropical SLs differ from mid-latitude storms is the depth of their cold pools relative to depth of the latent-unstable layer, and also relative to the distance that parcels need to ascend in order to reach their LCL and their LFC. This has implications for the sensitivity of tropical SLs to LFC variations, such that convection is enhanced as the distance that parcels need to be lifted to attain their LFC is reduced. It is worth mentioning that the environmental variations considered herein do not affect the convective process to the extent that layer-lifting convection is completely inhibited. This suggests that the manifestation of layer-lifting convection in the numerical simulations by Mechem et al. (2002) was modulated primarily by factors external to the SLs. But it is also important to highlight that moisture variations above the boundary layer can drastically affect the height up to which air ascends, as revealed by the histograms in Fig. 4.18.

It is also worth noting that, even though there is much crossover of particle trajectories at the deep convective line, results from the simulated storms do not display a crossover of low-*h* mid-tropospheric air and high-*h* air from low levels, as suggested by Zipser (1977). That study proposed that low-*h* air flows into the cold pool after crossing the deep convective line, while high-*h* air rises through the FTRF. The simulations considered herein develop highly turbulent conditions at the deep convective line, leading to substantial changes in the *h* along particle trajectories (not shown), such that most of the air that traverses the deep convective line has an *h* that is greater than the *h* within the cold pool. Nonetheless, it is important to acknowledge that the representation of these features might change in simulations with higher resolution, and they might also be dependent on the particular microphysics parameterization that is used.

4.5 Summary

This chapter focuses on inter-comparisons among idealized SLs simulated in various tropical environments. The thermodynamic environments considered herein bear similarity to the sounding used by Trier et al. (1996), and variations are designed through changes in the CAPE and LFC profiles, using the method described in chapter 2. Regarding environmental winds, two types of horizontal wind profiles are considered, both with low-level shear, but one having constant winds aloft, while the other has a reversal of the shear. Further kinematic variations are accomplished by changing the strength of the low-level shear for each of these wind profiles.

The morphology of simulated storms is strongly affected by the structure of mid-tropospheric environmental winds, with a reversal of the shear leading to more strongly tilted updrafts, lower precipitation rates, lower precipitation efficiency, and more intense cold pools. Changes in the strength of the shear at low levels also affects the simulated storms, with greater shear leading to stronger cold pools and enhanced precipitation rates. For a given kinematic environment, the precipitable water accounts for most of the variation in precipitation rates among cases with relatively moist conditions above the latent unstable layer. Dryer conditions above the latent unstable layer lead to a reduction in precipitation rates, but the effects are not as large as in cases with dry conditions within the latent unstable layer.

The thermodynamic variations considered herein are accomplished mainly through moisture variations, which affect the structure of tropical SLs in various ways. For example, moisture levels above the layer of latent instability can affect saturated updrafts through turbulent mixing, so that dryer conditions aloft can be detrimental to the intensity of convection and the

production of hydrometeors. This is relevant for the development of cold pools, a process that is highly dependent on the availability of hydrometeors. Results presented herein show that dryer environments do not necessarily lead to stronger cold pools, but this result might depend on the parameterization of microphysical processes.

This chapter also contemplates the impact of moisture on the structure of SLs in association with the CAPE and LFC profiles. Simulations with larger ICAPE tend to produce greater heating at mid and upper-tropospheric levels, which results from the buoyancy attained by air ascending under layer lifting convection. In addition, SLs simulated in environments where parcels reach their LFC at lower levels tend to produce greater upper-tropospheric heating. This feature may result from the relatively shallow cold pools in tropical SLs, which are not as effective at lifting air to saturation and to positive buoyancy as their mid-latitude counterparts.

Table 4.1. MUCAPE, MLCAPE, and CIN are in units of J kg^{-1}, ICAPE is in J m^{-2} x 10^{-6}, and PW is in kg m^{-2}. The parcel used for MLCAPE has the average potential temperature and water vapor mixing ratio of the lowermost 50 hPa.

Case	MUCAPE	MLCAPE	ICAPE	CIN	PW
baseline	1700	1520	.12	3.4	62.5
dry	1700	1520	.12	3.4	59.3
low	1150	1000	.08	3.6	62.1
high	2250	1950	.16	3.1	62.9
shallow	1700	1520	.1	3.1	61.8
deep	1700	1650	.14	4.1	63.2

Table 4.2. Diagnostics of simulations with $\Delta U = 8$ and JWP. The surface precipitation rate (PR) is in mm day^{-1}. The Propagation speed (PS), the cold pool intensity near the cold pool edge (c), the cold pool intensity averaged 60 km behind the cold pool edge ($\bar{c}$), and the maximum RIJ winds (u_{RIJ}) are in m s^{-1}. The precipitation efficiency was computed using environmental fields (PE) and winds of the LTSP (PE_{LTSP}) (see text for further details), and it presented as a percentage. Values averaged for 1 h around the time of maximum PR.

Case	PR	PS	c	$\bar{c}$	PE	PE_{LTSP}	u_{RIJ}
baseline	4.5	1.1	10.7	9.5	20	27	1.5
dry	3.3	.8	9.8	8.3	16	23	1
low	3	-.4	7.8	7.2	20	32	1.1
high	5.3	1.9	12.3	11.7	19	25	2.1
shallow	2	.5	9	6.8	10	15	.92
deep	5	1.4	11.5	10.6	20	27	1.8

Table 4.3. Diagnostics as in Table 4.2 of simulations with $\Delta U = 8$ and LTSP.

Case	PR	PS	c	$\bar{c}$	PE	u_{RIJ}
baseline	6.2	.95	10.5	8.6	40	1.3
dry	3.3	.8	9.5	8	33	1.1
low	3	-.5	6.5	6.5	33	1
high	7.2	1.53	11.8	10.1	38	1.45
shallow	2	-1	6.25	6.5	26	.88
deep	7.5	.83	10.5	9.3	49	1.4

Table 4.4. Diagnostics as in Table 4.2 of simulations with $\Delta U = 10$ and JWP.

Case	PR	PS	c	$\bar{c}$	PE	PE_{LTSP}	u_{RIJ}
baseline	5.6	.5	11	10.3	25	35	1.4
dry	4.5	.9	10.7	10	19	25	1
low	4.7	-.5	8.5	7.3	27	40	.5
high	6.7	1.5	12.5	12.2	24	31	1.5
shallow	4.7	-.3	9.5	8.5	26	39	.8
deep	7	1	12.3	11.7	28	38	1.7

Table 4.5. Diagnostics as in Table 4.2 of simulations with $\Delta U = 10$ and LTSP.

Case	PR	PS	c	$\bar{c}$	PE	u_{RIJ}
baseline	5.5	.8	8.3	7.6	32	.8
dry	4.5	0	10	8.2	43	1
low	-	-	-	-	-	-
high	9.2	1.2	11.9	10.3	46	1.8
shallow	-	-	-	-	-	-
deep	9.6	1.5	11.5	9.6	45	1.8

Figure 4.1. Environmental soundings used for simulating tropical SLs. In a) *baseline* and *dry* are represented by the black solid and dashed lines, respectively. In b) *high* and *low* are depicted by the black solid and dashed lines, respectively. In c) the *deep* and *shallow* environments are characterized by the black solid and dashed lines, respectively.

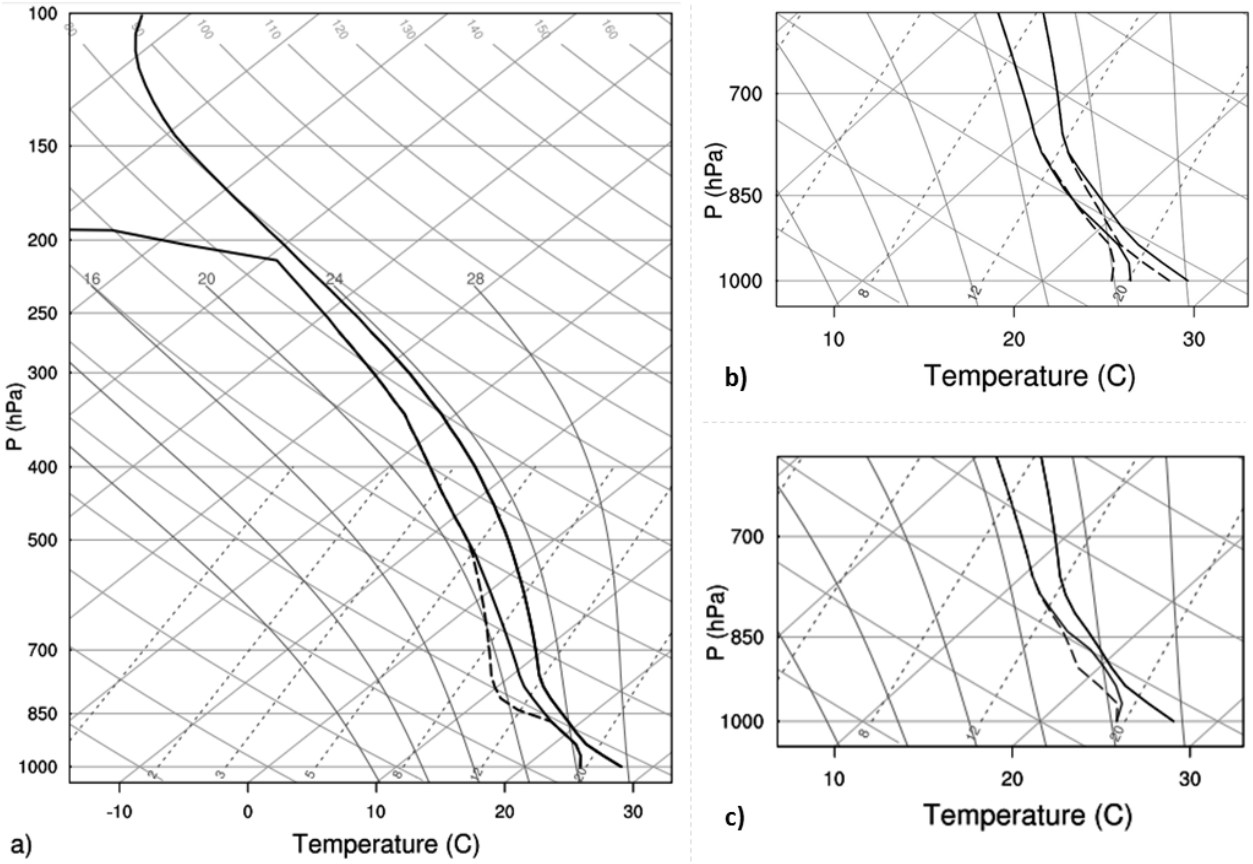

Figure 4.2. Profiles of CAPE are displayed in a), and the corresponding of LFC profiles are shown in b), corresponding to the soundings in Fig. 4.1. The baseline CAPE profile characterizes the *baseline* and *dry* environments; the LFC curve characterizes the *baseline*, *high*, *low*, and *dry* environments.

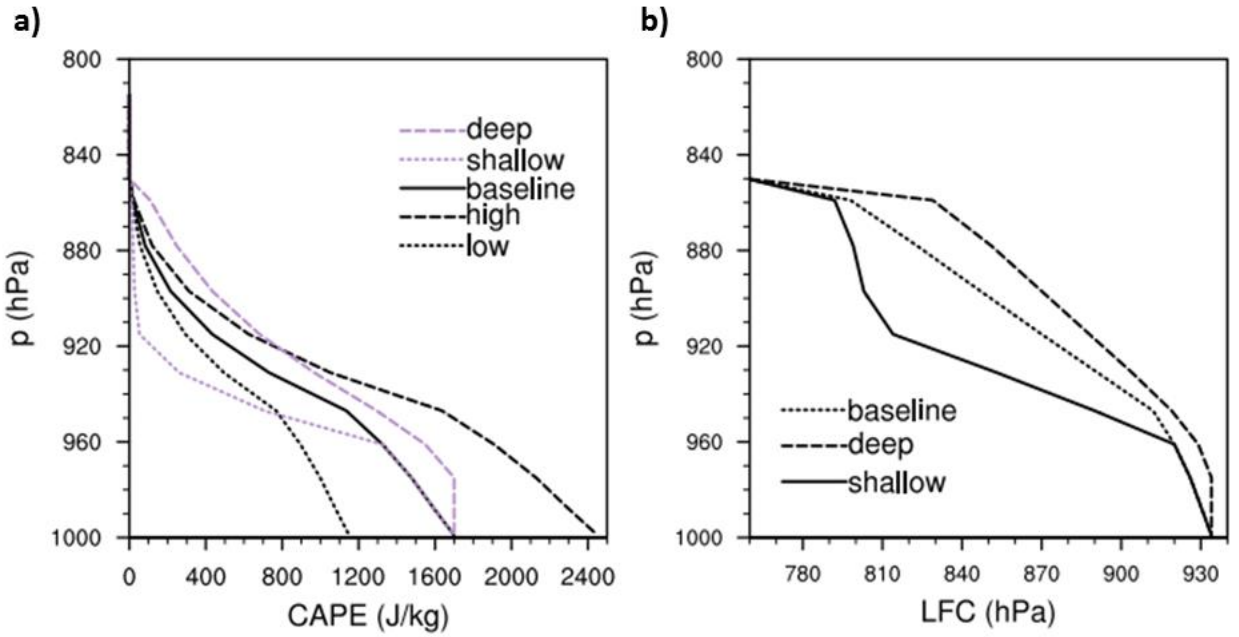

Figure 4.3. Environmental wind profiles used for simulating idealized tropical SLs. See text for further details.

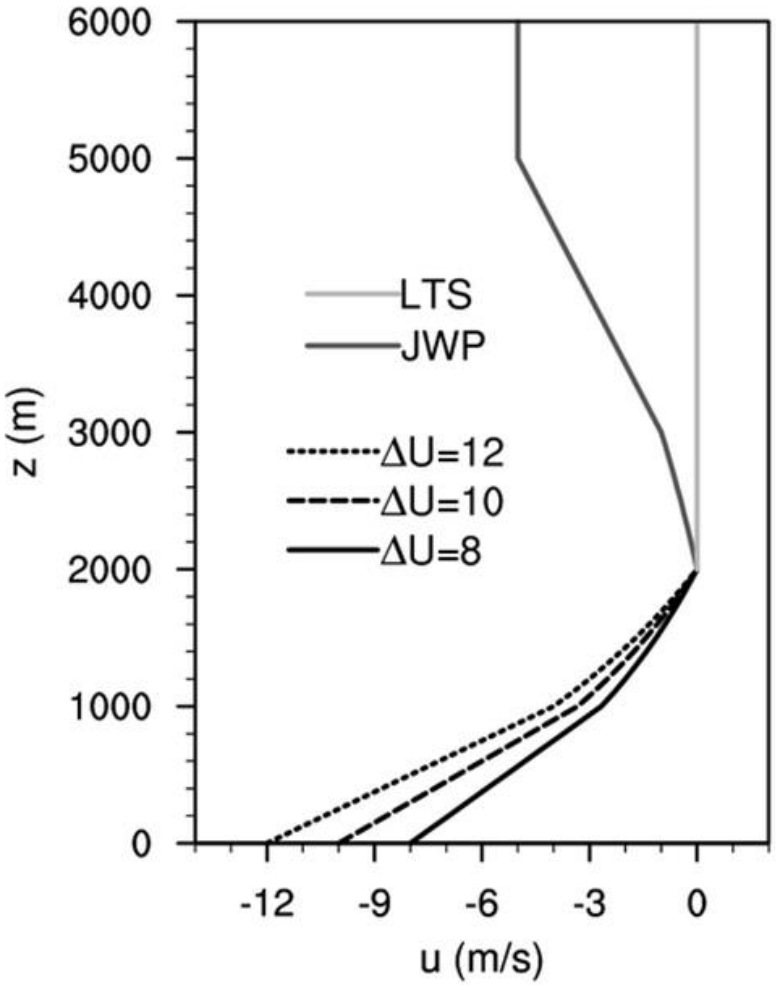

Figure 4.4. Contours of radar reflectivity at 4 h corresponding to *baseline_10J* (a and c) and to *baseline_10J* (b and d). Fields in a) and b) depict along-line averages on a plane perpendicular to the deep convective line, and fields in c) and d) show the radar reflectivity on the horizontal plane at 1 km height.

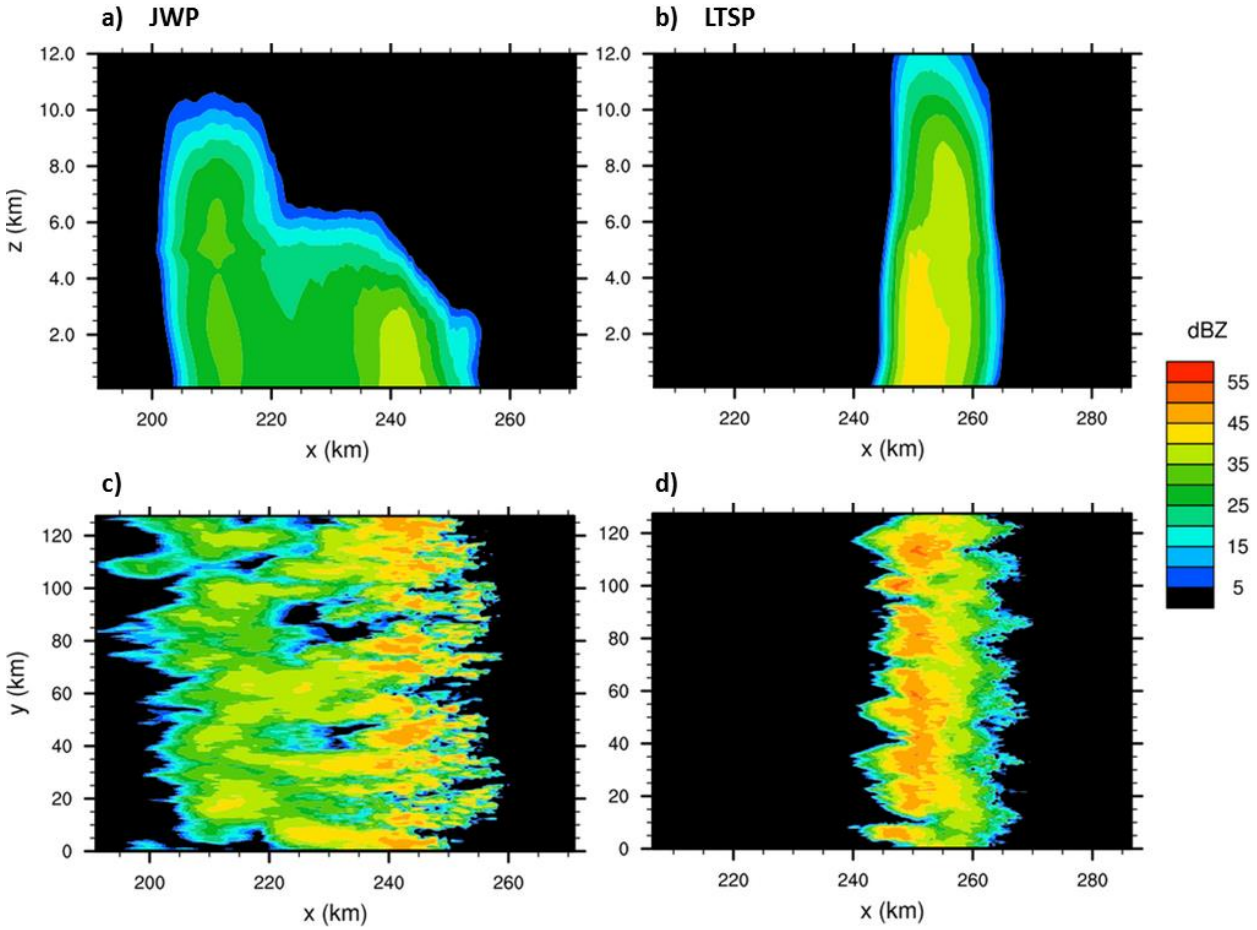

Figure 4.5. Along-line averaged contours of buoyancy (as in the color bar), pressure perturbations (black lines, every 10 hPa), and horizontal winds (red lines, every 2 m s^{-1}) corresponding to *baseline_10J* (a and c) and *baseline_10* (b and d). Plots are of fields at 3 h (a and b) and at 5 h (c and d). The white line corresponds to neutral buoyancy, and the thick red and black lines respectively denote zero horizontal winds and pressure perturbations. Negative contours are dashed in the case of the horizontal velocity and pressure perturbations.

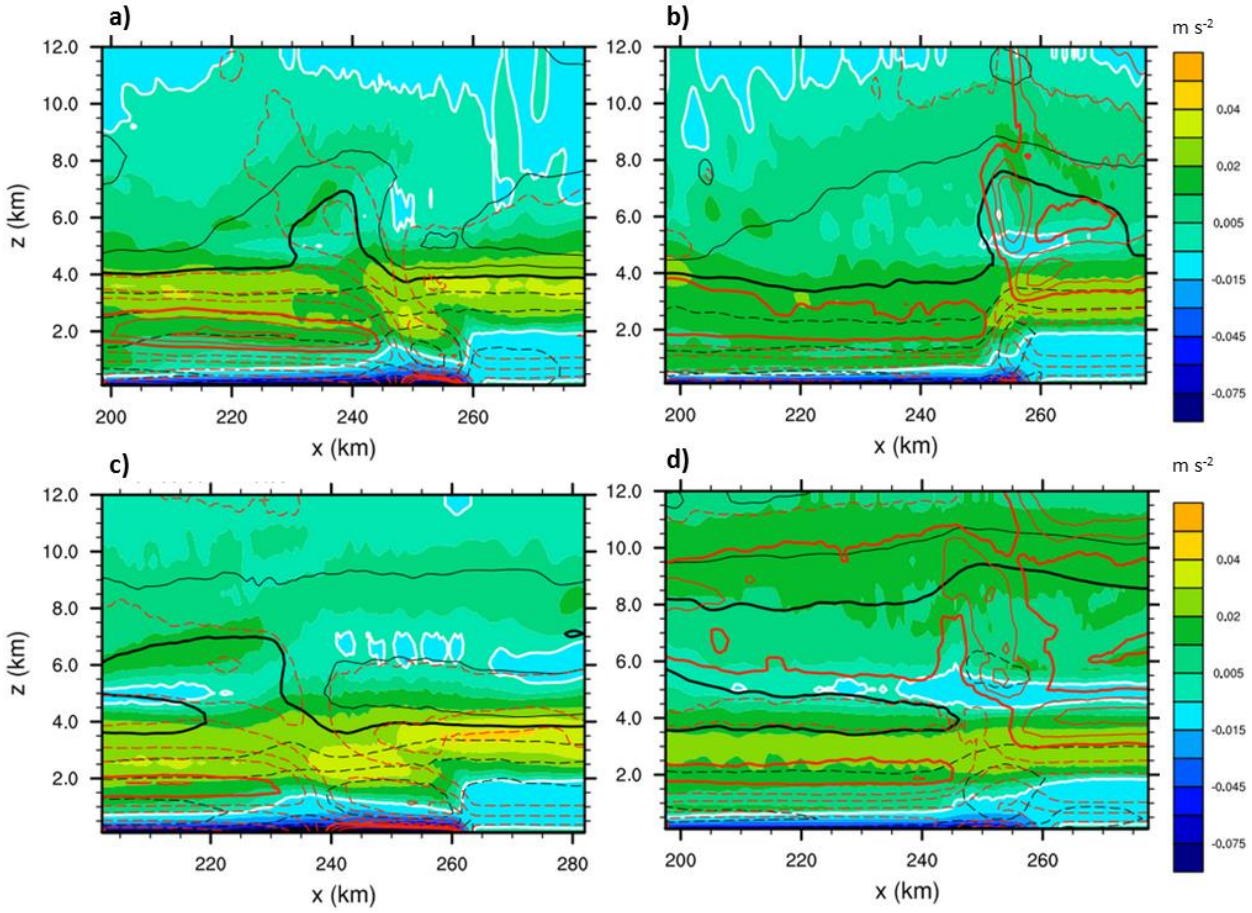

Figure 4.6. Particle trajectories projected onto the across-line/height plane, corresponding to *baseline_10J*. The particles were placed ≈ 6 km ahead of the cold pool edge at 3 h of simulation time, spaced by 1 km in the along line direction, and at height a) 300 m, b) 1300 m, c) 2300 m, and d) 3300 m. The paths are colored based on the temperature difference of the parcel and the initial sounding, with the black dots indicating 5 h simulation time. Contours of along-line averaged *h* at 6 h, every 3 K, and for *h* < 339 K are included in the background for reference.

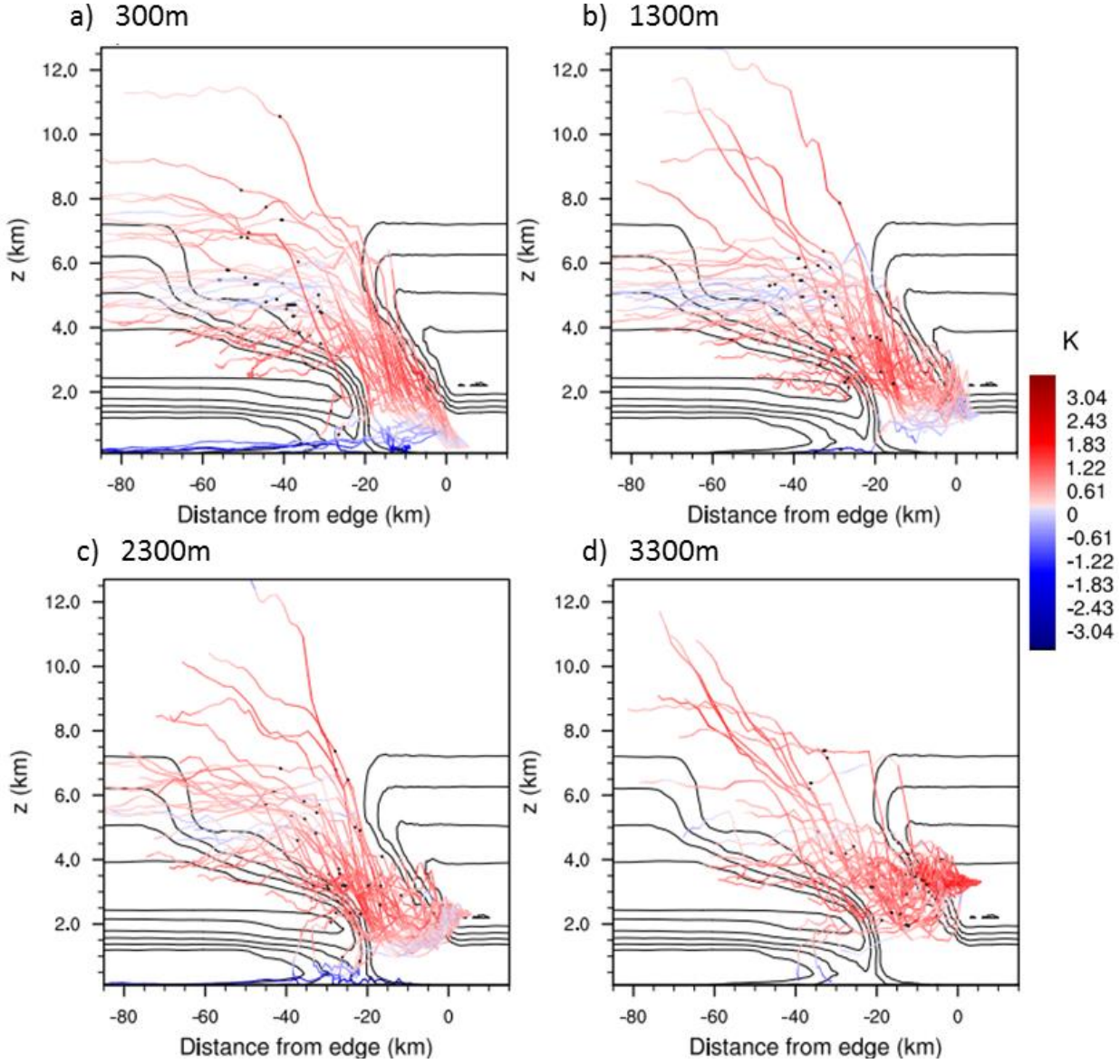

Figure 4.7. As in Fig. 4.6, corresponding to *baseline_10*.

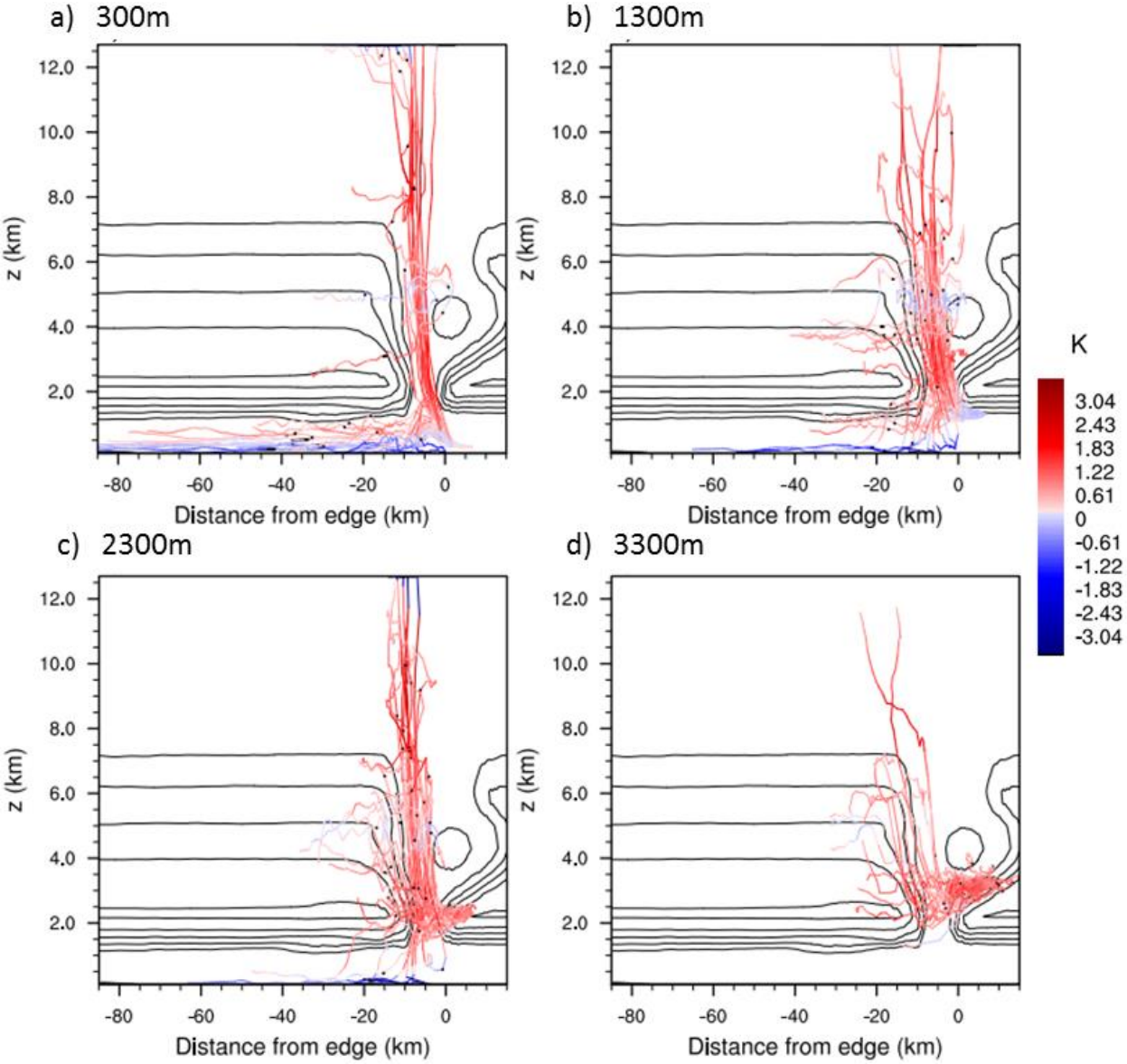

Figure 4.8. Contours of along-line averaged cooling produced by microphysical processes are color-filled according to the values given by the color table, corresponding to a) *baseline_10J* and b) *baseline_10* at 4 h. Line contours of mixing ratios of graupel (black and every .4 g kg^{-1}), snow (orange and every .15 g kg^{-1}), and rain (red and every .15 g kg^{-1}) are overlaid.

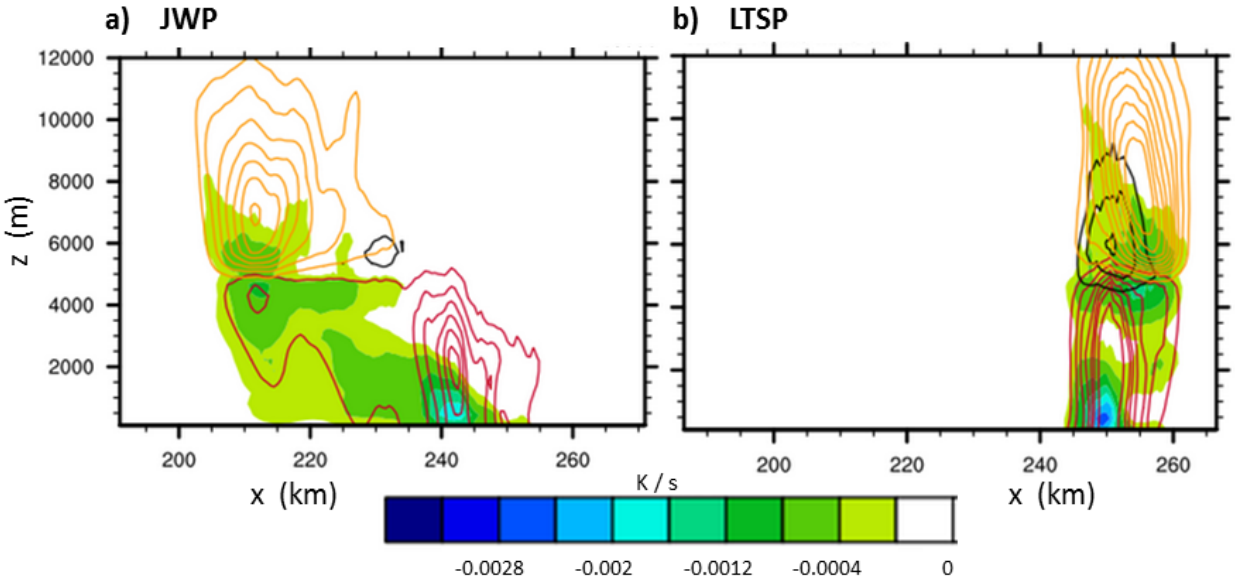

Figure 4.9. Particle trajectories as described in Fig. 4.6, projected onto a *y*-*z* plane. The trajectories in a) and b) correspond to *baseline_10*, and those in c) and d) are from *baseline_10J*. The height at which particles originate is 300 m in a) and c), and 1300 m in b) and d).

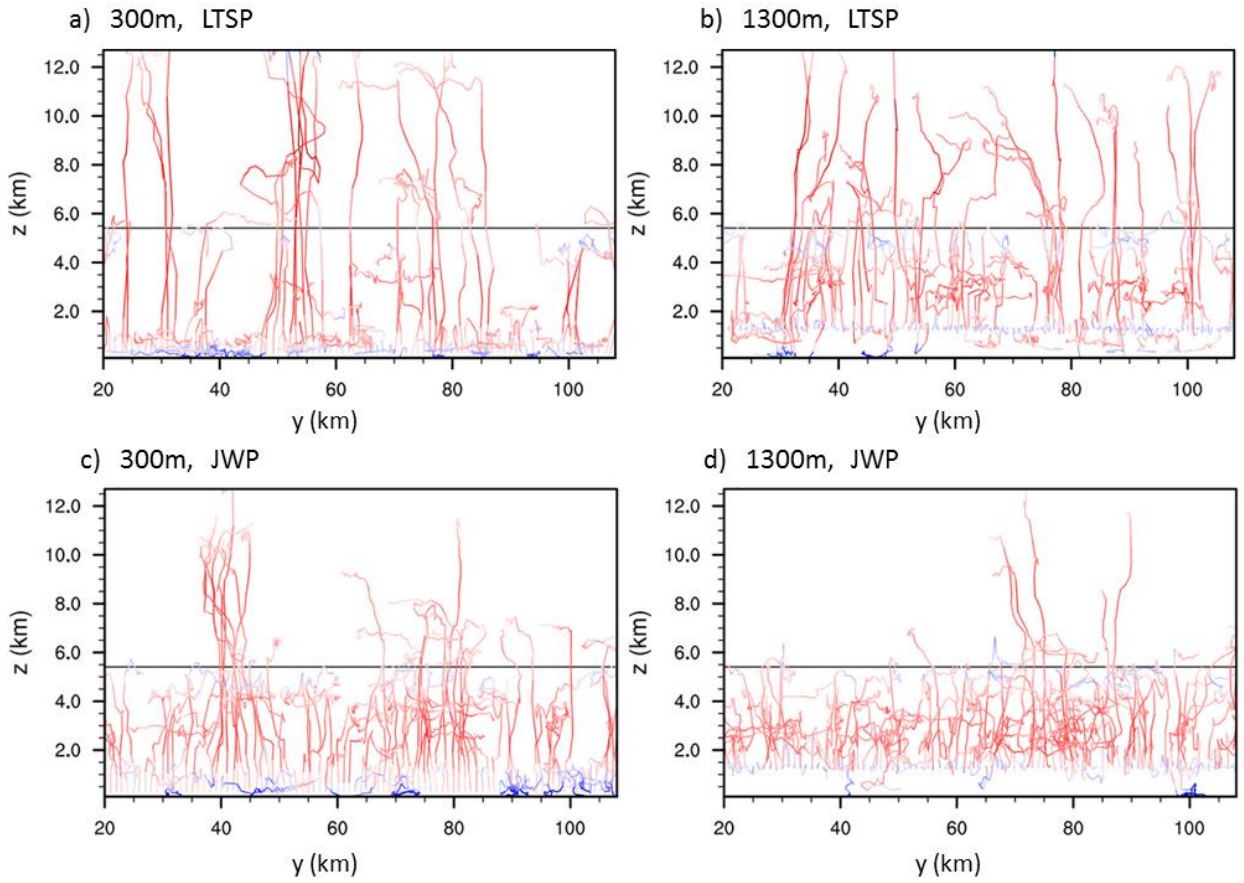

Figure 4.10. Surface precipitation rate over the whole domain for the $\Delta U = 8$ simulations, with JWP shown in a) and the LTSP in b).

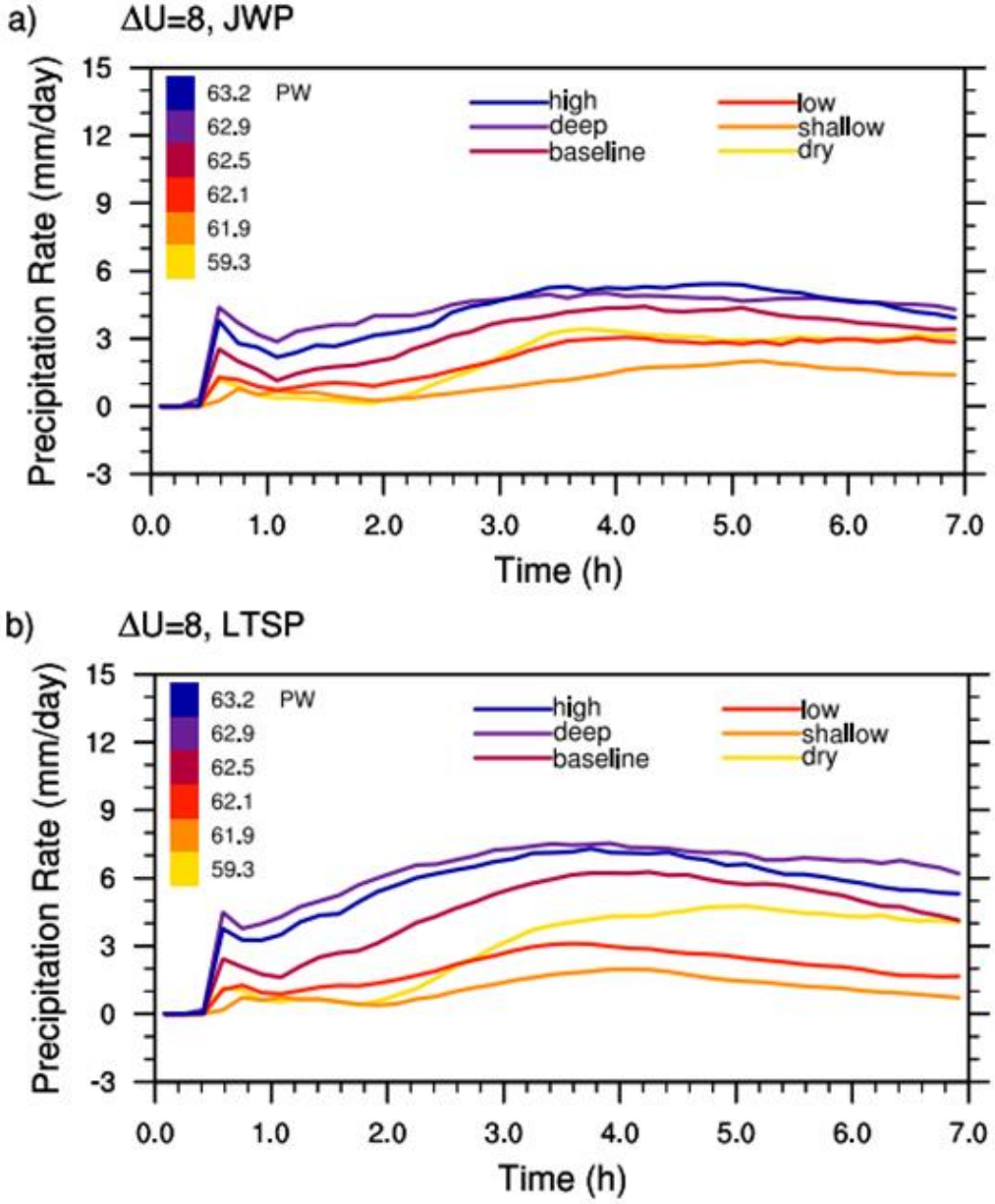

Figure 4.11. Fields as in Fig. 4.5 corresponding to a) *baseline_8J*, b) *dry_8J*, c) *baseline_8*, and d) *dry_8* at 5 h.

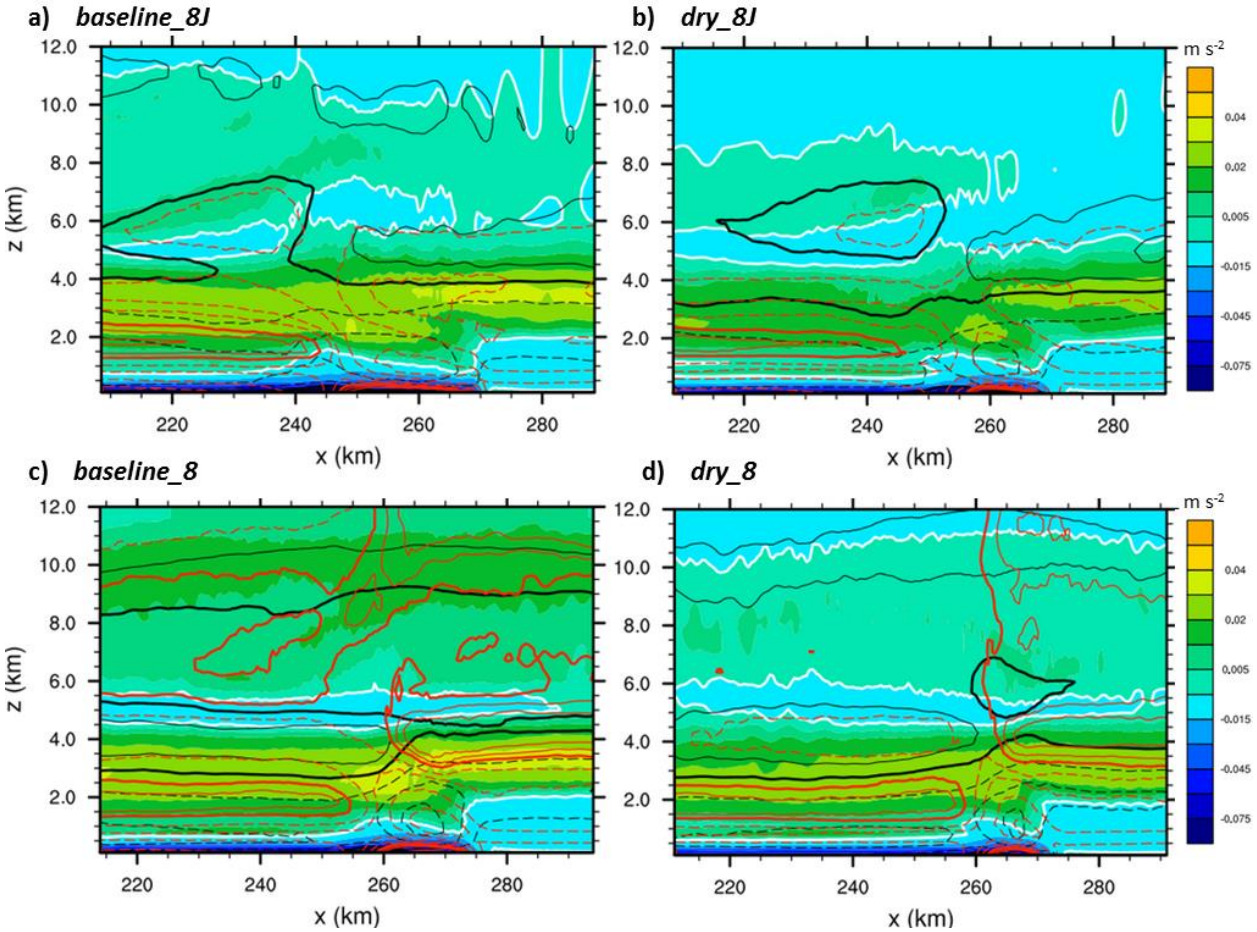

Figure 4.12. Fields as in Fig. 4.8 corresponding to a) *baseline_8J* and b) *dry_8J*, at 5 h. The contour values differ from those in Fig. 4.8 in that graupel is contoured every .1 g kg^{-1}.

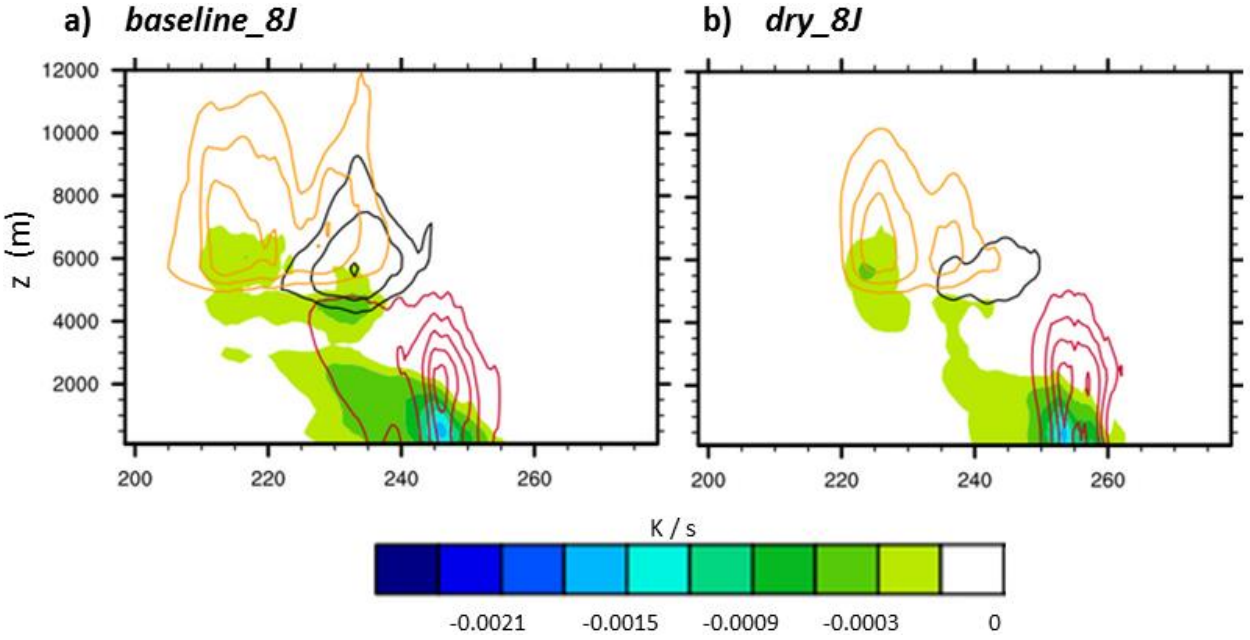

Figure 4.13. Fields as in Fig. 4.5 corresponding to a) *low_8J*, b) *high_8J*, c) *low_8*, and d) *high_8* at 5 h.

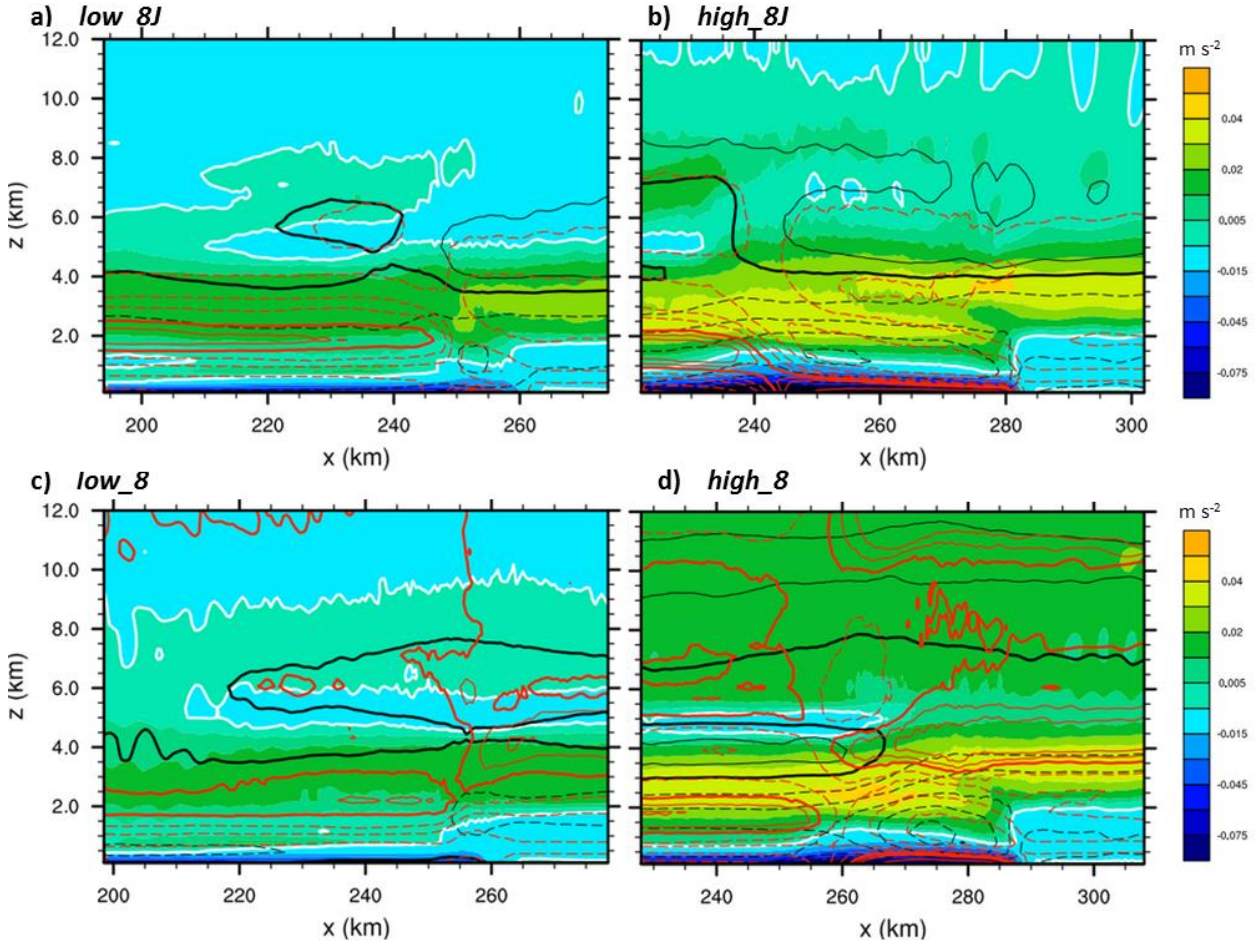

Figure 4.14. Fields as in Fig. 4.5 corresponding to a) *shallow_8J*, b) *deep_8J*, c) *shallow_8*, and d) *deep_8* at 5 h.

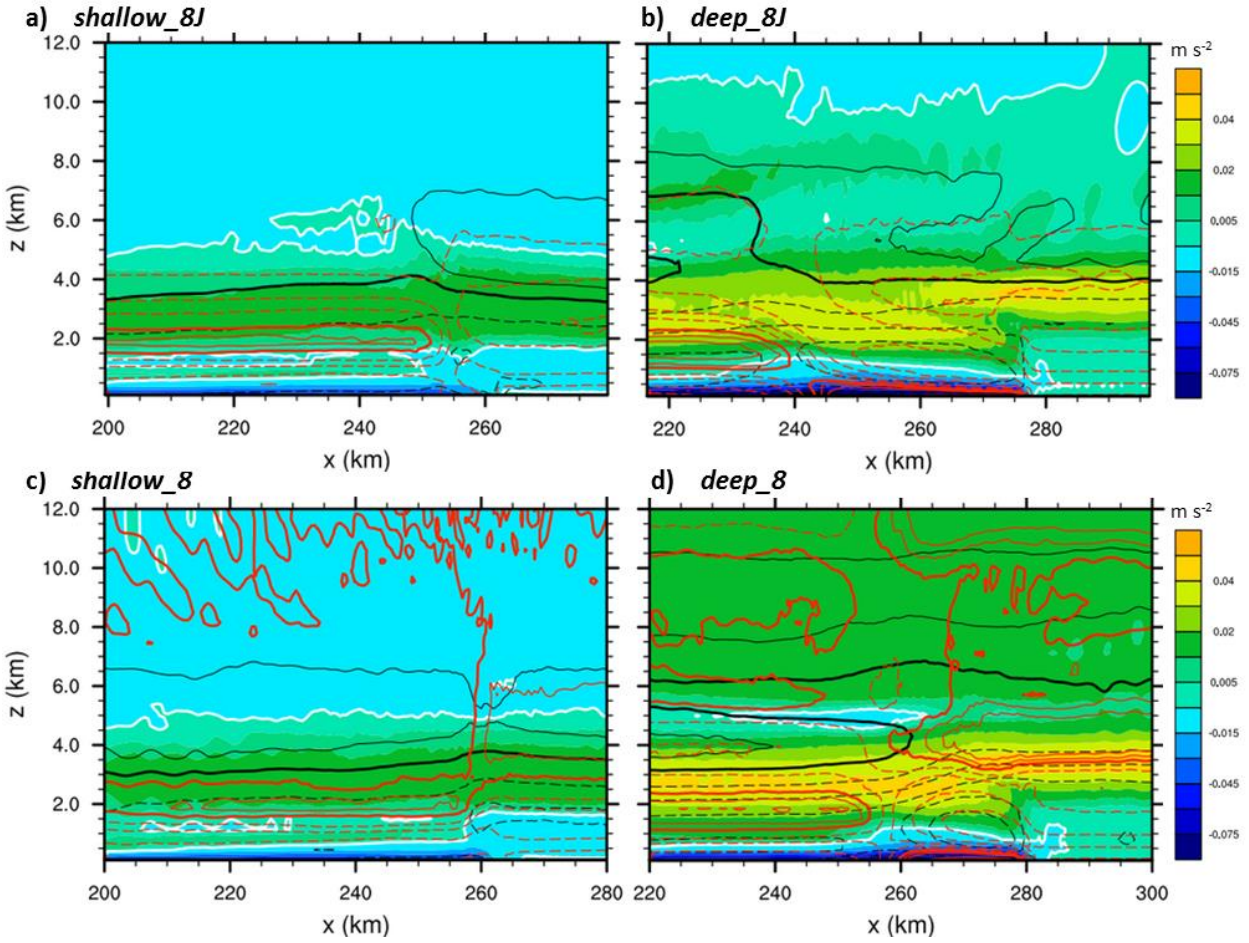

Figure 4.15. Horizontally averaged temperature perturbation (T') at 7 h corresponding to ΔU=8 JWP (a and c) and LTSP (b and d) simulations.

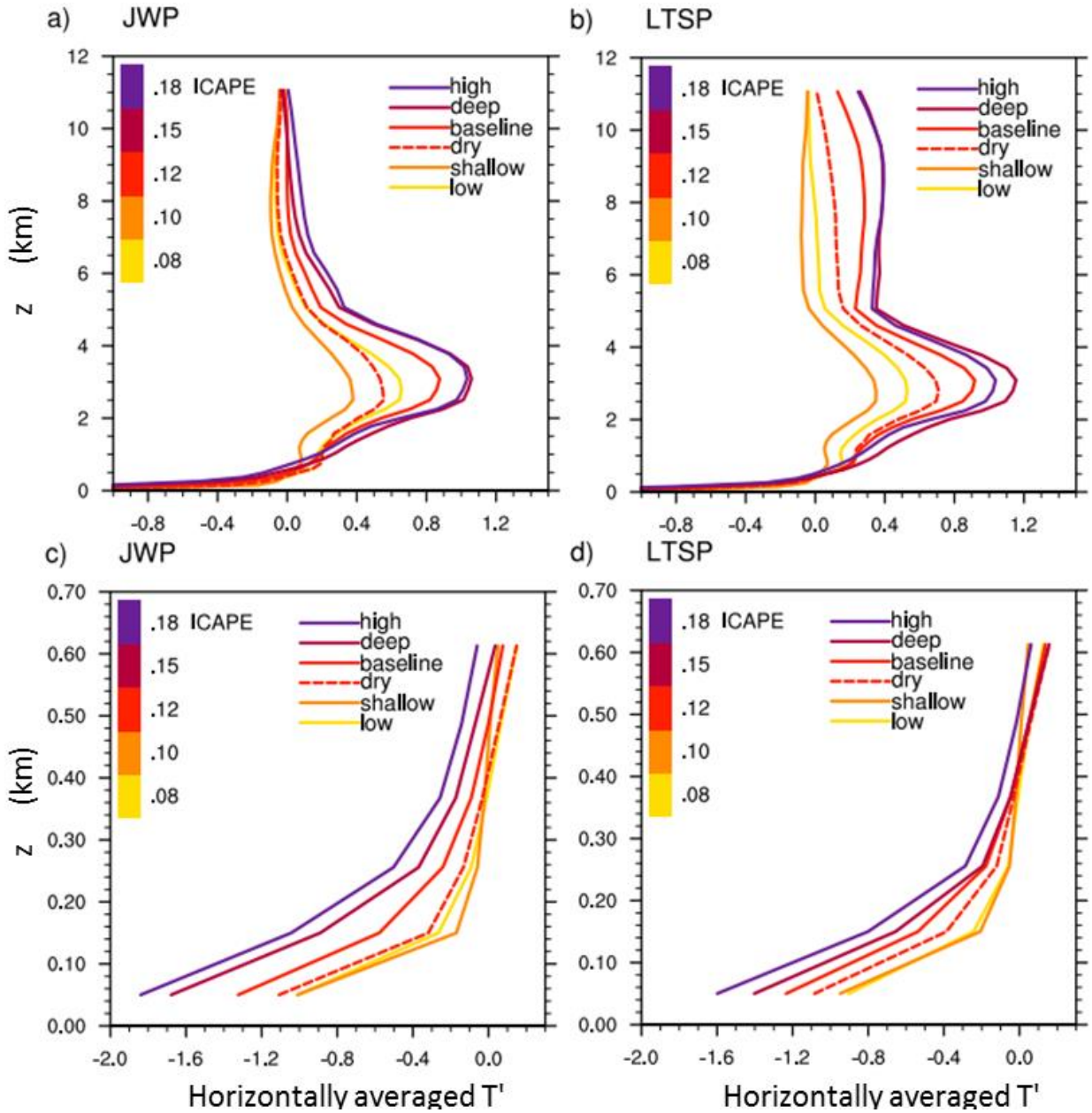

Figure 4.16. Environmental RH profile of *low* (black solid line), *high* (black dashed line), *shallow* (gray solid line), and *deep* (dashed gray line).

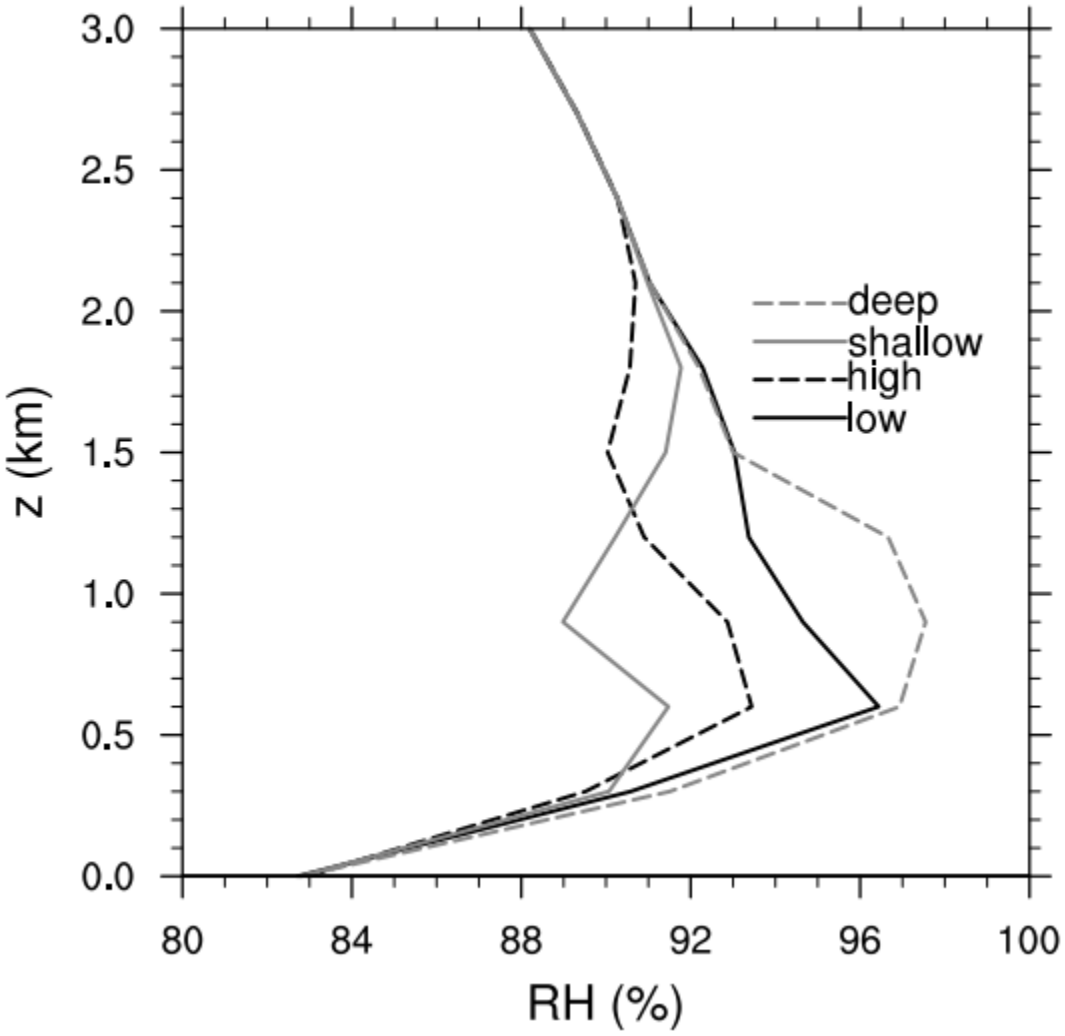

Figure 4.17. Distance that parcels originating at various heights need to ascend in order to reach their LCL (black lines) and their LFC (gray lines) in *high* (solid lines) and *deep* (dashed lines). The abscissa represents the level of origin of the parcel, and the ordinate gives the distance the parcel needs to be lifted.

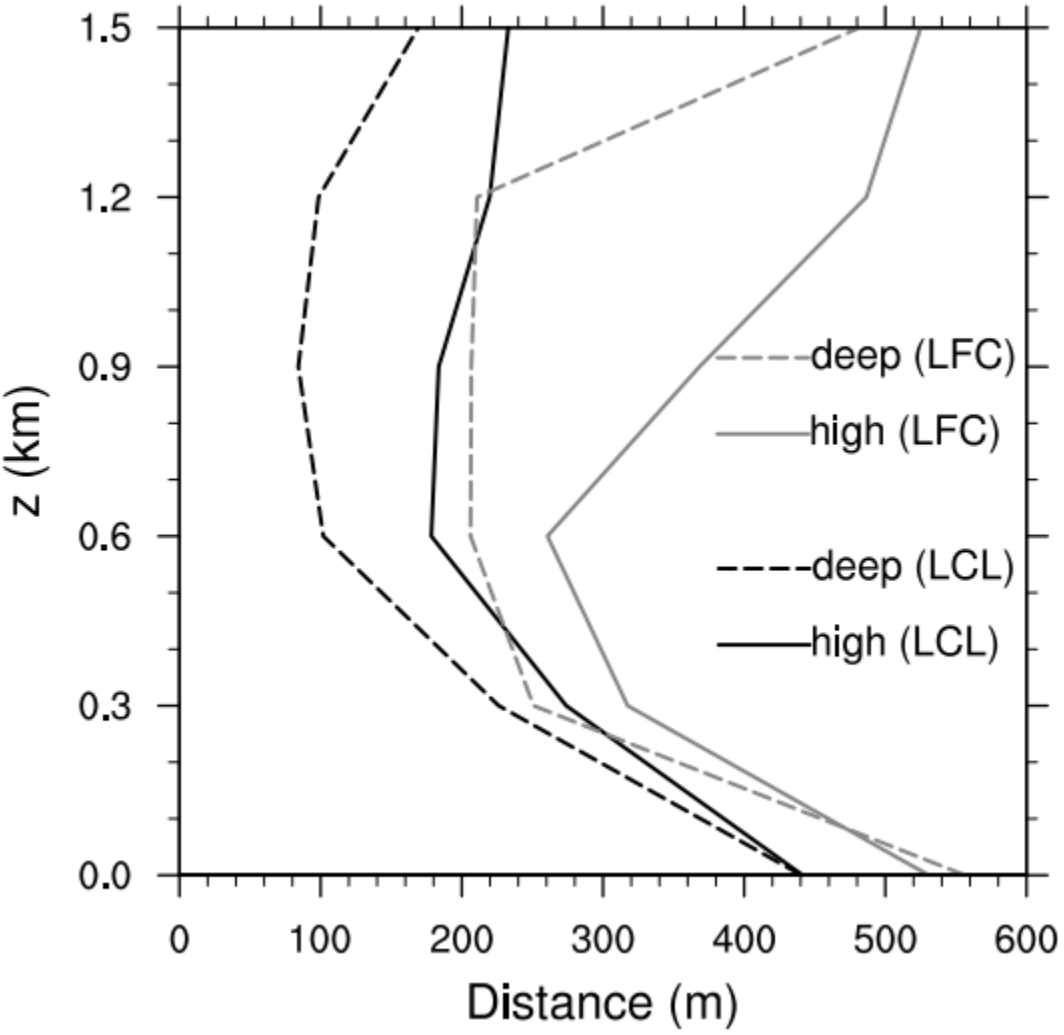

Figure 4.18. Histograms showing the count of particle heights at 7 h for different JWP (a, c, and e) and LTSP (b, d, and f) simulations, identified by color through the label bar in f). Particles were specified as in Fig. 4.6, originating at 300 m (a and b), 1300 m (c and d), and 2300 m (e and f). The bars corresponding to *dry* are red and to the left, while *baseline* bars are in red and to the right (they were both colored in red so that the color can be interpreted in terms of ICAPE).

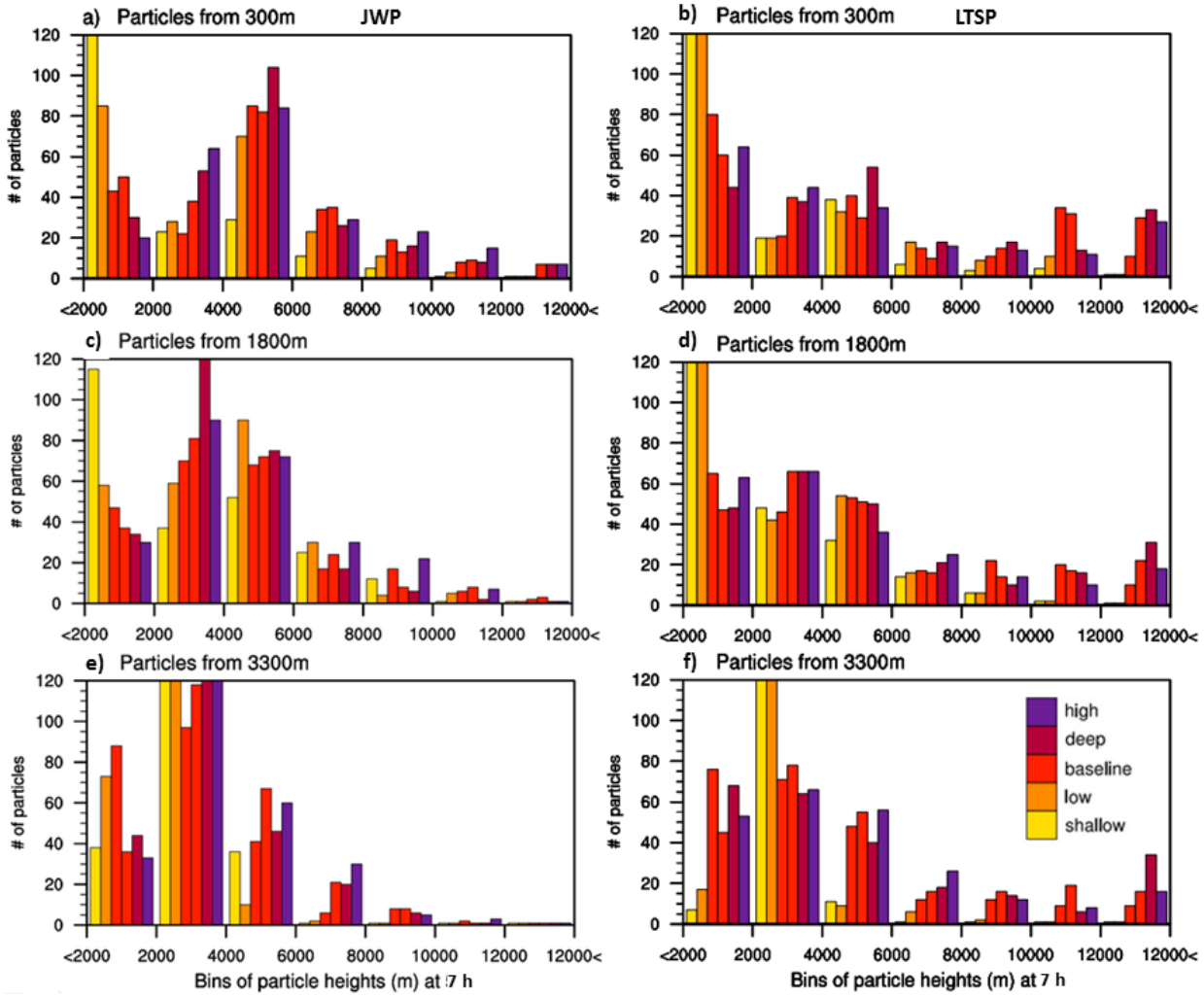

Figure 4.19. As in Fig. 4.10 for the $\Delta U = 10$ simulations.

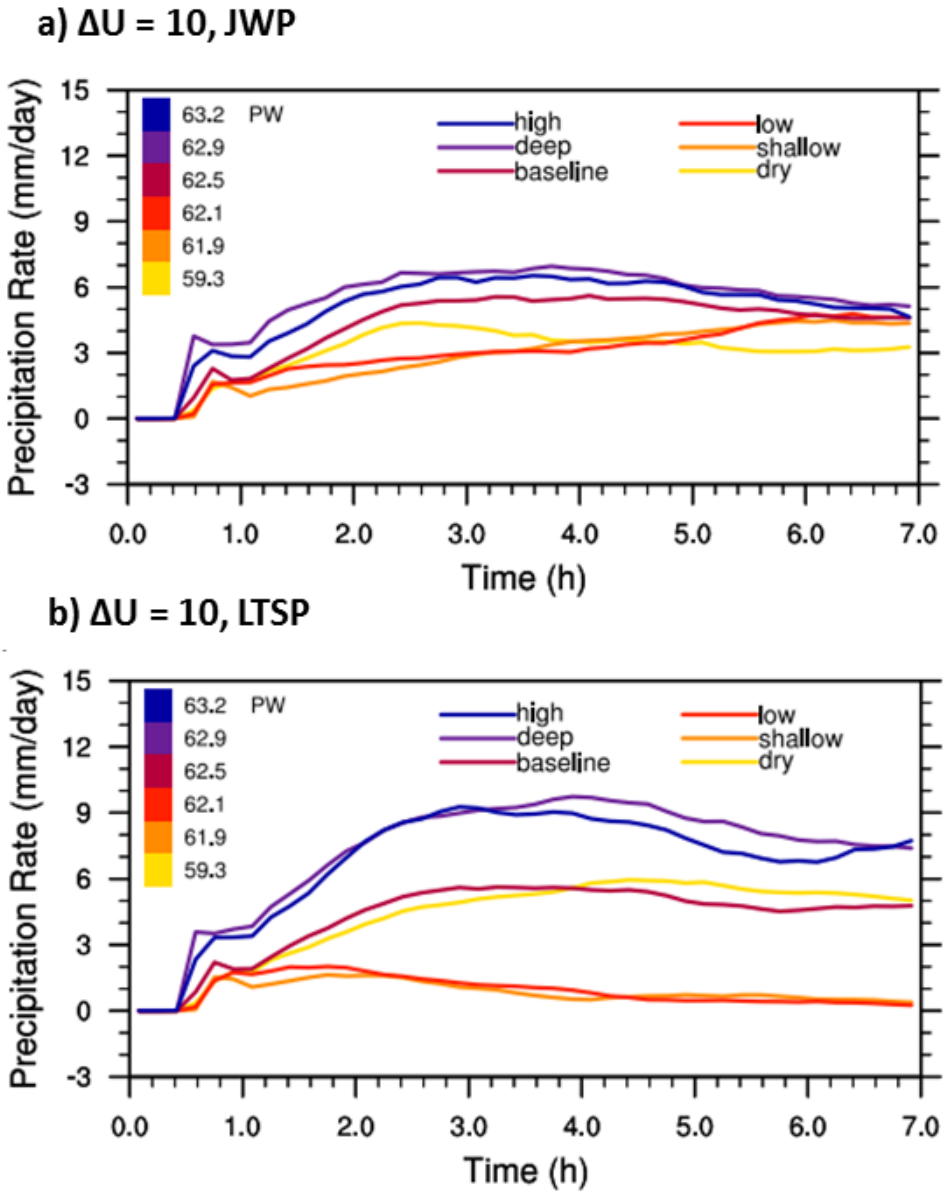

Figure 4.20. As in Figs. 4.15a and 4.5b for the $\Delta U = 10$ simulations.

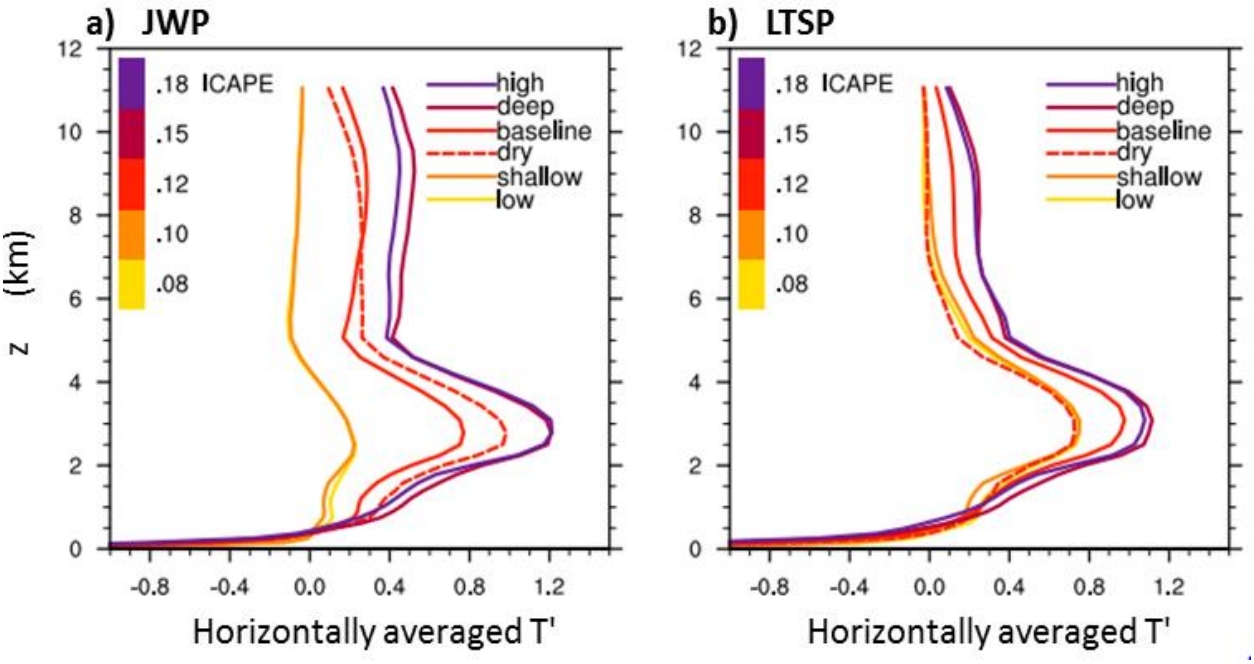

Chapter 5:

The effects of latent heating on the structure of updrafts in squall lines

The previous chapters have shown that the morphology of SLs is highly dependent on the latent instability properties throughout the depth of the troposphere. But it remains to determine whether these findings may impact on our understanding of SLs through previously formulated theories, such as the dependence of the PS on CAPE (e.g. Moncrieff and Miller 1976), as well as the applicability of RKW theory in cases with varying latent heating. The difficulty in addressing these issues lies in the fact that SLs are dynamically dependent on intricate microphysical processes, so that designing experiments where a given parameter is varied while holding the others constant is extremely complicated. With these considerations in mind, numerical simulations are performed in this chapter using a simplified microphysics scheme, which allows different degrees of latent heating under ascent, without compromising the intensification of cold pools due to the lack of environmental moisture. In this way, there is less variation in cold pool-shear balance among simulations with different latent instability profiles, a convenient feature for the analyses performed herein.

The organization of this chapter is as follows: Section 5.1 presents a background discussion, including a general presentation of density current flows (5.1.1), and a description of RKW theory. Section 5.2 presents the numerical framework used for performing the simulations, including a description of the numerical model and the specification of thermodynamic and kinematic environments considered herein. Results are presented in section 5.3, first discussing the effects of shear on the structure of simulated updrafts for a given thermodynamic profile, after which the analysis is expanded to incorporate latent instability variations. A brief discussion is presented in section 5.4, followed by a summary of results in section 5.5.

5.1 Background

a. Some relevant features about density currents and analytical models of MCSs

Many investigations into SLs have referred to the properties of density current flows, due mainly to the similarity of the latter with the outflows produced by the former (Charba 1974). Density currents have the advantage of being more tractable conceptually and analytically than SLs. Investigations into these flows have encompassed two fluid models in sheared environments (Xu 1992; Xue et al. 1997; Bryan and Rotunno 2014), extensions to three fluid models (Moncrieff and So 1989), density currents in a deep anelastic atmosphere (Bryan and Rotunno 2008), models incorporating circulations within the density current (Xu and Moncrieff 1994), stratified environments (Liu and Moncrieff 2000), among others. In addition to the above, steady analytical models by Moncrieff and collaborators (e.g. Moncrieff and Green 1972; Moncrieff and Miller 1976; Liu and Moncrieff 1996) include simple formulations that account for latent heating effects.

The purpose of this subsection is to describe some basic characteristics of density current flows which will be useful in subsequent analyses. It is important to stress that this does not constitute an in depth and formal investigation into density currents, for which the reader is referred to the aforementioned studies.

Consider a steady, incompressible and immiscible density current as depicted in Fig. 5.1, with static winds within the dense fluid (i.e. the flow with density ρ_2), implying a static density current nose (DCN). Boundaries L and R are meant to represent conditions at $x = -\infty$ and $x = \infty$, respectively, i.e. far from the DCN. The winds at R will be referred to as environmental winds, and winds at L will be referred to as outflowing winds. Pressure is hydrostatic at L and R, with vanishing environmental pressure perturbations. T and B represent rigid and frictionless boundaries, which are orthogonal to the gravitational acceleration and separated by unit distance.

The flow configuration depicted in Fig. 5.1 is analogous to that considered in Xue et al. 1997, which is determined by the following boundary parameters (the interior flow can be resolved after these parameters are specified): the height (H) and density (ρ_2) of the denser fluid, the environmental surface wind speed ($u_R(0)$), the outflowing wind speed at height H ($u_L(H)$), the environmental shear (α_R), the outflowing shear (α_L), the environmental shear depth (d_R), the outflowing shear depth (d_L), the outflowing surface pressure perturbation ($p'_L(0)$), and the outflowing pressure perturbation above the denser fluid ($p'_L(H)$). Not all parameters can be chosen freely, as these flows are bound by the constraints of mass conservation, energy conservation, vorticity conservation, and flow force balance (Benjamin 1968). Thus, the number of free parameters can be reduced by applying these constraints to the boundaries. Vorticity conservation implies that $\alpha_L = \alpha_R$, as there are no vorticity sources within the unit density flow. Mass conservation requires that the environmental inflow is equal to the outflow

$$\int_H^1 u_L dz = \int_0^1 u_R dz$$

while flow force balance guarantees that the flow at R and L is consistent with the momentum equation and mass conservation (e.g. Benjamin 1968)

$$\int_0^1 \left(u_R^2 + p'_R\right) dz = \int_0^1 \left(u_L^2 + p'_L\right) dz$$

The remaining constraint is energy conservation, which, under the assumptions considered herein, can be stated as the conservation of the Bernoulli energy, $(u^2 + w^2) / 2 + p'$, along streamlines. This constraint is particularly revealing in terms of determining $u_R(0)$ via $p'_L(0)$, as shown by the following arguments. Given that winds are static within the density current, then the surface pressure perturbation at the DCN must be equal to $p'_L(0)$ (otherwise the density current air would accelerate due to the implied horizontal pressure gradient). Considering also that the environmental surface streamline is bound by mass conservation to remain at the surface and to reach a stagnation point at the DCN, then the conservation of Bernoulli energy implies $u_R(0)^2 / 2 = p'_L(0)$. Similarly, the hydrostatic equation can be used to determine $u_R(0)^2 / 2$ from knowledge of H, ρ_2, and $p'_L(H)$ (note that p'_L must be constant above H), which obtains

$$u_R^2(0) = p'_L(H) + c^2 \tag{5.1}$$

where $c^2 = 2g(\rho_2\text{-}1)H$ is the cold pool intensity for the case with $\rho_1 = 1$. Equation (5.1) will be used in subsequent discussions.

Consider now the model depicted in Fig. 5.2, which is analogous to the one in Fig. 5.1, but

allowing stratification and latent heating due to condensation. Liu and Moncrieff (1996) incorporate environmental stratification by a constant environmental lapse rate of the log potential temperature, $\Gamma_R = d\phi_R/dz$ where $\phi = \ln\theta$ and θ is the potential temperature; the latent heating effects are represented by a constant lapse rate for upward fluid displacements, $\Gamma_0 = (d\phi/dz)_\psi$, where subscript ψ denotes differentiation along the ψ streamline (it is implicitly assumed that the environment is saturated). Conceptually, the cases that are of interest to this study satisfy $\Gamma_0 < \Gamma_R$, so upward displacements lead to increments in buoyancy. It is worth noting that horizontal buoyancy gradients may be present within the non-static flow, implying vorticity sources/sinks. In addition, sources of vertical momentum due to buoyancy must be considered in the energy conservation equation, so that the conserved quantity along streamlines becomes $(u^2 + w^2) / 2 + p' / \rho_R - \int_{z_R}^{z} b dz'$, where z_R is the height of the streamline that passes through the point of evaluation in the limit $x \rightarrow R$.

A consequence of heating due to condensation within the flow at L, which is hydrostatically balanced, is that positive buoyancies above H will contribute to lower the value of $p'_L(H)$, thus decreasing $p'_L(0)$ for a given c. Although this does not formally imply that more latent heating will necessary lead to lower $p'_L(H)$, results by Liu and Moncrieff (1996) corroborate that the value of $p'_L(H)$ decreases and becomes nearly hydrostatic (i.e. attributable to the buoyancies aloft) with increasing $\Gamma_0 - \Gamma_R$, i.e. with increasing buoyancy attained by the flow under vertical displacements. This is important because it shows that, for the steady model of Liu and Moncrieff (1996), greater upper-tropospheric buoyancies can lead to lower $p'_L(0)$, which in turn implies a reduction in $u_R(0)^2$ (e.g. see equation 5.1). If one assumes that surface winds are nearly static close to the ground, as is frequently observed in the atmosphere, then the propagation speed of the system would be equal to $-u_R(0)$, and thus greater upper-tropospheric heating would be associated with a greater PS. And if upper-tropospheric buoyancies were constrained by CAPE, it would follow that SLs propagate faster in environments with higher CAPE.

Observational studies (e.g. Wyss and Emanuel 1988; Alexander and Young 1992) have failed to detect any relationship between CAPE and PS, which may be due to the fact that CAPE computed for a boundary layer parcel does not constrain the upper-tropospheric heating. Actually, the conceptual model in Fig. 5.2 explicitly assumes that the upper-tropospheric buoyancy is determined by the latent heating of ascending air throughout the whole troposphere. It is thus conceptually more appropriate to contemplate ICAPE when estimating upper-tropospheric buoyancy, as shown in previous chapters. This observation is exploited in order to study the effects of the storm induced heating on the PS and the momentum structure of the simulated updrafts.

The numerical simulations analyzed in this chapter produce upper-tropospheric heating of varying amplitude, which is accomplished by designing environments with different ICAPE. The modeling framework considered herein differs from the one used in previous chapters in that large amounts of precipitation are produced by saturated updrafts, irrespective of the latent instability profile. This is done so that cold pools in low ICAPE environments are not limited by the production of precipitation, as occurred in the simulations analyzed in chapters 3 and 4. For example, Fig. 5.3 shows that the simulations producing greater upper-tropospheric warming, as measured by W, also produced greater c. This partly resulted from the fact that low ICAPE environments, which developed a smaller W, produced less precipitation, on which the development of the cold pool is highly dependent. The framework considered herein attempts to reduce the dependence of the development of the cold pool on ICAPE, which will facilitate

controlling for factors on which SLs are known to be strongly dependent, such as cold pool-shear balance.

b. RKW theory and the structure of updrafts in SLs

As described in the introduction, RKW theory provides a simple framework for understanding how the low-tropospheric shear affects the structure of SLs. There have been many numerical studies of idealized SLs supporting its validity and central importance to storm morphology (RKW88; Weisman et al. 1988; Fovell and Ogura 1989; Weisman 1992, 1993; Weisman and Rotunno 2004; Bryan et al. 2006). But it is important to stress that very few thermodynamic environments have been considered, and that many studies have questioned the principles underlying RKW theory (e.g. Nicholls et al 1988; Lafore and Moncrieff 1989; Stensrud et al. 2005; Coniglio et al. 2012). A brief review of the literature on RKW theory will be given in the discussion section. This subsection will provide a more detailed description of RKW concepts.

Following RKW88, consider a two-dimensional, inviscid, and adiabatic Boussinesq flow, similar to the density current in Fig. 5.1. The vorticity equation in this case is

$$\frac{\partial \eta}{\partial t} = -\frac{\partial}{\partial x}(\eta u) - \frac{\partial}{\partial z}(\eta w) - \frac{\partial b}{\partial x} \tag{5.2}$$

where $\eta = \partial w/\partial x - \partial w/\partial x$ and b is the buoyancy. RKW88 integrate (5.2) from L to R in the x direction, and from the surface to some height d exceeding both H and the environmental shear depth, d_R (see Fig. 5.1), obtaining

$$\frac{\partial}{\partial t}\iint \eta dz dx = \int_0^d (u\eta)_L dz - \int_0^d (u\eta)_R dz - \int_L^R (w\eta)_d dx + \int_0^d (b_L - b_R) dz$$

which, after assuming a steady state, and noting that $b_R = 0$, $(u\eta)_R = u_R \partial u_R/\partial z$, $(u\eta)_L = u_L \partial u_L/\partial z$, together with the fact that the density current air is static, gives

$$0 = \underbrace{\frac{u_L^2(d)}{2}}_{(A)} - \underbrace{\left(\frac{u_R^2(d)}{2} - \frac{u_R^2(0)}{2}\right)}_{(B)} - \underbrace{\int_L^R (w\eta)_d dx}_{(C)} + \underbrace{\int_0^d b_L dz}_{(D)} \tag{5.3}$$

where terms (A), (B), and (C) in (5.3) give the vorticity flux at L, R, and d, respectively. Term (D) represents the vorticity generation through horizontal buoyancy gradients. The analysis in RKW88 proceeds by considering two cases. First, assume that there is a rigid lid at d, and that there is no environmental shear. In this case, $u_R(d) = u_R(0)$ and $w(d) = 0$, resulting in

$$u_L^2(d) = 2\int_0^d b_L dz = c^2 \tag{5.4}$$

Referring to the interpretation of the terms in (5.3), equation (5.4) represents a balance between the outflow of vorticity at L and the generation of vorticity by the horizontal buoyancy gradient at the edge of the denser fluid.

For the second case considered by RKW88, the authors determine a priori the configuration of the flow that may allow the fluid to exit through d as a vertically oriented jet. Thus, the rigid lid at d is removed, and the following assumptions are made, which are associated with the sought flow configuration: $u_R(d) = u_L(d) = \int_L^R (w\eta)_d dx = 0$. Thus, (5.3) becomes

$$\Delta U = u_{\mathrm{R}}(d) - u_{\mathrm{R}}(0) = u_{\mathrm{R}}(0) = c \tag{5.5}$$

which is interpreted as a balance between the inflow of vorticity through environmental shear and the vorticity generated within the volume of integration. RKW88 generalize these arguments by proposing that flows with $\Delta U < c$ will develop upshear tilted updrafts, while flows with $c < \Delta U$ develop downshear tilted udprafts (see Fig. 1.2), with greater verticality achieved in cases with $\Delta U / c$ closer to 1 (e.g. Weisman and Rotunno 2004).

It is important to note that the arguments presented above do not imply that $\Delta U = c$ will necessarily produce the most vertically oriented and deep reaching updrafts; rather, it was deduced that (5.5) is necessary for the flow to satisfy the requirements that are associated vertically oriented updrafts, these being $u_{\mathrm{L}}(d) = u_{\mathrm{R}}(d) = 0$ and $\int_{\mathrm{L}}^{\mathrm{R}} (w\eta)_d \, dx = 0$. It will be useful to describe the implications of these requirements. First, the condition $\int_{\mathrm{L}}^{\mathrm{R}} (w\eta)_d \, dx = 0$ is discussed by RKW88, who note that positively buoyant ascending air is flanked by a thermally induced vortex pair, and that any initial shear will bias the updraft axis to tilt. Thus it is required that the η flux at d vanishes, which is interpreted as a condition for a balanced vorticity structure flanking the updraft. On the other hand, the condition $u_{\mathrm{L}}(d) = u_{\mathrm{R}}(d) = 0$ is not explicitly addressed by RKW88, which requires static environmental and outflow winds aloft. Some thoughts on this condition are presented below.

A simple flow is presented in Fig. 5.4a, showing a chimney in an unsheared environment with nonzero horizontal winds relative to the chimney. It is intuitively clear that the smoke from the chimney will lean in the direction of the winds, even in the absence of shear. This is due to the transfer of horizontal momentum from the environmental winds to the buoyant and smoky air. To get a deeper understanding of how this happens, consider the momentum equation of a non-rotating Boussinesq flow,

$$\frac{\partial \mathbf{v}}{\partial t} + \mathbf{v} \cdot \nabla \mathbf{v} = -\alpha \nabla p' + b\mathbf{k}$$

where $\mathbf{k}$ is the vertical unit vector. Taking the divergence of the above equation and using the continuity equation gives

$$\alpha \nabla^2 p' = \underbrace{-\nabla \cdot (\mathbf{v} \cdot \nabla \mathbf{v})}_{\text{(A)}} + \underbrace{\frac{\partial b}{\partial z}}_{\text{(B)}} \tag{5.6}$$

where (A) is related to the dynamic pressure perturbation (p'_{dyn}) and (B) is associated to the buoyancy pressure perturbation (p'_b). The linearity of the Laplacian operator allows independent treatment of these two components of the pressure perturbation. Although it is acknowledged that term (B) in (5.6) might be important (e.g. Parker 2010), this discussion will focus on (A) and the associated p'_{dyn}.

Consider a two-dimensional thermal rising from the chimney as illustrated in Fig. 5.4b. As the thermal meets environmental air, the velocity within it is nearly vertically oriented, and the velocity of the environmental air is nearly horizontal, as depicted by the thick arrows. The direction of $\mathbf{v} \cdot \nabla \mathbf{v}$ can be determined qualitatively at points *l*, *r*, and *c* and *u* in Fig. 5.4b by noting that $\mathbf{v} \cdot \nabla \mathbf{v}$ corresponds to the derivative of $\mathbf{v}$ in the direction $\mathbf{v}$. Therefore $\mathbf{v} \cdot \nabla \mathbf{v}$ will point downward and to the left in *c*, toward the right and upward in *r*, and it will be relatively small at *l* and *u*, which

is indicated by the thin arrows. Therefore, $\mathbf{v}\cdot\nabla\mathbf{v}$ will be horizontally divergent between *c* and *r*, convergent between *c* and *l*, and between *c* and *u* it will be vertically divergent. By associating negative (positive) values of (A) to maxima (minima) of p'_{dyn}, it follows that the gradient of p'_{dyn} will tend accelerate the air within the thermal downward and in the direction of the environmental winds (toward the left in Fig. 5.4b). This effect is qualitatively similar to that of horizontal wind shear on buoyant updrafts, as described in Asai (1964).

The flow near the cold pool in Figs. 5.1 and 5.2 resembles a chimney in that it guides the fluid from a stagnation point at the DCN, just as the chimney guides the thermal. Even though the example given above represents a simplified case compared to updrafts in SLs, where mesoscale circulations and microphysical processes impact substantially on the convective motions, it serves to highlight the importance of the condition $u_L(d) = u_R(d) = 0$ for updraft verticality. With these considerations in mind, the following questions are relevant to assess RKW theory: to what extent does cold pool-shear balance provide a constraint on the environmental and outflowing wind speeds aloft, such that more optimal configurations lead to smaller $u_L(d)$ and $u_R(d)$? In the case that environmental and outflowing wind speeds aloft are weakly constrained by cold pool-shear balance, does the RKW optimality criterion still predict updraft intensity and verticality?

The density current models described in the previous subsection can provide some insights regarding the aforementioned questions. Focusing on cases with upshear tilted updrafts, which conceptually conform with SLs having trailing stratiform precipitation, consider the dependence of $u_R(0)$ on both $p'_L(H)$ and *c*, which from (5.1) (i.e. in a neutrally stratified Boussinesq flow with unit environmental density) gives $u_R(0) = \left(p'_L(H) + c^2\right)^5$. Many density current flows in confined channels have $p'_L(H) < 0$ (e.g. Xu 1992), with lower values attained in cases with latent heating aloft (e.g. Liu and Moncrieff 1996).[13] In analogy with negative $p'_L(H)$, SLs generally develop a meso-low at the upper edge of the cold pool (see chapter 3), which depends on the amplitude of the buoyancy developed aloft. These arguments suggest the possibility that there exist many SL flows having the same (ΔU, *c*) configuration, but with different $p'_L(H)$, and thus different $u_R(0)$. This is relevant because, for a given ΔU, different $u_R(0)$ imply different $u_R(d)$, i.e. different environmental wind speeds aloft (recall the example with the chimney). Note that these considerations are intimately related to the question about whether the PS is strongly affected by the storm induced heating aloft, as explained in the previous chapter.

In addition to the implied effects of latent heating on the value of $u_R(d)$ for a given (ΔU, *c*) pair, it is important to acknowledge that updrafts in SLs are strongly dependent on the latent instability properties of the environment. In fact, RKW88 implicitly recognize the importance of latent heating when discussing the thermally induced vortex pair flanking the updraft, but they do not provide further discussion on their effects on the structure of updrafts. In this regard, a question worth asking is whether the tendency of an updraft to tilt due to cold pool-shear imbalances depends on the intensity of the thermally induced vortex pair flanking the updraft. In other words, are more buoyant updrafts equally inclined to tilt due to a given cold pool-shear imbalance than less buoyant updrafts? For example, Fig. 5.5 shows the average trajectories of deep reaching low-tropospheric particles corresponding to the $\Delta U = 16$ simulations described in section 3. Note that the cases with $c / \Delta U$ closer to 1, i.e. the more RKW optimal configurations (Weisman and Rotunno

[13] Xue (2002) shows that the tropopause acts as a rigid lid, which conceptually enhances the similarity between simple density current models and atmospheric flows.

2004), have the least vertical particle trajectories.

One of the objectives of this chapter is to investigate the degree to which RKW optimality constrains the morphology of SLs in environments with varying latent instability properties. A framework for doing so is described in the following section, in which intense cold pools are developed in all cases, even in those which would produce small amounts of precipitation due to relatively dry environmental conditions. It will be shown that such a framework allows simulations to develop similar c for different latent instability profiles. This will allow a comparison of updrafts produced by systems which develop different degrees of latent heating, for a given c / ΔU.

5.2 Experimental design

Studies of density currents have revealed interesting properties of fluids resembling storm induced outflows, and they have constituted an important means for investigating cold pool-shear balance as a framework for diagnosing the structure of updrafts (e.g. RKW88, Weisman and Rotunno 2004, hereafter WR04; Bryan and Rotunno 2015). An important advantage of these flows, both numerically and conceptually, is that they allow the specification of the temperature deficit within the cold pool, facilitating the investigation of matters related to RKW theory and steady density current flows. On the other hand, cold pools in SLs are dependent on complex microphysical processes which are intimately coupled with environmental thermodynamics. For example, among the environments considered in chapter 3, those with greater ICAPE tend to have more PW, aiding the production of precipitation and the development of intense cold pools. Thus, cases producing greater upper-tropospheric heating also had the strongest cold pools (Fig. 5.3), which partly resulted from differences in the amount of precipitation that was produced. The numerical framework described herein is motivated by the question of whether it is possible to simulate flows that bear greater resemblance to SLs than the previously described steady analytical models, in which the temperature deficit within the cold pool does not depend strongly on the latent instability properties of the environment. Such a framework would resemble the density current models in that the temperature deficit within the cold pool is approximately known beforehand, thus facilitating an analysis of RKW theory under different degrees of latent heating produced by convection.

The method proposed herein contemplates two prognostic non-precipitating moisture variables: one determines the latent heating under ascent, which will be varied among different simulations; the other determines the amount of precipitation that is produced under ascent, which is initially identical in all simulations, being large enough for cold pools to remain near saturation. In addition, a single moment microphysics scheme will be used, in which cold pools develop more readily than when a double microphysics scheme is used (e.g. see Morrison et al. 2009). A more detailed description is given below.

a. Model

The model used for this study is a modified version of SAM (Khairoutdinov and Randall 2003). Ice is neglected for simplicity. The conserved thermodynamic variable is the moist static energy, $h = T + (gz + L_c\, q_v)/c_p$, where all variables have their usual meaning. For additional simplicity, buoyancy has been modified to neglect virtual and water loading effects, so that $b = g(T'/T)$, were T' is the temperature perturbation with respect to T, which is the horizontally averaged temperature (pressure perturbations are ignored in the buoyancy calculation for energetic consistency).

The microphysics model is adapted from the single moment scheme described in Khairoutdinov and Randall (2003), such that only liquid processes are considered, and three prognostic moisture variables are included, of which two are non-precipitating (q_T and q_{prec}) and another one represents rain (q_r). The governing equations for these variables are,

$$\frac{\partial q_T}{\partial t} = -\frac{1}{\overline{\rho}} \nabla \cdot \left(\overline{\rho} q_T \mathbf{v} + \mathbf{F}_{qT} \right) + \left(\frac{\partial q_T}{\partial t} \right)_{\text{accr}} + \left(\frac{\partial q_T}{\partial t} \right)_{\text{auto}} + \left(\frac{\partial q_T}{\partial t} \right)_{\text{evap}} \tag{5.7}$$

$$\frac{\partial q_{prec}}{\partial t} = -\frac{1}{\overline{\rho}} \nabla \cdot \left(\overline{\rho} q_{prec} \mathbf{v} + \mathbf{F}_{prec} \right) + \left(\frac{\partial q_{prec}}{\partial t} \right)_{\text{accr}} + \left(\frac{\partial q_{prec}}{\partial t} \right)_{\text{auto}} \tag{5.8}$$

$$\frac{\partial q_r}{\partial t} = -\frac{1}{\overline{\rho}} \nabla \cdot \left(\overline{\rho} q_r \mathbf{v} + \mathbf{F}_{qr} - P_r \mathbf{k} \right) - \left(\frac{\partial q_{prec}}{\partial t} \right)_{\text{accr}} - \left(\frac{\partial q_{prec}}{\partial t} \right)_{\text{auto}} - \left(\frac{\partial q_T}{\partial t} \right)_{\text{evap}} \tag{5.9}$$

where $\mathbf{F}_i$ are the subgrid scale scalar fluxes, P_r is the rain precipitation flux, subscripts accr and auto refer to tendencies due to accretion and autoconversion of water droplets by rain, while the subscript evap denotes tendencies due to rain evaporation. The variable q_T is the total non-precipitating water, such that $q_T = q_v + q_c$, where q_c is the cloud water. It is assumed that all water in excess of 100% RH condenses, from which q_v can be diagnosed. Given the dependence of h on q_v, latent heating due to condensation depends exclusively on q_T. On the other hand, the production of rain in (5.9) depends on q_{prec}, which will allow the specification of environments with different latent instability profiles (i.e. different q_T), but with identical potential for producing rain (i.e. identical q_{prec}). The tendencies due to microphysics in (5.7) are computed as in Khairoutdinov and Randall (2003), and similarly for tendencies in (5.8), except that the latter are only allowed where $0 < q_c$.

An additional feature of this microphysical formulation is that rain evaporation, which is the only microphysical process for the development of the cold pool, is calculated with respect to q_T in (5.7), not q_{prec}. Therefore, drier environments will potentially lead to stronger cold pools. It will be shown that by using the present framework, simulations in different thermodynamic environments produce similar c for a given ΔU, which partly results from shallower cold pools being produced in drier environments.

The simulations considered herein are two-dimensional. They were carried out for 5 hours with a 5 s time step, being initialized using the horizontal wind convergence method described in chapter 3. The horizontal domain extends 1536 km, with 500 m grid spacing, while vertically it reaches up to 30 km through 96 levels with variable spacing, this being 100 m near the surface and gradually increasing up to 400 m at 5000 m height, above which it stays constant. Newtonian damping is applied to prognostic variables in the upper third portion of the domain. Subgrid-scale (SGS) processes are accounted for by a first order Smagorinsky closure model, and the lower boundary condition is free slip, with all surface fluxes, Coriolis effects, and radiative heat fluxes being neglected.

b. Kinematic and thermodynamic environments

The environments considered herein are derived from a *baseline* sounding which is identical to that considered in chapter 3. Variations from this sounding are accomplished by changing the initial distribution of q_v while leaving temperatures unchanged, which leads to the CAPE profiles displayed in Fig. 5.6 (note that, for these environments which have identical T, a

larger CAPE at any given level implies a greater q_v). In analogy to the nomenclature used in chapter 3, the soundings considered herein, listed in increasing order of ICAPE, are referred to as *shallow*, *deep*, and *high*. Fig. 5.6 shows that *shallow*, *deep*, and *baseline* have identical CAPE below 900 hPa, while the *deep* sounding is identical to *high* above 875 hPa. Fig. 5.7 displays the *h* of *shallow*, *baseline*, and *high* (*deep* is omitted for readability, which has the same *h* profile as *baseline* below 900 hPa, being identical to *high* above 875 hPa). Another sounding, which is referred to as *stable*, is identical to *baseline* above 500 hPa, and has *baseline*'s CAPE profile, but with greater mid-tropospheric temperatures, and relatively small temperature lapse rate at low-tropospheric levels. These differences are apparent in the saturated moist static energies (h^*) of *baseline* and *stable*, shown in Fig. 5.7. The *h* of *stable*, which is omitted from Fig. 5.7 for readability, is very similar to that of *baseline*. The *stable* environment was designed in such a way that it leads to *c* that is similar to *baseline*'s, so that it will allow an investigation into the effects of varying the buoyancy profile within the cold pool. The initial q_{prec} used in the present simulations corresponds to the q_v of *high*.

The environmental winds which will be used for the present simulations are displayed in Fig. 5.8. Constant and non-zero shear is present below 2.5 km, with $\Delta U = 8$ m s^{-1}, $\Delta U = 12$ m s^{-1}, and $\Delta U = 16$ m s^{-1}. Winds are static above 2.5 km. As in previous chapters, different simulations are referred to by the name of their thermodynamic sounding, followed by an underscore and the value of ΔU, e.g *shallow_8*, *deeper_12*, etc.

5.3 Results

a. The baseline simulations: the effect of varying ΔU

The structure of the flows simulated using the present technique is exemplified by the contour plots of Fig. 5.9, displaying temperature perturbations (Figs. 5.9a and 5.9d), horizontal winds relative to the cold pool edge (Figs. 5.9b and 5.9e), and pressure perturbations (Figs. 5.9c and 5.9f) corresponding to the *baseline_12* simulation. Figs. 5.9a - 5.9c correspond to fields at 2.5 h of simulation time, and Figs. 5.9d - 5.9f are time averages computed from model output every 2 min between 2.25 h and 2.75 h (the fields used for averaging are translated in the *x* direction in such a way that they have coincident cold pool edges). It is worth highlighting that after 2 h, the previously described time averages are nearly steady. The flow is qualitatively similar to the SL simulations of chapter 3, with positive upper-tropospheric temperature perturbations and a well-defined cold pool shown in Figs. 5.9a and 5.9d. The RIJ and the FTRF are also evident in Figs. 5.9b and 5.9e, as well as the mid-tropospheric meso-low and the positive pressure perturbations near the surface in Figs. 5.9c and 5.9f. It is important to bear in mind that the flows considered herein do not develop realistic stratiform regions, due in part to the neglect of ice processes (e.g. see Yang and Houze 1995), and also because of the use of a first order microphysics scheme (Morrison et al. 2009). Recall that it is not the intention of this section to simulate realistic SLs, but rather to simulate flows with simplified microphysics that bear resemblance to SLs, and which will facilitate an analysis of the effects of shear and latent heating on the characteristics of updrafts.

The results presented hereafter correspond to time averaged variables computed as Figs 5.9d – 5.9f, unless otherwise stated. The averaging smoothens the fields in a manner that is analogous to the along-line averages presented in chapters 3 and 4. For the subsequent discussion it will be useful to consider the time averaged horizontal momentum equation neglecting SGS fluxes,

$$\underbrace{\frac{\partial \overline{u}}{\partial t}}_{\text{A}} = \underbrace{-\frac{\partial \overline{u}\,\overline{u}}{\partial x}}_{\text{B}} \underbrace{-\frac{\partial\left(\rho \overline{u}\,\overline{w}\right)}{\rho \partial z}}_{\text{C}} \underbrace{-\frac{\partial u'u'}{\partial x}}_{\text{D}} \underbrace{-\frac{\partial\left(\rho u'w'\right)}{\rho \partial z}}_{\text{E}} \underbrace{-\frac{\partial \overline{p}}{\rho \partial x}}_{\text{F}} \tag{5.10}$$

where $u = \overline{u} + u'$ and $\overline{u} = \int_{\tau} u dt$, τ being the time period of averaging, and similarly for w and p. Fig. 5.10 displays contour plots of some of these terms derived from *baseline_12*. Term A is the tendency of the time averaged horizontal wind, which is small relative to other terms for the .5 h averages considered herein (not shown), and will not be further discussed. Terms B and C are the horizontal and vertical time averaged momentum flux divergences, respectively. Their combined effect on the momentum equation is displayed in Fig. 5.10a, showing that they contribute to increase $\overline{u}$ at the cold pool edge and, to a lesser degree, above the cold pool (between 2 km and 4 km height), while they contribute to decrease $\overline{u}$ at upper-tropospheric levels. It is worth mentioning that, for the flows considered herein, there is considerable cancellation between terms B and C, which is in agreement with results from Fovell and Ogura (1988). For example, compare Fig. 5.10a, which shows B + C, with Fig. 5.10b, which displays term C. Terms D and E are the horizontal and vertical transient momentum flux divergences, respectively. The contribution of these terms, in addition to SGS fluxes, is small, as shown in Fig. 5.10c, and they will not be further discussed in this study. Finally, term F is the pressure force, shown in Fig. 5.10d, and which nearly counters the combined effects of terms B and C. This latter term, which has a dynamic and a buoyancy component (e.g. see 5.6), is dominated by dynamically induced contributions, as those discussed in association with the thermal rising from a chimney.

Some insights regarding the effects of shear on the structure of the *baseline* flows can be gained by comparing Figs. 5.11 and 5.12, which show contour plots of different fields corresponding to *baseline_8* and *baseline_16*, respectively. The horizontal winds in Figs. 5.11a and 5.12a give a good indication of updraft verticality, as the updraft axis is nearly coincident with the axis of minimum horizontal winds. Considering also the horizontal winds of *baseline_12* in Fig. 5.9e, the systematic variation of the updraft tilt with changes in ΔU becomes apparent, such that greater ΔU leads to more vertical updrafts. The cold pool-shear balance of *baseline_8*, *baseline_12*, and *baseline_16*, as measured by CPSB = c / ΔU (e.g. Weisman and Rotunno 2004), is respectively 2.8, 2, and 1.5, so that greater RKW-optimality corresponds to more vertically oriented updrafts. In addition, notice the distinction between the wind fields ahead of the system, such that inflowing winds in the more optimal *baseline_16* simulation are mostly concentrated at low levels, while there is considerable system relative inflow throughout the lower and mid-troposphere in the *baseline_8* simulation. This, in association with the discussion in the previous section on updraft verticality and system relative winds aloft, suggests that CPSB does constrain environmental winds, such that more optimal configurations have less inflow at mid and levels.

Another feature of interest is that the RIJ, which is relatively intense and remains elevated near the cold pool edge of *baseline_16*, as opposed to the RIJ of *baseline_8*, which is weaker and progressively descends to the surface, as is described by Weisman (1992). These structural differences occur in association with variations in p'_{dyn}, as shown in Figs. 5.11b and 5.12b. Maximum pressure perturbations occur in the vicinity of the cold pool edge, with greater amplitude in *baseline_16* than in *baseline_8*. Horizontal wind convergence near the cold pool edge contributes to this feature, but in *baseline_16* it is also partly driven by vertical wind convergence of downdrafts encountering the rigid surface. Thus, this p'_{dyn} maximum manifests the conversion

of vertical momentum to the horizontal in *baseline_16*, as evinced by the divergence of horizontal winds behind the cold pool edge in Fig. 5.12a. The p'_{dyn} component of the pressure perturbation is much greater in amplitude than p'_b near the cold pool edge, the latter being displayed in Figs. 5.11c and 5.12c, which is indicative of the fact that the PS may be substantially affected by non-hydrostatic factors, in agreement with results by Mahoney et al. (2009).

By comparing the contribution of B + C from equation (5.10) corresponding to *baseline_8* and *baseline_12*, shown in Figs. 5.11d and 5.10a, respectively, it can be appreciated that their effect is diminished in amplitude for the weakly sheared environment; on the other hand, the same field corresponding to *baseline_16*, displayed in Fig. 5.12d, shows that a stronger shear leads to a pattern tending to increase $\bar{u}$ which is more elevated and of greater amplitude at mid-levels, also with an enhanced tendency to decrease $\bar{u}$ in the upper-troposphere. It is interesting to note that in the simulations under consideration, the contribution of B + C at mid-levels tending to increase $\bar{u}$ is collocated with the region of negative system-relative horizontal winds. Given that the updrafts considered herein tilt upshear, it is reasonable to interpret B + C as a component of (5.10) contributing to increase the verticality of the updraft. This motivates a more detailed discussion about B + C.

Even though the present analysis does not allow a causal attribution of the differences in B + C produced by the *baseline* simulations, it is worth highlighting that their contribution to updraft verticality at mid-levels results primarily from term C being of greater amplitude than B in regions where both terms have opposite sign. In other words, for the simulations considered herein, the positive $\bar{u}$ tendency due to B + C has the same sign therein as C, and opposite sign to that B. Thus, the aforementioned increase in B + C with the strengthening of the shear occurs in association with a systematic change in amplitude of the vertical flux divergence (i.e. C) relative to the amplitude of horizontal flux divergence (i.e. B). Term C corresponding to *baseline_8* and *baseline_16* is presented in Figs. 5.11e and 5.12e, respectively, showing that ΔU impacts substantially on the amplitude of the momentum flux divergences. But by the foregoing arguments, C is enhanced more than B as the shear strengthens, which probably results, at least in part, from the increase in vertical wind speed in more RKW-optimal simulations. The next subsection will investigate whether latent instability, which also affects the vertical wind speed within the updraft, produces similar effects on the structure of the simulated flows.

Before proceeding to the next subsection, note that in Fig. 5.12d it can be appreciated that B + C in *baseline_16* contribute to decrease $\bar{u}$ just ahead of the cold pool edge, a feature that is not evident in the B + C of *baseline_8* and *baseline_12* (Figs. 5.11d and 5.10a). This feature is discussed due to its relation to the PS. The tendency to increase $\bar{u}$ near the surface in *baseline_8* and *baseline_12* results mainly from term C, while the tendency of opposite sign in *baseline_16* is associated to B, i.e. horizontal momentum flux divergence. Differences in B ahead of the cold pool edge are related to the PS of the system, such that the environmental surface winds relative to the cold pool edge increase and are more strongly convergent as ΔU strengthens, which is a well-known effect of shear on the structure of SLs (e.g. see Fovell and Ogura 1989). In analogy to the density currents in Figs. 5.1 and 5.2, a greater $u_R^2(0)$ is associated with a greater surface pressure perturbation at the cold pool edge, which is consistent with the aforementioned differences in p'_{dyn} between *baseline_8* (Fig. 5.11b) and *baseline_16* (Fig. 5.12b).

b. The effect of latent instability

First it will be shown that the simulations considered herein produce varying degrees of upper-tropospheric heating, while having similar c. Scatterplots in Fig. 5.13 depict the simulations in terms of their ICAPE and their integrated upper-tropospheric buoyancies, W (Fig. 5.13a), and also in terms of their ICAPE their cold pool intensity, c (Fig. 5.13b). The definition of W is given by

$$W = \left(\frac{2}{\rho(0)} \int \rho \bar{b} dz \right)^{.5} \tag{5.11}$$

where $\bar{b}$ is the time averaged buoyancy, also averaged horizontally within 10 km of the location of maximum temperature perturbations, the integral encompassing tropospheric levels with positive buoyancy. The definition in (5.11) is similar to that of chapter 3, but it incorporates variations in ρ for estimating the effects of buoyancy aloft on the hydrostatic surface pressure perturbation. The cold pool intensity, c, is calculated analogously, with the time averaged buoyancy also averaged horizontally within 10 km of the maximum pointwise cold pool intensity, the latter referring to the cold pool intensity without any horizontal averaging. It is worth mentioning that the simulations considered herein display considerable horizontal variations in the pointwise cold pool intensity, as shown in Fig. 5.14. It is not obvious how to objectively define c in a manner that is most appropriate for assessing cold pool-shear balance, a matter that is not further discussed herein. Note in Fig. 5.13a the large inter-case variation in W produced by the different simulations, in contrast to the relatively small differences in c as depicted in Fig. 5.13b. These results are indicative of the suitability of the present framework for addressing the effects of latent heating on the PS and cold pool-shear balance for various ΔU.

Recalling that positive upper-tropospheric buoyancies could reduce the PS, it might be reasonable to expect *high* and *deep* to propagate slower than *shallow*. Fig. 5.15 displays the propagation of the cold pool edge with respect to its position at t = 1 h, in a horizontal frame of reference with -12 m s^{-1} environmental surface winds. This frame of reference was chosen in order to make the differences between the propagation of the storms more evident. Note that in this frame of reference the propagation speed can be interpreted as $-u_R(0)$ + 12 m s^{-1}, in analogy with equation (5.1), in which surface winds are relative to the cold pool edge. Even though *high* and *deep* propagate at a slightly slower speed than *shallow*, there is not a clear indication in Fig. 5.15 that latent heating effects impact substantially on the PS of the simulated flows. On the other hand, it is apparent that greater ΔU leads to higher PS, in spite of the fact that stronger shear leads to greater W (see Fig. 5.13a). These results indicate that the upper-tropospheric heating plays a limited role in modulating the PS, while the impacts of varying ΔU are greater. The amplitude of ΔU modulates the speed of the RIJ winds relative to the cold pool edge (e.g. compare Figs. 5.11a and 5.12a), and the vertical transport of momentum is probably the main contributor to differences in PS (e.g. Mahoney et al. 2009).

Fig. 5.16 shows the horizontal wind field corresponding to the ΔU = 12 simulations, evincing the impacts of latent heating on the structure of the updraft. The similarity between the wind fields in *baseline_8*, shown in Fig. 5.11a, and those of *shallow_12* (Fig. 5.16a) is remarkable, especially given that the latter produced a slightly weaker the cold pool than the former, leading to considerable differences in CPSB: 2.75 in the case of *baseline_8*, and 1.8 in the case of *shallow_12*. It is worth mentioning that the 1.8 CPSB produced by *shallow_12* is very close to the 1.5-1 range wherein WR04 simulated optimal flows. Furthermore, the wind fields of *deep_12* (Fig. 5.16d) and *high_12* (Fig. 5.16e) bear closer resemblance to the wind fields of *baseline_16* (Fig.

5.12a) than to those of *baseline_12* (Fig. 5.9e), in spite of the fact that *baseline_12*, *deep_12*, and *high_12* produced CPSB ≈ 2, while the CPSB of *baseline_16* is 1.5. These results confirm that the latent instability properties of air throughout the atmospheric column can drastically affect the structure of updrafts, to an extent that renders CPSB of little practical use as a diagnostic for updraft verticality.

To further expose the effects of latent instability, Fig. 5.17 shows contour plots of B + C from (5.10). Once again, the fields produced by *shallow_12* (Fig. 5.17a) are similar to those produced by *baseline_8* (Fig. 5.11d), and similarly when comparing the fields produced by *deep_12* (Fig. 5.17d) and *high_12* (Fig. 5.17e) to those in *baseline_16* (Fig. 5.12d). This implies that latent instability plays a crucial role determining the vertical transport of momentum. In fact, it is difficult to determine the extent to which CPSB by itself determines the verticality of updrafts in the upshear tilted systems considered herein, even when the environmental thermodynamics are held fixed. This is so because a stronger shear produces a greater fraction of inflowing latent unstable air among the total storm relative inflow (e.g. see chapter 3), implying that the thermodynamic and kinematic environmental characteristics which are relevant in terms of updraft verticality are intimately coupled, and difficult to separate. Indeed, Fig. 5.13 shows that the W produced by *baseline_16* is greater than that produced by *baseline_12*, and similar in amplitude to the values found in *deep_12* and *high_12*.

Regarding the effects of ΔU on the different thermodynamic environments, in all cases a stronger shear leads to more vertically oriented updrafts, an enhancement of the vertical momentum transport, and an enhancement of p'_{dyn} near the cold pool edge. This is consistent with the analysis corresponding to the *baseline* simulations in the previous subsection, and it agrees with previous studies showing how ΔU affects the structure of SLs (e.g. RKW88; Weisman et al. 1988; Fovell and Ogura 1989; WR04; Bryan et al. 2006). Nonetheless, CPSB by itself does not constitute an accurate diagnostic of the morphology of the simulations considered herein. For example, Fig. 5.18 shows the horizontal wind field of *shallow_16* (Fig. 5.18a) and *high_8* (Fig. 5.18b). Although the former does have a slightly more vertical updraft, this difference is small compared to that between *baseline_8* (Fig. 5.18c) and *baseline_16* (Fig. 5.18d). This is so despite the fact that the difference in CPSB between *shallow_16* and *high_16* is 1.2, even larger than the difference between the CPSB of *baseline_8* and that of *baseline_16*. On the other hand, the simulations considered herein suggest that the CPSB does constrain the environmental winds aloft. Note in Fig. 5.18 that in the more optimal cases, i.e. *shallow_16* (5.18b) and *baseline_16* (5.18d), inflowing winds are concentrated near the surface, while in *high_8* (Fig. 5.18a) and *baseline_8* (Fig. 5.18c) there is considerable inflow of air throughout the lowermost 7 km.

Particle trajectories of *shallow_12*, *baseline_12*, and *high_12* are shown in Fig. 5.19, corroborating the effects of latent instability on the development of deep reaching and vertically oriented updrafts. These particles are computed using the Lagrangian particle tracking algorithm of Yamaguchi and Randall (2012). Particles were placed at 2 h of simulation time, 350 m above the surface, with 4 km spacing in the x direction. Trajectories are more vertical and reach deeper in cases with greater ICAPE, despite similar CPSB. In fact, among the simulations displayed in Fig. 5.19, *shallow_12* is the most optimal in terms of CPSB, in spite of which it develops the weakest and least vertical updraft. This result is consistent with the trajectories shown in Fig. 5.5. It is an interesting finding that, in terms of the trajectories follows by Lagrangian particles, the effects of enhancing ICAPE are similar to the effects of increasing ΔU.

Before proceeding to the discussion section, it is worth mentioning that the *stable* simulations did not produce a substantially lower PS than the other cases, contrasting with the findings in chapter 3. One characteristic of the *stable* simulations considered in this chapter, which is not sheared by the *stable* simulations of chapter 3, is related to the relatively strong perturbations produced throughout the low and mid-troposphere ahead of the cold pool edge. For example, Fig. 5.15 shows that the horizontal winds ahead of *stable_12* differ from those with varying thermodynamic environments, being manifested as a reduction of the shear. An additional possibility has to do with the microphysics scheme. The first order scheme used herein produces very intense cold pools near the system edge. In contrast, the double moment scheme used for the simulations in chapter 3 does not produce such strong RIJ winds or cold pool intensities near the system's edge (e.g. see Morrison et al. 2009). The effects of the vertical distribution of buoyancy within the cold pool on the structure of convection in SLs require further investigation.

5.4 Discussion

RKW theory has been at the center of many scientific debates, as recounted by WR04 and Bryan et al. (2006). To place the results presented herein into perspective, a review of related studies is given in this discussion. Starting with studies pertaining to density current flows, Xu (1992), Xu and Moncrieff (1994), Xue et al. (1997), among others, highlight the importance of the flow force balance constraint for determining the structure of density current flows in a confined channel, a matter that is not incorporated in the analysis of RKW88. Those studies found that enhanced shear leads to deeper density currents, which could lift air further aloft, thus facilitating the triggering of convective cells. A more recent study by Bryan and Rotunno (2014) shows the existence of optimal density current flows, i.e. cases with a vertically oriented jet, in which the depth of the density current does not constrain the height up to which air is lifted. Their analyses contemplate the possibility of the separation between the surface streamline and the cold pool interface, while also incorporating the flow force balance constraint. It is important to mention that none of the flow configurations with $\Delta U \neq c$ considered in Bryan and Rotunno (2014) developed a vertically oriented jet.

Other studies question whether the balance between the shear at low levels and the cold pool is enough to characterize the verticality of updrafts, and the lifting of air. For instance, Nicholls et al. (1988) note that the buoyancy generated by storms at mid and upper levels can make significant contributions to the vorticity budget in tropical SLs. Lafore and Moncrieff (1989) highlight that tropical SLs are strongly affected by the environmental shear at upper levels, while also stressing the importance of the mesoscale circulations for determining the intensity and longevity of storms. Rotunno et al. (1990) replied to the latter study by showing that the surface precipitation rates reported by Lafore and Moncrieff (1989) are consistent with the findings by RKW88; in addition, a study by Weisman (1992) included the effects of vorticity generation in the FTRF-RIJ boundary, thus incorporating the broader effects of mesoscale circulations into the vorticity balance arguments.

More recent studies by Coniglio and Stensrud (2001, 2006) suggest that, not only does the low level shear promote deep lifting of air, but that shear at upper levels can be of great importance for sustaining deep convection in SLs. In this regard, WR04, who revisit the main hypothesis and conclusion of RKW88, considered SLs simulated under various environmental wind profiles, including cases with deep shear layers, and cases with shear confined to mid and upper levels. Results from that study confirmed the importance of a balance between the strength of the low

level shear and the cold pool intensity. Nonetheless, Stensrud et al. (2005) highlight that neither the results by WR04 nor observational data fully support the contention that cold pool shear balance is the primary factor determining SL characteristics. A multi-model study by Bryan et al. (2006), which supports the importance of cold pool shear balance, showed that some of the results reported in WR04 which were subject to criticism by Stensrud et al. (2005) were affected by a bias in cold pool temperatures produced by the numerical model used in RKW88 and WR04.

The review given above, while not exhaustive of the scientific literature regarding RKW theory, is indicative of the importance and the controversy associated with this subject. While it is undisputable that the strength of the environmental shear drastically affects the morphology of SLs, it is still a matter of scientific debate whether cold pool shear-balance relations really "represent the most fundamental internal control on squall-line structure and evolution", as indicated in WR04. In this regard, the results presented herein show that, within varying thermodynamic environments, cold pool-shear balance does not by itself constitute a robust constraint on the structure of SLs with trailing stratiform precipitation. Specifically, the analyses presented in this section show that the latent instability characteristics of the environment play a fundamental role in determining the structure of SLs, such that ICAPE variations can affect simulated updrafts in a manner that resembles the effects of modifying the CPSB. Such a similarity between the effects of varying the shear and ICAPE might indicate that the verticality and intensity of upshear tilted updrafts is primarily determined by the bulk latent heating accomplished through layer-lifting convection: stronger shear, which in the present simulations corresponds to more optimal C-ΔU configurations, leads to a greater fraction of inflowing latent unstable air among the total storm relative inflow, thus producing stronger updrafts and perturbations fields of greater intensity; such effects are similar to ICAPE variations for a given ΔU. Therefore, the effects of varying the shear on storm morphology depends on the CAPE profile, as suggested by the results presented herein. These matters have not been addressed by previous investigations related to RKW theory, most of which consider the same sounding that was used by RKW88 (e.g. Weisman et al. 1988; WR04; Bryan et al. 2006).

The strong dependence of simulated SLs on the latent instability properties of the environment may have relevant implications for the observational verification of the effects of shear on the intensity of system attributes. For example, Evans and Doswell (2001) failed to find a robust relationship between the intensity of SL characteristics, such as the propagation speed, surface wind speeds, and surface precipitation rates, and the degree of estimated cold pool-shear optimality. Although this might be partly due to uncertainties associated with the estimation of the cold pool intensity (e.g. see Bryan et al. 2005; chapter 3), it may also be related to the fact that, by itself, cold pool-shear balance does not constrain the structure of SLs to the extent that has been suggested by previous numerical studies (e.g. RKW88; Weisman et al. 1988; Fovell and Ogura 1989; WR04). And while previous observational (e.g. Wyss and Emanuel 1988; Evans and Doswell 2001; Cohen et al. 2007) and numerical (e.g. Weisman 1992; Weisman 1993) studies have considered latent instability effects, their focus has been on the properties of boundary layer air. Results presented in this chapter show that this characterization of the environment is inappropriate in the context of SLs. Therefore, it is possible that, by incorporating the latent instability properties of the environment throughout the atmospheric column, observational studies might reveal the well-known effects of varying shear on the structure of SLs.

The methodology considered herein was designed so that c would not vary much among the different simulations. A relevant question that was not addressed in this chapter, and which

could provide further insights regarding the workings of RKW theory, is whether cold pool-shear balance is symmetrical in terms of the impacts of varying c, relative to the traditional approach of varying ΔU. These issues have been pondered by Bryan et al. (2006), but to my knowledge there are no studies that formally investigate this problem. One reason why SLs might not respond symmetrically cold pool-shear balance variations in c and in ΔU is related to the fact that vertical accelerations produced in association with the generation of vorticity at the cold pool edge are dependent on c: a lower c produces reduced vertical accelerations, which already implies updrafts which are diminished in strength. A framework similar to the one considered herein can be formulated so that c is systematically varied, e.g. by changing the low-tropospheric lapse rate. This will be the subject of a future study.

5.5 Summary

This chapter has analyzed some implications of the varying degrees of latent heating that can be produced by SLs in environments with different latent instability properties. Some basic characteristics of density current models were discussed, and a description of RKW theory is presented. Of particular interest to this study is the matter of whether cold pool-shear balance provides a strong constraint on the structure of SLs in environments characterized by different ICAPE. To this end, a numerical framework which produces large amounts of precipitation irrespective of the environmental ICAPE is used to simulate flows resembling SLs. This methodology facilitates the development of intense cold pools in all cases, thus allowing an analysis of simulations having similar cold pool shear balance, but with different latent instability properties.

Results show that shear strongly affects the structure of the simulated updrafts, with a stronger shear, which in the present simulations corresponds to a more RKW-optimal flow, leading to more vertical updrafts, and enhanced heating aloft. This is in agreement with results from previous studies. A relevant finding is that, for a given cold pool-shear balance configuration, variations in ICAPE affect the updrafts in a manner that resembles the effects of varying the shear strength, such that greater ICAPE leads to stronger and more vertically oriented updrafts. Further similarity between the effects of varying ICAPE and the impacts produced when the shear is changed is found in the momentum flux divergence, such that a stronger shear and a larger ICAPE lead to enhanced vertical transport of horizontal momentum. It is concluded that the degree of cold pool-shear balance does not by itself provide a strong constraint on the morphology of simulated updrafts within varying degrees of latent heating. Yet, this study has only contemplated upshear tilted systems, and RKW theory is still considered to provide a useful framework for characterizing the orientation of updrafts.

The effects of latent heating on the propagation speed of the simulated storms are weaker than the effects of shear. This is probably due to non-hydrostatic effects near the cold pool edge resulting from the vertical transport of momentum. These results suggest that there is little reason to expect systems to travel faster in higher ICAPE environments, especially given that SLs tend to develop stronger cold pools in environments with greater ICAPE. Further investigation into the effects of the low-tropospheric lapse rate on SL morphology is required in order to explain the findings in chapter 3, showing that a more dry statically stable boundary layers leads to slower PS, diminished surface wind speeds, and more vertical updrafts.

Table 5.1. Diagnostics of all simulations. ICAPE is in units of J $m^{-2} \times 10^{-6}$. See text for further details.

	ICAPE	W [m s^{-1}]			c [m s^{-1}]			CPSB		
ΔU	-	8	12	16	8	12	16	8	12	16
shallow	3.1	17.1	21.5	26.2	20.8	21	24.3	2.60	1.75	1.52
baseline	4.3	23	24.5	30	21	24	24.6	2.63	2.00	1.54
stable	4.3	26.3	24	25.6	21.7	23.7	22.8	2.71	1.98	1.43
deep	5.2	25.8	28.3	29.8	20.9	23.5	22.5	2.61	1.96	1.41
high	6.2	29.6	32	33.3	20.3	24.5	23.3	2.54	2.04	1.46

Figure 5.1. Schematic representation of a two fluid density current model in a confined channel and with shear. See text for further details.

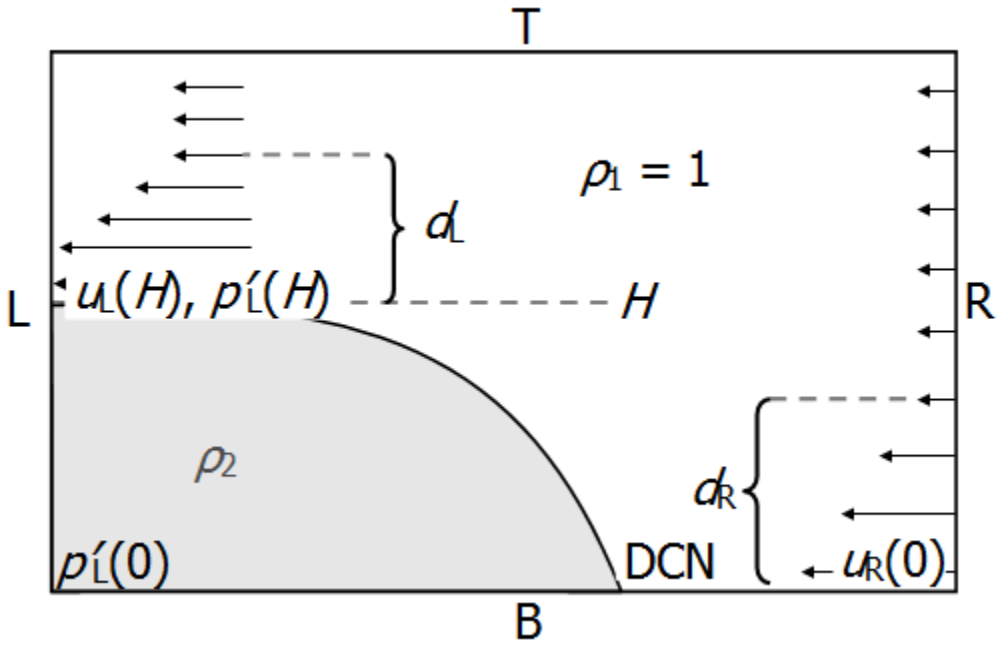

Figure 5.2. Schematic representation of a density current model including environmental stratification and latent heating effects. See text for further details.

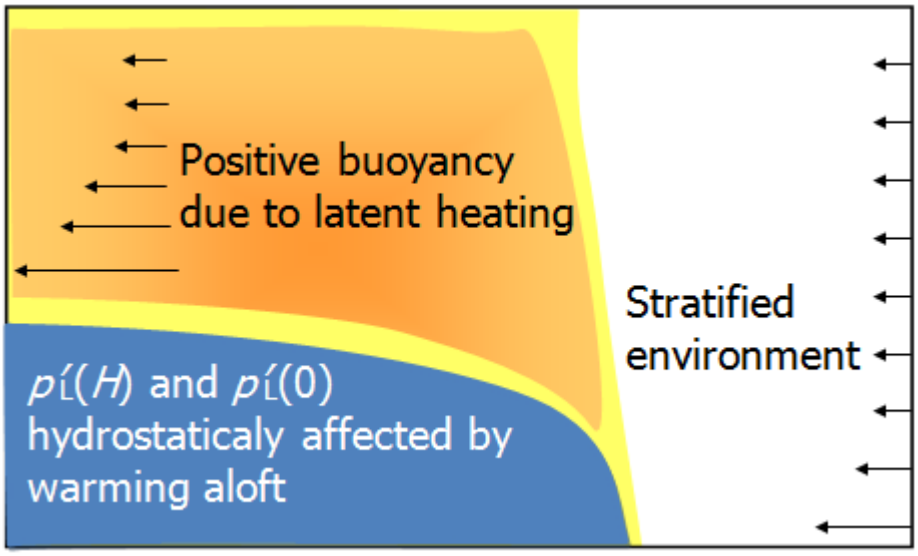

Figure 5.3. Scatter plot depicting the $\Delta U = 16$ simulations from chapter 3 in terms of their W (ordinate axis) and their c (abscissa axis).

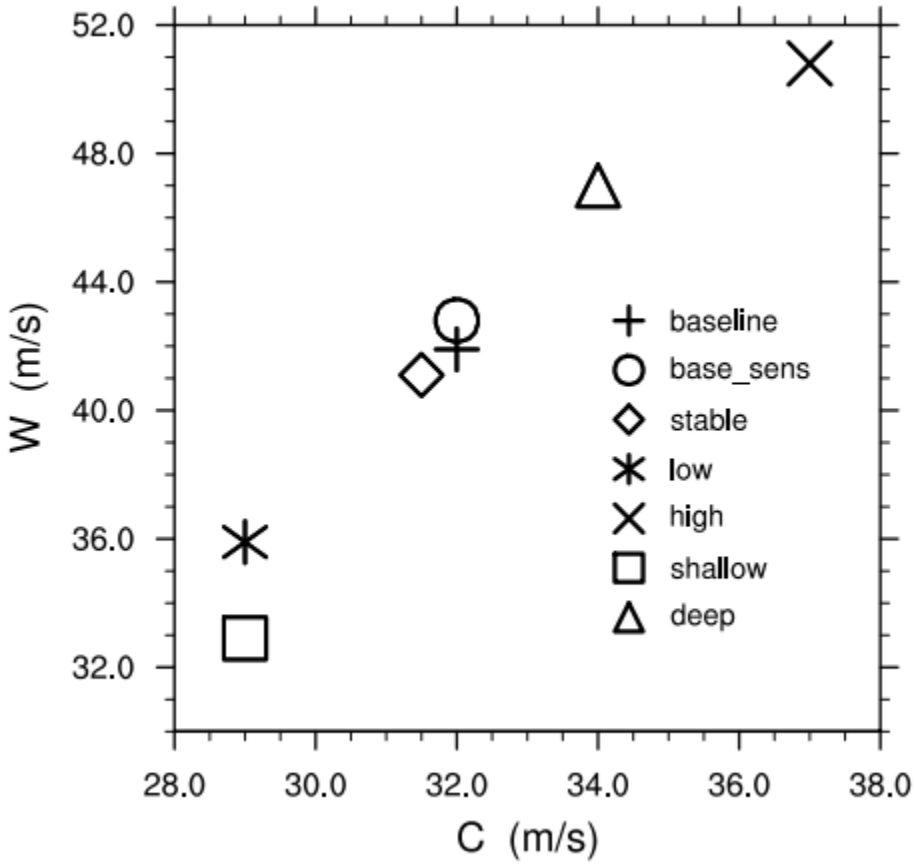

Figure 5.4. In a) the tilting of the axis of a buoyant plume of smoke in the direction of the wind velocity is depicted. In b) $\mathbf{v} \cdot \nabla \mathbf{v}$ is illustrated at different locations by the thin arrows in the case of a thermal ascending from a chimney, with horizontal winds outside the thermal blowing from right to left. The wind vectors are represented by the thick arrows, and the regions that are likely to develop positive and negative p'_{dyn} are indicated by plus and minus signs, respectively. See text for further details.

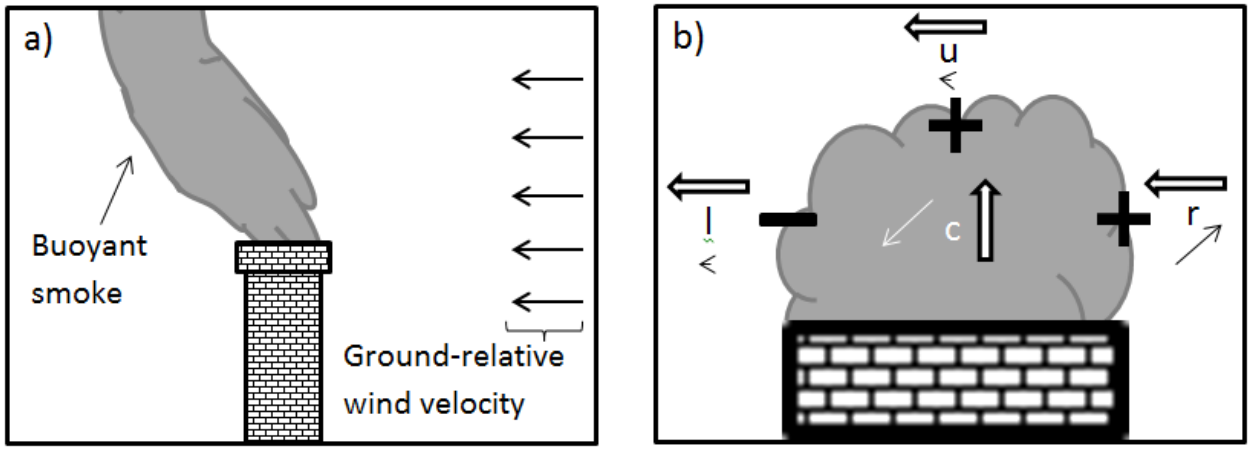

Figure 5.5. Trajectories computed as $\overline{(x(s), z(s))} = [\sum_{i \in I} (x(s), z(s))_i] / N(I)$, where $(x, z)_i$ is the *i*-th trajectory relative to the cold pool edge, *I* is a set with *N*(*I*) elements containing the indexes of particles that reached above 8 km at 5 h simulation time (deep convective partiles), and *s* is the length of the path traversed by the particle starting at $(x\ (0), z\ (0))_i$ =(5 km, 300 m).

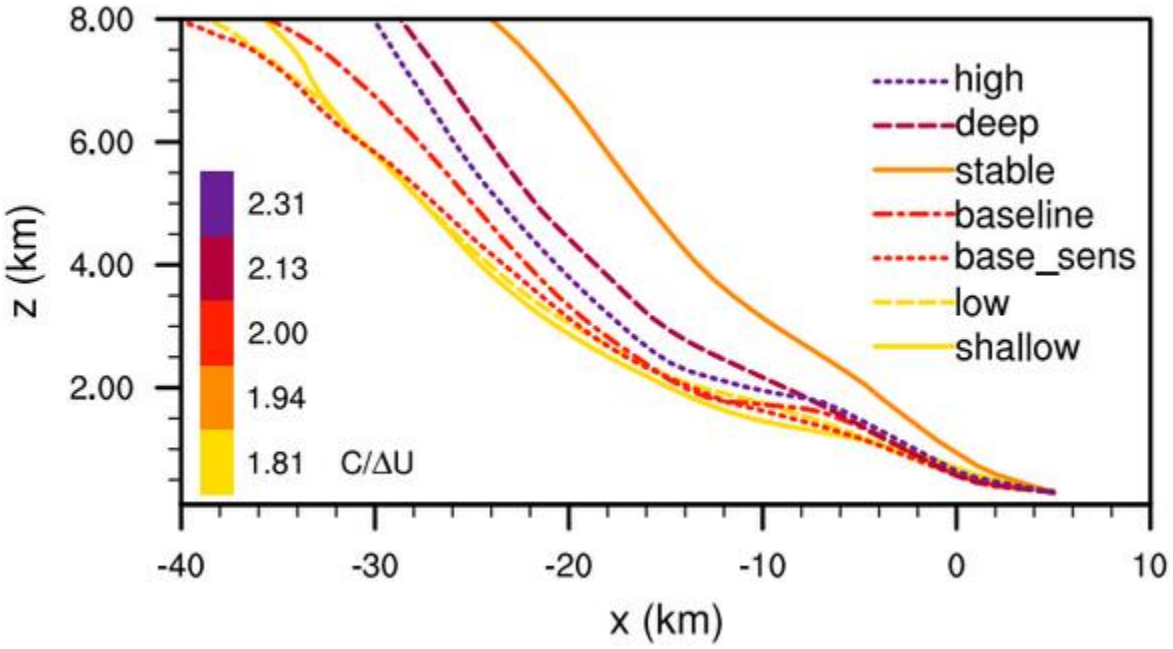

Figure 5.6. CAPE profiles corresponding to the soundings used for simulating SL-like flows.

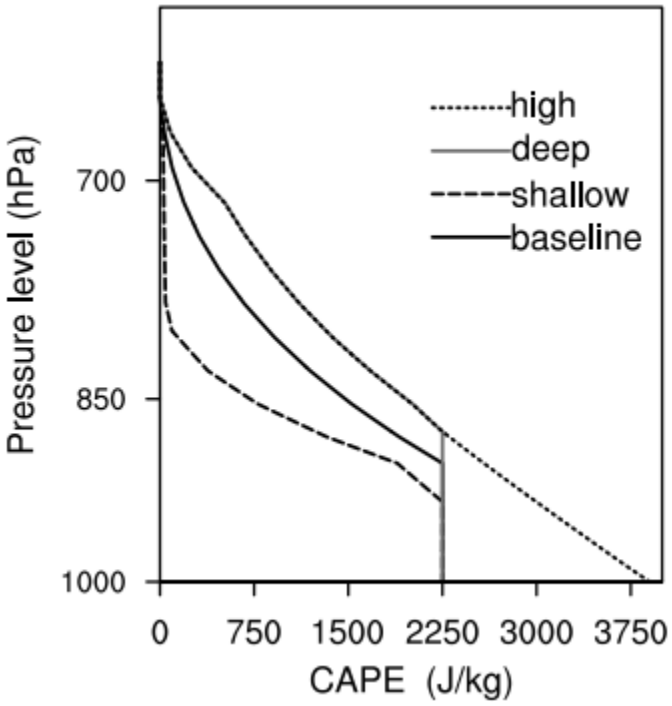

Figure 5.7. The moist static energy (*h*) and saturated moist static energy (*h**) corresponding to the different thermodynamic environments. The *h* of *stable* and *deep* are omitted for readability.

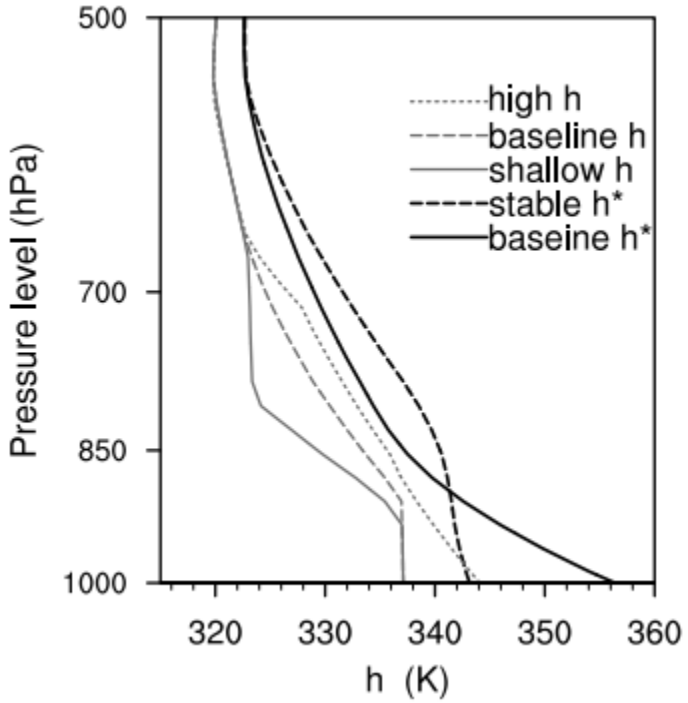

Figure 5.8. Environmental winds used for simulating SL-like flows.

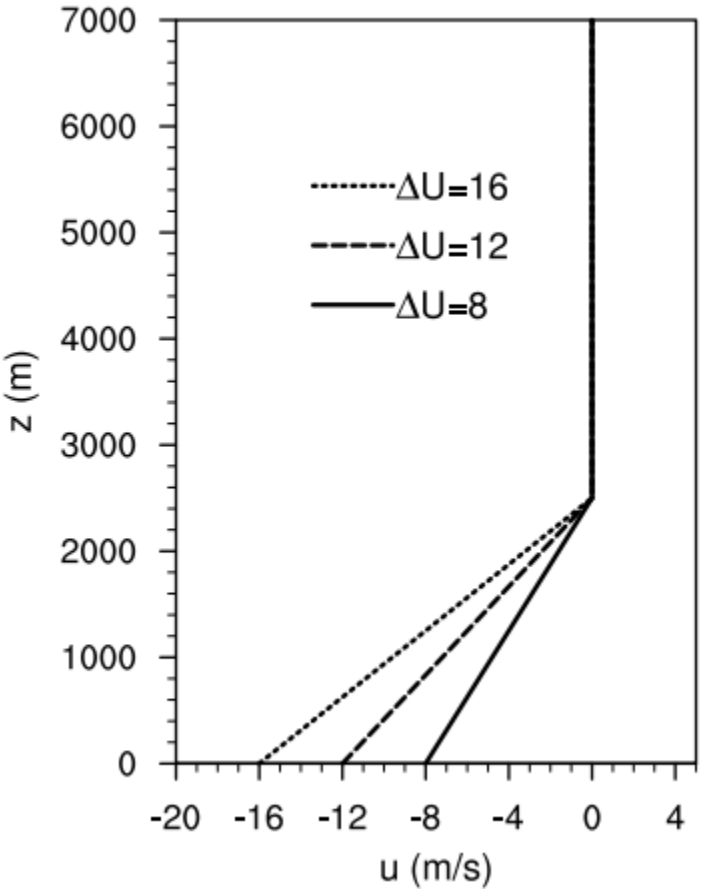

Figure 5.9. Contour plots corresponding to *baseline_12* of temperature perturbations (a and d), horizontal wind speeds relative to the cold pool edge (b and e), and pressure perturbations (c and f). Fields in a-c are snapshots at t = 2.5 h, and fields in d-f correspond to fields averaged between t = 2.25 h and t = 2.75 h.

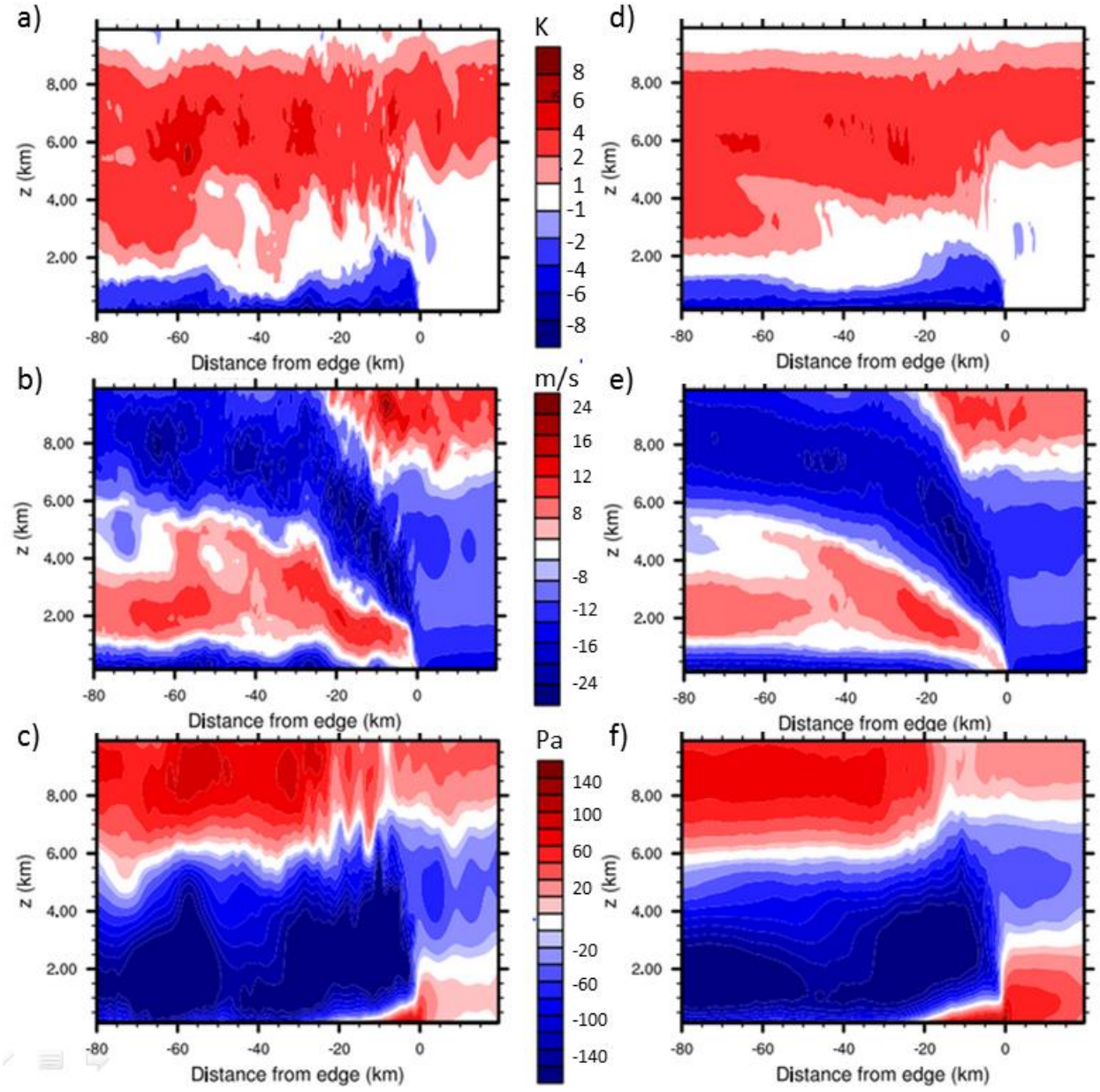

Figure 5.10. Contour plots displaying terms from equation (5.10), corresponding to *baseline_12* at 2.5 h: a) shows B + C, in b) term C is displayed, terms D + E + SGS effects are included in c), and the pressure gradient force, term F, is shown in d).

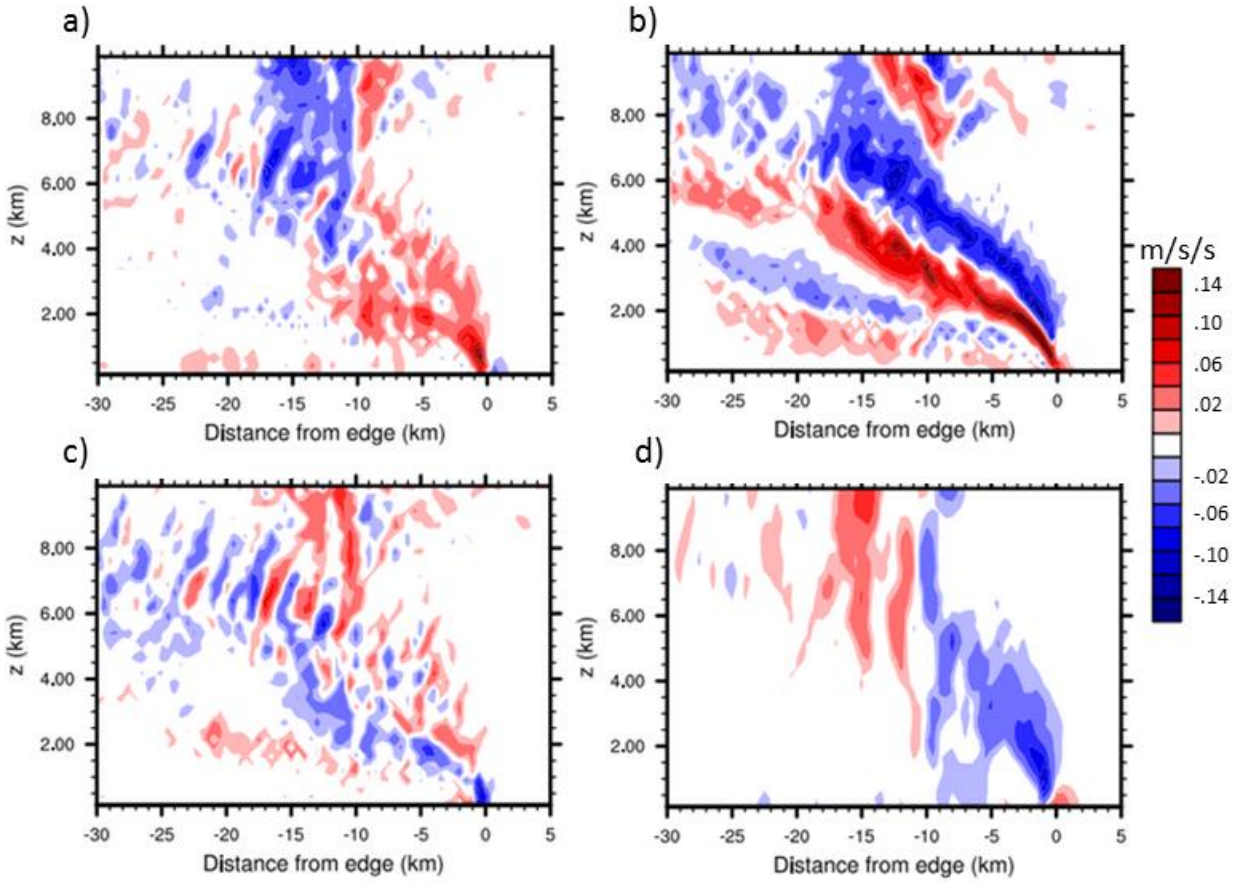

Figure 5.11. Contour plots of fields corresponding to *baseline_8* at 2.5 h. In a) the horizontal wind speed is displayed, b) and c) show p'_{dyn} and p'_{buoy}, respectively, while d) and e) display B + C and C from equation (5.10), respectively.

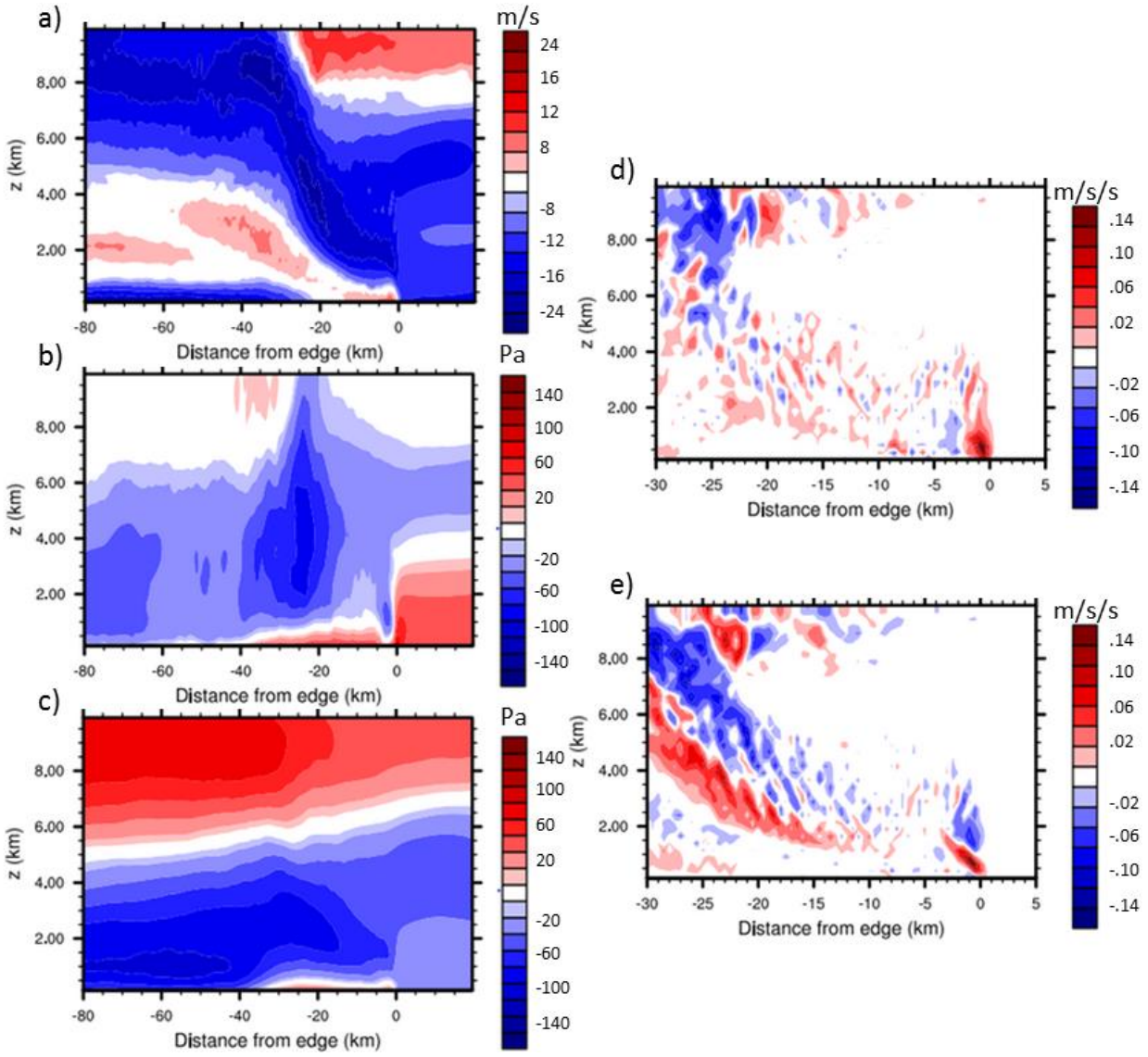

Figure 5.12. Fields as in Fig. 5.11 corresponding to *baseline_16*.

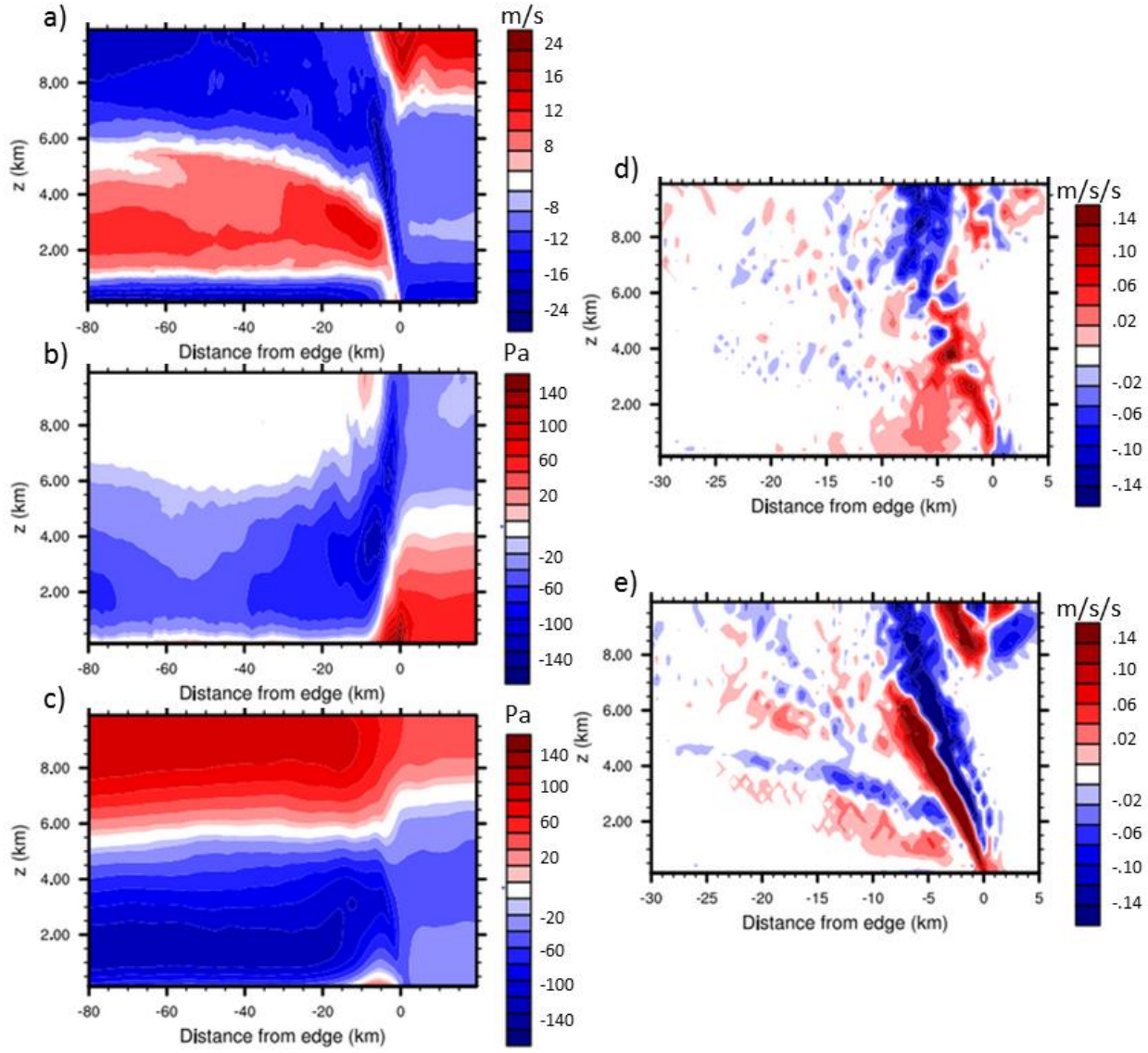

Figure 5.13. Scatter plots depicting the simulations in a plane with ICAPE in the abscissa axis, and with the ordinate axis representing a) *W* and b) *c*.

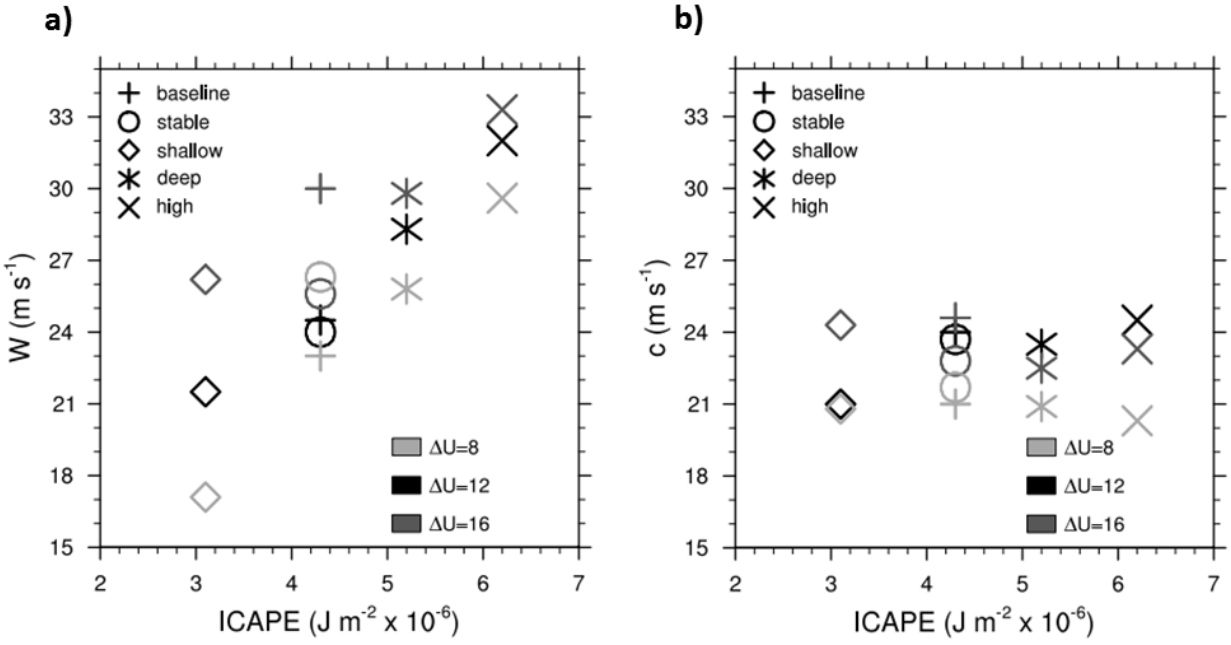

Figure 5.14. The cold pool intensity as a function of the distance from the cold pool edge for simulations with a) $\Delta U = 8$, b) $\Delta U = 12$, and c) a) $\Delta U = 16$.

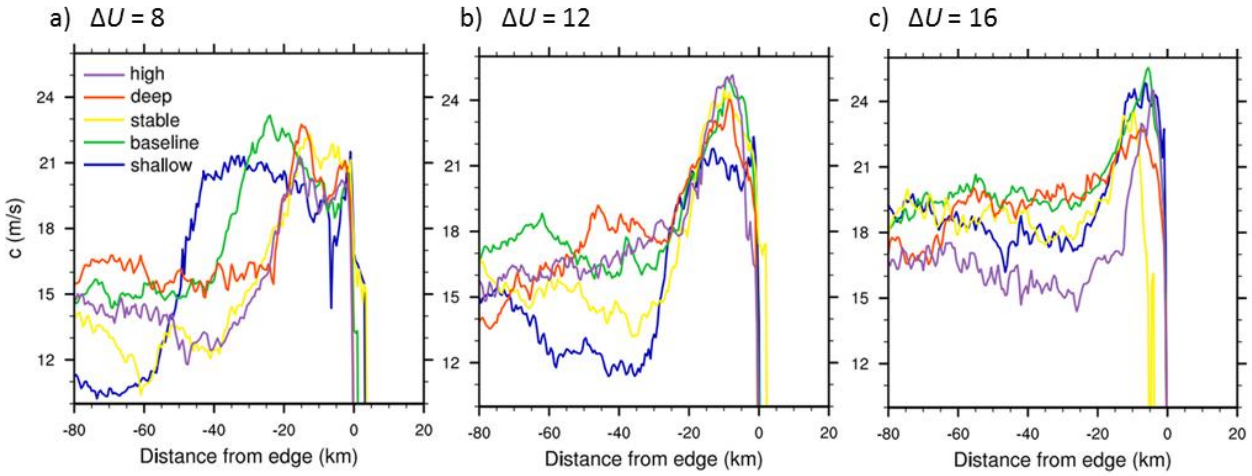

Figure 5.15. The time evolution of the position of the cold pool edge of all simulations in a frame of reference with -12 m s^{-1} environmental surface winds. The different environments can be identified by color, as indicated in the figure, with ΔU = 8 simulations represented by solid lines, ΔU = 12 by dashed lines, and ΔU = 16 by dotted lines.

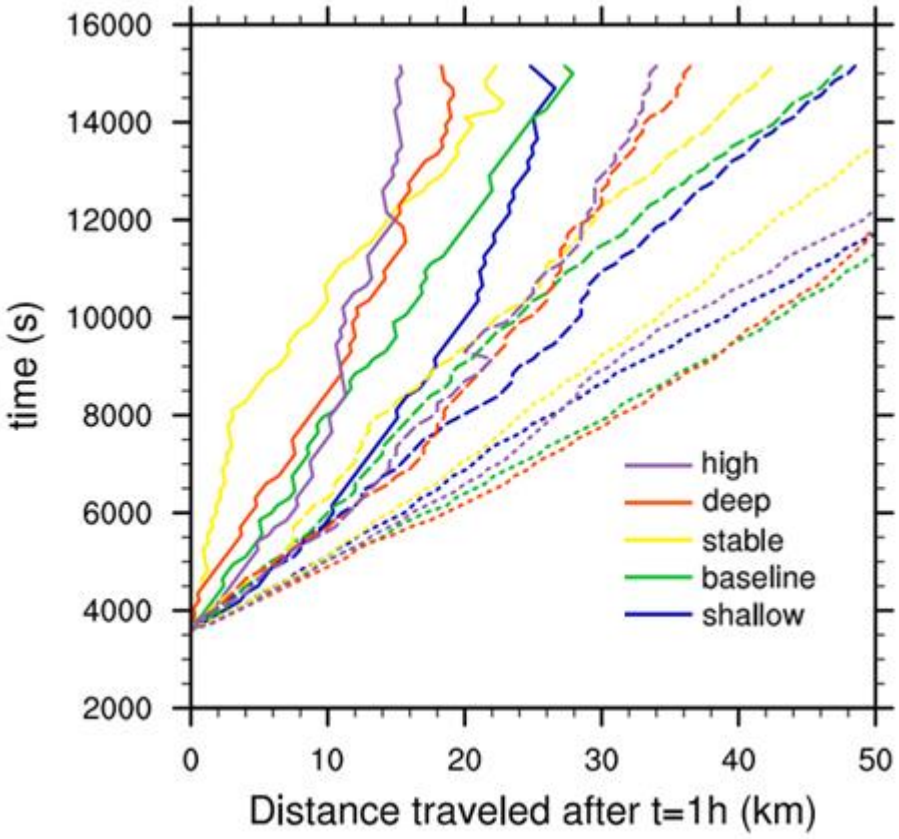

Figure 5.16. Horizontal wind fields corresponding to a) *shallow_12*, b) *baseline_12*, c) *stable_12*, d) *deep_12*, and e) *high_12*.

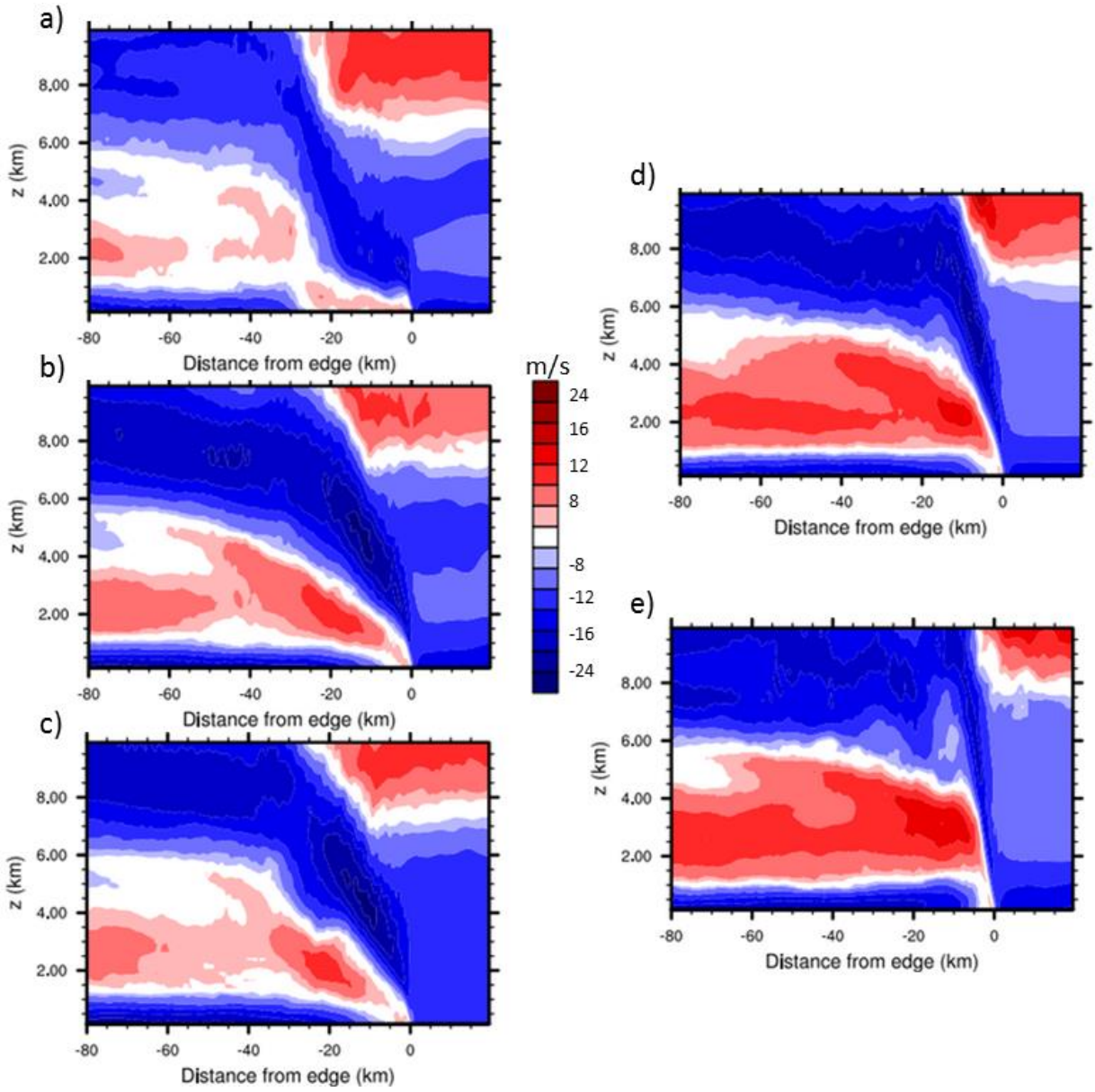

Figure 5.17. Contour plots of B + C in equation (5.10) corresponding to a) *shallow_12*, b) *baseline_12*, c) *stable_12*, d) *deep_12*, and e) *high_12*.

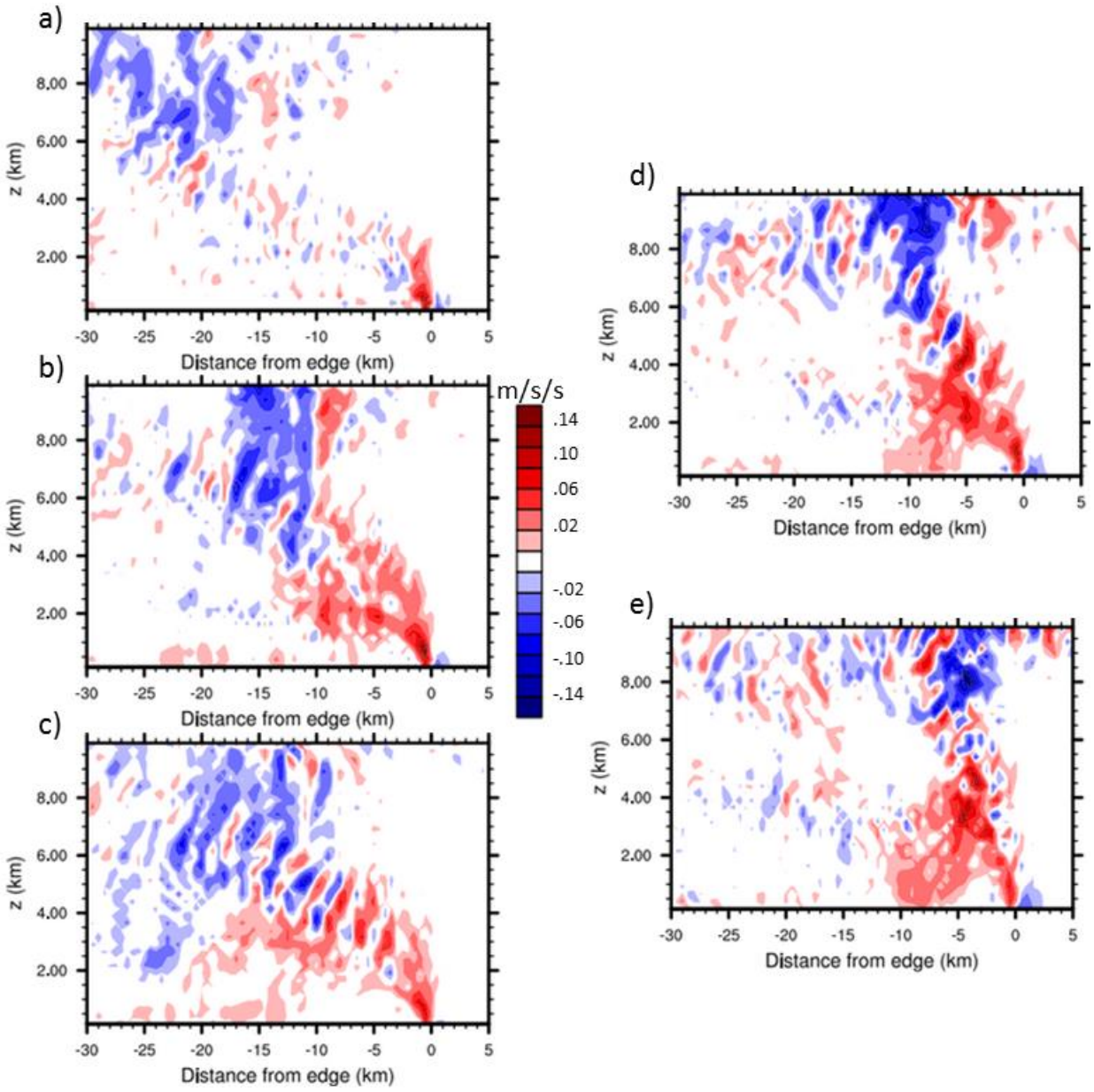

Figure 5.18. Contour plots of horizontal winds corresponding to a) *high_8*, b) *shallow_16*, c) *baseline_8*, and d) *baseline_16*.

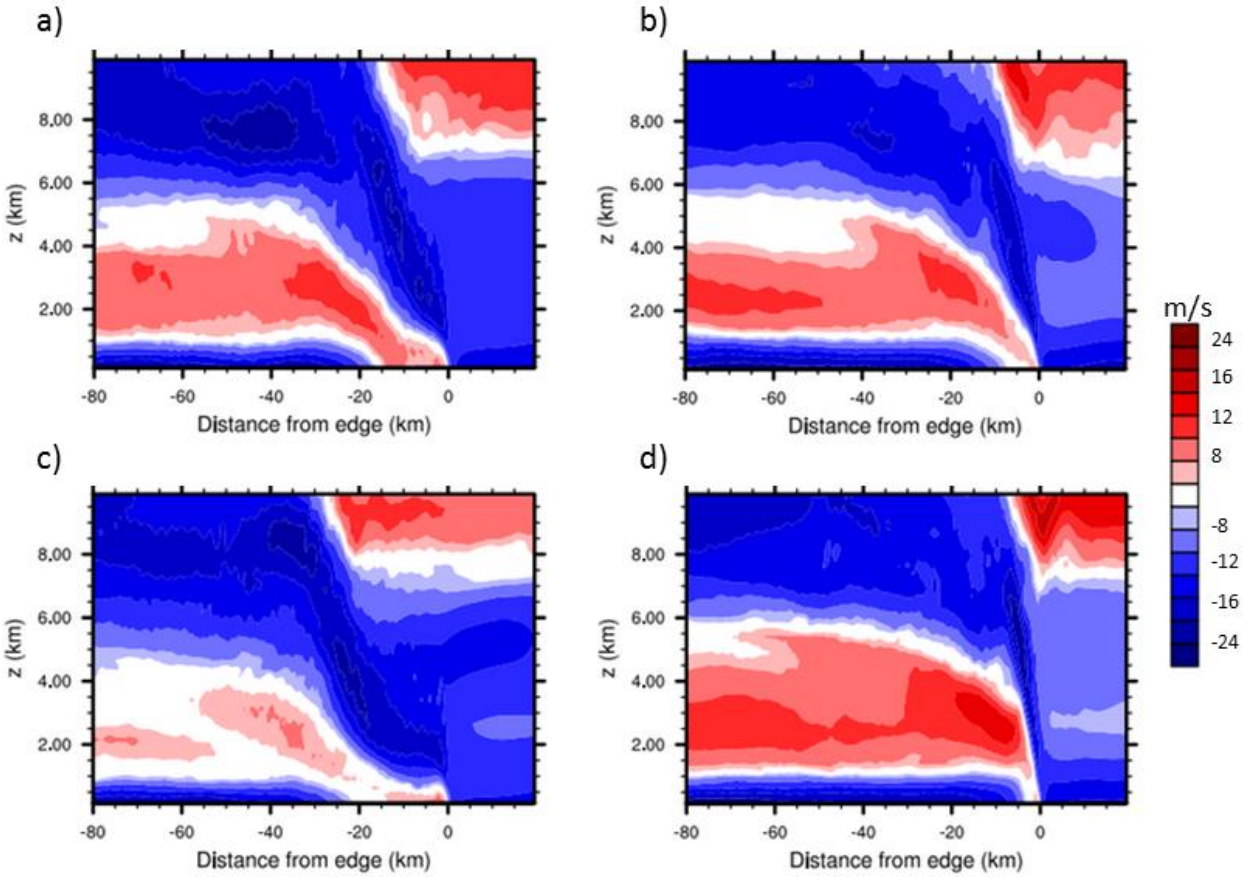

Figure 5.19. Particle trajectories computed relative to the position of the cold pool edge of a) *shallow_12*, b) *baseline_12*, and c) *high_12*, overlaid on contour plots of the horizontal wind field.

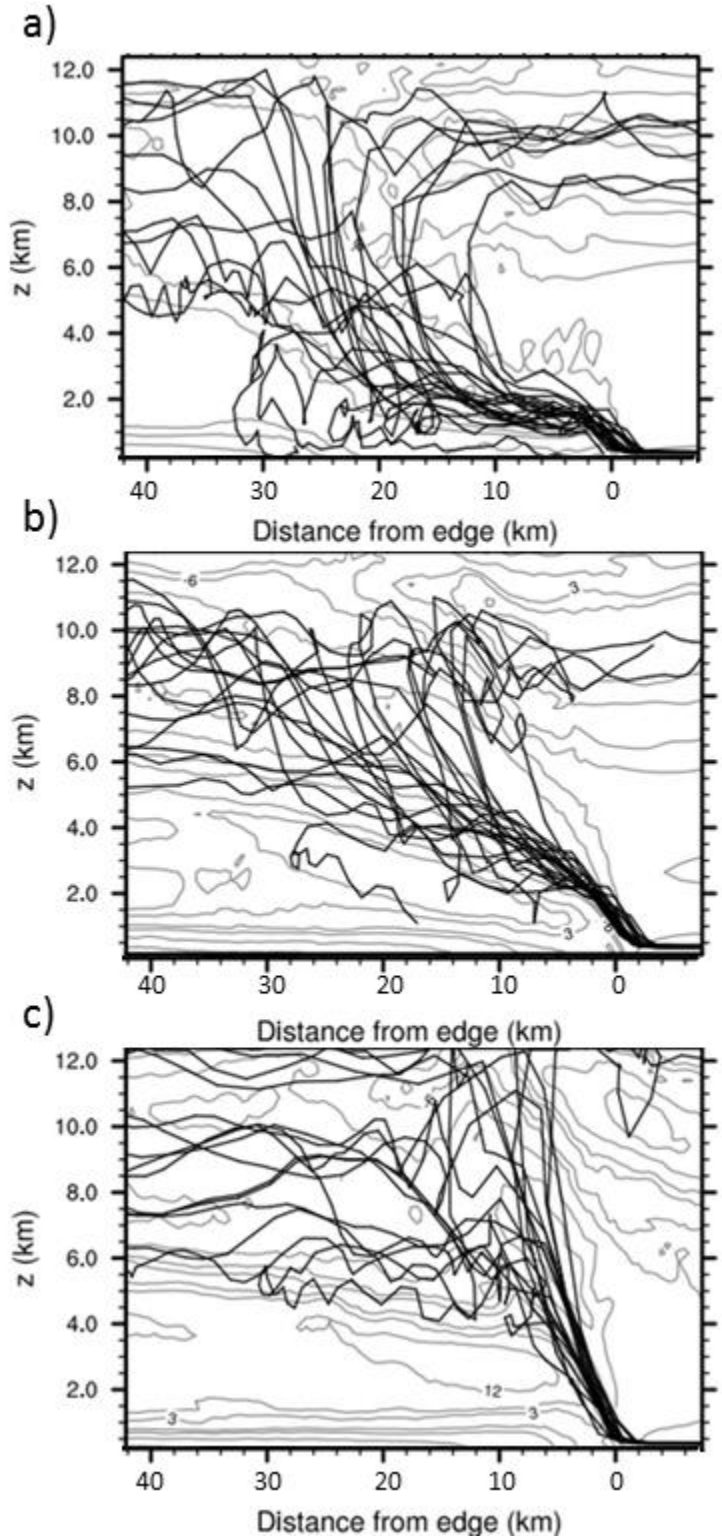

Chapter 6:

Conclusions and future work

6.1 Conclusions

This thesis presents results from an extensive investigation into the effects of latent instability on the morphology of squall lines, focusing on analyses of numerically simulated storms. The study of squall lines is motivated by their hydrological importance, being storms that interact significantly with the large scale flow, while also having the potential to produce severe weather conditions. The objective of this research is to improve our understanding of the structural dependence of squall lines on the characteristics of the environments in which they manifest. Although this is a matter that has received considerable attention in the past, it remains poorly understood, thus limiting our ability to forecast and model the effects of these storms. In particular, this work emphasizes the need of a robust conceptual framework for understanding the means by which the environmental thermodynamics constrain the characteristics of squall lines.

A framework for characterizing the thermodynamic environment is proposed, which is based on concepts of latent instability and the layer-lifting nature of convection in squall lines. This perspective contemplates parcel indices of latent instability, which are conceptually simple and physically significant for deep convective phenomena. The novelty of the suggested framework resides in considering the latent instability properties of air throughout the atmospheric column, in contrast with previous approaches, which focus on convection by air from the boundary layer. The suitability of this approach in the context of squall lines is argued on the basis of layer-lifting convection, wherein deep layers of atmospheric air constitute the core of deep convective motions. It is well-known that layer-lifting convection occurs in many squall lines, but until now this feature had not been incorporated into the characterization of latent instability.

The parcel indices used for describing the thermodynamic environment are CAPE and LFC, and their vertical profiles are considered throughout the latent-unstable layer. Besides their simplicity and physical significance, these indices are convenient because they strongly constrain the low and mid-tropospheric portion of thermodynamic soundings. The mathematical relations linking a varied class of soundings to their respective CAPE and LFC profiles are explored in this work, and they underlie an original technique for specifying soundings primarily through CAPE and LFC profiles. This method is conceived as a useful means for designing environments in which to numerically simulate squall lines, such that the sensitivity of SLs to variations of different thermodynamic environmental features can be readily interpreted in terms of CAPE, LFC, and layer-lifting convection.

Numerical simulations of mid-latitude squall lines reveal the unsuitability of conventionally defined CAPE indices for constraining the characteristics of simulated storms. On the other hand, a clear relationship is found between ICAPE and the amplitude of the storm induced

heating, for a given value of environmental shear. The relevance of this result follows from the modulation of the intensity of the mesoscale circulations by the storm induced heating, such that squall lines in greater ICAPE environments produce enhanced cold outflows, stronger surface wind speeds, and higher propagation speeds. It is argued that the skill of ICAPE results from its relation to the buoyancy attained by low and mid-tropospheric parcels as they ascend over the cold pool through layer-lifting convection. The generality of these results is explored further by reviewing studies that analyze numerically simulated squall lines, showing that previous findings can be interpreted in terms of ICAPE variations and layer lifting convection.

An original explanation for the well-known dependence of the storm induced heating on environmental kinematics is elaborated through layer-lifting thinking: low-level shear modulates the fraction of inflowing latent unstable air among the total storm relative inflow, thus affecting the bulk latent instability properties of convecting air. Previous interpretations, which alluded to cold pool-shear optimality, are not supported by the results obtained herein. Similarly, differences in precipitation rates and precipitation efficiencies arising from shear variations are interpreted in terms of changes in the water vapor inflow and variations of the inflow fraction of latent-unstable air, rather than cold pool-shear optimality. Such an interpretation is supported by the ordering of the intensity of surface precipitation rates among simulations with identical shear by the amount of precipitable water.

Surface cold pool temperatures are strongly constrained by the mid and upper portion of the sounding, being similar in all cases considered herein, excluding weakly sheared environments with a relatively dry mid-troposphere. But the application of this result for estimating the cold pool intensity from environmental soundings is limited, given that cold pool temperatures above the surface depend on the mid-tropospheric relative humidity and the shear. In particular, greater moisture inflow is favorable for the production of precipitation and the cooling of cold pool air, while reduced mid-tropospheric relative humidity leads to relatively warm cold pools. This finding contrasts with the notion that environments with a drier mid-troposphere produce enhanced cold pools, a view that stems from the fact that drier air has a greater potential to cool due to rain evaporation; nonetheless, mid-tropospheric air takes part in ascending motions through layer-lifting convection, so that drier conditions can diminish the production of precipitation, and thus limit the cooling of subsiding air. These considerations warrant caution when referring to indices that estimate the downdraft strength and the cold pool intensity through the assumption of saturated descent of mid-tropospheric air.

An unexpected result of these investigations is the existence of a descending branch of the front-to-rear flow, as revealed by Lagrangian particle trajectories. This mesoscale flow, which is not emphasized in previous studies, subsides as it remains negatively buoyant due to the melting of ice. The ascending and descending front-to-rear flow branches are separated in the vertical by the melting line, and the descending branch formally constitutes the upper portion of the cold pool. The existence of the latter might provide an explanation for why observations have revealed deeper cold pools than those reported in numerical studies, as many early simulations of squall lines were performed neglecting ice microphysical processes. In addition, this flow might affect the properties of the cold pool, as it crosses over the rear-inflow jet.

Squall lines are also simulated in tropical environments, allowing a direct comparison with mid-latitude storms, a matter that, to my knowledge, has not been considered in previous investigations. Simulations of tropical squall lines reveal many features in common with mid-latitude storms. For example, they display layer-lifting convective motions, and thus ICAPE

provides a guide for determining the amplitude of the storm induced heating. In addition, their precipitation rates are strongly modulated by the precipitable water, and their cold pool intensities are limited by the production of precipitation, such that drier mid-tropospheric conditions do not necessarily lead to stronger cold pools. But some differences between convection in tropical and mid-latitude environments are noted, especially in association with the depth of the latent instability layer and the depth of cold pools.

Results presented herein suggest that the storm induced heating in tropical squall lines depends on the LFC profile, for a given ICAPE and kinematic environment. This is in contrast to mid-latitude storms, which do not appear to be strongly sensitive to the LFC. It is proposed that the reason behind such a distinction lies in differences in the depth of the cold pools associated with these systems. Mid-latitude storms produce cold pools that are much deeper than the distance that latent unstable parcels need to be lifted in order to reach their LCL and their LFC. This is not the case of tropical squall lines, the cold pools of which are as deep as the lifting that parcels require in order to saturate and to reach their LFC. Thus, in tropical SLs the LFC might affect the probability that parcels reach saturation before rain evaporates into them, thus reducing the vigor of convection. The occurrence of this process was not formally shown in this study; rather, it was deduced by contemplating vertical profiles of parcel indices and layer-lifting convection. These matters require further investigation.

Another difference between tropical and mid-latitude squall lines is that the former storms are more sensitive to relative humidity variations above the latent-unstable layer. This fact probably results from differences in the depth of the layer with latent instability, together with the nearly exponential decrease of water vapor pressure with decreasing temperatures, as implied by the Clausius-Clapeyron equation. In the cases considered herein, the depth of the latent-unstable layer is around 3 km in mid-latitude environments, being half as deep in the tropics. This, together with the fact that average temperature lapse rates tend to be smaller in the tropics than in mid-latitudes, implies that the saturated specific humidity at the top of the latent unstable layer is considerably larger in tropical than in mid-latitude environments. Thus, for a given variation in relative humidity at the top of the latent instability layer, changes in specific humidity are larger in the tropics than in mid-latitudes, implying enhanced impacts related to latent heating and cooling.

The sensitivity of tropical squall lines to variations in relative humidity above the latent-unstable layer evinces the two distinct mechanisms through which the impacts of environmental thermodynamics on storm morphology are contemplated in the present framework: air above the latent-unstable layer mixes turbulently with ascending air, such that drier conditions produce enhanced dilution of buoyancy, while also reducing the amount of precipitation that may reach the surface; on the other hand, the latent unstable air determines the properties of the convective process itself, mainly through the buoyancy of undiluted ascending air. This view is qualitatively similar to the traditional conception of convection, differing on whether the boundary layer or the latent-unstable layer constitutes the reference for separating these processes. Although the distinction based on the latent-unstable layer is conceptually adequate in layer-lifting processes, it might not be discernible in the actual convective process. In other words, such a separation might be somewhat artificial. In fact, violations of the assumptions underlying CAPE and LFC in squall line convection might imply that the "true" latent unstable layer does not coincide with the definition based on parcel theory. Nonetheless, the experiments analyzed herein show the

usefulness of considering the vertical profiles of CAPE and LFC, a framework that is both simple and conceptually revealing.

One interesting consequence of having identified ICAPE as an environmental diagnostic of the storm induced heating, is that it is possible to test the degree to which cold pool-shear balance constrains the morphology of squall lines with varying degrees of latent heating. An original numerical framework is developed for investigating these matters. Results indicate that the latent heating effects can be as significant as those of varying the strength of the low level shear, at least in cases with upshear tilted updrafts. In fact, for a given cold pool intensity, the impact of increasing ICAPE can be similar to the effects of strengthening the low-tropospheric shear. Furthermore, it is argued that, within the layer-lifting convective framework, changes in the environmental shear affect the latent heating produced by convection, by means of modulating the inflow fraction of latent-unstable air. Thus, the relationship between cold pool-shear balance and the morphology of squall lines depends crucially on the vertical profile of CAPE. It is argued that these considerations are of fundamental importance to squall line convection.

It is worth mentioning that it is not the intention of this study to declare that RKW theory is invalid, nor that it lacks practical use. Cold pool-shear balance concepts are certainly useful for understanding the effects of environmental kinematics on the structure of squall lines, and the results reported herein agree with the findings of previous studies lending support to RKW theory. Moreover, RKW theory remains the central paradigm for diagnosing whether the updraft of a squall line will tilt upshear, downshear, or whether it will be vertically oriented. However, it is argued that cold pool-shear balance by itself is an insufficient criterion for determining the overall characteristics of updrafts in squall lines, and it might not be appropriate to consider this diagnostic as the primary determinant of storm morphology.

Practical applications of the results presented in this thesis include possible improvements in the development of statistical methods for forecasting the potential severity and longevity of mesoscale convective systems. For example, ICAPE could be included in analyses to identify best predictors of squall line characteristics, as was done by Coniglio et al. (2007). In addition, estimates of cold pool properties from proximity soundings might benefit from incorporating information provided by ICAPE, which could help address uncertainties of the characteristics of the cold pools of mid-latitude squall lines (e.g. Bryan and Parker 2010). And in the context of tropical meteorology, ICAPE could provide guidance for characterizing the effects of moisture on the interaction between convection and the large scale environment (e.g. see Raymond 2000).

The research reported in this thesis suggests the usefulness of characterizing squall line convection though the layer-lifting conceptual framework. Such processes cannot be described to first order of approximation by cold pool-shear balance, and the latent instability properties of the boundary layer air are insufficient to constrain the morphology of squall lines. By contemplating indices of latent instability which contemplate parcels throughout the atmospheric column, such as ICAPE, observational studies may provide fresh insights into the effects of shear and environmental thermodynamics on the structure of squall lines. Finally, it is worth emphasizing that these considerations do not apply exclusively to squall lines, as there are many other manifestations of layer-lifting phenomena in the atmosphere, such as supercell storms and mesoscale convective complexes.

6.2 Future work

There are many relevant features regarding the environmental modulation of squall line morphology that have not been addressed by the investigations reported herein. In addition, the proposed framework for characterizing the thermodynamic environments of squall lines might also be useful in the context of other deep convective phenomena. This section describes additional studies which can complement and extend the work presented in this dissertation.

It is important to acknowledge that the environments considered herein are not exhaustive of those associated with naturally occurring squall lines. For example, in the case of mid-latitude storms, it might be relevant to consider thermodynamic soundings with capping inversions. Such environments were not contemplated in this work because mid-tropospheric temperature inversions lead to multiple LFCs and ELs associated to a single parcel, which complicates the definition of CAPE with regards to whether the integral of buoyancy should exclude levels of negative parcel buoyancy. Given that the main dynamical link between the CAPE profile and storm morphology found in this study pertains to the modulation of the upper-tropospheric buoyancy, it might be useful to work with CAPE as measured by the positive buoyancy above 4 km. In this way, the dynamically relevant information is retained, and the ambiguity in the definition of the LFC-EL is eliminated (assuming that capping inversions occur below 4 km). The integration of buoyancy is proposed above 4 km height because both numerical experiments and observational evidence suggest that the characteristic depth cold pools in severe mid-latitude squall lines is 4 km.

Environmental variations in which ICAPE is held constant while modifying the vertical distribution of CAPE were not contemplated in this work. Such investigations are relevant because the environments of nocturnal systems can have MUCAPE layers that are elevated (e.g. Trier et al. 2006). Variations in the vertical distribution of CAPE for a given ICAPE and shear might affect the upper-tropospheric heating, due to the resulting changes in the storm-relative inflow of latent-unstable air. In this regard, it is also worth pondering if high CAPE values above the mixed layer are more favorable for the intensity of storm attributes than high surface based CAPE, which could be used for formulating a weighted ICAPE index.

Also of interest in the context of mid-latitude squall lines is the effect of horizontal environmental thermodynamic variations. In particular, it would be relevant to consider how storms respond as they move into regions with less mid-tropospheric moisture, and thus lower ICAPE. Such investigations might reveal insights on the longevity of mature squall lines. As a first attempt to numerically study this problem, it is possible to neglect virtual effects on buoyancy, so that the environmental water vapor can be varied horizontally without having any dynamical significance in dry adiabatic motions. Thus, the evolution of mature squall lines can be studied as their cold pools move into lower ICAPE environments.

With regards to tropical squall lines, future studies of convective quasi-equilibrium states with surface heat fluxes, radiation, and large scale forcing can be conducted using a cloud resolving model, such as SAM. Of particular interest is to investigate the processes that could lead to the buildup of ICAPE and mid-tropospheric moisture in quasi-convective equilibrium regimes. In this regard, I hypothesize that the environmental wind-shear could play an important role as an inhibitor of deep convection, thus leading to an increase of ICAPE in convective quasi-equilibrium regimes. In addition, it is of interest to study how the large scale moisture advection at mid-

tropospheric levels can affect the organization of convection, and thus the convective quasi-equilibrium regimes.

Another possible research project is to evaluate the generality of the results presented herein by simulating idealized squall lines in observationally derived thermodynamic environments. For this it would be necessary to conduct a thorough review of well documented squall line environments in the tropics and in mid-latitudes. A variety of quall lines can then be simulated in realistic thermodynamic environments with simple wind-shear profiles, using a single numerical framework. Incorporating these experiments into the spectrum of cases that have already been considered will enable an evaluation of whether the interpretations presented herein hold for observationally derived soundings, or whether important features have not been considered in previous analyses.

The framework proposed herein for characterizing the thermodynamic environment might also be relevant in the context of supercells, and in particular ICAPE can be tested as a useful environmental diagnostic. It is possible to simulate idealized supercell storms in environments similar to the ones considered for mid-latitude squall lines. And even though supercells propagate by means that differ from those of the squall lines that I have analyzed before, the latent-instability properties of mid-tropospheric parcels can still affect the behavior of such storms, as their associated dynamic pressure perturbations can lift environmental air of mid-tropospheric origin. This research could produce insights into severe weather in general, and tornadogenesis in particular.

Regarding the effectiveness of cold pool-shear balance as a diagnostic of squall line morphology, it remains to determine whether the effects of varying the cold pool intensity are similar to those of varying the environmental shear. In particular, it is worth considering the fact that while more optimal cold pool-shear configurations can lead to more vertical updrafts, the magnitude of the cold pool intensity itself might be important as the primary means for triggering convective cells. These matters, which can be studied using the numerical framework proposed in chapter five, are relevant because the cold pool intensity of mid-latitude squall lines can vary substantially, a feature that is probably underrepresented in the scientific literature.

References

Alexander, G. D., and Young, G. S., 1992: The relationship between EMEX mesoscale precipitation feature properties and their environmental characteristics. *Monthly Weather Review*, **120**(4), 554-564.

Arakawa, A., and Schubert, W. H., 1974: Interaction of a cumulus cloud ensemble with the large-scale environment, Part I. *Journal of the Atmospheric Sciences*, **31**(3), 674-701.

Asai, T., 1964: Cumulus convection in the atmosphere with vertical wind shear: Numerical experiment. *Journal of the Meteorological Society of Japan*, **42**, 245-259.

Ashley, W. S., and Mote, T. L., 2005: Derecho hazards in the United States. *Bulletin of the American Meteorological Society*, **86**(11), 1577-1592.

Barnes, G. M., and Sieckman, K., 1984: The environment of fast-and slow-moving tropical mesoscale convective cloud lines. *Monthly Weather Review*, **112**(9), 1782-1794.

Blanchard, D. O., 1998: Assessing the vertical distribution of convective available potential energy. *Weather and Forecasting*, **13**, 870-877.

Benjamin, T. B., 1968: Gravity currents and related phenomena. *Journal of Fluid Mechanics*, **31**, 209–248.

Bluestein, H. B., and Jain, M. H., 1985: Formation of mesoscale lines of precipitation: severe squall lines in Oklahoma during the spring. *Journal of the Atmospheric Sciences*, **42**, 1711-1732.

Bretherton, C. S., and Smolarkiewicz, P. K., 1989: Gravity waves, compensating subsidence and detrainment around cumulus clouds. *Journal of the atmospheric sciences*, **46**(6), 740-759.

Bryan, G. H., and Fritsch, M. J., 2000: Moist absolute instability: The sixth static stability state. *Bulletin of the American Meteorological Society*, **81**, 1207-1230.

Bryan, G. H., Wyngaard, J. C., and Fritsch, J. M., 2003: Resolution requirements for the simulation of deep moist convection. *Monthly Weather Review.*, **131**, 2394-2416.

Bryan, G. H., 2005: Spurious convective organization in simulated squall lines owing to moist absolutely unstable layers. *Monthly Weather Review*, **133**, 1978-1997.

Bryan, G., Ahijevych, D., Davis, C., Trier, S., and Weisman, M., 2005: Observations of cold pool properties in mesoscale convective systems during BAMEX. In Preprints, 11th Conf. on Mesoscale Processes, Albuquerque, NM, *American Meteorological Society*, JP5J (Vol. 12).

Bryan, G. H., Knievel, J. C., and Parker, M. D., 2006: A Multimodel Assessment of RKW Theory's Relevance to Squall-Line Characteristics. *Monthly Weather Review*, **134**, 2772-2792.

Bryan, G. H., and Rotunno, R., 2008: Gravity currents in a deep anelastic atmosphere. *Journal of the Atmospheric Sciences*, **65**(2), 536-556.

Bryan, G. H., and Parker, M. D., 2010: Observations of a squall line and its near environment using high-frequency rawinsonde launches during VORTEX2. *Monthly Weather Review*, **138**(11), 4076-4097.

Bryan, G. H., and Morrison, H., 2012: Sensitivity of a Simulated Squall Line to Horizontal Resolution and Parameterization of Microphysics. *Monthly Weather Review*, **140**, 202-225.

Bryan, G. H., and Rotunno, R., 2014: The optimal state for gravity currents in shear. *Journal of the Atmospheric Sciences*, **71**(1), 448-468.

Bunkers, M. J., B. A. Klimowski, and J. W. Zeitler, 2002: The importance of parcel choice and the measure of vertical wind shear in evaluating the convective environment. Preprints, 21st Conf. on Severe Local Storms, San Antonio, TX, *American Meteorological Society*, 379–382.

Carlson, T. N., Benjamin, S. G., Forbes, G. S., and Li, Y. F., 1983: Elevated mixed layers in the regional severe storm environment: Conceptual model and case studies. *Monthly Weather Review*, **111**(7), 1453-1474.

Charba, J., 1974:. Application of gravity current model to analysis of squall-line gust front. *Monthly Weather Review*, **102**(2), 140-156.

Cohen, A. E., Coniglio, M. C., Corfidi, S. F., and Corfidi, S. J., 2007: Discrimination of mesoscale convective system environments using sounding observations. *Weather and Forecasting*, **22**, 1045-1062.

Coniglio, M. C., and Stensrud, D. J., 2001: Simulation of a Progressive Derecho Using Composite Initial Conditions. *Monthly Weather Review*, **129**, 1593–1616.

Coniglio, M. C., D. J. Stensrud, and L. J. Wicker, 2006: Effects of upper-level shear on the structure and maintenance of strong quasi-linear mesoscale convective systems. *Journal of the Atmospheric Sciences*, **63,** 1231–1252.

Michael C. Coniglio, Harold E. Brooks, Steven J. Weiss, and Stephen F. Corfidi, 2007: Forecasting the Maintenance of Quasi-Linear Mesoscale Convective Systems. *Weather and Forecasting*, **22**, 556–570.

Coniglio, M. C., Corfidi, S. F., and Kain, J. S., 2012: Views on applying RKW theory: An illustration using the 8 May 2009 derecho-producing convective system. *Monthly Weather Review*, **140**(3), 1023-1043.

Cotton, W. R., Bryan, G., and van den Heever, S. C., 2010: *Storm and Cloud Dynamics*. Academic Press, 820 pp.

Droegemeier, K. K., and Wilhelmson, R. B, 1987: Numerical simulation of thunderstorm outflow dynamics. Part I: Outflow sensitivity experiments and turbulence dynamics. *Journal of the Atmospheric Sciences*, **44**(8), 1180-1210.

Dudhia, J., Moncrieff, M. W., and So, D. W. K., 1987: The two-dimensional dynamics of West African squall lines. *Quarterly Journal of the Royal Meteorological Society*, **113**(475), 121-146.

Emanuel, K. A., 1994: *Atmospheric Convection*. Oxford University Press, 580 pp.

Emanuel, K. A., David Neelin, J., and Bretherton, C. S., 1994: On large-scale circulations in convecting atmospheres. *Quarterly Journal of the Royal Meteorological Society*, **120**(519), 1111-1143.

Evans, J. S., and Doswell III, C. A., 2001: Examination of derecho environments using proximity soundings. *Weather and Forecasting*, **16**, 329-342.

Fawbush, E. J., and Miller, R. C., 1954: The types of air masses in which North American tornadoes form. *Bulleting of the American Meteorological Society*, **35**, 154-165.

Fovell, R. G., and Ogura, Y., 1988: Numerical simulation of a midlatitude squall line in two dimensions. *Journal of the Atmospheric Sciences*, **45**(24), 3846-3879.

Fovell, R. G., and Ogura, Y., 1989: Effect of vertical wind shear on numerically simulated multicell storm structure. *Journal of the Atmospheric Sciences*, **46**, 3144-3176.

Fovell, R. G., Mullendore, G. L., and Kim, S. H., 2006: Discrete propagation in numerically simulated nocturnal squall lines. *Monthly Weather Review*, **134**(12), 3735-3752.

Fritsch, J. M., R. J. Kane, and C. R. Chelius, 1986: The contribution of mesoscale convective weather systems to the warm-season precipitation in the United States. *Journal of Applied Meteorology and Climatology*, **25,** 1333–1345.

Gilmore, M. S., and Wicker, L. J., 1998: The influence of midtropospheric dryness on supercell morphology and evolution. *Monthly Weather Review*, **126**, 943-958.

Houze Jr, R. A., Biggerstaff, M. I., Rutledge, S. A., and Smull, B. F., 1989: Interpretation of Doppler weather radar displays of midlatitude mesoscale convective systems. *Bulletin of the American Meteorological Society*, **70**, 608-619.

Houze, R. A., 1993: *Cloud Dynamics*. Academic Press, 496 pp.

Houze, R. A., 2004: Mesocale convective systems. *Reviews of Geophysics*, **42.** RG4003, doi:10.1029/2004RG000150.

Houze, R. A., 2012: Orographic effects on precipitating clouds. *Reviews of Geophysics*, **50**(1).

James, R. P., Fritsch, J. M., and Markowski, P. M., 2005: Environmental distinctions between cellular and slabular convective lines. *Monthly Weather Review*, **133**(9), 2669-2691.

James, R. P., Markowski, P. M., and Fritsch, J. M., 2006: Bow echo sensitivity to ambient moisture and cold pool strength. *Monthly Weather Review*, **134**, 950-964.

James, R. P., and Markowski, P. M., 2010: A numerical investigation of the effects of dry air aloft on deep convection. *Monthly Weather Review*, **138**, 140-161.

Jirak, I. L., Cotton, W. R., and McAnelly, R. L., 2003: Satellite and radar survey of mesoscale convective system development. *Monthly Weather Review*, **131**(10), 2428-2449.

Jorgensen, D. P., LeMone, M. A., and Trier, S. B, 1997: Structure and evolution of the 22 February 1993 TOGA COARE squall line: Aircraft observations of precipitation, circulation, and surface energy fluxes. *Journal of the Atmospheric Sciences*, **54**(15), 1961-1985.

Keenan, T. D., and Carbone, R. E, 1992: A preliminary morphology of precipitation systems in tropical northern Australia. *Quarterly Journal of the Royal Meteorological Society*, **118**(504), 283-326.

Khairoutdinov, M. F., and Randall, D. A., 2003: Cloud resolving modeling of the ARM summer 1997 IOP: Model formulation, results, uncertainties, and sensitivities. *Journal of the Atmospheric Sciences*, **60**, 607-625.

Khairoutdinov, M., and Randall, D., 2006: High-resolution simulation of shallow-to-deep convection transition over land. *Journal of the Atmospheric Sciences*, **63**(12), 3421-3436.

Klemp, J. B., and Wilhelmson, R. B., 1978: The simulation of three-dimensional convective storm dynamics. *Journal of the Atmospheric Sciences*, **35**(6), 1070-1096.

Lafore, J. P., and Moncrieff, M. W., 1989: A numerical investigation of the organization and interaction of the convective and stratiform regions of tropical squall lines. *Journal of the Atmospheric Sciences*, **46**, 521-544.

LeMone, M. A., Zipser, E. J., and Trier, S. B., 1998: The role of environmental shear and thermodynamic conditions in determining the structure and evolution of mesoscale convective systems during TOGA COARE. *Journal of the Atmospheric Sciences*, **55**(23), 3493-3518.

Lilly, D. K., 1979: The dynamical structure and evolution of thunderstorms and squall lines. *Annual Review of Earth and Planetary Sciences*, **7**, 117.

Liu, C., and Moncrieff, M. W., 1996: A numerical study of the effects of ambient flow and shear on density currents. *Monthly Weather Review*, **124**(10), 2282-2303.

Liu, C., and Moncrieff, M. W., 2000: Simulated density currents in idealized stratified environments. *Monthly Weather Review*, **128**(5), 1420-1437.

Lucas, C., Zipser, E. J., and Ferrier, B. S., 2000: Sensitivity of tropical west Pacific oceanic squall lines to tropospheric wind and moisture profiles. *Journal of the Atmospheric Sciences*, **57**(15), 2351-2373.

Mapes, B. E., 1993: Gregarious tropical convection. *Journal of the Atmospheric Sciences*, **50**, 2026-2037.

Mahoney, K. M., Lackmann, G. M., and Parker, M. D., 2009: The role of momentum transport in the motion of a quasi-idealized mesoscale convective system. *Monthly Weather Review*, *137*(10), 3316-3338.

Markowski, P., and Richardson, Y., 2006: On the classification of vertical wind shear as directional shear versus speed shear. *Weather and Forecasting*, **21**(2), 242-247.

McCaul Jr, E. W., and Weisman, M. L., 2001: The sensitivity of simulated supercell structure and intensity to variations in the shapes of environmental buoyancy and shear profiles. *Monthly Weather Review*, **129**, 664-687.

McCaul Jr, E. W., and Cohen, C., 2002: The impact on simulated storm structure and intensity of variations in the mixed layer and moist layer depths. *Monthly Weather Review*, **130**(7), 1722-1748.

McCaul Jr., E. W., and C. Cohen, 2004: The initiation, longevity, and morphology of simulated convective storms as a function of free-tropospheric relative humidity. Preprints, 22d Conf. on Severe Local Storms, Hyannis, MA, *American Meteorological Soc*iety, CD-ROM, 8A.5.

Mechem, D. B., Houze, R. A., and Chen, S. S., 2002: Layer inflow into precipitating convection over the western tropical Pacific. *Quarterly Journal of the Royal Meteorological Society*, **128**, 1997-2030.

Moncrieff, M. W., and Green, J. S. A., 1972: The propagation and transfer properties of steady convective overturning in shear. *Quarterly Journal of the Royal Meteorological Society*, **98**(416), 336-352.

Moncrieff, M. W., and Miller, M. J., 1976: The dynamics and simulation of tropical cumulonimbus and squall lines. *Quarterly Journal of the Royal Meteorological Society*, **102**(432), 373-394.

Moncrieff, M. W., and So, D. W. K., 1989: A hydrodynamical theory of conservative bounded density currents. *Journal of Fluid Mechanics*, **198**, 177-197.

Moncrieff, M.W., 2010: The multiscale organization of moist convection and the intersection of weather and climate, Climate Dynamics. *Why Does Climate Vary? Geophysics Monographs*, No. 189, Amer. Geophys. Union, 3-26, doi: 10.1029/2008GM000838.

Morrison, H., Curry, J. A., and Khvorostyanov, V. I., 2005: A new double-moment microphysics parameterization for application in cloud and climate models. Part I: Description. *Journal of the Atmospheric Sciences,* **62**, 1678-1693.

Morrison, H., Thompson, G., and Tatarskii, V., 2009: Impact of cloud microphysics on the development of trailing stratiform precipitation in a simulated squall line: Comparison of one-and two-moment schemes. *Monthly Weather Review*, **137**, 991-1007.

Morrison, H., Milbrandt, J. A., Bryan, G. H., Ikeda, K., Tessendorf, S. A., and Thompson, G., 2015: Parameterization of cloud microphysics based on the prediction of bulk ice particle properties. Part 2: Case study comparisons with observations and other schemes. *Journal of the Atmospheric Sciences,* **72**, 312-339.

Newton, C. W., 1950: Structure and mechanism of the prefrontal squall line. *Journal of Meteorology*, **7**(3), 210-222.

Nicholls, M. E., Johnson, R. H., and Cotton, W. R., 1988: The sensitivity of two-dimensional simulations of tropical squall lines to environmental profiles. *Journal of the Atmospheric Sciences*, **45**(23), 3625-3649.

Nicholls, M. E., Pielke, R. A., and Cotton, W. R., 1991: Thermally forced gravity waves in an atmosphere at rest. *Journal of the Atmospheric Sciences*, **48**(16), 1869-1884.

Pandya, R. E., and Durran, D. R., 1996: The Influence of Convectively Generated Thermal Forcing on the Mesoscale Circulation around Squall Lines. *Journal of the Atmospheric Sciences*, **53**, 2924-2951.

Parker, M. D., and Johnson, R. H., 2000: Organizational modes of midlatitude mesoscale convective systems. *Monthly Weather Review*, **128**(10), 3413-3436.

Parker, M. D., 2008: Response of simulated squall lines to low-level cooling. *Journal of the Atmospheric Sciences*, **65**, 1323-1341.

Matthew D. Parker, 2010: Relationship between System Slope and Updraft Intensity in Squall Lines. *Monthly Weather Review*, **138**, 3572–3578.

Raymond, D. J., and Blyth, A. M., 1986: A stochastic mixing model for nonprecipitating cumulus clouds. *Journal of the Atmospheric Sciences*, **43**, 2708-2718.

Raymond, D. J., 1995: Regulation of moist convection over the west Pacific warm pool. *Journal of the Atmospheric Sciences*, **52**(22), 3945-3959.

Raymond, D. J., 2000: Thermodynamic control of tropical rainfall. *Quarterly Journal of the Royal Meteorological Society*, **126**, 889–898.

Rickenbach, T. M., and S. A. Rutledge, 1998: Convection in TOGA COARE: Horizontal scale, morphology, and rainfall production. *Journal of the Atmospheric Sciences,* **55,** 2715–2729.

Robe, F. R., and Emanuel, K. A., 2001: The effect of vertical wind shear on radiative-convective equilibrium states. *Journal of the Atmospheric Sciences*, **58**(11), 1427-1445.

de Rooy, W. C., Bechtold, P., Fröhlich, K., Hohenegger, C., Jonker, H., Mironov, D., Siebesma A. P., Teixeira J. and Yano, J. I., 2013: Entrainment and detrainment in cumulus convection: an overview. *Quarterly Journal of the Royal Meteorological Society*, **139**(670), 1-19.

Rotunno, R., and Klemp, J. B., 1982: The influence of the shear-induced pressure gradient on thunderstorm motion. *Monthly Weather Review*, **110**(2), 136-151.

Rotunno, R., Klemp, J. B., and Weisman, M. L., 1988: A theory for strong, long-lived squall lines. *Journal of the Atmospheric Sciences*, **45**, 463-485.

Richard Rotunno, Joseph B. Klemp, and Morris L. Weisman, 1990: Comments on "A Numerical Investigation of the Organization and Interaction of the Convective and Stratiform Regions of Tropical Squall Lines". *Journal of the Atmospheric Sciences*, **47**, 1031–1033.

Schultz, D. M., Schumacher, P. N., and Doswell III, C. A., 2000: The intricacies of instabilities. *Monthly Weather Review*, **128**(12), 4143-4148.

Seigel, R. B., van den Heever, S. C., and Saleeby, S. M., 2013: Mineral dust indirect effects and cloud radiative feedbacks of a simulated idealized nocturnal squall line. *Atmospheric Chemistry and Physics*, **13**, 4467-4485.

Sherwood, S. C., 2000: On moist instability. *Monthly Weather Review*, **128,** 4139–4142.

Skamarock, W. C., M. L. Weisman, and J. B. Klemp, 1994: Three-dimensional evolution of simulated long-lived squall lines. *Journal of the Atmospheric Sciences*,**51,** 2563–2584.

Stensrud, D. J., Coniglio, M. C., Davies-Jones, R. P., and Evans, J. S., 2005: Comments on "'A Theory for Strong Long-Lived Squall Lines' Revisited". *Journal of the Atmospheric Sciences*, **62**, 2989-2996.

Takemi, T., and Rotunno, R., 2003: The effects of subgrid model mixing and numerical filtering in simulations of mesoscale cloud systems. *Monthly Weather Review*, **131**(9), 2085-2101.

Takemi, T., 2007: Environmental stability control of the intensity of squall lines under low-level shear conditions. *Journal of Geophysical Research: Atmospheres*, **112**(D24).

Takemi, T., 2010: Dependence of the precipitation intensity in mesoscale convective systems to temperature lapse rate. *Atmospheric Research*, **96**, 273-285.

Thorpe, A. J., Miller, M. J., and Moncrieff, M. W., 1982: Two-dimensional convection in non-constant shear: A model of mid-latitude squall lines. *Quarterly Journal of The Royal Meteorological Society*, **108**(458), 739-762.

Trier, S. B., Skamarock, W. C., LeMone, M. A., Parsons, D. B., and Jorgensen, D. P., 1996: Structure and evolution of the 22 February 1993 TOGA COARE squall line: Numerical simulations. *Journal of the Atmospheric Sciences*, **53**(20), 2861-2886.

Trier, S. B., Davis, C. A., Ahijevych, D. A., Weisman, M. L., and Bryan, G. H., 2006: Mechanisms supporting long-lived episodes of propagating nocturnal convection within a 7-day WRF model simulation. *Journal of the Atmospheric Sciences*, **63**(10), 2437-2461.

Wallace, J. M., & Hobbs, P. V., 2006: *Atmospheric Science: an introductory survey* (Vol. 92). Academic press, 504 pp.

Weisman, M. L., and Klemp, J. B., 1982: The dependence of numerically simulated convective storms on vertical wind shear and buoyancy. *Monthly Weather Review*, **110**, 504-520.

Weisman, M. L., and Klemp, J. B., 1984: The structure and classification of numerically simulated convective stormsin directionally varying wind shears. *Monthly Weather Review*, **112**(12), 2479-2498.

Weisman, M. L., Klemp, J. B., and Rotunno, R., 1988: Structure and evolution of numerically simulated squall lines. *Journal of the Atmospheric Sciences*, **45**, 1990-2013.

Weisman, M. L., 1992: The role of convectively generated rear-inflow jets in the evolution of long-lived mesoconvective systems. *Journal of the Atmospheric Sciences*, **49**, 1826-1847.

Weisman, M. L., 1993: The genesis of severe, long-lived bow echoes. *Journal of the Atmospheric Sciences*, **50**, 645-670.

Weisman, M. L., Skamarock, W. C., and Klemp, J. B., 1997: The resolution dependence of explicitly modeled convective systems. *Monthly Weather Review*, **125**, 527-548.

Weisman, M. L., 2001: Bow echoes: A tribute to TT Fujita. *Bulletin of the American Meteorological Society*, **82**(1), 97-116.

Weisman, M. L., and Rotunno, R., 2004: "A theory for strong long-lived squall lines" revisited. *Journal of the Atmospheric Sciences*, **61**, 361-382.

Wilhelmson, R. B., and Klemp, J. B., 1978: A numerical study of storm splitting that leads to long-lived storms. *Journal of the Atmospheric Sciences*, **35**(10), 1974-1986.

Wyss, J., and Emanuel, K. A., 1988: The pre-storm environment of midlatitude prefrontal squall lines. *Monthly Weather Review*, **116**, 790-794.

Xu, Q., 1992: Density currents in shear flows-A two-fluid model. *Journal of the Atmospheric Sciences, 49*(6), 511-524.

Xu, Q., and Moncrieff, M. W., 1994: Density current circulations in shear flows. *Journal of the Atmospheric Sciences*, **51**(3), 434-446.

Xue, M., Xu, Q., and Droegemeier, K. K., 1997: A theoretical and numerical study of density currents in nonconstant shear flows. *Journal of the Atmospheric Sciences*, **54**(15), 1998-2019.

Xue, M., 2002: Density currents in shear flows: Effects of rigid lid and cold-pool internal circulation, and application to squall line dynamics. *Quarterly Journal of the Royal Meteorological Society*, **128**(579), 47-73.

Yamaguchi, T., and Randall, D. A., 2012: Cooling of Entrained Parcels in a Large-Eddy Simulation. *Journal of the Atmospheric Sciences*, **69**, 1118-1136.

Yang, M. H., and Houze Jr, R. A., 1995: Sensitivity of squall-line rear inflow to ice microphysics and environmental humidity. *Monthly Weather Review*, **123**(11), 3175-3193.

Yano, J. I., and Plant, R. S. 2012: Convective quasi-equilibrium. *Reviews of Geophysics*, *50*(4).

Zhang, G. J., and McFarlane, N. A., 1995: Sensitivity of climate simulations to the parameterization of cumulus convection in the Canadian Climate Centre general circulation model. *Atmosphere-Ocean*, **33**(3), 407-446.

Zhang, C., 2005: Madden-julian oscillation. *Reviews of Geophysics*, **43**(2).

Zipser, E. J., 1977: Mesoscale and convective-scale downdrafts as distinct components of squall-line structure. *Monthly Weather Review*, **105**, 1568-1589.